UNIVERSITAT DE BARCELONA

Inkjet-Printed Flexible Electronic Devices: from High-k Capacitors to h-BN/Graphene Thin Film Transistors

Giovanni Vescio

UNIVERSITAT DE BARCELONA

Inkjet-Printed Flexible Electronic Devices: from High-k Capacitors to h-BN/Graphene Thin Film Transistors

PhD Thesis Dissertation
submitted in partial fulfilment of the requirements for the degree of
Doctor by the University of Barcelona

Author

Giovanni Vescio

Supervisors

Prof. Albert Cornet Calveras

Dr. Albert Cirera Hernández

Tutor

Dr. Albert Cirera Hernández

Barcelona, 2017

Engineering and Advanced Technologies Program

Micro and Nanotechnology and Nanoscopies for Electronic Devices (MIND)

Institute of Nanoscience and Nanotechnology (IN^2UB)

Department of Engineering, Section of Electronics, Physics Faculty, University of Barcelona

UNIVERSITAT DE BARCELONA

Inkjet-Printed Flexible Electronic Devices: from High-k Capacitors to h-BN/Graphene Thin Film Transistors

PhD Thesis Dissertation
submitted in partial fulfilment of the requirements for the degree of
Doctor by the University of Barcelona

Author
Giovanni Vescio

Supervisors
Prof. Albert Cornet Calveras
Dr. Albert Cirera Hernández
Tutor
Dr. Albert Cirera Hernández

Barcelona, 2017

Engineering and Advanced Technologies Program
Micro and Nanotechnology and Nanoscopies for Electronic Devices (MIND)
Institute of Nanoscience and Nanotechnology (IN^2UB)
Department of Engineering, Section of Electronics, Physics Faculty, University of Barcelona

a Valentino Orlando

Abstract

The soaring global demand for flexible, wearable and transparent devices has been driven by the advent of the Internet-of-Things (IoT), where smart electronic objects are expected to be, at anytime and everywhere, aware of and interactive with the environment by means of a wireless network. During the last decade, printed electronics holds the promise of enabling low-cost, scalable solutions by exploiting the ability of innovative fabrication technologies that are both cost-competitive and eco-friendly, using disrupting materials to be employed as processed inks onto a large-area flexible substrate.

To date, different printing technologies have been employed to demonstrate appealing flexible devices such as organic light-emitting diode (OLED) displays, radio-frequency identification (RFID) antennas for intelligent packaging, solar cells or wearable healthcare sensors (most of time based on organic thin-film transistors, OTFTs). However, compared to the well-established silicon technology, all-printed devices must overcome several hurdles. Among them, the most critical issues concern parameters such as the electrical mobility (μ) and the relative permittivity (ε), whose low values in current available inks result in a low integration density.

The main objective of this Thesis was focused on demonstrating inkjet printing technology as a powerful tool for the oncoming flexible printed electronics development. Indeed, in this Thesis Project inkjet printing technology is validated as a versatile method for the manufacturing of different robust applications (in particular flexible sensors and hybrid circuitry), and especially as a complement and alternative to standard silicon technology for the development of high-quality flexible fully-inkjet printed passive and active devices such as capacitors, memristors and transistors based on novel outstanding functional nanomaterials. Basically, this Thesis addresses the exploration of new promising application areas, where inkjet-printing technology could contribute solving traditional issues by improving the manufacturing processes and the development of novel outstanding smart devices on flexible substrates.
First of all, the dissertation deals with the demonstration of inkjet printing as promising technique in comparison to the other current printing methods for the fabrication of robust gas sensor circuitry platforms and as an alternative method to surface mount-technology (SMT), in order to assemble surface mount-devices (SMDs) onto previous inkjet-printed circuitry for flexible electronic applications.

The second main topic of this Thesis was focused on the implementation of new solutions to chase and follow the guidelines of the ITRS roadmap for the next generation of flexible electronic applications by the ink formulation of novel dielectric inks. The latter allowed the design, manufacturing and characterization (from both morphological and electrical points of view) of excellent fully-inkjet printed electronic devices.

Primarily, the study was centred on the high-*k* HfO_2 dielectric ink and devoted to the investigation of the physical and chemical properties of the inkjet-printed insulator. Afterwards, the dielectric material was demonstrated as a suitable high-*k* material to achieve flexible fully-inkjet printed electronic devices such as metal-insulator-metal (MIM) capacitors (ε_{HfO2}~12.6 and a capacitance per unit area of ~1 nF mm^2) and ReRAM memories (I_{ON}/I_{OFF} ratio of around six orders of magnitude and more than 516 resistive switching cycles).

Bearing in mind the well-known outstanding properties of heterostructures based on two-dimensional (2D) atomic crystals, the aim of the Thesis moved to the formulation of an eco-friendly water-based ink made from 2D nanosheets of hexagonal boron nitride (h-BN), specially designed to be printed as dielectric material. The h-BN ink showed a high-*k* dielectric constant value ε_{hBN} ~ 6.9 and was demonstrated as suitable gate oxide for flexible fully-inkjet printed graphene/h-BN heterostructures for TFT devices. Distinctive electrical properties with state-of-the-art mobility up to 110 $cm^2V^{-1}s^{-1}$ are reported, demonstrating the outstanding performance of the h-BN ink both in flat and under bending conditions, which have been achieved, to the best of our knowledge, for the first time in literature.

Abstract idioma oficial

La creciente demanda de dispositivos flexibles, portátiles y transparentes ha sido impulsada por la irrupción del *Internet de las cosas* (IoT, de sus siglas en inglés), donde se pretende que los objetos electrónicos inteligentes estén constantemente sujetos a cambio e interactúen con el medio ambiente mediante una conexión inalámbrica (red 5G). Durante la última década, la electrónica impresa ha adquirido gran protagonismo con la promesa de permitir soluciones escalables y de bajo coste por medio de nuevas tecnologías de fabricación, rentables y respetuosas con el medio ambiente, empleando materiales novedosos en forma de tinta.

En primer lugar, esta Tesis demuestra la viabilidad de la impresión por inyección de tinta como técnica prometedora, en comparación con otros métodos de impresión actuales, para la fabricación de circuitos sensores de gas y como método alternativo para el ensamblaje de *chips* sobre circuitos previamente impresos mediante inyección de tinta para aplicaciones electrónicas híbridas y flexibles.

La segunda parte de esta Tesis se centró en el desarrollo de nuevas tintas dieléctricas como solución para seguir la hoja de ruta para la próxima generación de aplicaciones electrónicas flexibles. Primeramente, el estudio se centró en la caracterización de las propiedades físicas y químicas de la tinta de HfO_2 de elevada constante dieléctrica (ε_{HfO2} ~ 12.6) impresa mediante inyección de tinta. Acto seguido se demostró que el HfO_2 es un dieléctrico adecuado para conseguir dispositivos electrónicos flexibles totalmente impresos por inyección de tinta, tales como condensadores MIM (C_{ox} ~ 1 nF mm^{-2}) y memorias ReRAM (más de 516 ciclos de conmutación resistiva).

Finalmente, teniendo en cuenta las propiedades destacadas de las heteroestructuras bidimensionales (2D), la Tesis se focalizó en la formulación de una tinta a base de agua a partir de nano-láminas 2D de nitruro de boro (h-BN), especialmente desarrollada para ser impresa como material dieléctrico (permitividad ε_{hBN} ~ 6.9). La tinta de h-BN actúa correctamente como óxido de puerta para transistores flexibles con estructura semiconductor / aislante (grafeno / h-BN), respectivamente. Los dispositivos han sido totalmente fabricados por inyección de tinta sobre PET, lográndose una movilidad de huecos del canal semiconductor de grafeno de hasta 110 $cm^2V^{-1}s^{-1}$.

Acknowledgements

Questa tesi di dottorato é il risultatato di un cammino imprevisto ed impervio nel corso di 5 lunghi anni, però ricco di soddisfazioni e sopratutto di grandi relazioni di lavoro e amicizie. Il completamento del progetto di dottorato non sarebbe stato possibile senza l'appoggio incondizionato de moltissime persone che mi hanno motivato e sopportato ("siempre me quejo de algo") continuamente.

Prima di tutto voglio dare il mio più profonzo ringraziamento ai miei direttori di tesi Prof. Albert cornet Calveras e al Dr. Albert Cirera Hernández. Entrambi hanno reso possibile la realizzazione di un percorso di formazione ricchissimo di esperienze positive e sempre con totale disponibilità dimostrata per l'immensa pazienza nel sopportare le pedanti richieste di delucidazioni.

Inoltre devo ringraziare la Universitat de Barcelona e tutto il team delle segreterie (di elettronica e fisica) che mi hanno sotenuto ed aiutato per ottenere la borsa di studio FPU del Ministerio de Educaciòn y de Cultura y Deporte che ha finanziato completamente la mia formazione in Barcellona e in Cambridge nel Cambridge Graphene Centre. Colgo l'occasione per ringraziere tutto il team del gruppo di ricerca del Prof. Andrea Ferrari e il Dr. Felice Torrisi. La loro accoglienza é stata una svolta importante nella mia formazione professionale.

Grazie mille al gruppo MIND della Universitat de Barcelona che mi ha accolto come un catalano doc, facendomi sentire sempre uno di loro. Non ci sono parole tanto buone per poter ringraziare in primis colleghi e amici allo stesso tempo così speciali come Julià ("mi post-doc"), Oriol M. ("jefe del laboratorio"), Xavi ("el mejor emprendedero en la tierra"), Beatriz ("la malagueña"), Nuria ("me hizo descubrir el mundo del tè"), Sergi C.("mi post-doc en la UAB") y Radouane L. che mi ha motivato dal primo minuto. Ringrazio tutti gli altri colleghi per aver condiviso molti dei loro momenti tra una "cerveza y otra", Dani P., Olga C., Aida V, Cristian, Llorenç, Elena X, Guillelm,Anna, Luis F., y toda la grande planta del BlasFET group i del Lens.

Alla mia famiglia italiana, e oramai molto piú allargata ed internazionale. Ti adoro Montse. Al clan Corbella e alla loro incondizionata disponibilitá e presenza (sopratutto con i tupper finesettimanali della Lola). A tutti i familiari, anche a quelli che gioiranno da là in alto, che hanno supportato sempre con orgoglio i miei traguardi e motivato, con calorosi sorrisi, a raggiungerne dei nuovi. Ai colleghi – compagni – amici – fratelli che mi hanno teso sempre una mano condividendo parti di inestimabile valore della mia vita.

List of Figures

List of acronyms

2D: two dimensional

3D: three dimensional

AgNP: silver nanoparticles

APS: atmospheric plasma spray

BNNSs: hexagonal boron nitrides nanosheets

CF: conductive filament

CGC: Cambridge Graphene Centre

CMOS: complementary metal-oxide-semiconductor

CNT: carbon nanotubes

C_{ox} : capacitance per unit area

DMP: dimatix 2831 series

DOD: drop-on-demand inkjet

EHD: electro-hydro-dynamic

FET: field-effect transistors

Gr: graphene

h-BN: hexagonal boron nitride

HfO_2: hafnium oxide

high-k: high dielectric constant material

HRS: high-resistance state

IoT: internet-of-things

ITRS: international terrestrial reference system

LCD: liquid-crystal displays

LPE: liquid phase exfoliation

LRS: low-resistance state

MIM: metal–insulator-metal

MoS2 : molybdenum disulfide

MOSFET: metal–oxide–semiconductor field-effect transistor

MPa: mega pascal

NVM: non-volatile memories

OE-A : organic and printed electronics roadmap

OLED: organic light-emitting diode

PET: polyethylene terephthalate

PI: polyimide

PLED: polymer light-emitting diode

R2R: roll-to-roll

ReRAM: resistive random-access memory

RFID: radio-frequency identification

RS: resistive switching

SMD: surface mount-device

SMT: surface mount-technology

TFT: thin-film transistors

TiO_{2-x}: titanium sub-oxide

TMDs: transition metal dichalcogenide monolayers

UAB: Universitat Autònoma de Barcelona

UB: Universitat de Barcelona

ε : dielectric constant , permittivity

μ : carrier mobility

Index

Chapter 1: Dissertation Summary

1.1 Introduction

The graphic printing of multi-coloured clothes by means of silk-screen printing (serigraphy) technique was probably the first large-scale explosion of human being creativity more than a thousand years ago.[1,2] Since that time, printing technology was enormously developed after the beginning of typography with the production of the first newspapers and books.[3] Nowadays, despite the advent of digital media that scaled down the significant notoriety of print reproduction on paper, an appealing new project of printing functional materials onto flexible substrates was induced to boost the so-called soft electronics, i.e. wearable and stretchable circuits.[4]

The use of functional materials converted disruptively printed electronics into an established cost-efficient technology for flexible electronics by changing the standard system for the fabrication of large area flexible electronic devices. [5] Printing electronics techniques, which are additive bottom-up methods, promote low-cost fast prototyping and production of small batches due to the reduced material waste and because subtractive processes such as lithography and etching are not necessary.

Many efforts have been spent in order to formulate a variety of innovative material compounds to supply conductive, semiconductive and insulating inks.[6] To date, various technologies, generally used in traditional graphical printing, such as gravure-[7], screen-[8], flexographic-[9,10]and inkjet-printing[11,12] have been employed to deposit multi-layered electronic components as either single devices or complex fully-printed circuits. Recently, several exciting advances in flexible printed electronics have been achieved by the fabrication on plastic[13] and paper substrates[14] of devices such as radio-frequency identification (RFID) antennas,[15] diodes,[16] capacitors (metal–insulator-metal, MIM)[17–19], thin-film transistors (TFT),[20–22] organic light-emitting diode (OLED) displays,[23] photovoltaic cells (solar cells),[24,25] batteries and supercapacitors.[26] The integration of all these device paves the way for roll-up displays (information displays), wearable energy-harvesting systems (identification tagging),[27] electronic sensors for robots as artificial-skins (distributed sensing),[28] biological sensors (health diagnostic and human interfacing),[29,30] that will partially fulfil the requirements for pervasive sensing, transducing and computing in the forthcoming Internet-of-Things (IoT).[31–33]

Amongst the current digital printing technologies, the selection of the most appropriate printing technique is strongly related to the geometrical, physical and electrical device requirements. Under these conditions, drop-on-demand inkjet printing stands out as a cost-efficient technique, quick (up to 15 m/s) digital-pattern design (fast prototyping), mask-less (non-contact method), which guarantees controlled selective deposition of few picoliters (down to 1 pL for each single drop) of novel nanomaterial or precursor inks.[34,35] Besides minimizing the device size and the material waste, inkjet printing allows for large-area manufacturing when it is integrated in a roll-to-roll (R2R) [16] system which promotes new scalable electronics markets with profitable benefits by introducing flexible eco-friendly substrate and nanomaterials for applications in everyday life. Understanding the interaction between the functional material, the printing process and the substrate has been and is being done to successfully develop sophisticated electronic devices.

In this work, inkjet printing technology is demonstrated as a versatile method for the manufacturing of different robust platform applications (circuitry and sensors) and as a complement and alternative to standard fabrication process for soldering flexible hybrid circuit on previously inkjet-printed circuitry.

Moreover, although flexible substrate (polymeric plastic or paper) allows for properties such as transparency and/or resistance to mechanical deformation, printed devices also must fulfil current electronic roadmap requirements.[37–39] Because of this, electrical mobility (μ) and relative permittivity (ε) are the most critical parameters in printed electronic devices due to the liquid dispersion status of semiconductive and insulating inks, respectively, in comparison to the well-established silicon technology.

The main work of this thesis embraces topics that range from the dielectric ink customization of the 3D nanoparticles-based high-k HfO_2 compound to the formulation of biocompatible 2D nanosheets-based high-k h-BN composite, aiming at their implementation into fully inkjet-printed electronic devices such as capacitors, memories and transistors that have been fabricated on flexible polymeric substrates.

1.2 Main Contribution of This Thesis

The soaring global demand for flexible, wearable and transparent devices has been driven by the advent of the Internet-of-Things (IoT), where smart electronic objects are expected to be, at anytime and everywhere, aware of and interactive with the environment by means of a wireless network. Current CMOS technology cannot fulfil this necessity for pervasive computing and sensing applications. Indeed, within this context, considering the horizon of *IoT*, the main objective of this Thesis was focused on demonstrating inkjet printing technology as a powerful tool for the oncoming flexible printed electronics development.

At the first stage of the Thesis, the main goal was the investigation of new promising application areas where inkjet-printing technology could contribute solving traditional issues and improving the manufacturing processes. The necessity of a new kind of flexible and wearable sensors arose with a technology reliable able to deposit novel materials. As a consequence, inkjet printing was used as tool for gas sensor circuitry platforms production, the same devices being later compared to new ones manufactured by the mature and more consolidated screen-printing technology. (***Paper I***) The implementation of gas sensing devices was demonstrated by the development of a metal oxide layer (titanium sub-oxide, TiO_{2-x}) deposited onto the inkjet-printed circuitry by atmospheric plasma spray (APS) as active layer. (***Paper II***) Taking into account that the proposed sensors require the implementation of a more sophisticated system for their data processing and transmission, it was proposed a flexible hybrid printed circuit, where the complex electronic components (chips) are directly integrated to the previously inkjet-printed circuitry. Therefore, we explored the high-resolution deposition of controlled drop volume of 10 pL silver ink for a novel approach to connect (assemble) surface-mount devices (SMDs) onto previously inkjet-printed circuitry (***Paper III***).

At the second stage of the thesis, aware of the promising potentialities of inkjet printing and conscious of the reliability of the conductive silver ink, the investigation was focused on reliable high-k materialsthe due to the lacks in dielectric inks for inkjet technology and its fundamental role in electronic systems. Thus, all the efforts were spent on the customization of a commercial high-k dielectric (HfO_2) solution, adjusting the rheology in order to be inkjet-printable. The characterization study and the electrical properties of the inkjet-printed HfO_2 high-k dielectric are, to the best of our knowledge, demonstrated for the first time in literature by the fabrication of

flexible fully inkjet-printed electronic devices such as capacitors (***Paper IV***) and memory devices(***Paper V*** and ***Paper VI***).

Last but not least, in the third stage of the thesis the research objectives moved to the formulation of a biocompatible water-based h-BN ink, designed to be printed as high-k dielectric material. Fully inkjet-printed MIM-structured devices on flexible substrate and flexible fully inkjet-printed graphene/h-BN TFT devices were fabricated, to the best of our knowledge for the first time in literature, achieving a hole carrier mobility of graphene up to 110 $cm^2V^{-1}s^{-1}$, and demonstrating the distinctive electrical properties, in normal mechanical conditions or under bending (***Paper VII*** *Submitted*).

Taking the advantages of a synergy between different European Universities, this Thesis has been carried out in the facilities of the Universitat de Barcelona (UB), the Universitat Autònoma de Barcelona (UAB) and the Cambridge Graphene Centre (CGC) of the University of Cambridge (United Kingdom). Consequently, this thesis has been developed relying on an established and consolidated knowledge on inkjet-printing technology, memory device characterization and ink formulation of graphene-based 2D materials, respectively.

1.2.1. Objectives of the Thesis

I would like to draw attention to the main contributions of this work and the importance can be stated because of the following reasons:

- To check the robustness and reliability of the inkjet-printed in a functional gas sensing platform. Because of the UB expertise in gas sensing, this field has been selected as a demonstration benchmark for inkjet-printing, whose results will be compared to the more mature and consolidated screen-printing technology. The different failure phenomena of the printed platforms will be analysed, and different solutions presented. Consequently, the manufacturing of robust and reliable flexible gas sensor platforms using inkjet printing technology for the development of a metal oxide layer (titanium sub-oxide, TiO_{2-x}) deposited onto the inkjet-printed circuitry by atmospheric plasma spray (APS) as active layer.

- To demonstrate inkjet printing technology as an alternative method to surface mount-technology (SMT) for the assembling (soldering) of surface mount-devices (SMDs) onto previous inkjet-printed circuitry on flexible substrates.

- To correlate inkjet printing of a thin film oxide with the electrical properties of devices based on high-*k* materials. Because of its dielectric and printing properties, hafnium oxide (HfO_2) has been selected, with different controlled resolution towards manufacturing flexible fully inkjet-printed metal – insulator (HfO_2) – metal (MIM) capacitors.

- To study in-depth the bipolar resistive switching phenomenon of fully-inkjet deposited memristors (ReRAMs) with simple structure such as MIMs. HfO_2 will be selected as insulating material for the reasons stated above, thus forming simple and flexible Au/HfO_2/Ag and Pt/HfO_2/Ag structures by means of drop-on-demand inkjet printing technology. The inkjet-printed memristors performances will be compared to CMOS conventional technology.

- To develop of a systematic process for the large production of a proper dielectric ink that can act as insulating layer in flexible state-of-the-art 2D graphene-based electronics. Hexagonal boron nitride (h-BN) has been selected because of its high-*k* dielectric and biocompatibility properties. As well, the long-term expertise of the CGC in 2D graphene-based electronics will be paramount for the expected achievements within this Thesis Project.

1.2.2. Thesis Outline

The structure of the present thesis dissertation can be divided into 6 well-defined Chapters in order to achieve a full comprehension on the present topic: the introduction (Chapter 1) is followed by the state-of-the-art of printed electronics (Chapter 2), and then results interpretation (Chapters 2 to 5) and conclusion (Chapter 6) are presented. In the following lines, the basic objectives of each Chapter are thoroughly described:

Chapter 1 presents the dissertation overview, where the most relevant aspects of this thesis are briefly introduced.

Chapter 2 explains and describes the background of printed electronics, with an overview of the current printing techniques and of the common flexible electronics applications. The main topic is the review of the existing ink functional materials (conductive, semiconductive and insulating) and the lack of suitable ink nanomaterials in order to accomplish the ITRS roadmap target requirements. Moreover,inkjet printing technology is presented as a powerful tool in comparison to established standard processes of manufacturing.

Chapter 3 is focused on the application versatility of the inkjet-printed silver nanoparticles-based ink (AgNP). From one side the conductive material is employed as circuitry for gas sensor platforms, and in order to identify the causes of possible device failure, a complete characterization of the flexible inkjet-printed circuitry platforms is performed by a long-term characterization and aging tests (*Paper I*). Once the optimization of the gas sensor platforms is achieved, the implementation of gas sensing devices is demonstrated by the development of a metal oxide layer (titanium sub-oxide, TiO_{2-x}) deposited onto the inkjet-printed circuitry by atmospheric plasma spray (APS) as active layer.

On the other side the AgNP is applied such as soldering material for fully inkjet-printed junctions on flexible hybrid electronics circuits (*Paper III*). Electrical, mechanical and morphological characterization is carried out to assess the performance of the new method, which is compared to common benchmark materials (i.e. silver epoxy and solder); as well, the manufacturing of a flexible hybrid circuit, controlled by an Arduino board, demonstrates the applicability and scalability of the AgNP as a suitable material for SMD soldering.

Chapter 4 presents the use of the high-k HfO_2 nanoparticles-based dielectric ink, towards the fabrication of flexible fully inkjet-printed devices, capacitors (MIMs) (*Paper IV*) and memristors (*Paper V*), and is devoted to the physical and chemical properties of the printed insulator. Electrical characterization evidenced, by means of capacitance- and voltage-dependent measurements, that the MIMs work properly within the ITRS 2016 roadmap requirements and, by means of cyclic current-voltage measurements, that the HfO_2-based ReRAM devices work properly reaching more than 516 Resistive Switching cycles.

Chapter 5 shows the formulation, for large scale production, of an insulating biocompatible ink based on 2D h-BN nanosheets. Flexible fully inkjet-printed MIMs are demonstrated to confirm the expected high-k dielectric constant value of h-BN ink. The high-k dielectric h-BN layer is proved to be a suitable material to act as gate oxide for flexible fully-inkjet-printed graphene/h-BN heterostructures for TFT devices, and it demonstrates distinctive electrical properties, both in normal mechanical conditions or under bending.

Finally, *Chapter 6* summarizes the main results of this thesis, as well as the conclusions that are drawn from the research.

1.3 List of publications

Only the publications included in this list shall be considered for the evaluation of this PhD Dissertation. A reproduction of each publication can be found on the indicated pages below. A complete list of the author publications, updated on April 2017, is included in the scientific curriculum vitae (*Appendix E*).

Paper I. Beatriz Medina-Rodriguez, Francisco Ramos, Giovanni Vescio, Xavier Arrese, Aïda Varea, and Albert Cirera, "Fabrication, Performances and Aging of Flexible Gas Sensor Platforms," *J. Mater. Sci. Eng. B*, vol. **5**, no. 4, pp. 170–176, Apr. 2015.

** The author's contribution: planning and performing parts of the experiments and writing parts of the manuscript.*

Paper II. M. Gardon, O. Monereo, S. Dosta, G. Vescio, A. Cirera, and J. M. Guilemany, "New procedures for building-up the active layer of gas sensors on flexible polymers," *Surf. Coatings Technol.*, vol. **235**, pp. 848–852, Nov. 2013.

** The author's contribution: planning and performing parts of the experiments and writing parts of the manuscript.*

Paper III. J. Arrese, G. Vescio, E. Xuriguera, B. Medina-Rodriguez, A. Cornet, and A. Cirera, "Flexible hybrid circuit fully inkjet-printed: Surface mount devices assembled by silver nanoparticles-based inkjet ink," *J. Appl. Phys.*, vol. **121**, no. 10, p. 104904, Mar. 2017.

** The author's contribution: planning and performing parts of the experiments and writing parts of the manuscript.*

Paper IV. G. Vescio, J. López-Vidrier, R. Leghrib, A. Cornet, and A. Cirera, "Flexible inkjet printed high-k HfO 2 -based MIM capacitors," *J. Mater. Chem. C*, vol. **4**, no. 9, pp. 1804–1812, 2016.

** The author's contribution: planning and performing the experiments, evaluation of the results and writing the main parts of the manuscript.*

Paper V. G. Vescio, A. Crespo-Yepes, D. Alonso, S. Claramunt, M. Porti, R. Rodriguez, A. Cornet, A. Cirera, M. Nafria, and X. Aymerich, "Inkjet Printed HfO 2 -Based ReRAMs: First Demonstration and Performance Characterization," *IEEE Electron Device Lett.*, vol. **38**, no. 4, pp. 457–460, Apr. 2017.

** The author's contribution: planning and performing the experiments, evaluation of the results and writing the main parts of the manuscript.*

Paper VI. The article has been SUBMITTED; G. Vescio*, G. Martín, A. Crespo-Yepes, S. Claramunt, D. Alonso, J. López-Vidrier, S. Estradé, M. Porti, R. Rodriguez, F. Peiró A. Cornet, A. Cirera, M. Nafría. — Low-Power High-Performance Low-Cost Non-Volatile Inkjet Printed HfO2-based ReRAM: from nanoscale to device characterization.

** The author's contribution: planning and performing the experiments, evaluation of the results and writing the main parts of the manuscript.*

Paper VII. The article has been SUBMITTED; Vescio G., Lombardi L., López-Vidrier J., Martín G., López-Conesa L., Estradé S., Karagiannidis P., Hodge S., Peiró F., Cornet A., Ferrari A. C., Cirera A., Torrisi F. — Flexible fully inkjet-printed Gr/h-BN thin film transistor ;

** The author's contribution: planning and performing the experiments, evaluation of the results and writing the main parts of the manuscript.*

References:

1. Sheng, A. Why Ancient Silk Is Still Gold: Issues in Chinese Textile History. *Ars Orient.* (1999). doi:10.2307/4629553
2. Li, J. Silk-screen printing ink formulation. *Faming Zhuanli Shenqing* (2015).
3. Gee, S. Meggs' History of Graphic Design. *Tech. Commun.* (2013).
4. Arias, A. C., MacKenzie, J. D., McCulloch, I., Rivnay, J. & Salleo, A. Materials and applications for large area electronics: Solution-based approaches. *Chem. Rev.* (2010). doi:10.1021/cr900150b
5. Skotheim, T. A. & Reynolds, J. R. *Handbook of Conducting Polymers: Conjugated Polymers Processing and Applications*. *Chemistry & …* (2007).
6. Kamyshny, A. & Magdassi, S. Conductive nanomaterials for printed electronics. *Small* **10,** 3515–3535 (2014).
7. Pudas, M., Halonen, N., Granat, P. & Vähäkangas, J. Gravure printing of conductive particulate polymer inks on flexible substrates. *Prog. Org. Coatings* **54,** 310–316 (2005).
8. Krebs, F. C. *et al.* A complete process for production of flexible large area polymer solar cells entirely using screen printing—First public demonstration. *Sol. Energy Mater. Sol. Cells* **93,** 422–441 (2009).
9. Søndergaard, R. R., Hösel, M. & Krebs, F. C. Roll-to-Roll fabrication of large area functional organic materials. *J. Polym. Sci. Part B Polym. Phys.* **51,** 16–34 (2013).
10. Choi, H. W., Zhou, T., Singh, M. & Jabbour, G. E. Recent developments and directions in printed nanomaterials. *Nanoscale* **7,** 3338–3355 (2014).
11. Calvert, P. Inkjet printing for materials and devices. *Chemistry of Materials* **13,** 3299–3305 (2001).
12. Singh, M., Haverinen, H. M., Dhagat, P. & Jabbour, G. E. Inkjet printing-process and its applications. *Adv. Mater.* **22,** 673–685 (2010).
13. Kaltenbrunner, M. *et al.* An ultra-lightweight design for imperceptible plastic electronics. *Nature* **499,** 458–63 (2013).
14. Tobjörk, D. & Österbacka, R. Paper Electronics. *Adv. Mater.* **23,** 1935–1961 (2011).
15. Subramanian, V., Chang, P. C., Lee, J. B., Molesa, S. E. & Volkman, S. K. Printed organic transistors for ultra-low-cost RFID applications. *IEEE Trans. Components Packag. Technol.* **28,** 742–747 (2005).
16. Choi, H. W., Zhou, T., Singh, M. & Jabbour, G. E. Recent developments and directions in printed nanomaterials. *Nanoscale* **7,** 3338–3355 (2014).
17. Vescio, G., López-Vidrier, J., Leghrib, R., Cornet, A. & Cirera, A. Flexible inkjet printed high-k HfO 2 -based MIM capacitors. *J. Mater. Chem. C* **4,** 1804–1812 (2016).
18. Cheng, C. H. *et al.* High-Performance MIM Capacitors Using a High-κ TiZrO Dielectric. *J.*

Electrochem. Soc. **155,** G295 (2008).

19. Lim, J. *et al.* All-inkjet-printed Metal-Insulator-Metal (MIM) capacitor. *Curr. Appl. Phys.* **12,** e14–e17 (2012).
20. Koo, H. *et al.* Scalability of carbon-nanotube-based thin film transistors for flexible electronic devices manufactured using an all roll-to-roll gravure printing system. *Sci. Rep.* **5,** 14459 (2015).
21. Burns, S. E., Cain, P., Mills, J., Wang, J. & Sirringhaus, H. Inkjet Printing of Polymer Thin-Film Transistor Circuits. *MRS Bull.* **28,** 829–834 (2003).
22. Secor, E. B., Smith, J., Marks, T. J. & Hersam, M. C. High-Performance Inkjet-Printed Indium-Gallium-Zinc-Oxide Transistors Enabled by Embedded, Chemically Stable Graphene Electrodes. *ACS Appl. Mater. Interfaces* **8,** 17428–17434 (2016).
23. Chang, S.-C. *et al.* Multicolor Organic Light-Emitting Diodes Processed by Hybrid Inkjet Printing. *Adv. Mater.* **11,** 734–737 (1999).
24. Hoth, C. N., Schilinsky, P., Choulis, S. A. & Brabec, C. J. Printing highly efficient organic solar cells. *Nano Lett.* **8,** 2806–2813 (2008).
25. Kaltenbrunner, M. *et al.* Ultrathin and lightweight organic solar cells with high flexibility. *Nat. Commun.* **3,** 770 (2012).
26. Li, Y. *et al.* Nanocellulose as green dispersant for two-dimensional energy materials. *Nano Energy* **13,** 346–354 (2015).
27. Zou, Z. *et al.* A low-power and flexible energy detection IR-UWB receiver for RFID and wireless sensor networks. *IEEE Trans. Circuits Syst. I Regul. Pap.* (2011). doi:10.1109/TCSI.2011.2142930
28. Chen, X. *et al.* Polymer photonic sensing skin. in *Proceedings of SPIE - The International Society for Optical Engineering* (2010). doi:10.1117/12.866367
29. Wilson, D. a J. Handbook of Chemical and Biological Sensors. *Physiol. Meas.* (2009). doi:10.1088/0967-3334/17/4/010
30. Jenkins, A. T. A. in *Surface Design: Applications in Bioscience and Nanotechnology* (2009). doi:10.1002/9783527628599.ch4
31. Vermesan, O. *et al.* Internet of Things Strategic Research Roadmkap. *Internet Things-Global Technol. Soc. Trends* (2011).
32. International Telecommunication Union. *The Internet of Things*. *Itu Internet Report 2005* (2005). doi:10.2139/ssrn.2324902
33. Kortuem, G., Kawsar, F., Sundramoorthy, V. & Fitton, D. Smart objects as building blocks for the internet of things. *J. Internet Comput. IEEE* (2009). doi:10.1109/MIC.2009.143
34. Calvert, P. Inkjet Printing for Materials and Devices. *Chem. Mater.* **13,** 3299–3305 (2001).
35. Singh, M., Haverinen, H. M., Dhagat, P. & Jabbour, G. E. Inkjet printing-process and its applications. *Adv. Mater.* **22,** 673–85 (2010).
36. Association, S. I. 2015 ITRS Section 5: More Moore. 1–52 (2015).
37. Wong, W. S., Chabinyc, M. L., Ng, T. & Salleo, A. in *Flexible Electronics: Materials and*

Applications, (2009). doi:10.1007/978-0-387-74363-9

38. Jackson, W., Heeney, M., Mcculloch, I. & Jackson, W. Flexible Electronics. *Flex. Electron.* (2009). doi:10.1007/978-0-387-74363-9

39. Cheng, I.-C. & Wagner, S. *Flexible Electronics*. *Flexible Electronics* (2009). doi:10.1007/978-0-387-74363-9

Chapter 2 : Printed Electronics

2.1 Overview of Printed Electronics

Nowadays, printing electronics is an established fabrication technology for flexible electronics.[1–5] It consists of several manufacturing processes that arose to provide large-area, light-weight, high-throughput and low-cost production of flexible smart electronics applications (Fig. 2.1). Many printing techniques are under rapid development as promising technologies capable to adapt to the natural shape of our environment by implementing electronic devices on bendable or stretchable substrates in a roll-to-roll manufacturing process.[6,7] Reducing the production costs and the fabrication complexity, printed electronics is a complementary solution to the consolidated and strengthened silicon technology.

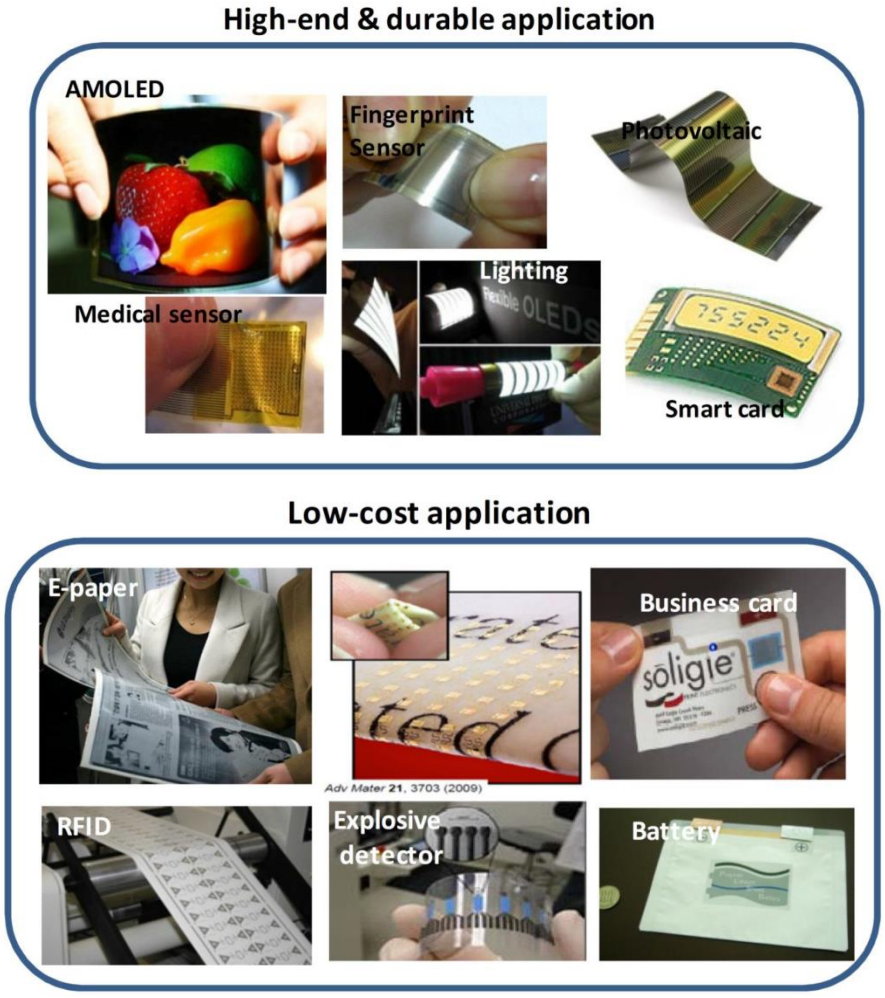

Fig. 2.1 *High-end and low-cost application of flexible electronics.*[8]

In order to fulfil the industrial electronics requirements (Fig. 2.2), specialized printing techniques, such as bottom-up additive methods, allow for the deposition of functional materials to create passive or active electronic devices.[9,10] Amongst the current printing technologies,[11] offset lithography,[12–14] flexography,[15–17] gravure,[7,18,19] screen printing,[20,21] and inkjet printing[22,23] stand out for their versatility. Conductive, semiconductive or insulating inks are combined in simple patterns or complex multi-layered structures creating active or passive devices on flexible substrates.

Fig. 2.2 *Roadmap for Organic and Printed Electronics Applications.* [24]

2.2 Printing Techniques

Printing electronics is based on different printing techniques that operate in a different manner depending on the many interface relations concerning the designed pattern structure (thickness and resolution requirements), the physical and chemical properties of the deposited functional material, and the selected substrate characteristics. In addition, according to the substrate proximity of the deposition process, it is possible to define two main printing methods: printing techniques that require an exclusive mask or special framework for a contact process (offset, gravure, flexographic and screen printing) and the mask-less non-contact method (inkjet printing). The relevant printing techniques, focused on a roll-to-roll manufacturing process, are hereby presented as well as their main characteristics.

2.2.1. Offset Printing

Offset printing[25] is the representative printing method employed in written press for high-resolution magazine and newspaper industry. This technique is a no-direct printing method which is based on the difference of surface energy between the plate cylinder that transfers the hydrophobic ink (water-repellent) from a printing plate and the substrate (Figure 2.3).[26] The localized surface energy gradient on the substrate defines the patterned areas (hydrophobic region) from the empty areas (hydrophilic region). Although the required high viscosity (30-100 Pa·s) and the related high pressure system (~1 MPa, impracticable for pre-patterned substrates with soft materials), offset printing ensures thin layers of thickness ranging from 0.5 to1.5 μm.[27] Up to date, few electronic applications have been achieved with this technique due to starting expensive costs and the water presence into the system.[28]

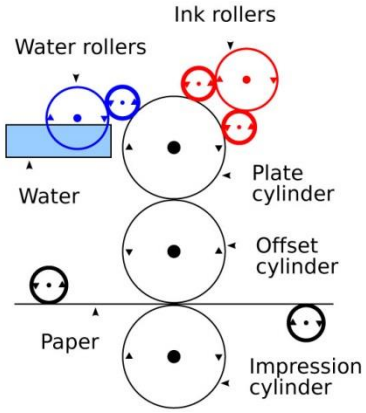

Fig. 2.3 *Offset printing process.*[29]

2.2.2. Gravure Printing

Gravure printing[18,19] is a common method applied for the production of high-quality commercial magazines (as offset printing) and for packaging. This printing technique relies on an engraved pattern into a ceramic or metallic cylindrical plate surface (with resolution around 20 μm), whereas the unpatterned regions remain at the original level of the plate (Figure 2.4).[30,31] First of all, the engraved printing cylinder is dipped into a selected ink reservoir, then a doctor blade is used to remove the unwanted excess of ink. Finally the gravure-plate transfers the ink onto the moving substrate under high-pressure (~3 MPa, impracticable for pre-patterned substrates with soft materials) with thickness resolution ranging from 0.8 to 8 μm. In spite of the very expensive engraved cylindrical plate and the waste material, gravure printing offers high printing resolution (~10-20 μm), high print velocity and requires low viscosity ink (50-200 mPa·s). These features have been exploited for the fabrication of fully-printed electronic devices, such as antennas, organic solar cells and OLEDs.[32,33]

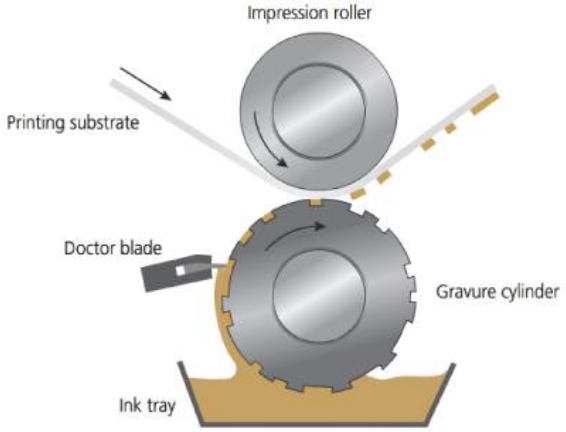

Fig. 2.4 *Gravure printing process.*[11]

2.2.3. Flexography Printing

Generally, flexography printing is used in packaging applications.[15,16] In flexographic printing there are at least three cylindrical plates: the anilox roller, the raised imaged-patterned plate and the substrate plate.[34] First of all, the anilox cylinder, a polymeric plate with well-distributed and uniform-volume cells, is dipped into a reservoir ink and, as in gravure printing, the excess of ink is removed by a doctor blade. Afterwards, the ink, filled into the anilox cells, is transferred with controlled thickness (ranging from 0.8 to 1 μm) onto the raised patterned-plate. Finally, using a soft pressure (~0.3 MPa, practicable for pre-patterned substrates with soft materials) the direct contact

transfers the ink from the raised image plate to the substrate (Figure 2.5).[35] Printing resolution (20-75 µm) and desired ink viscosity (50-500 mPa·s) are comparable to gravure printing, but flexographic printing uses soft pressure contact for the transfer, which permits a wider range of suitable substrates.[34,35] However, the printing quality and velocity are lower than gravure printing. Electronics applications[36] such as RFID antennas[16] and transistors[37] have been demonstrated by flexographic printing.

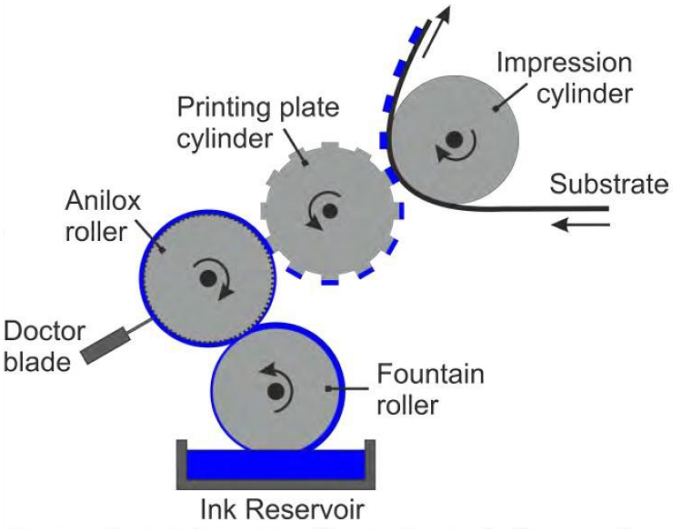

Fig. 2.5 *Schematic illustration of Flexographic printing process.* [38]

2.2.4. Screen Printing

Screen printing is a widespread technique which finds application in textile industry, commercial ceramics or wallpaper advertisements.[20,21] The key component in this technology is the screen, which is made of a mesh support, generally from materials like stainless steel or polyester. The mesh support is pre-coated with an emulsion that fills the unwanted pores in order to define the desired pattern. Thus, once the screen is placed on top of the substrate, the ink is dragged across the screen surface using a squeegee which squeezes the ink through the open pores (Figure 2.6). A trade-off between ink properties, such as the viscosity (0.5 – 50 Pa·s) and mesh density (depending on the fineness of the screen) demarcate the best printing resolution (~30-80 µm) and an expected layer thickness ranging from 3 to100 µm.[39] These parameters are comparable to the abovementioned printing techniques, but screen printing does not need a pressure system, which makes this a cheaper system able to be integrated in a roll-to-roll manufacturing process. Many

functional materials have been successfully screen printed for electronics applications, for example, antennas, photovoltaic cells,[40] transistors and even fully-printed circuits.[41]

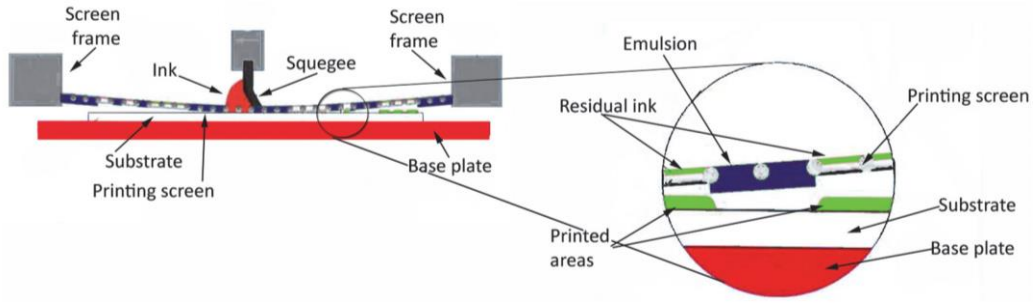

Fig. 2.6 *Different components of the screen printing and (b) screen printing process.*[11]

2.2.5. Inkjet Printing

Recently, among all the additive printing methods, inkjet printing[42,43] has drawn increasing interest to many areas, from graphical printing to packaging, from biotechnology to 3D hybrid printing structures.[22,44] Inkjet printing technology includes two printer families: continuous or drop-on-demand,[45,46] where the former means an uninterrupted jetting of ink on a substrate and the latter states for a digitally-controlled drop ejection. Moreover, the ejection can be carried out by thermal bubble[47,48] or piezoelectric jets system (Figure 2.7).[49] In case of the thermal-bubble system, the ink chamber into the cartridge is controlled by a heating element that, when it is heated up by an applied current, generates a bubble into the nozzle. Consequently, this thermal bubble promotes a pressure wave that ejects an ink droplet. In contrast, in the case of piezoelectric jets (actuator element into the nozzle), a voltage waveform is applied to the piezoelectric plate in order to promote its deflection. The deflection causes an acoustic pressure wave that propagates inside the nozzle to eject the droplet. In this thesis, drop-on-demand piezoelectric inkjet printing has been always employed, because thermal-bubble system is less suitable for printed electronics. Inkjet-printable functional inks are generally based on low boiling point solvents, which are easily vulnerable to undesired process into the so-called clogging nozzle.[50,51]

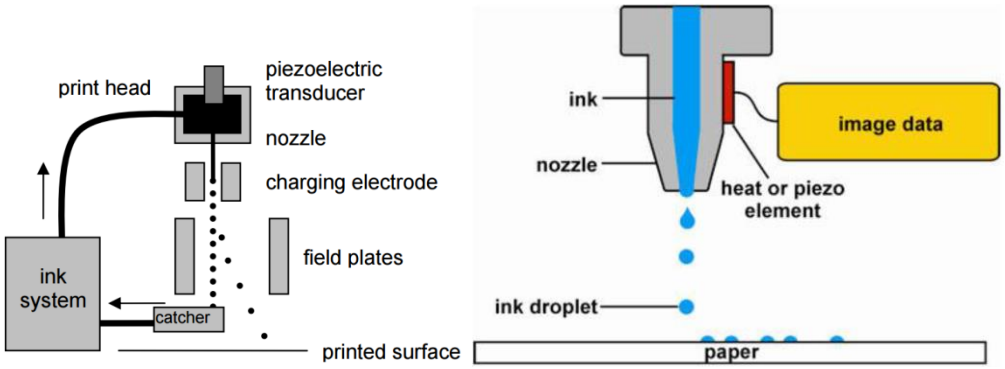

Fig. 2.7 *a) Schematic diagram of a single-jet of continuous inkjet printer* [52]*, b) Principle of drop-on-demand inkjet printer.* [53]

In the light of the different mechanisms involved in drop jetting, inkjet printing is a digital patterning technique that permits to deposit few picoliters drops (from 1 to 80 pL) on either rigid or flexible substrate in a non-contact process (from 250 nm to ~5 cm above the substrate). The resulting drop volume ensures a printing resolution ranging from 10 to 60 µm, and a thickness layer in the range 50 - 750 nm. Nevertheless, the smaller the drop volume, the more difficult it is to guarantee a long term printing stability. For this reason, inkjet printing requires particular ink properties to ensure stable drop ejection, such as viscosity (2 – 20 mPa·s), surface tension (28-33 dynes/cm) or density (~1-2 g/mL). Low material consumption (i.e. no material waste during the printing process), fast digital prototyping (quick changes of pattern), wide range of suitable flexible and rigid substrates, non-contact manufacturing and R2R compatibility make inkjet printing the most versatile technique amongst the ones described in this section. However, and although inkjet printing is R2R-compatible, printing speed (0.01-0.05m^2 s^{-1}) could be considered the mayor drawback when compared to the mass printing methods.[50,51,54]

Inkjet printing relies on disposable cartridges which boost the development of new functional materials for the fabrication of all the previously mentioned electronic applications.[55] Moreover, inkjet printable inks must fulfil some requirements in order to avoid issues concerning the non-uniform drying of the printed films. The most relevant problem could be the so called *coffee-stain effect,*[56,57] when inkjet-printed drops or strips have a *doughnut shaped cross-section* (Figure 2.8). The *coffee-stain* or *coffee-ring effect* is defined as: "During drying, rate of evaporation is faster at the edges due to curvature gradients and contact line pinning at the edge, which is compensated by the outward movement of the solute."[56,57] Although the same problem could be present in the other printing techniques, the *coffee-stain effect* is particularly evident in inkjet-printed patterns due to the remarkable low viscosity value of the inks (2 – 20 mPa·s).[58] The *coffee-stain* effect can be

mitigated using several methods.[59] The most used one is the incorporation during ink formulation of a higher boiling point and lower surface tension co-solvent which induces, after the higher evaporation at the contact lines, that the solvent compositions at the edges become mainly due to the co-solvent with high boiling point. As a result, the solvent at the edges has a lower surface tension than in the centre, resulting in a surface tension gradient. This gradient promotes the Marangoni flow that carries the solute inward to the drop centre, thus reducing the *coffee-stain effect*.[60,61]

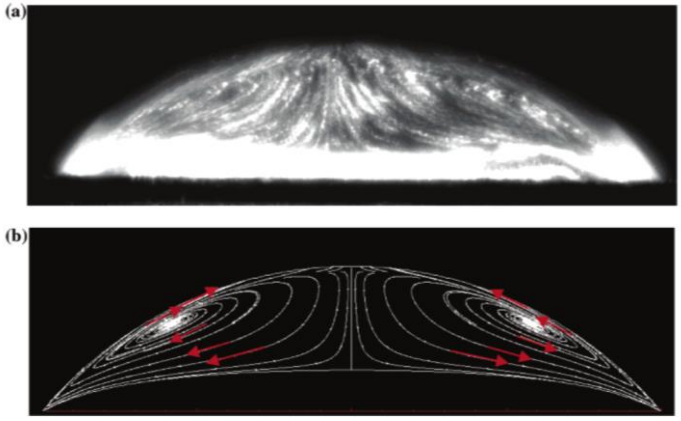

Fig. 2.8 *(a) Motion of particles in a droplet showing coffee-stain formation. (b) Internal droplet fluid motion under the influence of Marangoni flows.*[60]

2.2.6. Summary of Printing Methods

Printing techniques permit in different ways to deposit functional materials with a defined pattern on a desired substrate within the limitations of each printing method.

How to define the printing quality or accuracy of a printing method? For sure, the narrowest stripe, the lowest pitch (distance between two stripes) and the printed layer thickness are the most relevant features because they implicate the performances of the final printed electronics applications such as circuitry, sensors, capacitors or transistors. A comparison between the main properties of each printing technique is shown on Table 1. On the one hand, gravure printing offers the best throughput with a very low resolution. On the other, screen printing permits to obtain the highest single layer thickness but at the expense of a low throughput and quality patterning. In terms of the thinnest printed layer, gravure, flexography, offset and inkjet printing are the most feasible choices. Overall, although inkjet printing is a slow method, it has by far the best adjustability of the printing

pattern during the printing process, making it suitable for fine–tuning the structure to be printed (Figure 2.9).

Table 1. General parameters and requirements for typical printing techniques.[11]

Printing method	Offset	Rotogravure	Flexography	Letterpress	Inkjet	Screen
Transfer method	rollers	rollers	rollers	plate	thermal, piezo, continuous	ink pressed through holes in screen
Pressure applied	1MPa	3MPa	0.3MPa	10MPa		
Drop size	-	-	-	-	1–100pl	-
Ink viscosity	40–100Pa·s	0.05–0.2Pa·s	0.05–0.5Pa·s	50–150Pa·s	1–20mPa·s	1–50Pa·s
Thickness of ink layer on substrate	0.5–1.5µm	0.8–8µm	0.8–2.5µm	0.5–1.5µm	<0.5µm	<12µm
Comments	high print quality	excellent image reproduction	high quality	slow drying	special paper required	versatile method, low quality
Cost-effective run length (copies)	>5,000 (sheet-fed) >30,000 (web-fed)	>500,000			<350	

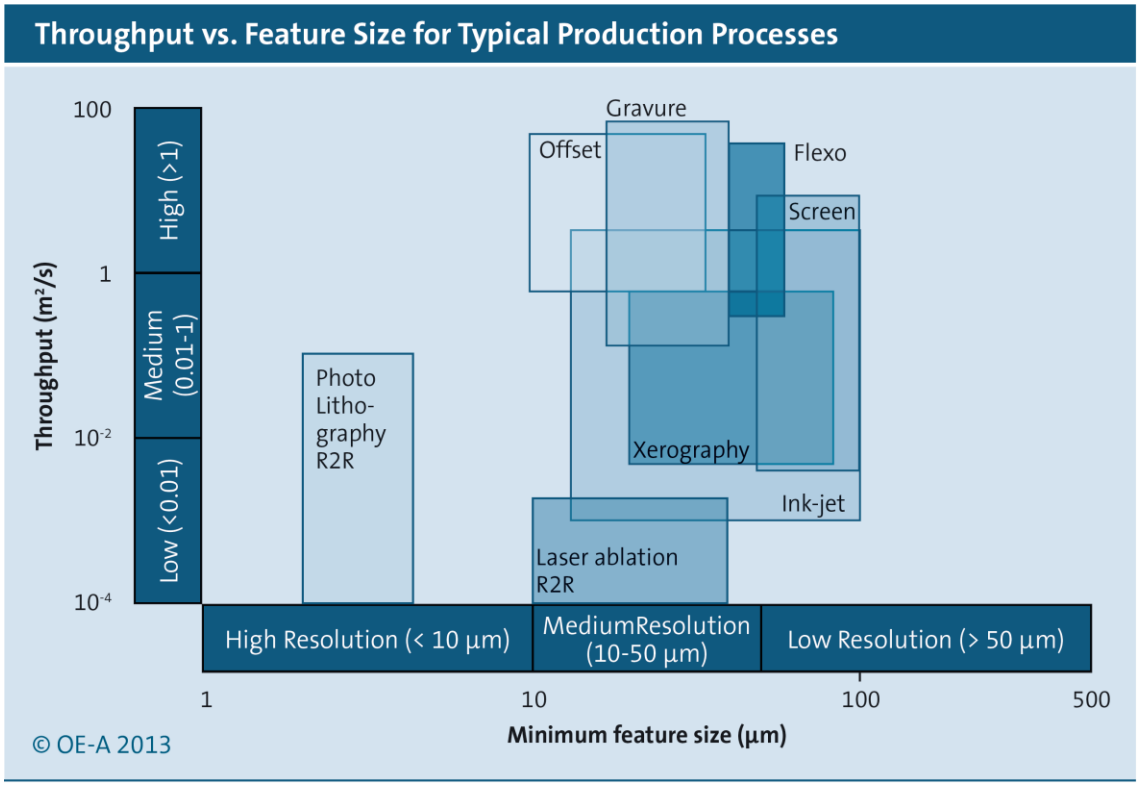

Fig. 2.9 *Throughput vs. feature size for a range of typical production processes.*[24]

2.3 Applications of Printed Electronics

Electronic devices and components are generally divided into two main families: passive or active elements. On one hand, passive devices are commonly two-terminal uncomplicated structures, commonly achieved by a single functional conductive and/or material. For instance, passive components are conducting pads-stripes, resistors, memristors, capacitors and inductors which do not introduce any energy into the electronic system and do not rely on any source of power. On the other side, active devices are typically more complex structures than passive elements. Transistors, diodes, batteries and solar cells rely on a source of power and inject net energy into the electronic system. Doubtless, valid for both rigid and flexible electronics, the main building blocks for any electronic circuit are the transistors, which may require a power supplier such as a battery connected to a solar cell that could transfer the energy by an inductive antenna structure. A combination of simple printed passive and active devices paves the way for low-cost and large-area production of more complex flexible electronics circuits. A brief overview of the principal active and passive electronic components is exposed in this section in order to give an idea of the printed electronics potentiality.

2.3.1. Capacitors

The structure of a capacitor consists of two electrodes separated by an insulating material, in which the energy is stored by the mechanism of charge polarization. The capacitor insulator could be a polymeric composite, a dielectric metal-oxide or an electrolyte. Usually, the easiest and common way of large production of capacitors is taking advantage of the same flexible substrate as insulator,[62,63] so that only the conductive electrodes must be printed. When high technical and electrical performances are required, more complex structures rely on a metal-oxide as dielectric layer with high permittivity (high-*k* material).[64–66]

2.3.2. Batteries - Supercapacitors

The global increasing interest on emerging wearable electronics requires the relentless search for flexible efficient energy storage or energy conversion devices for portable self-powered systems.[67,68] Supercapacitors exhibit high power density, a long cycle lifespan and excellent charge-

discharge ratio and environmentally friendly characteristics despite their relatively low energy densities.[63,69,70]

Analogously to the electrolyte-based capacitor structure, the battery component relies on an electrochemical red-ox reaction taking place at the surface of the specialized printed electrodes. Electrical charge in this case is stored as chemical energy. The most common flexible thin-film batteries are based on Li-ion, Li-polymer, Zn-MnO_2, or Zn-C. Batteries based on Zn-C/MnO_2 are already commercially fabricated on paper by screen printing and lamination techniques.[71,72]

2.3.3. Solar cells

Flexible and portable solar cells are facing a boost in development due to the possibility of generating a clean and continuous energy source from the surrounding environment to supply wearable devices. [73,74]

Printed flexible thin-film solar cells are generally defined as a second generation or third generation solar panel, being the first generation related to the conventional crystalline silicon solar cell (c-Si). The second generation is made by depositing one or more thin layers of semiconductor materials (CdTe, CIGS, a-Si, *p*-Si)[75] [76] on a selected substrate, so that the solar cell is cheaper but less efficient (~16%)[75] than conventional c-Si technology (~26%). Lower environmental impact and production costs recently moved the photovoltaic market to the $Cu_2ZnSn(S,Se)$ (CZTSSe)[77–79] solar cells, which can reach an efficiency of 12.6%.[77–79]

2.3.4. Thin Film Transistor (TFT)

Thin film transistors (TFTs) are a specific configuration of the so-called field-effect transistors (FET) where three conductive terminals (gate, source and drain), as well as a dielectric and a semiconductive layers, are deposited in different geometry on an insulator substrate such as glass, flexible paper or polymeric films. The operation of TFTs lies on the electric field and current flow between the different involved terminals. Actually, in order to control the current flowing through the semiconductive layer via a conductive channel, which is promoted between the source and drain contacts, an electric field is generated at the dielectric-semiconductor interface by a voltage applied between the gate and the source terminals.

Depending on the geometry, there are different possible TFT structures that permit to reach the main device operation while respecting the following rules: (i) the semiconductor must be placed between source and drain electrodes and (ii) the dielectric layer must be located between the gate electrode and the semiconductor layer. Figure 2.10 shows four possible configurations, which can be divided into two different types: bottom gate and top gate devices. In turn, each of these structure types could be classified in either top source-drain or bottom source-drain contacts. Each of the four designs has advantages and drawbacks which will be properly enhanced or reduce depending on the appropriate selection of the involved production processes. [80,81]

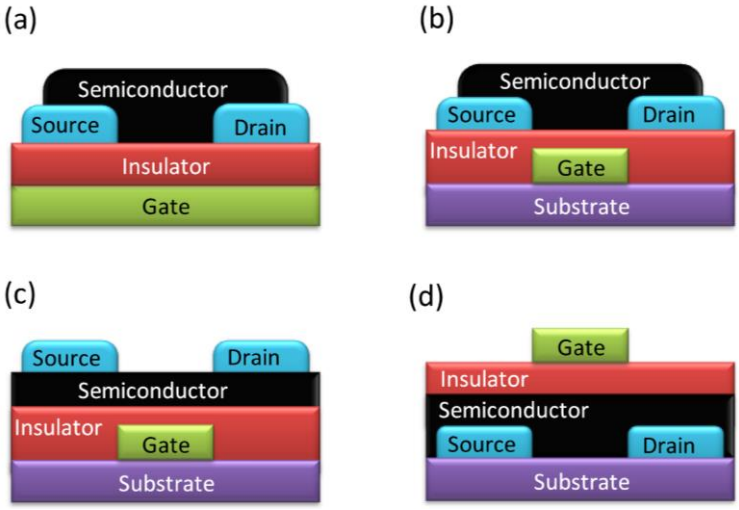

Fig. 2.10 *Scheme of the four possible structure for a TFT device. (a)back-gate with bottom-contact (b) bottom-gate with bottom-contact (c) bottom-gate with top-contact (d)top-gate with bottom-contact* [82]

Generally, TFTs are used for flexible substrates when large-area and low temperature productions are required. For instance, the most common TFT is used for high-quality flat panel liquid-crystal displays (LCDs),[83,84] where each display pixel is controlled by a transistor. [10,69,85,86]

2.3.5. OLEDs for Flexible Displays

At present, LCDs that use TFT technology (Figure 2.11) rely on a current that switches on and off a display (active-matrix) at a faster rate, which permits to have a display brighter.[87,88,89] Generally, this technology requires high-temperature (>1000 °C) and vacuum-deposition methods on glass or silicon substrates. In order to extend the LCD active-matrix to flexible substrates towards bendable displays, an alternative solution is the manufacturing process of organic light emitting diodes (OLEDs)[32,90] or light-emitting electrochemical cells.[91] Although flexible displays only require an

operation rate of 10-100 kHz, main features such as the aperture ratio maximization and the component miniaturization while maintaining the same current levels are crucial.

Fig. 2.11 *Photographs of the 10.2-inch WUXGA flexible AMOLED with integrated gate driver circuits.*[92]

Among the different existing display technologies (multicolour screens, indicator lights), light-emitting diodes (LEDs) are gaining attention as the most suitable optoelectronic components due to their reasonable trade-off between the high refresh rate and the contrast ratio, as well as a competitive power efficiency. Three main LED technologies can nowadays be implemented in flexible displays: organic light-emitting diodes (OLEDs), polymer light-emitting diodes (PLEDs)[93] and quantum dot-based LEDs (QDLEDs).[94] During ink formulation, the easy processability of conjugated organic materials allows achieving a wide range of colours (i.e., different emission wavelengths). Therefore, OLEDs are breakthrough flexible devices suitable for large scale production by any of the existing printing technologies.

2.3.6. RFID Tags

The widespread demand of wireless communication is increasing the development of wearable antennas that can transmit and receive high-frequency signals, such as radio frequency identification (RFID) tags. A RFID tag is essentially a well-designed conductive pattern that acts as an antenna capable of receiving and transmitting data (Figure 2.12). RFID tags are developed as potential replacements for the common bar codes into the industry for inventory control and package-tracking. The RFID complete structure also includes an additional circuitry to process the acquired signal and to store data, all with the support of a power supply (battery). Nowadays, promising fully-printed RFID tags are an open research issue, which take advantage of the self-derivation of the energy resulting from the readout.[95–99]

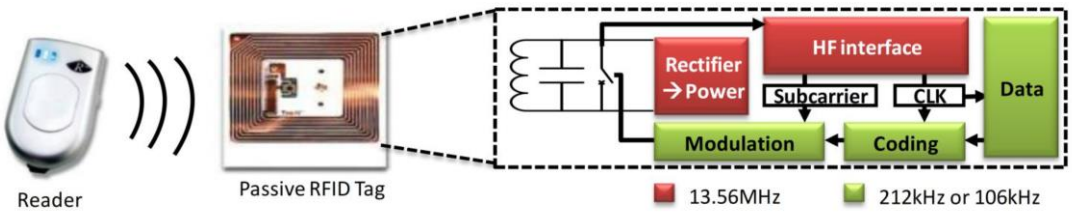

Fig. 2.12 *A basic RFID system comprises a reader and a passive tag.* [82]

2.3.7. Memories

An essential electronics element for the storage of digital information, such as that one collected by sensors or RFID tags, are memory devices. A memory component could be obtained by the implementation of different structures that are able to store the bit data ("0" or "1"), from the transistor (the applied gate voltage define the on-off current, and thus the bit state), to a capacitor (the density charge value determines the bit state), from a resistor (the resistance value or a permanent short circuit defines the bit state) to a memristor device (a capacitor where a programmable-controlled high-resistance or low-resistance state expresses the bit state).
Amongst all the memory devices, the transistor-based memory needs continuous power, whereas a capacitor-based one holds the bit data as long as the density charge is retained within a range (hence they are called volatile memories). Moreover, the fabrication costs and complexity of these memory devices address the industry towards easier and cheaper systems. For this reason, both the resistor and the memristor memories have recently gained popularity, given the advantages posed by not requiring a source power to maintain the bit info (non-volatile memories, NVM).[100–103]

2.3.8. Sensors

Smart devices, connected systems and automation are key words ineveryday's life. Under the Internet of Things (IoT) definition, and in addition to the abovementioned device applications, there are several kinds of sensors, which interact with the environment by the acquisition (reversibly or irreversibly) of selective information. The stimulus that promotes the sensor detection could be due to a chemically aggressive vapour (gases) variation, a pH gradient, a change of temperature, illumination intensity or light incidence, biological interaction, etc. For these applications, sensors,

such as electromechanical, chemical, biosensors and photodetectors, have been developed. Besides, apart from both the low-cost and low-power consumption, a flexible sensor must accomplish required fundamental properties such as selectivity, cross-sensitivity, reliability and stability. Once a sensor has detected a stimulus, the new data will be processed by a logic circuit (usually a TFT-based system), then stored in a memory (memristors) and transferred by an antenna to another system (RFIDs hybrid circuitry).

2.4 Essential Functional Materials

Functional materials employed for printing wearable electronics could be divided into conductive, semiconductive or insulating ink compounds according to the most elemental electrical property. Besides, another important classification is their division between organic and inorganic ink materials. On one hand, inorganic materials demonstrated the best electrical performances, but requiring high temperature processing. On the other, organic materials showed higher flexibility, low-cost formulation and low-temperature sintering, suitable for flexible electronics; however, low electrical performances impede their development spreading. The solution could be a compromise where hybrid complementary heterostructures, based on organic and inorganic materials, take the advantages of both categories. Additionally, more sophisticated properties are required for some functional materials such as electrochromism, luminescence or sensing properties in order to fulfil the expected electronic applications. On the following lines, we will describe the three basic types of functional inks according to their electrical properties.

2.4.1. Conductive Inks

Conductive inks constitute the building block of flexible wearable electronic devices due to their function as connector between the different components of the final application. Several conducting materials are adaptable and compatible with current printing technologies. Up to date, metals inks, conducting polymers and other conducting carbon-based materials have been developed to fulfil the widespreading demand for fully-printed flexible electronics.

Metals inks, based on nanoparticle or precursors, are commonly employed as conductive elements in printing electronics due to reliable stable conductivity ($\sim 10^7 S \cdot cm^{-1}$). As an illustrative example, gold (Au) offers the highest conductivity, stability and inertness. Moreover, it has been

demonstrated as a biocompatible conductor that can stay in contact with living tissues, therefore suitable for printed wearable electronics. However, very expensive costs and high temperature post-sintering processes reduce its spectrum of applications in the electronics field. These issues are solved by silver (Ag) ink, which guarantees outstanding conductive properties while maintaining affordable costs. Cheaper elements are copper (Cu), aluminium (Al) and nickel (Ni), which are not noble metals, i.e., they oxidize quickly in air due to their low oxidation potential.[55]

Typical organic conductive materials are polymer composites, such as poly(3,4-ethylene dioxythiophene)- poly(styrene sulfonate) (PEDOT:PSS),[104] polypyrrole (PPy)[105] and polyaniline (PANI)[69],which are appealing since they are semi-transparent, flexible (easy-adaptable to the flexible polymer), light-weight, biocompatible and at the same time they ensure low-cost synthesis. Nevertheless, organic polymers reach low conductivity values (~10^{3}–10^{-4}S·cm^{-1}), which states a very restricting drawback in several electronic application areas.

Recently, other conducting organic materials, including carbon-based graphene (Gr)[106–108] and carbon nanotubes (CNTs),[109,110] have been demonstrated as suitable conductive materials (they exhibit the highest electrical conductivity, the best chemical stability and the highest elasticity) for flexible transparent printed devices. To date, the main issues of Gr and CNTs conductors are the low concentrated inks and the lab-scale production.

Taking into consideration the advantages of each of the abovementioned conducting materials, conductive hybrid compounds such as metal-conducting polymers, metal–carbon-based materials, and carbon-based material–conducting polymers, are at present considered as appealing alternatives for printed electronics.

2.4.2. Semiconducting inks

Semiconducting materials represent the key element for multipurpose TFTs in printed electronics.

During ink formulation of semiconducting compounds, and analogously to the case of conductive inks, different choices are possible taking into account the electrical requirements and the material restrictions. While inorganic semiconductors show better electrical performance and stability, organic semiconductors generally ensure cheaper and easier synthesis production (low-temperature processing), and higher mechanical flexibility.

Common inorganic semiconductor materials are metal-oxide (ZnO, In_2O_3,…)[111,112] and chalcogenide chemical compounds (MoS_2, ...) [113–115]. Despite the promising greater electrical

performances, high-temperature post-processing and low concentration due to the scarce dispersion achieved make inorganic semiconducting compounds incompatible for many flexible applications.
Organic semiconductor inks for printed electronics can be prepared from either polymeric organic composites such as poly[5,50-bis(3-dodecyl-2-thienyl)-2,20-bithiophene] (PQT-12)[116] and poly(3-hexylthiophene) (P3HT), [31] or benzothieno-[3,2-b]benzothiophene (BTBT)[117].Although its electrical performance is not comparable to the one exhibited by inorganic semiconducting inks, P3HT material shows promising high mobility; this mobility is in turn affected by oxygen doping, which in transistor use will lead to high off-currents. In contrast, PQT and BTBT demonstrate better air stability, although their conductivity is slightly lower compared to P3HT. [31]

Although CNTs have been previously presented as metal conductor, they can furthermore perform as a semiconductor with promising high-mobility, depending on the CNTs chirality (i.e., wrapping direction of the graphene sheet)[118,119]. Lately, considerable attention and resources has been dedicated to the category of 2D semiconducting nanomaterials (Gr, transition metal dichalcogenide monolayers – *TMDs*– such as MoS_2 and $MoSe_2$,[113–115] black phosphorous (BP), silicone, germanene, or borophene) due to their theoretical and experimental outstanding electronic properties provided by their single-atomic layer structure.

Additionally, semiconducting hybrid materials are also being investigated in order to combine the advantages of each material while compensating their drawbacks, such as organic semiconductor merging a carbon-based semiconductor or an inorganic semiconductor combining with an organic semiconductor.

2.4.3. Dielectric inks

Insulators have diverse useful purposes, spanning from avoiding possible short-circuits into multi-layered conductive structures to enhancing the capacitance in electronic devices such as capacitors or transistors. Printable dielectric materials can be classified in inorganic materials, polymers and organic/inorganic hybrid materials.

Existing inorganic dielectric inks are fused silica (SiO_2)[10] and alumina (Al_2O_3),[120] which require high-temperature processing in order to achieve high-density thin films (to evaporate the high boiling point solvents), so that low leakage current is ensured. As well, several metal-oxide

dielectrics gained increasing interest due to their appealing high dielectric constant (ε), such as the high-*k* hafnium oxide (HfO_2)[121], $BaTiO_3$[122,123]. Finally, and as previously mentioned for organic conductors and semiconductors, also organic dielectric materials are mostly employed due to the low-temperature processing, high dielectric strength and high flexibility.

Currently, the most frequently employed insulating polymers in flexible electronic applications are poly(4-vinylphenol) (PVP)[124], poly(methyl methacrylate) (PMMA),[125] polyethylene terephthalate (PET), polyimide (PI), polypropylene (PP), polyvinyl alcohol (PVA)[126] and polystyrene (PS). In addition, thin 2D nanomaterials with wide bandgap energy can be used as dielectric layer for capacitors and for gate dielectrics. The noteworthy exfoliation techniques facilitate the availability as nano-dielectric inks of new layered bulk materials, such as hexagonal boron nitride (h-BN)[127], silicates such as montmorillonite (MTM)[128] or oxides such as graphene oxide (GO)[129].

2.5 Flexible Substrate

2.5.1. Polymeric films

Wearable electronic applications rely on flexible substrates, which commonly are polymeric films. Several properties such as smooth surface, no porosity, homogeneity and semi-transparency promoted the extensive use of polymeric films. Depending on the printing methods and deposited materials, the correlated post-processing temperature treatments condition the choice of the substrate. Here, the main polymeric films, focused on a roll-to-roll manufacturing process, are exposed:

- Polyimide (PI) films, well-known by the commercial name Kapton®, are employed due to their smooth surface, as well as their chemical and physical resistance to prolonged exposure up to 300 °C. However, the high surface energy normally causes a large ink wetting, a surface energy treatment being necessary to reach narrowest strips. In addition, polyimide films are relatively expensive in comparison to other materials.

- Polyethylene (PE), Polycarbonate (PC) and Polyethylene Terephtalate (PET) are commonly used as low-cost (considered as cheap substitutes of PI) flexible substrates for packaging. Nevertheless, their low softening points (below 150 °C) and the related large thermal expansion coefficients constitute their main drawback. Due to low glass transition temperature, they are not compatible with application where high sintering temperatures are needed.

2.5.2 Paper

Nowadays, among the existing flexible substrates, paper substrate is doubtless acquiring relevance for printed electronics because of being wholly-recyclable and the cheapest material by far (it could be made out of renewable raw materials). However, there are concerns regarding the composition and structure properties of paper substrates, which can easily be affected by the surrounding environment propitiating water molecules absorption into the cellulose fibers. A solution to this issue is the photo paper, which in turn increases the material costs.[2,4,130]

References:

1. Jiang, J. *et al.* Fabrication of Transparent Multilayer Circuits by Inkjet Printing. *Adv. Mater.* **28,** 1420–1426 (2016).
2. Tobjörk, D. & Österbacka, R. Paper Electronics. *Adv. Mater.* **23,** 1935–1961 (2011).
3. Berggren, M., Nilsson, D. & Robinson, N. D. Organic materials for printed electronics. *Nat. Mater.* **6,** 3–5 (2007).
4. Siegel, A. C. *et al.* Foldable printed circuit boards on paper substrates. *Adv. Funct. Mater.* **20,** 28–35 (2010).
5. Cheng, I.-C. & Wagner, S. *Flexible Electronics*. *Flexible Electronics* (2009). doi:10.1007/978-0-387-74363-9
6. S??ndergaard, R. R., H??sel, M. & Krebs, F. C. Roll-to-Roll fabrication of large area functional organic materials. *J. Polym. Sci. Part B Polym. Phys.* **51,** 16–34 (2013).
7. Logothetidis, S., Roth, B., Søndergaard, R. R. & Krebs, F. C. *Handbook of Flexible Organic Electronics*. *Handbook of Flexible Organic Electronics* (2015). doi:10.1016/B978-1-78242-035-4.00007-5
8. Choi, N. Metal Oxide Thin Film Transistors on Paper Substrate: Fabrication, Characterization, and Printing Process. (2012).
9. Ko, S. H., Chung, J., Pan, H., Grigoropoulos, C. P. & Poulikakos, D. Fabrication of multilayer passive and active electric components on polymer using inkjet printing and low temperature laser processing. *Sensors Actuators, A Phys.* **134,** 161–168 (2007).
10. Arias, A. C., MacKenzie, J. D., McCulloch, I., Rivnay, J. & Salleo, A. Materials and applications for large area electronics: Solution-based approaches. *Chem. Rev.* (2010). doi:10.1021/cr900150b
11. Kipphan, H. *Handbook of Print Media*. *Handbook of Print Media* (2001). doi:10.1007/978-3-540-29900-4
12. Southee, D. J., Hay, G. I., Evans, P. S. & Harrison, D. J. Flexible dot-matrix display manufacture by offset lithography. *Proc. Inst. Mech. Eng. Part B J. Eng. Manuf.* (2008). doi:10.1243/09544054JEM939
13. Ramsey, B., Evans, P. & Harrison, D. A novel circuit fabrication technique using offset lithography. *J. Electron. Manuf.* (1997).
14. Harrey, P. M., Evans, P. S. A., Ramsey, B. J. & Harrison, D. J. Interdigitated capacitors by offset lithography. *J. Electron. Manuf.* (2000). doi:10.1142/S096031310000006X
15. Kattumenu, R. C. Flexography printing of silver based conductive inks on packaging substrates. *Western Michigan University. Department of Paper Engineering, Chemical Engineering\rImaging,* (2008).
16. Vena, A. *et al.* Design of chipless RFID tags printed on paper by flexography. *IEEE Trans. Antennas Propag.* (2013). doi:10.1109/TAP.2013.2281742

17. Hsieh, Y. C., Cheng, H. W., Cheng, Y. H., Chen, S. Y. & Ng, V. S. Flexible hybrid screening solutions for flexography. in *Proceedings - International Conference on Computer Science and Software Engineering, CSSE 2008* (2008). doi:10.1109/CSSE.2008.1390
18. Pudas, M., Halonen, N., Granat, P. & Vähäkangas, J. Gravure printing of conductive particulate polymer inks on flexible substrates. *Prog. Org. Coatings* **54,** 310–316 (2005).
19. Secor, E. B. *et al.* Gravure printing of graphene for large-area flexible electronics. *Adv. Mater.* **26,** 4533–4538 (2014).
20. Gilleo, K. Rheology and Surface Chemistry for Screen Printing. *Screen Print.* (1989).
21. Flower, G. The future for printing. *Screen Print.* (2011).
22. Choi, H. W., Zhou, T., Singh, M. & Jabbour, G. E. Recent developments and directions in printed nanomaterials. *Nanoscale* **7,** 3338–3355 (2015).
23. Singh, M., Haverinen, H. M., Dhagat, P. & Jabbour, G. E. Inkjet printing-process and its applications. *Adv. Mater.* **22,** 673–85 (2010).
24. www.oe-a.org. Roadmap for Organic and Printed Electronics Applications. (2015).
25. Pavlović, Ž., Dedijer, S., Draganov, S., Karlović, I. & Jurič, I. in *Printing on Polymers: Fundamentals and Applications* (2015). doi:10.1016/B978-0-323-37468-2.00013-0
26. Joost, R. & Salomon, R. High Quality Offset Printing – An Evolutionary Approach. *Comput. Eng.* (2007). doi:10.1145/1276958.1277360
27. Nomura, K. I., Ushijima, H., Mitsui, R., Takahashi, S. & Nakajima, S. I. Screen-offset printing for fine conductive patterns. *Microelectron. Eng.* (2014). doi:10.1016/j.mee.2014.05.009
28. Kim, H. *et al.* Development of a precision reverse offset printing system. *Rev. Sci. Instrum.* (2016). doi:10.1063/1.4939237
29. www.arte-essentia.eu/creative-blog-artifacts/artifacts-offset-printing. Offset printing process.
30. Jung, M. *et al.* All-Printed and roll-to-roll-printable 13.56-MHz-operated 1-bit RF tag on plastic foils. *IEEE Trans. Electron Devices* (2010). doi:10.1109/TED.2009.2039541
31. Ding, J. M., de la Fuente Vornbrock, A., Ting, C. & Subramanian, V. Patternable polymer bulk heterojunction photovoltaic cells on plastic by rotogravure printing. *Sol. Energy Mater. Sol. Cells* (2009). doi:10.1016/j.solmat.2008.12.003
32. Kopola, P., Tuomikoski, M., Suhonen, R. & Maaninen, A. Gravure printed organic light emitting diodes for lighting applications. *Thin Solid Films* (2009). doi:10.1016/j.tsf.2009.03.209
33. Hrehorova, E. *et al.* Gravure printing of conductive inks on glass substrates for applications in printed electronics. *IEEE/OSA J. Disp. Technol.* (2011). doi:10.1109/JDT.2010.2065214
34. Izdebska, J. in *Printing on Polymers: Fundamentals and Applications* (2015). doi:10.1016/B978-0-323-37468-2.00011-7
35. Liu, X. & J.T., G. A Review of Flexographic Printing Plate Development. *Springer* (2003).
36. Deganello, D., Cherry, J. A., Gethin, D. T. & Claypole, T. C. Patterning of micro-scale conductive networks using reel-to-reel flexographic printing. *Thin Solid Films* (2010).

doi:10.1016/j.tsf.2010.05.125

37. Yan, H. *et al.* A high-mobility electron-transporting polymer for printed transistors. *Nature* **457,** 679–686 (2009).
38. Lo, C. Y. *et al.* MEMS-controlled paper-like transmissive flexible display. *J. Microelectromechanical Syst.* (2010). doi:10.1109/JMEMS.2009.2038287
39. MacDougall, A. Tools and Techniques for Economical, Environmentally Friendly Screen Printing. *Screen Print.* (2004).
40. Krebs, F. C. *et al.* A complete process for production of flexible large area polymer solar cells entirely using screen printing-First public demonstration. *Sol. Energy Mater. Sol. Cells* **93,** 422–441 (2009).
41. Krebs, F. C. Fabrication and processing of polymer solar cells: A review of printing and coating techniques. *Sol. Energy Mater. Sol. Cells* **93,** 394–412 (2009).
42. Izdebska, J., Thomas, S. & Soleimani-Gorgani, A. in *Printing on Polymers* (2016). doi:10.1016/B978-0-323-37468-2.00014-2
43. Chwalek, J. M. Inkjet printing technology solutions for the 21st century. in *NIP 23: 23RD INTERNATIONAL CONFERENCE ON DIGITAL PRINTING TECHNOLOGIES, TECHNICAL PROGRAM AND PROCEEDINGS/DIGITAL FABRICATION 2007* (2007).
44. Gao, M., Li, L. & Song, Y. Inkjet printing wearable electronic devices. *J. Mater. Chem. C* **5,** 2971–2993 (2017).
45. Verkouteren, R. M. & Verkouteren, J. R. Inkjet metrology II: Resolved effects of ejection frequency, fluidic pressure, and droplet number on reproducible drop-on-demand dispensing. *Langmuir* **27,** 9644–9653 (2011).
46. Calvert, P. Inkjet Printing for Materials and Devices. *Chem. Mater.* **13,** 3299–3305 (2001).
47. Morita, N. Thermal Inkjet. *Inkjet-based Micromanufacturing* (2012).
48. Zhao, J., Chen, S. & Shang, Z. Thermal bubble micro-injection technology. *Zhongguo Jixie Gongcheng/China Mech. Eng.* (2005).
49. Brunahl, J., Grishin, A. M., Khartsev, S. I. & Osterberg, C. Piezoelectric shear mode inkjet actuator. *Mater. Sci. Microelectromechanical Syst. Devices IV, Novemb. 25, 2001 - Novemb. 28, 2001* (2002). doi:10.1557/PROC-687-B1.4
50. Abe, T. Present State of Inkjet Printing Technology for Textile. *Eco-Dyeing, Finish. Green Chem.* (2012). doi:10.4028/www.scientific.net/AMR.441.23
51. Lee, M. J. Inkjet printing technology still in progress. *J. Korean Ceram. Soc.* (2011). doi:10.419/kcers.2011.48.6.543
52. Martin, G. D., Hoath, S. D. & Hutchings, I. M. Inkjet printing - the physics of manipulating liquid jets and drops. *J. Phys. Conf. Ser.* (2008). doi:10.1088/1742-6596/105/1/012001
53. Nge, T. T., Nogi, M. & Suganuma, K. Electrical functionality of inkjet-printed silver nanoparticle conductive tracks on nanostructured paper compared with those on plastic substrates. *J. Mater. Chem.*

C (2013). doi:10.1039/c3tc31220h

54. Raje, P. V. & Murmu, N. C. A Review on Electrohydrodynamic-inkjet Printing Technology. *Ijetae.Com* (2014).
55. Kamyshny, A. & Magdassi, S. Inkjet Ink Formulations. *Inkjet-based Micromanufacturing* (2012). doi:10.1002/9783527647101.ch12
56. Deegan, R. D. *et al.* Capillary flow as the cause of ring stains from dried liquid drops. *Nature* (1997). doi:10.1038/39827
57. Mackley, M. in *Fundamentals of Inkjet Printing* (2016). doi:10.1002/9783527684724
58. Soltman, D. & Subramanian, V. Inkjet-printed line morphologies and temperature control of the coffee ring effect. *Langmuir* **24,** 2224–2231 (2008).
59. Li, Y. *et al.* Coffee-Ring Defined Short Channels for Inkjet-Printed Metal Oxide Thin-Film Transistors. *ACS Appl. Mater. Interfaces* **8,** 19643–19648 (2016).
60. Hu, H. & Larson, R. G. Marangoni effect reverses coffee-ring depositions. *J. Phys. Chem. B* **110,** 7090–7094 (2006).
61. Hu, H. & Larson, R. G. Analysis of the effects of marangoni stresses on the microflow in an evaporating sessile droplet. *Langmuir* **21,** 3972–3980 (2005).
62. Nyholm, L., Nystrom, G., Mihranyan, A. & Stromme, M. Toward flexible polymer and paper-based energy storage devices. *Adv Mater* (2011). doi:10.1002/adma.201004134
63. Nyström, G., Razaq, A., Strømme, M., Nyholm, L. & Mihranyan, A. Ultrafast all-polymer paper-based batteries. *Nano Lett.* (2009). doi:10.1021/nl901852h
64. Tsai, K.-C., Wu, W.-F., Chao, C.-G. & Kuan, C.-P. High-Reliability Ta[sub 2]O[sub 5] Metal–Insulator–Metal Capacitors with Cu-Based Electrodes. *J. Electrochem. Soc.* **153,** G492 (2006).
65. Cheng, C. H. *et al.* High-Performance MIM Capacitors Using a High-κ TiZrO Dielectric. *J. Electrochem. Soc.* **155,** G295 (2008).
66. Cook, B. S., Cooper, J. R. & Tentzeris, M. M. Multi-Layer RF Capacitors on Flexible Substrates Utilizing Inkjet Printed Dielectric Polymers. *IEEE Microw. Wirel. Components Lett.* **23,** 353–355 (2013).
67. Sousa, R. E., Costa, C. M. & Lanceros-M??ndez, S. Advances and Future Challenges in Printed Batteries. *ChemSusChem* (2015). doi:10.1002/cssc.201500657
68. Huebner, G. & Krebs, M. in *Handbook of Flexible Organic Electronics: Materials, Manufacturing and Applications* (2014). doi:10.1016/B978-1-78242-035-4.00018-X
69. Skotheim, T. A. & Reynolds, J. R. *Handbook of Conducting Polymers: Conjugated Polymers Processing and Applications*. *Chemistry & …* (2007).
70. Bonaccorso, F. *et al.* 2D materials. Graphene, related two-dimensional crystals, and hybrid systems for energy conversion and storage. *Science (80-.).* **347,** 1246501 (2015).
71. Madej, E., Espig, M., Baumann, R. R., Schuhmann, W. & La Mantia, F. Optimization of primary printed batteries based on Zn/MnO2. *J. Power Sources* (2014). doi:10.1016/j.jpowsour.2014.03.103

72. Hwa, Y., Sung, J. H., Wang, B., Park, C.-M. & Sohn, H.-J. Nanostructured Zn-based composite anodes for rechargeable Li-ion batteries. *J. Mater. Chem.* (2012). doi:10.1039/c2jm31776a
73. Hoth, C. N., Schilinsky, P., Choulis, S. A. & Brabec, C. J. Printing highly efficient organic solar cells. *Nano Lett.* **8,** 2806–2813 (2008).
74. Kaltenbrunner, M. *et al.* Ultrathin and lightweight organic solar cells with high flexibility. *Nat. Commun.* **3,** 770 (2012).
75. Green, M. A., Emery, K., Hishikawa, Y., Warta, W. & Dunlop, E. D. Solar Cell Efficiency Tables 45. *Prog. Photovoltaics Res. Appl.* (2015). doi:10.1002/pip.2573
76. Boose, Y., Heller, C., Stern, O. & Lynass, M. The effect of spectral mismatch on the annual energy output of CdTe-, CIGS- and Si-based photovoltaic modules. in *27th European Photovoltaic Solar Energy Conference and Exhibition* (2012).
77. Shin, B., Gershon, T. & Guha, S. *CZTS-Based Thin-Film Solar Cells Prepared via Coevaporation*. *Copper Zinc Tin Sulfide-Based Thin-Film Solar Cells* (2015). doi:10.1002/9781118437865.ch15
78. Redinger, A. & Siebentritt, S. in *Copper Zinc Tin Sulfide-Based Thin-Film Solar Cells* (2015). doi:10.1002/9781118437865.ch16
79. Siebentritt, S. & Schorr, S. Kesterites-a challenging material for solar cells. *Prog. Photovoltaics Res. Appl.* (2012). doi:10.1002/pip.2156
80. McCulloch, I. *et al.* ORGANIC DEVICES. Avoid the kinks when measuring mobility. *Science* (2016). doi:10.1126/science.aaf9062
81. Subramanian, V. *et al.* All-Printed Flexible Organic Thin Film Transistors: Current Status and Outlook for the Future. *Proc. - Electrochem. Soc.* (2004).
82. Tseng, H.-Y. Scaling of Inkjet-Printed Transistors using Novel Printing Techniques. (2011).
83. Bahadur, B. Liquid Crystal Displays. *Mol. Cryst. Liq. Cryst.* (2011). doi:10.1080/00268948408080827
84. den Boer, W. in *Active Matrix Liquid Crystal Displays* (2005). doi:http://dx.doi.org/10.1016/B978-075067813-1/50004-5
85. Burns, S. E., Cain, P., Mills, J., Wang, J. & Sirringhaus, H. Inkjet Printing of Polymer Thin-Film Transistor Circuits. *MRS Bull.* **28,** 829–834 (2003).
86. Fukuda, K., Takeda, Y., Mizukami, M., Kumaki, D. & Tokito, S. Fully solution-processed flexible organic thin film transistor arrays with high mobility and exceptional uniformity. *Sci. Rep.* **4,** 3947 (2014).
87. Amegadze, P. S. K. & Noh, Y.-Y. Development of high-performance printed polymer field-effect transistors for flexible display. *J. Inf. Disp.* (2014). doi:10.1080/15980316.2014.980856
88. Ahn, Y.-J. *et al.* An organic light emitting flexible display. *U.S. Pat. Appl. Publ.* (2014).
89. Ryu, G.-S., Lee, M. W. & Song, C. K. Printed flexible OTFT backplane for electrophoretic displays. *J. Inf. Disp.* (2011). doi:10.1080/15980316.2011.621336
90. Chang, S.-C. *et al.* Multicolor Organic Light-Emitting Diodes Processed by Hybrid Inkjet Printing.

Adv. Mater. **11,** 734–737 (1999).

91. Hernandez-Sosa, G. *et al.* The compromises of printing organic electronics: A case study of gravure-printed light-emitting electrochemical cells. *Adv. Mater.* (2014). doi:10.1002/adma.201305541
92. Miura, K. *et al.* SP-2 Flexible AMOLED Display Driven by Amorphous InGaZnO TFTs. *Am-Fpd '13* 29–32 (2013).
93. Goes, M., Verhoeven, J. W., Hofstraat, H. & Brunner, K. OLED and PLED devices employing electrogenerated, intramolecular charge-transfer fluorescence. *ChemPhysChem* (2003). doi:10.1002/cphc.200390061
94. Al Naimee, K. *et al.* Complex dynamics in quantum dot light emitting diodes. *Eur. Phys. J. D* (2015). doi:10.1140/epjd/e2015-60201-x
95. Yang, L., Staiculescu, D., R. Zhang, Wong, C. P. & Tentzeris, M. M. A novel 'green' fully-integrated ultrasensitive RFID-enabled gas sensor utilizing inkjet-printed antennas and carbon nanotubes. in *IEEE Antennas and Propagation Society, AP-S International Symposium (Digest)* (2009). doi:10.1109/APS.2009.5171787
96. Yang, L., Rida, A., Vyas, R. & Tentzeris, M. M. RFID tag and RF structures on a paper substrate using inkjet-printing technology. in *IEEE Transactions on Microwave Theory and Techniques* (2007). doi:10.1109/TMTT.2007.909886
97. Zou, Z. *et al.* A low-power and flexible energy detection IR-UWB receiver for RFID and wireless sensor networks. *IEEE Trans. Circuits Syst. I Regul. Pap.* (2011). doi:10.1109/TCSI.2011.2142930
98. Subramanian, V., Chang, P. C., Lee, J. B., Molesa, S. E. & Volkman, S. K. Printed organic transistors for ultra-low-cost RFID applications. *IEEE Trans. Components Packag. Technol.* **28,** 742–747 (2005).
99. Shin, D. Y., Lee, Y. & Kim, C. H. Performance characterization of screen printed radio frequency identification antennas with silver nanopaste. *Thin Solid Films* (2009). doi:10.1016/j.tsf.2009.05.019
100. Jung, S., Sou, A., Gili, E. & Sirringhaus, H. Inkjet-printed resistors with a wide resistance range for printed read-only memory applications. *Org. Electron.* **14,** 699–702 (2013).
101. Mohapatra, S. R., Tsuruoka, T., Hasegawa, T., Terabe, K. & Aono, M. Flexible resistive switching memory using inkjet printing of a solid polymer electrolyte. *AIP Adv.* **2,** 22144 (2012).
102. Bessonov, A. a *et al.* Layered memristive and memcapacitive switches for printable electronics. *Nat. Mater.* **14,** 199–204 (2014).
103. Lien, D.-H. *et al.* All-Printed Paper Memory. *ACS Nano* **8,** 7613–7619 (2014).
104. Eom, S. H. *et al.* Polymer solar cells based on inkjet-printed PEDOT:PSS layer. *Org. Electron. physics, Mater. Appl.* **10,** 536–542 (2009).
105. Weng, B. *et al.* Wholly printed polypyrrole nanoparticle-based biosensors on fl exible substrate †. *J. Mater. Chem. B* **2,** 793–799 (2014).
106. Ciesielski, A. & Samorì, P. Supramolecular Approaches to Graphene: From Self-Assembly to Molecule-Assisted Liquid-Phase Exfoliation. *Adv. Mater.* **28,** 6030–6051 (2016).

107. Novoselov, K. S., Mishchenko, A., Carvalho, A., Neto, A. H. C. & Road, O. 2D materials and van der Waals heterostructures. *Science (80-.).* **353,** aac9439 (2016).

108. Withers, F. *et al.* Heterostructures produced from nanosheet-based inks. *Nano Lett.* **14,** 3987–3992 (2014).

109. Coleman, J. N. Liquid-phase exfoliation of nanotubes and graphene. *Adv. Funct. Mater.* **19,** 3680–3695 (2009).

110. Bergin, S. D. *et al.* Towards solutions of single-walled carbon nanotubes in common solvents. *Adv. Mater.* **20,** 1876–1881 (2008).

111. Fortunato, E. M. C. *et al.* Fully transparent ZnO thin-film transistor produced at room temperature. *Adv. Mater.* **17,** 590–594 (2005).

112. Lepp??niemi, J., Eiroma, K., Majumdar, H. S. & Alastalo, A. In2O3 thin-film transistors via inkjet printing for depletion-load nMOS inverters. *IEEE Electron Device Lett.* **37,** 445–448 (2016).

113. Radisavljevic, B., Radenovic, a, Brivio, J., Giacometti, V. & Kis, a. Single-layer MoS2 transistors. *Nat. Nanotechnol.* **6,** 147–50 (2011).

114. Kim, T. Y. *et al.* Electrical Properties of Synthesized Large-Area MoS2 Field-Effect Transistors Fabricated with Inkjet-Printed Contacts. *ACS Nano* **10,** 2819–2826 (2016).

115. Backes, C. *et al.* Edge and confinement effects allow in situ measurement of size and thickness of liquid-exfoliated nanosheets. *Nat. Commun.* **5,** 4576 (2014).

116. Yuen, A. P. *et al.* Improved stability of solution processed photovoltaic devices using PQT-12. *Sol. Energy Mater. Sol. Cells* (2010). doi:10.1016/j.solmat.2010.09.003

117. Ebata, H. *et al.* Highly Soluble [1] Benzothieno [3 , 2-b] benzothiophene (BTBT) Derivatives for. *J. Am. Chem. Soc.* (2007). doi:10.1021/ja074841i

118. Brady, G. J. *et al.* Quasi-ballistic carbon nanotube array transistors with current density exceeding Si and GaAs. *Sci. Adv.* **2,** 1–9 (2016).

119. Cao, C., Andrews, J. B., Kumar, A. & Franklin, A. D. Improving Contact Interfaces in Fully Printed Carbon Nanotube Thin-Film Transistors. *ACS Nano* **10,** 5221–5229 (2016).

120. Hourdakis, E. & Nassiopoulou, a. G. High performance MIM capacitor using anodic alumina dielectric. *Microelectron. Eng.* **90,** 12–14 (2012).

121. Lukosius, M., Kaynak, C. B., Rushworth, S. & Wenger, C. HfO2, Sr-Ta-O and Ti-Ta-O High-k Dielectrics for Metal-Insulator-Metal Applications. *J. Electrochem. Soc.* **158,** G119 (2011).

122. Yoon, D. H., Zhang, J. & Lee, B. I. Dielectric constant and mixing model of BaTiO3 composite thick films. *Mater. Res. Bull.* **38,** 765–772 (2003).

123. Sakai, Y., Futakuchi, T. & Adachi, M. Preparation of BaTiO3 thick films by inkjet printing on oxygen-plasma-modified substrates. *Japanese J. Appl. Physics, Part 1 Regul. Pap. Short Notes Rev. Pap.* **45,** 7247–7251 (2006).

124. Ali, S., Bae, J., Lee, C. H., Choi, K. H. & Doh, Y. H. All-printed and highly stable organic resistive switching device based on graphene quantum dots and polyvinylpyrrolidone composite. *Org.*

Electron. **25,** 225–231 (2015).

125. Mikolajek, M. *et al.* Direct Inkjet Printing of Dielectric Ceramic/Polymer Composite Thick Films. *Adv. Eng. Mater.* **17,** 1294–1301 (2015).
126. Sengwa, R. J. & Sankhla, S. Dielectric dispersion study of coexisting phases of aqueous polymeric solution: Poly(vinyl alcohol) + poly(vinyl pyrrolidone) two-phase systems. *Polymer (Guildf).* **48,** 2737–2744 (2007).
127. Alem, N. *et al.* Atomically thin hexagonal boron nitride probed by ultrahigh-resolution transmission electron microscopy. *Phys. Rev. B - Condens. Matter Mater. Phys.* **80,** 1–7 (2009).
128. Xu, W. B., Zhou, Z. F., Ge, M. L. & Pan, W.-P. Polyvinyl chloride/ montmorillonite nanocomposites. *J. Therm. Anal. Calorim.* (2004). doi:10.1023/B:JTAN.0000042157.96074.44
129. Porro, S. & Ricciardi, C. Memristive behaviour in inkjet printed graphene oxide thin layers. *RSC Adv.* **5,** 68565–68570 (2015).
130. Bollström, R. *Paper for printed electronics and functionality*. (2013).

Chapter 3: Inkjet printing versatility of silver ink

It is the aim of this chapter to provide the reader an overall introduction about inkjet printing technology, used extensively throughout this thesis, by describing its unique features, such as ink versatility, digital patterning, contact-less and mask-less processing, and additive and high-resolution method. Afterwards, the results concerning different applications designed and fabricated using inkjet-printed Ag nanoparticles (AgNP) ink are presented.

3.1 Inkjet Printing Technology

Inkjet printing has gained extensive interest due to the possibility of disposable cartridges that permit to broaden the set of printable functional materials. As explained briefly in Chapter 2, the first-existing inkjet technology is well-known as *continuous inkjet*[1,2]because it relies on a continuous ink ejection, where the stream is adapted into volume-controlled droplets by acoustic pressure waves. In order to obtain the proper pattern, all the unwanted droplets are charged by an electric field during drop formation and thus deflected to be collected and re-used in the system. Therefore, only conductive inks are suitable for *continuous inkjet* method, fact that drastically reduces the range of printable materials. The resulting evolution of *continuous inkjet* leads to the *drop-on-demand (DOD) inkjet*,[1,2] where a single drop is ejected by the cartridge nozzles only where it is required to achieve the final pattern. In this case, the drop ejection can be controlled by choosing a cartridge with thermal-bubble jet system or a piezoelectric jet technology (Figure 3.1).

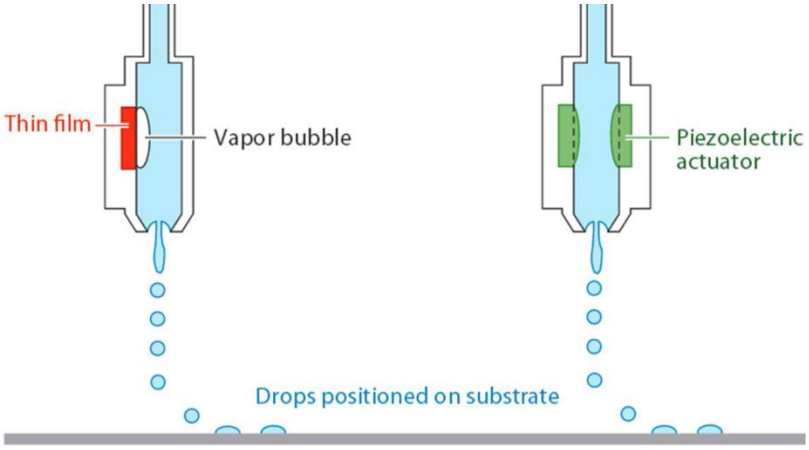

Fig. 3.1 *Schematic diagram showing the operation of drop-on-demand inkjet printing, where drops are formed and ejected in two ways:Thermal inkjet (on the left) and piezoelectric inkjet (on the right)*[3]

3.1.1. Thermal Inkjet

In thermal inkjet cartridges, each nozzle (from a row of 16 up to 1028) consists of an ink chamber and a heating element (thermal transducer), commonly a heater (typically made from poly-silicon) which can be heated up by an applied pulsed current (Figure 3.2). When the temperature reaches the value corresponding to the expected drop volume (from 6 to 80 pL), a bubble is generated due to the quick vaporization of the ink. Then, instantly, the increasing pressure pushes out the ink through the nozzle and a droplet is ejected when the vapour bubble condensates (due to heating element the droplet rapidly cools down), thus provoking a contraction into the ink chamber (figure 3.1a). Consequently, functional inks should be composed by a volatile component, such as aqueous solutions, to promote the vapour bubble phenomenon. Common water-based solutions ejected by thermal inkjet are dispersions of living cells, proteins, enzymes, DNA or other biological material.[4–7] Although the ink must be suitable for rapid thermal change, cartridge nozzles generally suffer from a short lifespan due to the sintered remaining material on the heater element.

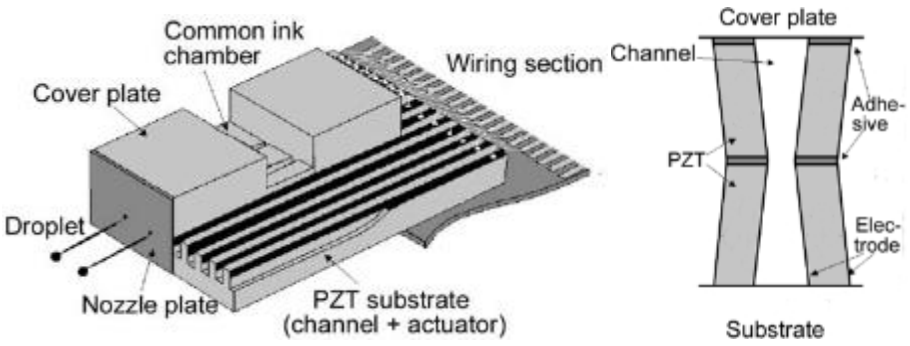

Fig. 3.2 *Piezoelectric inkjet with shear mode. (a) Scheme of a piezoelectric inkjet print head with shear mode. (b) Cross section of a channel (PZT).*[8]

3.1.2. Piezoelectric Inkjet

In the case of the piezoelectric inkjet printhead, each nozzle consists of an ink chamber and a piezoelectric element (lead zirconate-titanate, PZT), commonly a plate which can be deflected by an applied pulsed voltage over the plate (Figure 3.2b). When the voltage reaches the maximum value corresponding to the expected drop volume (from 1 to 50 pL), an acoustic wave is generated due to the pressure pulse in the fluid. Immediately afterwards, the increasing pressure pushes out the ink through the nozzle and a droplet is ejected when the applied voltage is drastically reduced. The pulsed voltage variation over time is generally defined as a *trapezoidal driving waveform* and it is

tailored to the print-head characteristics and fluid properties in order to guarantee a reliable and stable droplet.[5,9,10] The frequency rate at which the waveform is repeated influences the acoustic wave velocity; hence, the droplet ejection depends on the fluid properties, in particular its viscosity. Standard frequencies of the waveform droplets ejection are in the range from 0.1 to 30 kHz, higher than in thermal bubble inkjet, which is limited by the cooling time required after each ejected drop. As illustrated in Figure 3.3, droplet formation is driven by a waveform that can be divided into the voltage rising time, t_r, the dwell time, t_d, the voltage falling time, t_f, and the sum of t_r and t_d.[11]

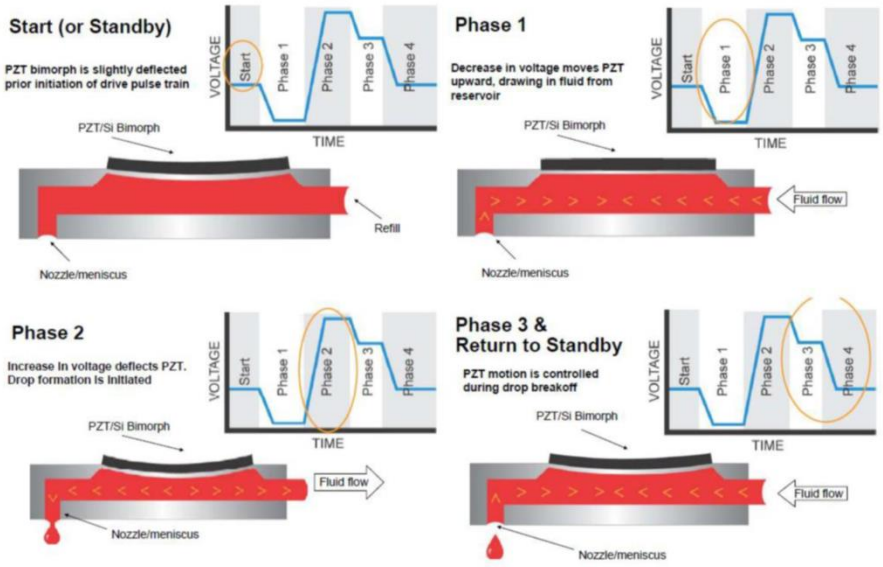

Fig. 3.3 *The amplitude and the slew rate of the waveform determine the amount and the rate of the piezoelectric plate deflection, respectively. In the first phase, a decreased voltage is applied to retract the plate in order to draw fluid into the pumping chamber, followed by a settling time. This section creates two in-phase acoustic waves that propagate from both ends of the chamber and travel in opposite directions. The duration of the first phase is thus selected such that, at phase two, the piezoelectric plate expands precisely when the two waves meet at the chamber centre to push out a droplet with its maximum energy. At phase three, the piezoelectric plate slightly retracts from phase two to break the droplet from the chamber. Finally, the voltage returns back to the standby state in phase four.*[12]

A well-defined waveform allows controlling and generating droplets with the same volume and deposited with high resolution (synchronised with the substrate stage movements). Once the droplet is ejected, achieving velocities up to 6-10 $m \cdot s^{-1}$under the action of gravity and air resistance, it takes from micro- to milliseconds to reach the substrate, depending on the distance of the cartridge from the stage. Finally, the droplet dries through complete solvent evaporation. A typical droplet formation is shown as a sequence of images in Figure 3.4. [11]

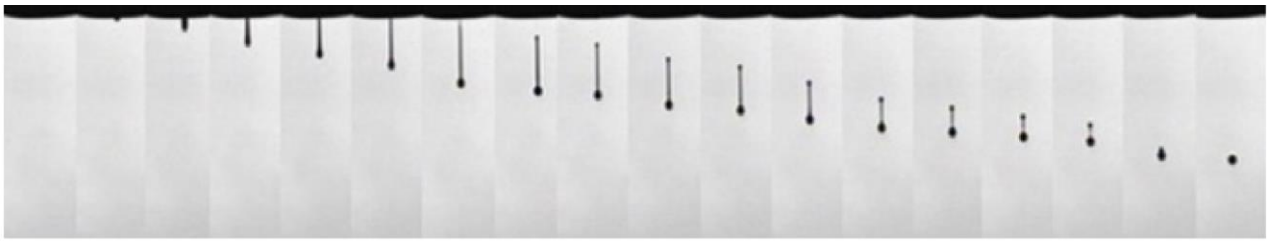

Fig. 3.4 *First, a liquid column of ink is ejected from the nozzle, which will immediately adapt to a spherical shape due to the surface tension of the liquid. The liquid remains attached to the nozzle by a fluid filament, which can form a secondary filament. Disintegration of the fluid filament starts with the formation of a pinch point behind the primary droplet, followed by the formation of secondary droplets, also known as satellite droplets. Therefore, the satellite can merge with the main droplet. After merging of the two droplets, the total droplet oscillates and balances into a stable spherical shaped droplet, as depicted in the last image on the right-hand side of the figure.*[13]

Piezoelectric cartridges are generally selected to deposit functional materials (conductive, semiconductive and insulating), since the piezoelectric system preserves the nozzle from possible clogging due to the evaporation of the volatile solvents into the ink chamber.

3.1.3. Electro-Hydro-Dynamic (EHD) Jet Printing

Even though piezoelectric cartridges control picoliter-drop volume that allows for micro-sized droplets, the prospect of being competitive with silicon technology requires obtaining the ejection of finer droplet feature sizes with the development of subfemtoliter inkjet-printing systems based on electro-hydro-dynamic (EHD) jet printing. EHD system can attain stripes as thin as ~240 nm by the use of high electric fields (keV), rather than vapour or acoustic wave pressure.[16]

Figure 3.5 shows a typical EHD system where a gold-coated glass micro-capillary nozzle as a cartridge and a substrate supported by an electrically-grounded plate are the main components. A droplet is ejected when a high voltage is applied between the nozzle and the metal substrate (to date maximum areas of 15×15 cm^2) in order to deform the meniscus from the nozzle tip and to push out the finest droplet. However, the smaller the drop volume, the more printing steps are required to obtain a conductivity value comparable to standard DOD inkjet, which limits the throughput of the printing. For this reason, although the EHD printing can be scaled up to large area, printing velocity and multi-nozzle control are complicated relevant drawbacks.[17,18]

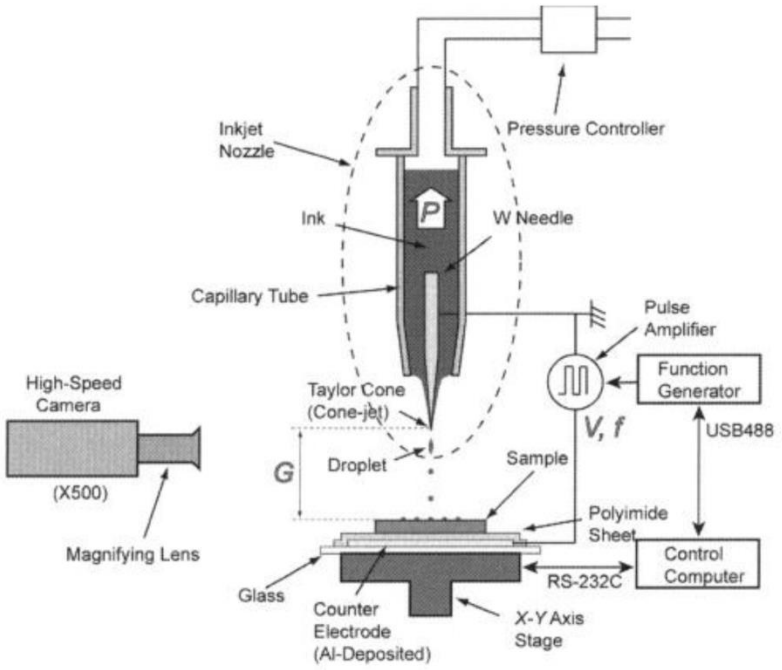

Fig. 3.5 *Set-up and schematic of the electrostatic ink-jet printing system*[16]

3.1.4. Printing Conditions

Many factors can influence the final inkjet-printed pattern or structure, such as the ink rheology (viscosity, density, surface tension, pH), the substrate properties before and after possible surface treatments, the surrounding environment (humidity), the pattern geometry, the interfaces interaction within multilayered-device structures, the sintering method(laser, pulsed light, microwave, electricity-driven, conventional oven sintering), etc. [4,14] An accurate procedure that dominates the combination of these factors is crucial, otherwise the expected functional pattern or device can degenerate resulting in undesired film flaws, such as cracking upon volume contraction, intrinsic stress and, in extreme cases, peeling-off or delamination. Despite all these aspects, inkjet printing overcomes any unfavourable condition by tailoring and tuning the functional material which must be inkjet-printed (Figure 3.6).

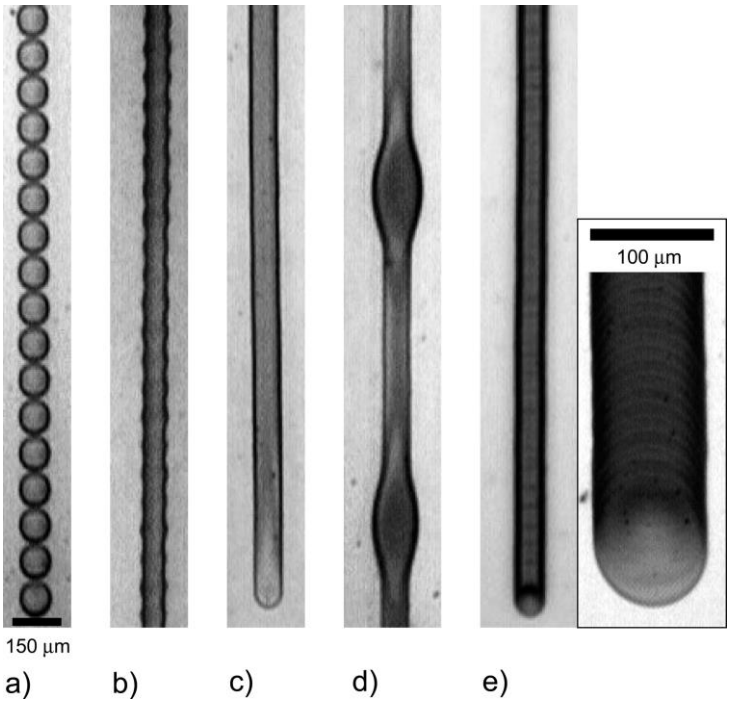

Fig. 3.6 *Tailoring and tuning the inkjet printing parameters to eject properly the selected functional material. Drop spacing decreases from left to right: (a) individual drops, (b) scalloped, (c) uniform (ideal case), (d) bulging, and (e) stacked coins (formed when one drop lands onto another drop already dry).* [15]

3.1.5. Inkjet Printers

The inkjet printers used in this thesis are all piezoelectric jet systems, including a Dimatix (DMP 2831 series, Figure 3.7) and a custom-built inkjet printer Xenia 4000. The placement accuracy of the drop is governed by the width of the jet and the resolution provided by the moving stage of each printer. On the one hand, the DMP system, a state-of-the-art commercial research inkjet printer, was used for all the conductive electrode stripes, due to its smaller drop volume and hence smaller achievable line-width, as well as to minimize the thickness of the dielectric layers. On the other hand, the custom-built printer Xenia was used for printing large-scale production of gas sensor platforms and of MIM devices. The details of both printers can be found in the APPENDIX A.

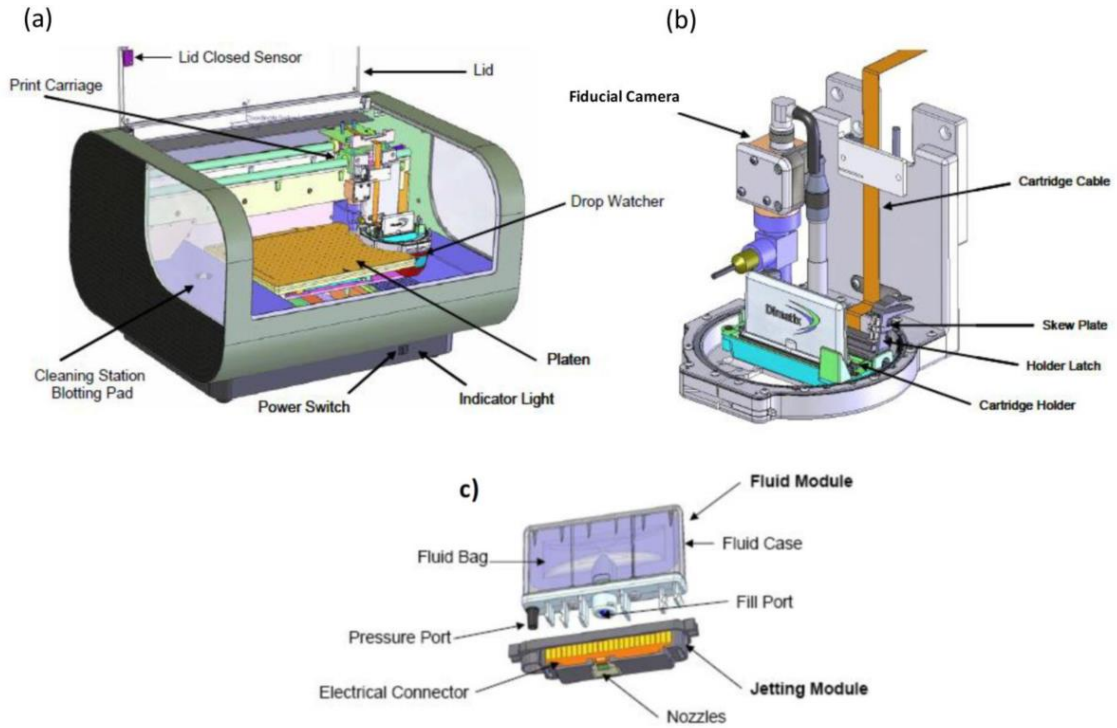

Fig. 3.7 *(a) Dimatix material printer (b) printer cartridge assembly (c) cartridge structure*[12]

3.2 Ink Requirements for Inkjet

Piezoelectric cartridge technology can generate stable droplets whose feature size is strictly dependent on the volume (related to the nozzle diameter) of the ejected drop and the characteristic functional material. In order to prevent nozzle clogging when inks contain dispersed nanoparticles or nanosheets, the nanostructures should be smaller than 1/50 the nozzle diameter, δ, of the selected cartridge. In consequence, the selected inks must fit the physical and the rheological parameters of fluid flow into the cartridge nozzle, such as density (ρ), viscosity (η) and surface tension (γ), which determine the drop formation, taking into account the inertial, viscous and surface tension forces, respectively. These parameters are required to estimate the quality of the ejected drop by the correlated dimensionless figure of merit (FOM) Z number (eq. [1]), equivalent to the inverse of the Ohnesorge (Oh) parameter, which is independent of fluid velocity. The parameter Z predicts the formation of a stable drop when the calculated value lies within the range $1<Z<14$[19] (Figure 3.8). As well, printing ink resolution, homogeneity and adhesion to the substrate material are quality factors that can be fulfilled by adapting parameters such as frequency of injection, nozzle temperature, drops per inch, substrate temperature, etc.[20 21]

$$Z = \frac{1}{Oh} = \frac{\sqrt{\delta \cdot \rho \cdot \gamma}}{\eta} \qquad \text{[eq. 1]}$$

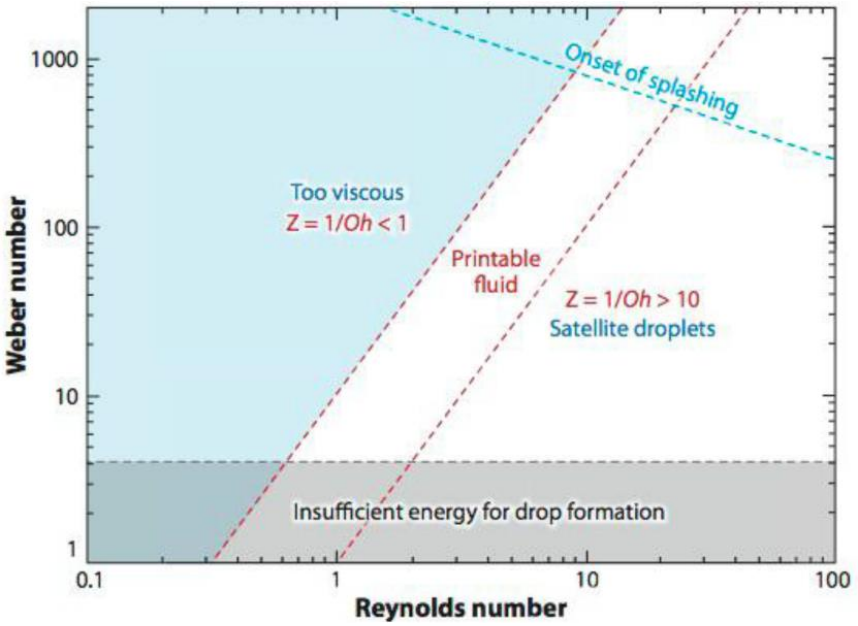

Fig. 3.8 *Regime of the fluid property for a stable ink-jet print system.* [3]

3.3 Metal Nanoparticles-based Inkjet Inks

Nowadays, many inkjet-printable conductive dispersions are commercially available, and simultaneously several other inks are under development. This is the case of inks based on conductive 2D materials (Gr)[22,23], conductive polymer composites,[24] CNTs,[25] silver nanowires, and metal nanoparticles.[14,26] When high throughput, large-areas and reliable conductivity are required, nanoparticles-based inks ensure the best compromise (Figure 3.9).

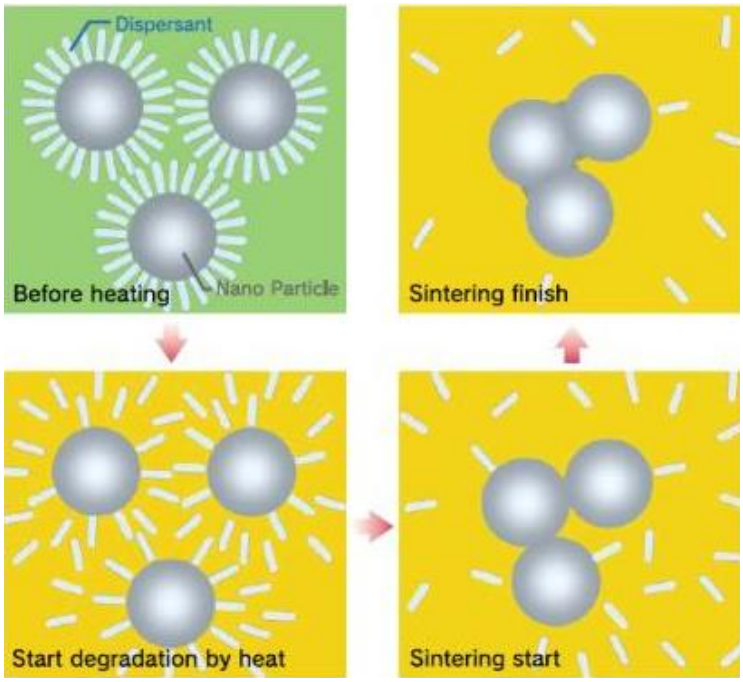

Fig. 3.9 *Schematic illustration of a general sintering process of nanoparticles-based inks.* [27]

The ink formulation, as in the case of most metallic inks, can be carried out by two strategies: bottom-up via either organo-metallic route (Metal-Organic Decomposition, MOD) or reducing agent, or top-down by metal nano-powders dispersed by a certain surfactant. Despite the low temperature processing and unnecessary use of surfactants due to the absence of solid particle, metal-organic inks usually require non-polar organic solvents (e.g., xilene or toluene) which are generally hazardous (high volatile solvents) and promote low printing resolution.[14,2] On the other hand, nanoparticles-based inks are very common because of their easy printability and their larger content of nanoparticle-based solute. Furthermore, the surface modification of the nanoparticles can be tuned according to different solvent medium that can be aqueous, alcoholic or polymeric. [14,2] The choice of the solvent medium and the size of the nanoparticles determine the temperature range for the post-process sintering. Due to their high surface-to-volume ratio, the melting point of metal

nanoparticles is significantly reduced in comparison to the bulk melting point. With the dual advantages of high conductivity and low sintering temperature, silver nanoparticles-based ink is employed as conductor in this thesis for electrodes printing.

3.3.1 Silver Inkjet Ink

Different works showed electronic applications on various substrates using nanoparticles-based inks of gold (Au), silver (Ag), copper (Cu), nickel (Ni) and aluminium (Al). Gold is by far the most expensive element, and therefore not suitable for large-scale production unless the material consumption is small, and its specific properties are needed such as in biological applications (Au is a biocompatible conductor that can stay in contact with living tissues). Ag nanoparticles-based ink can achieve outstanding conductivity, similar to the Au one, while keeping a low reactivity in air, which is advantageous in front of cheaper but easily-oxidized Cu, Al and Ni.[14,26] Polyvalent nanoparticles-based Ag patterns have been designed and inkjet-printed throughout this chapter with the purpose of demonstrating the versatility and potentiality of the inkjet printing technology.

3.3.2 Applications of Silver Nanoparticles-based Inkjet Ink

The soaring global demand for flexible, wearable and transparent devices has prompted an enormous effort towards the development of new technologies that must be both cost-competitive and eco-friendly. Printed electronics holds the promise for enabling low-cost, scalable solutions by exploiting the ability of nanoparticle-based inks as functional materials onto a large area substrate, unlike traditional electronic fabrication techniques such as monolithic silicon electronics.

Among the different printing techniques, screen-printing is one of the main conventional and mature printing methods that demonstrated to be a useful technique in high-volume devices production. Currently, inkjet printing is a new promising alternative to established techniques such as screen printing, but still under development. The increasing interest on inkjet-printing is due to the possibility of manufacturing finer conductive paths than screen printing, thus eliminating the material waste and minimizing the device size, which are deposited in a non-contact process taking advantage of a costless and fast prototyping digital patterning.

Although PET and PEN substrates are commonly used in the existing flexible electronic industry, they reduce drastically their mechanical stability due to the low thermal resistance, thus being unstable at prolonged temperature above 80 °C (PET) and130 °C (PEN). Others polymers ensure high stability and endurance for post-treatment of the functional materials within a wider range of temperatures. For instance, polyimide substrate bears the widest temperature range due to its glass transition temperature around 360 °C, which favours the development of flexible applications in different technological fields.

Kapton® (polyimide), commercially available from DuPont, with thickness of 50 µm, was chosen as flexible substrate. It has a typical dielectric strength of 240 kV mm^{-1}, which makes it suitable for electronic circuitry. The key advantages of this polyimide compared to other polymers are that it can be heated up to 350 °C (a second order glass transition occurs between 360 °C and 410 °C). Therefore, it is a suitable substrate for sintering of functional materials, such as silver nanoparticles-based ink, and also prolonged moderate thermal treatments of the materials can be performed even after being deposited, such as the heating of an inkjet-printed heater by a pulsed current up to 200 °C.

Regarding printed materials, silver is the most widely used conductive material in flexible electronics. Its excellent electrical conductivity and the possibility to be sintered at low temperatures (lower than 300 °C) foster an excellent panorama for flexible devices.

3.4 Results Concerning Inkjet-Printed Silver

One of the main objectives of this thesis was the evaluation of the inkjet-printed silver nanoparticles-based ink as a reliable and high-performance functional material for gas sensing devices. With this purpose, inkjet-printed gas sensor platforms were fabricated on flexible polyimide with two main research lines developed in Sections 3.4.1 and 3.4.2.

In Section 3.4.1, the performances of the designed and inkjet-printed gas sensor platforms were studied by long-term characterization and aging tests, in order to identify the possible causes of device failure, and afterwards the process was further optimized to overcome the drawbacks of silver defects while simultaneously decreasing the total device power consumption. In addition, a complete comparison with screen printed devices was demonstrated. The results concerning this research line are reported in ***Paper I***.

Section 3.4.2 demonstrates the implementation of the inkjet-printed gas sensor platforms for the development of a thin film area of an active metal oxide layer, TiO_{2-x}-based, deposited by Atmospheric Plasma Spray (APS). The gas sensor consisting of a flexible polymeric thin film was the target of the research. A factorial design of experiments was carried out in order to find out the operation conditions that could avoid the thermal degradation of the polymer due to the heat involved in the plasma spraying process. ***Paper II*** summarizes the obtained results within this topic.

The acquired data from the flexible sensors must be processed, so that the wearable devices can be integrated in complex electronic applications that ensure a high degree of reliability and quality. In order to accomplish these application requirements, hybrid electronics is fulfilled by combining the advantages of the printing technologies with the surface-mount technology. Regarding this topic, Section 3.4.3 presents a novel soldering method which consists on using inkjet-printing technology throughout the whole electronics manufacturing process, the circuitry and the chips bonding on flexible and rigid substrates. Inkjet-printed silver ink was proposed as assembling/soldering functional material and compared with benchmark assembling materials. The corresponding results are reported in ***Paper III***.

3.4.1. Gas Sensor Platforms Design and Fabrication

In the first paper hereby presented, ***Paper I****: Fabrication, Performances and Aging of Flexible Gas Sensor Platforms,* the following issues were studied and discussed in detail:

(1) Fabrication of versatile, low-cost, flexible and reliable sensor platforms for resistive sensors. The designed sensor platform consisted thereby of a sensing part (on the top side of the substrate) and a heater (on the bottom side of the substrate).

(2) The gas sensor platforms calibration and characterization applying voltage pulses and monitoring their temperature for life test and aging test analyses. Afterwards, a comparison with screen-printed equivalent gas sensor platforms is presented.

(3) Design improvement to avoid platform failures and to reduce the power-consumption due to the heater element.

The main objective of this work was to demonstrate flexible gas sensor platforms manufactured using inkjet-printing technology. Test characterization by continuous life tests (maintaining 120 °C during heater operation) was studied and compared to equivalent screen-printed gas sensor platforms. Early device failure, caused by chemical degradation, was observed in screen-printed devices due to the flake-like morphology of the deposits. No noticeable deterioration occurred in inkjet-printed conductive tracks of silver nanoparticles. However, the very thin film obtained by inkjet printing promotes a failure by hot spot phenomenon when a current bottle-neck is promoted (excess of current allowed by the printed stripe in terms of thickness and width), any chemical degradation was observed as the case of screen-printed platforms. As well, the work also demonstrated that the synergetic combination of polymeric substrates with printed electronics is a good alternative to the monolithic silicon and the ceramic technologies.

The article has been reproduced from Journal of Materials Science and Engineering B; vol. 5; Beatriz Medina-Rodriguez, Francisco Ramos, Giovanni Vescio, Xavier Arrese, AïdaVarea and Albert Cirera, ‖ *Fabrication, Performances and Aging of Flexible Gas Sensor Platforms* ‖; pp. 170-176;

** Note that sections, equations and references numbering in the reproduced research article follow the ones of the published version. This statement applies to all Papers presented in this Thesis Dissertation.*

Journal of Materials Science and Engineering B 5 (3-4) (2015) 170-176
doi: 10.17265/2161-6221/2015.3-4.009

Fabrication, Performances and Aging of Flexible Gas Sensor Platforms

Beatriz Medina-Rodriguez[1*, 2], Francisco Ramos[1], Giovanni Vescio[2], Xavier Arrese[2], Aïda Varea[2] and Albert Cirera[2]

1. Advanced Materials Dept., FAE-Francisco Albero S. A. U., L'Hospitalet de Llobregat 08908, Spain

2. Department of Electronics, University de Barcelona, Barcelona 08028, Spain

Abstract: Flexible electronics are attracting much interest in gas sensor field on on-site monitoring applications due to their wear ability, lightweight and low-cost production. These performances are fully accomplished by silver-based platforms, but silver corrosion represents the main drawback for the integrity of the devices. In this work, self-heating sensor platforms fabricated by screen- and inkjet-printing techniques have been developed. The reliability of both types of sensors has been tested by long-term lifetime characterization and aging tests. These tests proved that the actuation time is interrupted by silver corrosion phenomena in screen-printing devices and by hot spots in inkjet-printing ones. Appropriate solutions regarding isolation and design improvements achieved not only an increase of lifetime and reliability, but also a decrease of power consumption.

Key words: Inkjet printing, screen printing, silver corrosion, flexible gas sensor.

1. Introduction

Global market demands for high quality and low-cost electronic devices. Printing techniques onto flexible polymeric substrates not only can lower the production costs but also offer the possibility to fabricate lightweight and wearable devices, unlike traditional electronic fabrication techniques such as monolithic silicon electronics using lithography and other patterning techniques [1-5].

Printed techniques have a high potential due to the possibility to work under room temperature and ambient pressure allowing a low-cost production [6]. SP (Screen-printing) is one of the main conventional and mature printing techniques, often used for simple industrial tasks (text printing and resist etch) and also complex tasks (printing conductors for flexible electronics and keypads). SP has demonstrated to be a useful technique in high-volume devices production; however, the need of masks makes the process tiresome for short series or customized products. For this reason, industrial companies search for new forms of printing techniques.

In the case of IP (Inkjet-printing), individual and micrometric drops are deposited onto the substrate on demand. The precise drop deposition opens the possibility of printing very thin conductive paths, minimizing both, device size and material expenses as well as the time and cost saving due to the ease in accomplishing design changes where the mask is not needed. IP is still under development and shows a huge challenge in terms of performance and reproducibility compared to matured techniques such as SP, and also in the current assortment of functional materials available on the market [8].

PET (Polyethylene terephthalate) and PEN (Polyethylene naphthalene) are both highly widespread as substrates in the current flexible electronic industry [9-14]. Nevertheless, PET and PEN have low thermal resistance and become unstable at temperature beyond 80 °C and 140 °C, respectively, and lose their mechanical properties. Up these

Corresponding author: Beatriz Medina-Rodriguez, Ph.D. student, research field: printed electronics. E-mail: b.medina@fae.es.

temperatures some others polymers, such as PI (Polyimide) are required for the post-treatment of the functional material [13, 15]. PI can endure a widest temperature range. Its glass transition temperature is 360 °C what enhances its potential application in different technological fields.

Regarding printed materials; silver is the most widely used conductive material in flexible electronics. Its excellent electrical conductivity and the possibility to be sintered at low temperatures (lower than 300 °C) make it a good prospect for flexible devices. Even so, silver corrodes easily in industrial environments containing sulfide [17] or in outdoor applications due to the humidity [18] and chloride [19] even not near saltwater sources where there are inland chloride species, such as $ClNO_2$ [20]. Therefore the reliability of the devices is highly compromised.

In this work, a comparison between low-cost flexible sensor platforms fabricated by means of SP and IP techniques has been developed. The performance of the sensor platforms was checked by long-term characterization and aging tests to identify the causes of the device failure. Design improvement to overcome the drawbacks of silver corrosion and power consumption has been achieved, obtaining a sturdy, wearable and reliable gas sensor platform.

2. Experimental Setup

2.1 Techniques and Materials

For the SP-devices a paste based on silver flakes (C2080415D2 from Gwent Group) was used as the conductive material to print the sensing and the heating parts of the gas sensor platform (Fig. 1a). Apical® PI from Sertek was used as the substrate and the SP process has been carried out with a DEK Horizon 03i. After printing, the silver paste was cured at 135 °C during 15 min in a box oven. These SP-devices were fabricated in FAE Company.

The IP-devices were printed with a Xenjet 4000 from Xennia Technology Ltd. The cartridge was a Xaar 126/50, based on piezoresistive technology to eject the ink. U5603 silver ink with 20 wt% of silver nanoparticles was provided by Sun Chemical. In this case, Kapton® PI from DuPont was used as the substrate. These devices were fabricated in the Electronics Department of the University of Barcelona. The IP-patterns were sintered at 225 °C for 20 min on a box oven. The adhesive PI tape used for the heater isolation was ISOAD 7104 provided by Isovolta.

The devices were calibrated and tested applying voltage pulses and monitoring their temperature by a thermographic camera (NEC Thermoshot F30). Long-term tests were carried out by applying a constant voltage to achieve an initial sensor temperature value of 120 °C. Previous works done in our group showed that these platforms, implemented with carbon nanofibers as sensing material, better respond at 120 °C for NH_3 and NO_2 gas sensing [21]. The tests were interrupted different times to measure the heater resistance at room temperature. The chemical composition of the deposited materials was determined by EDXS (energy dispersive X-ray spectroscopy). The surface morphology of the deposited silver was checked by FE-SEM (field emission scanning electron microscopy). Both EDXS and FE-SEM analysis were carried out on a FE-SEM JEDL J-7100 microscope. Corrosion resistance of the deposits was analyzed by salt-spray chamber and by a

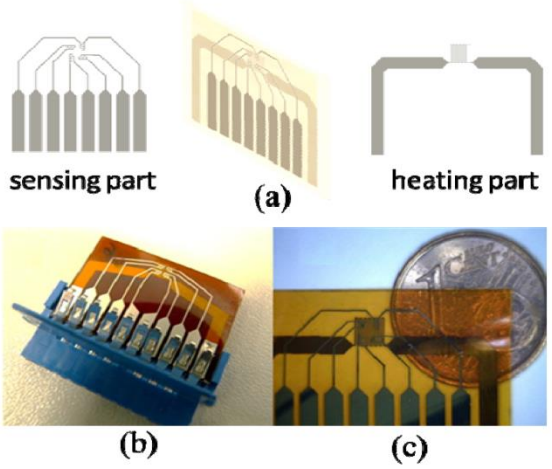

Fig. 1 (a) Scheme of the sensing and heating parts of the printed platforms, (b) SP-printed and (c) IP-printed

devices.

climate chamber. Salt-spray tests were performed with a 50 g/L of NaCl concentration during 72 h while climate chamber tests were performed with 95% humidity using two-hours on/off cycles keeping a temperature constant at 100 °C during 72 h.

2.2 Design and Fabrication

The sensor platform consists of a sensing part and a heater. The sensing part is composed by four interdigitated sensor electrodes and eight connection pads (Fig. 1a). The connection pads were designed in such a way that fit in a clamp-like connector, as it can be seen in Fig. 1b. While sensing part was printed in the topside of the PI tape, the heater was printed on the bottom side, being located just in the area where the printed electrodes are allowing heating up the sensing part. This kind of design (Fig. 1c) is already proved to be suitable for gas sensors [21]. The line width of the interdigitated electrodes and the line strip of the heater were 100 µm and 150 µm, respectively.

3. Experimental Results

Once the devices were fabricated by means of SP and IP, heaters were calibrated. The sensing part temperature is plotted as a function of heater power consumption (Fig. 2). Both platforms showed similar behavior; the sensor temperature linearly increases as power consumption of the heater is higher, achieving around 120 °C for 200 mW. This means that with SP and IP techniques, it is possible to fabricate devices with similar initial electrical characteristics.

To check the endurance of the heaters, a long-term test was carried out. It is known that silver oxidizes quicker as the temperature increases [22], so the heaters were connected to a voltage source to increase the sensor part temperature up to 120 °C. Meanwhile, this temperature was kept constant; the printed devices were maintained in continuous operation until their failure. The heater electrical resistance was measured in different times of the test (square pattern line of Fig. 3a and b). After just few hours of operation, SP-heaters evidenced a change on the surface color, from silvery to brown; this fact clearly indicates the presence of surface corrosion. A total device failure occurred after 300 h (Fig. 3a) where the electrical resistance of the heater increases asymptotically with time. Higher power consumption is needed for the same temperature, which being detrimental for the heater performance and leading to a malfunction of the devices. It is important to underline the fact that all the area which is heated up is degraded quickly; not only the heaters, but the sensing electrodes too. The EDXS analysis showed that only Ag and C elements were present in the as-deposited tracks (Table 1). After the SP-device failure, new elements as S, Cl and O were found, which indicates a change of the track composition due to a surface corrosion. Furthermore, different studies [23-26] show that the porosity and roughness of metal coating surfaces accelerates the corrosion process. The FE-SEM images of SP-printings showed a no-homogenous, porous and full of holes surface, induced by the flake-like structure (Fig. 3c), which makes easier the penetration of the reactive species, like S, Cl and O, into the deposit structure, causing then the premature failure.

Regarding to IP-devices, the total failure occurred in 140 h (square pattern line Fig. 3b), earlier than SP-devices, but no surface corrosion evidences were found. EDXS analysis showed no significant variation on the deposit composition of IP-devices after the

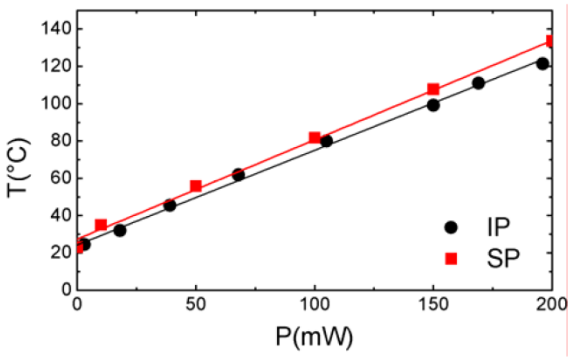

Fig. 2 Calibration plot of SP- and IP-devices. A linear dependence of the temperature of the sensing part is evidenced as a function of heater power consumption.

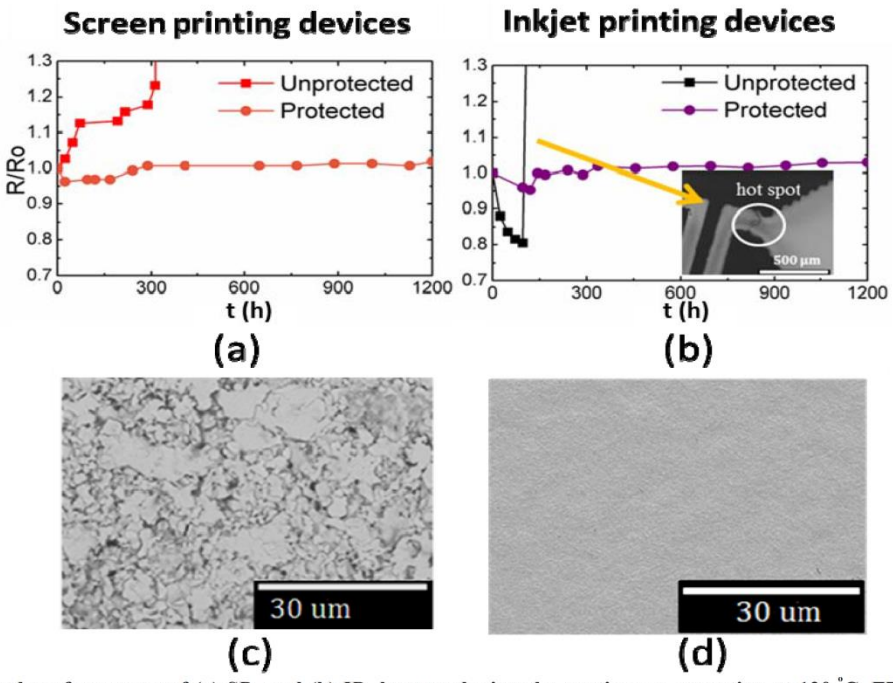

Fig. 3 Electrical performances of (a) SP- and (b) IP- heaters during the continuous operation at 120 °C. FE-SEM images of the silver track printed by (c) screen printing and (d) inkjet printing. Inset: discontinuity on the inkjet-printed heater caused by a hot spot.

Table 1 EDX results for the composition of the printed deposits before and after the long-term test.

Element	SP devices (wt. %)		IP devices (wt. %)	
	Before	After	Before	After
Ag	92	79	98	95
C	8	8	2	3
S	0	6	0	0
Cl	0	3	0	0
O	0	4	0	2

failure (Table 1). FE-SEM images (Fig. 3d) showed a homogeneous surface without the presence of holes or defects. A completely smooth surface is reached by means of the sintering process of the silver nanoparticles. IP-devices showed then an almost inexistent porosity that minimizes the silver exposed to the atmosphere, slowing down the penetration of reactive elements and so the corrosion. Thereby, corrosion is not the cause of these IP-devices failure.

A detailed examination revealed the presence of some discontinuities on the silver tracks after the long-term tests. These discontinuities appeared at vulnerable and weak parts of the design (Fig. 3b) or at printing defects (bubbles, impurities). Unlike the SP-devices, where the single layer track thickness was around 20 µm, the single printed layer of the IP-tracks was 300 nm thick, what might promote the formation and the fast evolution of cracks and hot spots in a short period of time.

The aging tests showed more obvious the penetration of the reactive species into the silver deposit structure. The SP-heater resistance was increased around 7.6% and 10% after the climate and the salt-spray chambers exposure, respectively. However, for IP-devices the increase of the resistance was quite low; 1.3% and 2.7% for climate and spay-salt chambers, respectively, lower than SP-devices (Table 2).

With the aim to improve the life-time of the designed platforms and to prevent the premature failure of both, SP- and IP-devices, an atmospheric isolation of the silver heaters by a suitable adhesive PI tape was carried out. The sensing part has to be exposed to atmosphere to work as a gas sensor device,

thereby it cannot be isolated. It has to be noticed that after the device protection, devices were laminated to remove all the air that could be trapped between the two layers. By means of the heater protection, long-term test showed an increase of the lifetime of protected SP- and IP-devices more than ten times compared with the un-protected ones (circle pattern line in Fig. 3a and Fig 3b). No degradation after 1,000 h of continuous operation at 120 °C and no consequential deterioration on the device performance were observed. However, the SP-electrodes of the sensing part, which could not be protected from the atmosphere, corroded in few hours due to the porous presence, as it was previously mentioned. Instead, the IP-devices showed no corrosion on the electrodes after 1,000 h of continuous operation. Furthermore, it has been demonstrated that heater protection not only improves SP- but also the IP-devices. The aging tests carried out on the protected devices revealed smaller increase of electrical resistance than for unprotected-devices. An increase around 0.6% and 2% was observed in the case of SP-devices for climatic and salt-spray chambers, respectively. No significant variation in electrical resistance of IP-devices was measured. Then, long-term reliability was achieved by means of the heater protection for both SP- and IP-devices, just the unprotected electrodes made the difference.

At this point, it seems that IP-technique can be pointed as the best route to fabricate such flexible sensing platforms. For this reason, IP heater design was optimized to achieve lower power consumption. As said previously, the very first devices showed a power consumption of almost 200 mW at a temperature of 120 °C (Fig. 2). For new design, the heated area was reduced by narrowing the strips as it is shown in Fig. 4a. Once these changes were carried out, the power consumption was reduced to 125 mW at 120 °C for protected inkjet-printed heaters (Fig. 4b) which implies a reduction of a 38% on power consumption, which value also correspond to the heating area reduction.

Silicon technology is energetically a little more efficient, around few tens of mW for 200 °C [27, 28], but the fabrication process is extremely expensive and time consuming. An alternative can be the ceramic technology because it is cheaper, but in this case the power consumption increases excessively on the order of hundred times more [29, 30], as well than on glass-based devices [31]. Therefore, the methodology here proposed can be considered like a good alternative to both technologies, reaching a low-consumption and low-cost sensor platform.

Additionally, it has to mention that this novel flexible-platform was implemented with deposited carbon-based materials as the gas sensing material, by means of electrospray technique. The success of this system has been proved in Ref. [21] by measuring different gases such as NH_3 or NO_2.

Table 2 Variation of the electrical resistance for the different devices after the aging test.

	Salt-spray chamber test ΔR/Ro (%)	Climate chamber test ΔR/Ro (%)
SP	10.0	7.6
Protected SP	2.0	0.6
IP	2.7	1.3
Protected IP	0.1	0.1

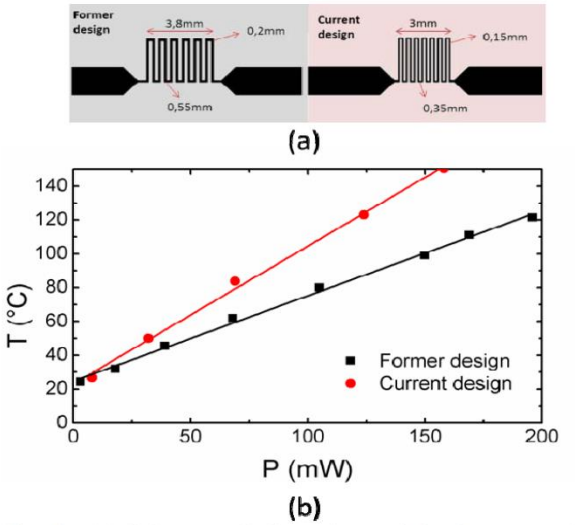

Fig. 4 (a) Scheme and dimensions of the heaters; (b) Sensor temperature as a function of the heater power consumption.

Ravesi, S. and Pignataro, S. 2010. "Low-Temperature Sintered Conductive Silver Patterns Obtained by Inkjet Printing for Plastic Electronics." *Surface and Interface Analysis* 42 (6-7): 1163-7.

[17] Minzari, D., Jellesen, M. S., Moller, P. and Ambat, R. 2011. "Morphological Study of Silver Corrosion in Highly Aggressive Sulfur Environment." *Engineering Failure Analysis* 18 (8): 2126-36.

[18] Lin, H., and Frankel, G. S. 2013. "Accelerated Atmospheric Corrosion Testing of Ag." *Corrosion* 69 (11): 1060-72.

[19] Liang, D., Allen, H. C., Frankel, G. S., Chen, Z. Y., Kelly, R.G. and Wu, Y. et al. 2010. "Effects of Sodium Chloride Particles, Ozone, UV, and Relative Humidity on Atmospheric Corrosion of Silver." *Journal of Electrochemical Society* 157: 146-56.

[20] Lemon, C. E. 2012. "Atmospheric Corrosion of Silver Investigated by X-ray Photoelectron Spectroscopy." Ph.D. Thesis, The Ohio State University.

[21] Claramunt, S., Monereo, O., Boix, M., Leghrib, R., Prades, J. D. and Cornet, A. et al. 2013. "Flexible Gas Sensor Array with an Embedded Heater Based on Metal Decorated Carbon Nanofibres." *Sensors and Actuators B: Chemical* 187: 401-6.

[22] Sakai, J., Aoki, L., Ohsaka, K. and Ishikawa, Y. 2005. "Sub-micrometer Order Corrosion of Silver by Sulfur Vapor in Air Studied by Means of Quartz Crystal Microbalance." In *International Corrosion Congress*, 19-24.

[23] Varea, A., Pellicer, E., Pané, S., Nelson, B. J., Suriñach, S. and Baró, M. D. et al. 2012. "Mechanical Properties and Corrosion Behaviour of Nanostructured Cu-rich CuNi Electrosdeposited Films." *International Journal of Electrochemical Science* 7: 1288-302.

[24] Bersirova, O., Kublanovsky, V., Anufryiev, L. and Rubtsevich, I. 2004. "Corrosion Behavior of Electroplated Silver Coatings." *Materials Science* 10 (1): 11-4.

[25] Bersirova, O. L. and Kublanovskii, V. S. 2012. "Corrosion Properties of Electrodeposited Thin Coatings of Polycrystalline Silver." *Materials Science* 48 (2): 197-202.

[26] Kaushik, V. K. 1991. "XPS Core Level Spectra and Auger Parameters for Some Silver Compounds." *Journal of Electron Spectroscopy and Related Phenomena* 56 (3): 273-7.

[27] Cerdà, J., Cirera, A., Vilà, A., Cornet, A. and Morante, J. R. 2001. "Deposition on Micromachined Silicon Substrates of Gas Sensitive Layers Obtained by a Wet Chemical Route: a CO/CH_4 High Performance Sensor." *Thin Solid Films* 391 (2): 265-9.

[28] Vilaseca, M., Coronas, J., Cirera, A., Cornet, A., Morante, J. R. and Santamaria, J. 2008. "Development and Application of Micromachined Pd/SnO_2 Gas Sensors with Zeolite Coatings." *Sensors and Actuators B: Chemical* 133 (2): 435-41.

[29] Moldavan, C., Nedelcu, O., Johander, P., Goenaga, I., Gomez, D. and Petkov, P. et al. 2007. "Ceramic Micro Heater Technology for Gas Sensors." *Romanian Journal of Information Science and Technology* 10 (1): 43-52.

[30] Jiang, B., Maeder, T., Santis-Alvarez, A. J., Poulikakos, D. and Muralt, P. 2014. "A Low-Temperature Co-Fired Ceramic Micro-Reactor System for High-Efficiency On-Site Hydrogen Production." *Journal of Power Sources* 273: 1202-17.

[31] Santis-Alvarez, A. J., Nabavi, M., Jiang, B., Maeder, T., Muralt, P. and Poulikakos, D. 2012. "A Nanoparticle Bed Micro-Reactor with High Syngas Yield for Moderate Temperature Micro-Scale SOFC Power Plants." *Chemical Engineering Science* 84: 469-78.

3.4.2. Gas Sensor Platforms Application

In ***Paper II****: "New procedures for building-up the active layer of gas sensors on flexible polymers"*, an evident extension of the work presented in *Paper I* was reported, which dealt with the following points:

(1) The feasibility of flexible inkjet-printed gas sensor platforms for the manufacturing of metal oxide titanium sub-oxide (TiO_{2-x}) by atmospheric plasma spray. Despite the high temperatures involved in APS (~300 °C), the inkjet-printed platforms was not degraded during the process, thus obtaining a well-bonded titanium sub-oxide coating.

(2) The characterization of TiO_{2-x}response to NH3.

(3) The characterization of the NH3 response modulation with the temperature (from RT to 220 °C) driven by the heater.

In this work, the main goal was the fabrication of a metal oxide titanium sub-oxide (TiO_{2-x}) gas sensor by Atmospheric Plasma Spray (APS) onto a flexible polymeric thin film. Titanium dioxide is a widely used material in the field of sensors and actuators. Both its chemical stability and relatively low cost make it attractive for industrial application; as a consequence, TiO_{2-x}hasbeen extensively selected as feedstock in APS. Despite the high temperatures involved in APS, the polymeric substrate was not degraded during the process, thus obtaining a well-bonded titanium sub-oxide coating. Finally, the sensing behaviour of the metal oxide layer was tested by means of NH_3 (hazardous gas),proving positive results on NH_3 concentrations ranging from10 to 100 ppm.

** Note that sections, equations and references numbering in the reproduced research article follow the ones of the published version.*

The article has been reproduced from Surface & Coatings Technology; vol. 235; M. Gardon , O. Monereo, S. Dosta, G. Vescio, A. Cirera, J.M. Guilemany— *New procedures for building-up the active layer of gas sensors on flexible polymers*‖; pp. 401-406; Copyright 2013; with permission from Elsevier.

Surface & Coatings Technology 235 (2013) 848–852

Contents lists available at ScienceDirect

Surface & Coatings Technology

journal homepage: www.elsevier.com/locate/surfcoat

New procedures for building-up the active layer of gas sensors on flexible polymers

M. Gardon [a,*], O. Monereo [b], S. Dosta [a], G. Vescio [b], A. Cirera [b], J.M. Guilemany [a]

[a] Thermal Spray Centre, CPT, University of Barcelona, Martí i franquès 1, 08028 Barcelona, Spain
[b] MIND, Department of Electronics, University of Barcelona, Martí i franquès 1, 08028 Barcelona, Spain

ARTICLE INFO

Article history:
Received 17 June 2013
Accepted in revised form 9 September 2013
Available online 14 September 2013

Keywords:
Gas sensor
Flexible electronics
Thermal spray
Titanium sub-oxide
Coating

ABSTRACT

The development of an active metal oxide layer by Atmospheric Plasma Spray in a gas sensor consisting of a flexible polymeric thin film was the target of the research. A factorial design of experiments was carried out in order to find out the operation conditions that could avoid the thermal degradation of the polymer due to the heat involved in the plasma spraying process. $NH_{3(g)}$ was used in a range of concentrations for ratifying the gas sensing capability of the device.

1. Introduction

Enhanced control of the pollutants in the environment by means of metal oxide gas sensors is increasing because of the upward contamination in urban atmospheres. Furthermore, wearable flexible sensors have become an important market of application among smart clothes, medical status monitoring and industrial or military field [1]. Thus, cost-effective and rapid manufacturing processes able to deposit active layers used in the detection of harmful gaseous species are openly expected. Typically, thin film technologies like sol–gel or PVD have been usually applied as coating techniques in this field. However, Thermal Spray (TS) processes can also be used as an attractive technology for depositing the active layer of a metal oxide gas sensor with the aim of providing competitive results [2]. Among the very distinct spraying techniques in this field, Atmospheric Plasma Spray (APS) has been deeply used for achieving metal oxide coatings as passive-protecting layers [3,4]. Nevertheless, developing functional surfaces is also feasible with this technology. APS propels powder particles in its melted state towards a substrate by means of a plasma jet in order to build-up the coating. By controlling the plasma composition, which is typically an Ar/H_2 mixture, it is possible to take over the energy of the jet. Although the plasma temperatures may achieve 15.000 °C [5], substrates that are not so thermally resistant can also be used in APS. Therefore, this process seems to be a very interesting procedure to carry out the scale-up of active layers for these actuators.

The basic principle of operation metal oxide gas sensors is the change of the electrical resistance depending on the gas surrounding due to the chemical reactions that are developed on the metal oxide surface. Nonetheless, the involved sensing mechanisms that assure a proper performance of the device are not simple. Its performance may depend on three key-steps: i) receptor function, which determines the adsorption of the gas on the metal oxide surface, ii) transducer function, which is in command to transform the chemical interaction towards an output signal and iii) approachability, that eases the access of the gas into the inner grains of the solid.

The applications in electronics and sensors of coatings obtained by TS technologies have been reviewed before [6]. TS may offer new opportunities for hybrid thick-film electronics and thick-film sensors. This explanation is based on the advantages associated to these processes: high manufacturing capability, in situ application of different types of materials and geometries, readily available system for customizing special electronics and sensor systems (i.e., prototyping) and it is a greener technology compared to plating, lithography, and so forth. The possibility of developing metal oxide gas sensors by APS has been patented by other authors in the past [7]. Besides this, C. Coddet et al. contributed scientifically with a publication related to tungsten oxide (WO_3) sensitive layers onto an alumina plate by means of APS technology for controlling gaseous NO_2 [8]. In this work, the reducing atmosphere in Ar/H_2 plasma developed a certain amount of WO_{3-x} composition, which made difficult to obtain a stable resistivity. For this reason, the samples were heat-treated in order to recover the oxygen deficiency. However, no significant differences were observed in the response time and sensitivity when comparing those samples obtained in a reduced and non-reduced atmosphere. It was proved that APS could be successfully used a technique for achieving satisfactory results in the fabrication and performance of the active layer of gas sensors.

Despite temperature of either melted particles or plasma jet may be especially critical for thin polymeric substrates; the spraying conditions

* Corresponding author.
E-mail address: mgardon@cptub.eu (M. Gardon).

0257-8972/$ – see front matter © 2013 Elsevier B.V. All rights reserved.
http://dx.doi.org/10.1016/j.surfcoat.2013.09.011

can be adjusted in order to avoid its thermal degradation. This opens the possibility of coating flexible polymers that are being used in electronic systems. Titanium dioxide is a widely used material in the field of sensors and actuators. Its chemical stability and relative low cost make it attractive for its industrial application and have been extensively selected as feedstock in APS. Therefore, the fabrication of titanium sub-oxide (TiO_{2-x}) coatings by means of Atmospheric Plasma Spray onto the flexible polymer Kapton® is studied in this paper and its application as the active layer of metal oxide gas sensors is presented. The performance of the device has been tested using $NH_{3(g)}$ at different concentrations.

2. Experimental details

A commercially available powder containing a mixture of TiO_2 (rutile), Ti_8O_{15} and Ti_9O_{17} was used (Metco 102, Sulzer Metco). The coatings were built-up onto the flexible polymeric film Kapton® with a thickness of 50 μm. In a few samples, Ag electrodes and a heater were previously printed over and below the substrate with an inkjet technique in order to perform gas sensing experiments, respectively. The feedstock powder was sprayed using an Atmospheric Plasma Spray (APS) A-3000S system with an F4 plasma torch (Sulzer Metco, Germany). Temperature of the in-flight particles was measured using the SprayWatch System (Oseir, Tampere, Finland). Particularly, particle temperature was measured using a two-color pyrometer. Powder and coating cross-section area were observed by Optical Microscopy (DMI-M Leica) and Scanning Electron Microscopy (JSM-5310 Jeol). Porosity was measured by image analysis (Matrox Inspector 1.71). The sensing experiments were performed in a test chamber with 15 ml in volume maintaining constant gas flow at 200 ml/min with a gas mixer controller (MGP-2, Gometrics S.L., Spain). Gaseous environments were obtained by mixing calibrated bottles of dry synthetic air (SA, which contains 21% of O_2 and 79% of N_2) and $NH_{3(g)}$ (100 ppm diluted in SA). Water vapor was introduced in the gas mixture bubbling dry synthetic air through a vase containing deionized water at room temperature (25 °C). A Source-Measurement double unit (2602A, Keithley) was used to measure the electrical signal of the sensor and power of an integrated heater, which was set at 210 °C during the sensing experiments. The response of the sensor to gas (Response [%]) was defined as the difference between the measured resistance when there is a change in the atmosphere composition (R) and the initial resistance value (R_0) normalized to R_0.

3. Results and discussion

3.1. Coating development

Particle size range of the feedstock was from −55 to +10 μm and had an angular shape. Besides, its average crystallite size was well above nanoscaled materials commonly used as the active layer of metal oxide gas sensors (Fig. 1). In a previous work, the influence of different percentages of hydrogen in the plasma jet was studied [9]. Hydrogen present in the plasma jet could reduce from Ti^{4+} to Ti^{3+}, which led to large accumulation of oxygen vacancies in the coating. As a result, titanium sub-oxide (TiO_{2-x}) coatings with very low electric resistivity were obtained and their performance as electrodes in simulated lead batteries was later studied as well [10]. Same spraying conditions were selected in this study. Particle temperature was approximately 2050 °C. Thus, substrate degradation was of special concern. Glass transition temperature of the polymer was theoretically expected between 380 and 410 °C and melting temperature above 500 °C [11]. In this way, starting trials were carried out in order to modify the power of the plasma jet by means of altering the plasma intensity and hydrogen/argon rates. Although it was possible to considerably decrease the temperature of the particles, which reduced the thermal effect on the polymer, the coating was not properly built-up due to feedstock material was not sufficiently molten for being adequately deposited.

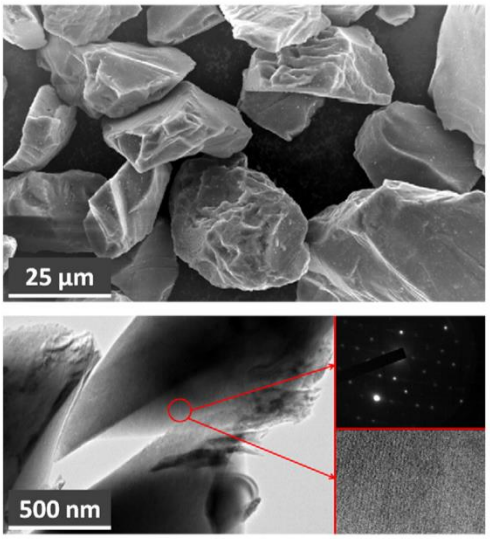

Fig. 1. Above: SEM micrograph of the powder. Below: TEM micrograph of the powder.

Therefore, it was decided to fix operation parameters such as spraying angle, feeding rate, plasma intensity and Ar/H_2 rates from abovementioned previous reports. Number of cycles and stand-off distance were the analyzed factors for carrying out a factorial design of experiments. Concretely, the studied levels were: i) five equidistant number of cycles (in ascending order: 1A, 1B, 1C, 1D, 1E) and; ii) five equidistant stand-off distances (in ascending order: 2A, 2B, 2C, 2D, 2E). Table 1 compiles the operation ranges. It was observed that as long as the stand-off distance was enlarged, temperature of the plasma jet decreased, which was in agreement with previous findings and the work published by other authors [5,9]. Although plasma jet may be cool enough for preventing damage of the substrate, particles were still arriving at high temperatures. At spraying distances 2A, 2B and 2C, polymer degradation was produced independently of the number of cycles. Just those samples obtained above 2C distance were satisfactorily obtained without substrate degradation. Thus, heat provided to the substrate by impacting molten particles that were being solidified was low enough for avoiding the alteration of the starting nature of the polymer. Number of cycles had no critical effects on the system; increased values did not thermally degrade the substrate for appropriate stand-off distances (2D and 2E). However, proper electric contact was not achieved for the lowest number of cycles, which was attributed to uncoated spots. As long as the number of cycles increased, it was found that the resistance decreased between the printed electrodes from 1.05 to 0.05 Ω caused by an improved connection between the electrodes. Coating porosity was not influenced by this spraying parameter and remained constant.

Fig. 2 shows a characteristic cross-section area of the coated polymer. It can be observed that the coating was properly bonded onto the polymeric film. Mismatch in the coefficient of thermal expansion (CTE)

Table 1
Values of the spraying parameters used.

Ar/H_2 flow ratio	3–7
Feeding rate (carrier gas)	2–4 l/min
Spraying angle	90°
Gun speed in each pass	100–500 mm/s
Stand-off distance	50–250 mm
Plasma intensity	450–550 A
Coating thickness	20–90 μm

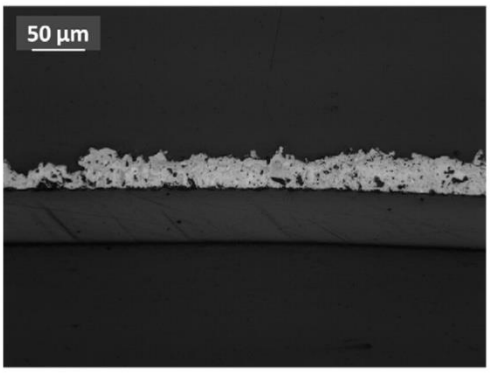

Fig. 2. Cross-section area of a characteristic coating.

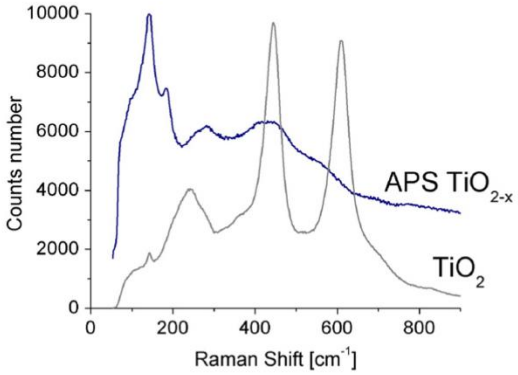

Fig. 4. Raman spectra of coated sample and rutile.

between the substrate and the coating is usually a worrying phenomenon in APS. Nevertheless, in this study delamination or vertical cracks caused by accumulated stress induced by distinct expansion and contraction of the coating–substrate system was not observed. Besides, it is noteworthy to mention that nitrogen cooling was not required, which is commonly applied in APS when working with delicate substrates. Fig. 3 includes a cross-section area of deposited splats and a top surface micrograph of a heterogeneous spot of the coating, where it is possible to observe that the polymer near to the deposits was not affected by the heat. As regards their surface composition, micro-Raman spectra of a coating compared to pure rutile can be observed in Fig. 4. Shift and intensity of the peaks observed when comparing oxygen-defective APS TiO_{2-x} with completely oxidized rutile powder are caused by the different Ti/O ratios contained in each material [12].

Polymer film was sprayed using a mask that made possible to build-up the coating on a circular area with a diameter of 8 mm, where the electrodes were previously printed by inkjet printing (Fig. 5).

3.2. Sensor performance

$NH_{3(g)}$ gas experiments were conducted with the purpose of testing the sensing performance of the samples that had: i) electric contact among the splats and; ii) a flexible behavior (spraying conditions: 1C, D–2C). The expected behavior of the reduced surface could be explained by the large amount of oxygen vacancies that were present on the APS TiO_{2-x} coating. Each vacancy could act as an active centre for the adsorption of $O_{2(g)}$. Then, the interaction of the adsorbed $O_{2(g)}$ with the electric current led to anionic oxygen species, which are highly reactive towards $NH_{3(g)}$. In this way, the receptor function was boosted due to a possible increase in the affinity of the metal oxide surface and the desired sensing reactivity. A scheme of plane (1 1 0) of rutile with a certain amount of oxygen vacancies and the involved gaseous species are shown in Fig. 6. The chemical reactions developed on the surface of the metal oxide are shown below [13]:

$$O_{2(g)} + e^- \rightarrow O^{2-}_{(ads)} \quad (1)$$

$$O^{2-}_{(ads)} + e^- \rightarrow 2O^-_{(ads)} \quad (2)$$

$$2NH_3 + 3O^-_{(ads)} \rightarrow N_2 + 3H_2O + 3e^- \quad (3)$$

Feedstock powder was microstructured (Fig. 1); according to transducer function, these materials are not very sensitive to surface reactions. Adsorbtion and dissociation of O^2 and O^{2-} (reactions 1 and 2) lead to a space charge region on the surface of each metal oxide grain due to the transfer of the electrons from the bulk to adsorbed oxygen species [2]. This region also known as depleted zone determines the sensitivity of the device if its thickness is comparable to crystallite size. Nonetheless, microstructured materials are supposed to have a grain size much bigger than the space charge region. Then, overall electric resistivity is not so affected by surface reactivity, which decreases the transducer function of the sensor. On the other hand, an approximate of 5–8% porosity was measured. Besides, the access of the inner grains could be enhanced, which can also help in providing acceptable levels of sensitivity in front of the target gas. In this way, TiO_{2-x} active

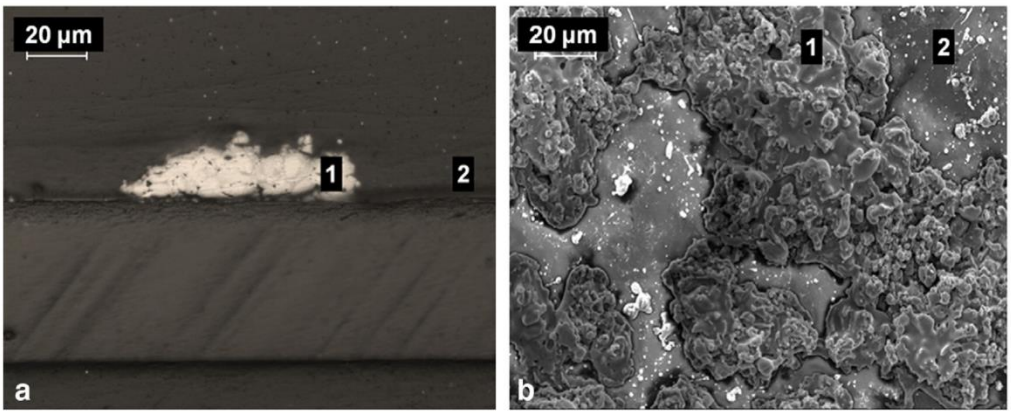

Fig. 3. a) Cross-section micrograph of a splat. b) Top surface micrograph of a heterogeneous area of the coating (1. Splat/coating and 2. Polymer).

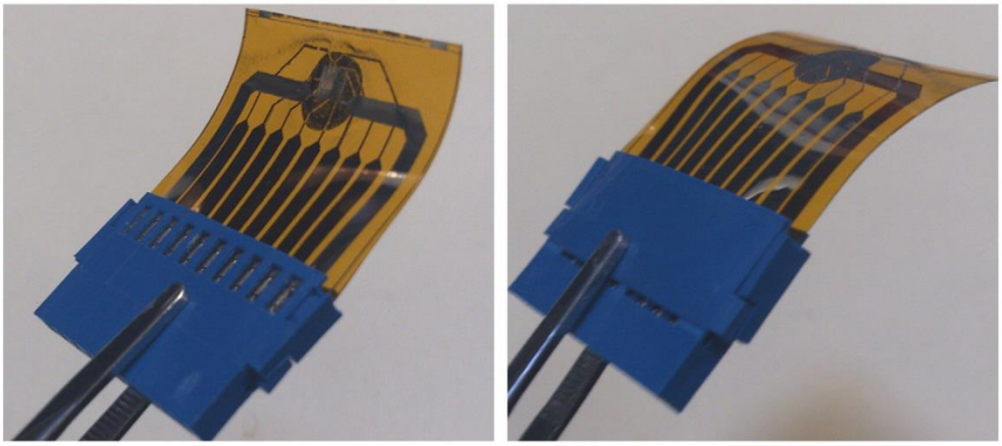

Fig. 5. Macrography of the obtained device.

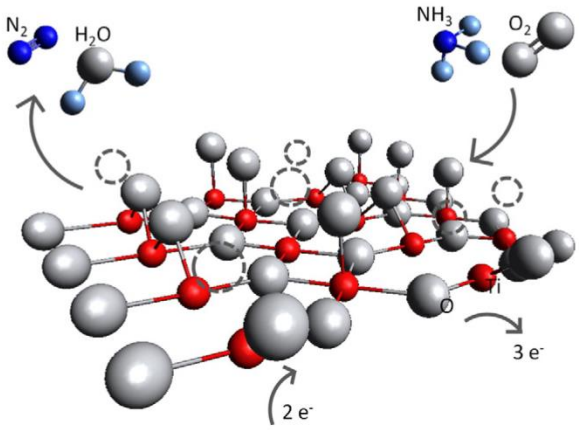

Fig. 6. Scheme of the interaction between the solid surface and the gaseous species. The dashed circles represent oxygen vacancies of the plane (1 1 0) of rutile.

layer provided by APS may have poor capacity of transforming chemical reactions at the top surface of the coating to a monitored output signal due to its microsized crystallites. However, proper sensitivity of the system may be assured by means of: i) coating enhanced capacity of adsorbing gaseous species because of the presence of oxygen vacancies at the metal oxide surface and ii) the porosity, which may favor the interaction between solid and target gas. Despite the influence of humidity was not analyzed in this study, its presence may determine the final behavior of the sensor. Adsorbed water molecules on TiO_{2-x} lead to a higher coverage of surface hydroxyl groups, which interact with the target gas altering the monitored output signal [2].

Fig. 7 shows the change in the electric resistivity of the active layer with respect to different $NH_{3(g)}$ concentrations (100–50–25–12.5 ppm). Although this demonstrated that it made difficult to monitor gas exposures as long as the concentration decreased, satisfactory output down to 12.5 ppm was observed, which makes it suitable for monitoring hazardous human environments or pollution control [14]. Then, the performance of the sensor when exposing the active layer to intervals of the target gas in a constant concentration was tested. The results showed that the device performs with reproducibility, indicating its suitability from an industrial point of view. In both cases, an average response and recovery times of 2 and 8 min were determined respectively. Almost linear response trend of the sensor against different $NH_{3(g)}$ concentrations was observed. For higher concentrations like 100 ppm, a response of 7% in the active layer was reached. The response of the MOX sensor for concentrations around 12.5 ppm was approximately 1.30%. The obtained results matched with data available in different publications, especially related to the sensing response [15,16].

4. Conclusions

A metal oxide gas sensor has been feasibly produced by Atmospheric Plasma Spray (APS) onto a flexible polymeric thin film. Despite the high temperatures involved in APS, the polymer was not degraded during the process, obtaining a well-bonded titanium sub-oxide coating. Stand-off distance was in command to provide adequate particle

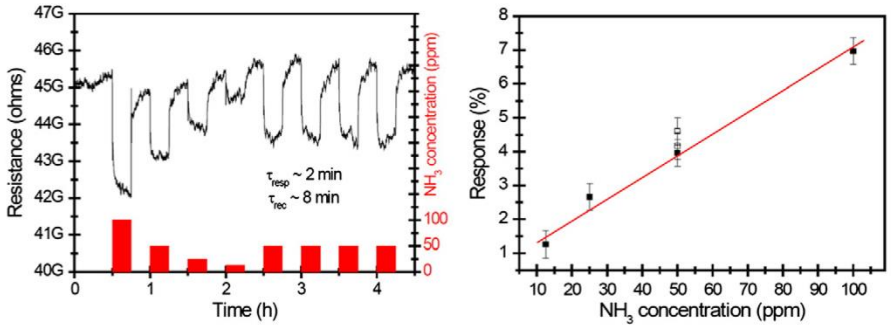

Fig. 7. Left: Response and recovery times (line) of the sensor using decreasing and constant target gas concentrations (columns). Right: Response of the sensor against the different target gas concentrations.

temperature for avoiding damage of the polymer. The sensing behavior of the metal oxide layer was tested by means of $NH_{3(g)}$ proving positive results ranging from 100 to 10 ppm. This could be attributed to the high amount of oxygen vacancies present on the top surface of the coating material and the porosity contained in the thickness of the active layer, which respectively increase adsorption capacity and enlarge the surface of interaction.

Acknowledgments

The authors wish to thank the Generalitat de Catalunya for the financial support of this research project 2009 SGR 00390.

References

[1] M. Suh, K. Carroll, N. Cassill, J. Text. Apparel. Technol. Manage. 6 (4) (2010) 1–18.
[2] M. Gardon, J.M. Guilemany, J. Mater. Sci. Mater. Electron. 24 (5) (2013) 1410–1421.
[3] L.L. Shaw, D. Goberman, R. Ren, M. Gell, S. Jiang, Y. Wang, T.D. Xiao, P.R. Strutt, Surf. Coat. Technol. 130 (1) (2000) 1–8.
[4] H.M. Hawthorne, L.C. Erickson, D. Ross, H. Tai, T. Troczynski, Wear 203 (204) (1997) 709–714.
[5] L. Pawlowski, The Science and Engineering of Thermal Spray Coatings, Second edition John Wiley & Sons, Chichester, U.K., 2008
[6] S. Sampath, J. Therm. Spray Tech. 19 (5) (2010) 921–949.
[7] A. Iwata. United States Patent US2004/0074072 A1.
[8] C. Zhang, M. Debliquy, A. Boudib, H. Liao, C. Coddet, Sensors Actuators B Chem. 144 (2010) 280–288.
[9] M. Gardon, J.M. Guilemany, in: B.R. Marple (Ed.), Thermal Spray 2012: Proceedings from the International Thermal Spray Conference and Exposition, ASM International, Houston, USA, 2012, pp. 622–626, (May 21–24, 2012).
[10] M. Gardon, S. Dosta, J.M. Guilemany, M. Kourasi, B. Mellor, R. Wills, J. Power Sources 238 (2013) 430–434.
[11] http://www2.dupont.com/Kapton/en_US/assets/downloads/pdf/HN_datasheet.pdf (Accessed 19/12/2012).
[12] J.C. Parker, R.W. Siegel, Appl. Phys. Lett. 57 (1990) 943–945.
[13] C.W. Lin, H.I. Chen, T.Y. Chen, C.C. Huang, C.S. Hsu, R.C. Liu, W.C. Liu, Sensors Actuators B Chem. 160 (1) (2011) 1481–1484.
[14] http://gestis-en.itrust.de/nxt/gateway.dll?f=templates&fn=default.htm&vid=gestiseng:sdbeng (Accessed 04/02/2013).
[15] B. Timmer, W. Olthuis, A. Van den Berg, Sensors Actuators B Chem. 107 (2) (2005) 666–677.
[16] S. Claramunt, O. Monereo, M. Boix, R. Leghrib, J.D. Prades, A. Cornet, P. Merino, C. Merino, A. Cirera, Sensors Actuators B Chem. 187 (2013) 401–406.

3.4.3. Inkjet Printing Soldering

In the third presented paper, ***Paper III****: "Flexible hybrid circuit fully inkjet-printed: Surface mount devices assembled by silver nanoparticles-based inkjet ink"*, the following issues were addressed in detail:

(1)The manufacturing for the first time of fully inkjet-printed junctions employing high-resolution drop-jetting of silver nanoparticle-based ink by means of drop-on-demand inkjet-printing technology.
(2)The demonstration of viability and reliability of silver nanoparticles as high conductive interconnecting material for assembling surface-mount devices (SMDs) onto previous inkjet-printed substrates by electrical contact resistance and shear strength measurements, comparing the results to benchmark assembling materials.
(3)The observation of homogeneous assembling contact (~1 μm thick) between SMD and printed pads onto printed substrates, thus confirming the reduction of material consumption.
(4)The manufacture of a flexible hybrid circuit on paper to demonstrate the applicability and scalability of the proposed assembling technique, where different size-shaped SMDs sensors are controlled by an Arduino board.

The paper aims at the demonstration of inkjet printing technology, as alternative method to surface-mount technology (SMT), for assembling SMDs onto previous inkjet-printed substrates. The applications and implications of this work could be far-reaching. We believe that our work will improve the existing RF Tags, boost and promote smart packaging, and enhance wearable, flexible and paper electronics.

* *Note that sections, equations and references numbering in the reproduced research article follow the ones of the published version.*

JOURNAL OF APPLIED PHYSICS **121**, 104904 (2017)

Flexible hybrid circuit fully inkjet-printed: Surface mount devices assembled by silver nanoparticles-based inkjet ink

J. Arrese,[a] G. Vescio, E. Xuriguera, B. Medina-Rodriguez, A. Cornet, and A. Cirera
MIND–IN2UB, Department of Engineering: Electronics, Universitat de Barcelona, Martí i Franquès 1, E-08028 Barcelona, Spain

(Received 30 November 2016; accepted 21 February 2017; published online 14 March 2017)

Nowadays, inkjet-printed devices such as transistors are still unstable in air and have poor performances. Moreover, the present electronics applications require a high degree of reliability and quality of their properties. In order to accomplish these application requirements, hybrid electronics is fulfilled by combining the advantages of the printing technologies with the surface-mount technology. In this work, silver nanoparticle-based inkjet ink (AgNP ink) is used as a novel approach to connect surface-mount devices (SMDs) onto inkjet-printed pads, conducted by inkjet printing technology. Excellent quality AgNP ink-junctions are ensured with high resolution picoliter drop jetting at low temperature (∼150 °C). Electrical, mechanical, and morphological characterizations are carried out to assess the performance of the AgNP ink junction. Moreover, AgNP ink is compared with common benchmark materials (i.e., silver epoxy and solder). Electrical contact resistance characterization shows a similar performance between the AgNP ink and the usual ones. Mechanical characterization shows comparable shear strength for AgNP ink and silver epoxy, and both present higher adhesion than solder. Morphological inspections by field-emission scanning electron microscopy confirm a high quality interface of the silver nanoparticle interconnection. Finally, a flexible hybrid circuit on paper controlled by an Arduino board is manufactured, demonstrating the viability and scalability of the AgNP ink assembling technique. *Published by AIP Publishing.*
[http://dx.doi.org/10.1063/1.4977961]

I. INTRODUCTION

Printed electronics[1] is a rapidly expanding research area, enabling low-cost, large-area, light-weight, and flexible electronics for bendable integrated circuits.[2] Concerning this, several printing technologies have been developed to accomplish these electronics requirements. Gravure printing,[3–5] screen printing,[4,6,7] flexographic printing,[3] laser-induced forward transfer printing,[8] and inkjet printing[9–14] find extensive applications in stretchable electronics.[15,16]

Among these techniques, drop-on-demand inkjet printing is a very promising printing technique since it guarantees high resolution that allows selective deposition, in a non-contact process, of a few picoliters amount of ink.[17,18] Avoiding masks and vacuum systems, inkjet printing permits to attain fast prototyping of circuits, thus becoming a cost-efficient technology. Furthermore, inkjet printing can achieve, in particular, conditions, nanometric resolution by means of submicron droplet ejectors or using self-alignment methods.[19,20]

Despite the huge efforts made for formulating new functional inks,[18,19,21,22] the main drawback in the inkjet printing technique is the lack of semiconductor and insulating inks.[14,23,24] In fact, there are recent exciting advances in multi-layered electronic components, such as transistors,[25–30] metal-insulator-metal (MIM) devices,[31,32] organic light-emitting diodes (OLEDs),[33] and diodes,[4] towards fully inkjet-printed electronic circuits.[34,35]

Nowadays, high technical requirements in electronic modules are fulfilled with hybrid techniques, combining the advantages of the printing technologies with the traditional components of surface-mount technology (SMT).[36–40] The main issue related to this procedure is the surface-mount device (SMD) attachment onto inkjet patterned substrates. An usual material employed for SMT is reflow paste,[41] a sticky mixture of flux and solder particles, but it shows incompatibility with inkjet-printed pads. Concerning this, solder particles on the reflow process were found to provoke a leaching effect by removing and damaging printed pads and generating undesired functional errors.[38] Recently, Niittynen *et al.* implemented SMDs on inkjet-printed substrates by isotropically conductive adhesive (ICA) screen printing.[38] Moreover, Andersson *et al.* assembled SMDs onto ink-jet printed paper with silver epoxy, solder, and conductive adhesive tapes.[36,37]

In this work, the recently patented use of silver nanoparticle-based inkjet ink (AgNP ink) as a new approach for assembling SMDs by means of high-resolution inkjet printing technology is presented.[42] Taking advantage of surface energies existing at the nanoscale, AgNP ink ensures high electrical conductivity after the thermal process at very low temperatures, and thus a high electrical conductive interconnection, practically of 98% silver, is achieved.[43–47] The new proposed method is compared with usual commercial benchmark materials employed for standard assembling. Therefore, AgNP ink, silver epoxy, and solder are tested on an inkjet-printed flexible and rigid substrate. Assembling methods' performance and their reliability were evaluated by means of electrical contact resistance and shear strength

[a]Author to whom correspondence should be addressed. Electronic mail: xarrese@el.ub.edu

TABLE I. Electrical resistivity of the assembling materials used.

Manufacturer	Assembling material	Resistivity ($\mu\Omega$·cm)
ANP, Silverjet DGP	AgNP ink	≈16
Chemtronics, W2400	Conductive silver epoxy Glue	$>10^3$
Qualitek Sn97/Cu3	Solder alloy Sn97/Cu3	>11, 8

of the SMDs onto the inkjet-printed pads. Finally, a fully inkjet-printed hybrid electronic circuit has been successfully manufactured onto paper substrate in order to show the feasibility of the new proposed method.

II. EXPERIMENTAL DETAILS

A. Materials

All the experimental tests were carried out by means of a printer machine Dimatix 2831 model series (Fujifilm USA). A cartridge with an ink droplet volume fixed at 10 pl was used. For the printed pads and wires, Silverjet DGP HR (ANP, South Korea) with 40% of silver weight concentration with a viscosity around ∼16 cP was used. The experimental set-up during printing processes was maintained stable at room temperature (22 °C), and meantime, nozzle firing drops and the inkjet platen substrate were fixed at 40 °C. Nozzle-platen with equal temperature was chosen to promote volatile solvent evaporation that ensures the best drop size on the surface after impacting the substrate.

Paper substrate Powercoat 230 (Arjowiggins, USA) with a thickness of 222 μm and single faced adhesive plastic polyimide Kapton® (ISOAD TAPE 7004, DuPont, USA) with a thickness of 25 μm were used as flexible substrates. The paper substrate presents an organic coating around ∼15 μm that prevents the paper in terms of ink penetration. A microscopy slide glass was employed as a rigid substrate.

Three materials were tested to assemble the SMDs onto the inkjet-printed pads: Silverjet ink compound, the same used for the inkjet-printed pattern; silver epoxy (CircuitWorks Conductive Epoxy CW2400, Chemtronix); and the solder (Qualitek, Sn 97% Cu 3%) after a previous flux (Omnifix) application on printed pads. The resistivity values are summarized in Table I. The resistivity values of selected assembling materials are specified by the manufacturers.

SMD resistors of 0 Ω and model size 1206 (3.2 mm × 1.6 mm) were selected for assembling characterization.

Concerning a fully printed hybrid electronic circuit on paper, carbon nanofibers (dispersed on isopropanol 70% w/w) were deposited by drop coating onto inter-digit printed electrodes (supplementary material, S1) as an active layer for the humidity gas sensor, taking advantage of previous works of our group.[48–50] A SMD NTC thermistor, case size 0402 (1 mm × 0.5 mm), was used as a temperature sensor. SMD resistors, case sizes 0603 (1.55 mm × 0.85 mm) and 0402, of different resistance values, properly estimated for the circuit requirements, were selected. Finally, SMD LED (LW P473 from OSRAM) was employed to obtain light-response information from the sensors. The fully inkjet-printed hybrid electronics circuit was controlled by an Arduino One board.

B. Procedure

Prior to the printing process, standard cleaning of the surface substrates was carried out (supplementary material, S2). A pattern of AgNP ink was printed and thermally cured in a convection oven at 150 °C for 30 min, in order to evaporate the organic ink solvents and to sinter the silver nanoparticles to achieve a resistivity around 16 $\mu\Omega$·cm, which is among the best values found in the literature.[45,47,51] As a result, a pattern based on tracks and pads with an average thickness of ∼250 nm was deposited.

Inkjet-printed pads of two stripes 7 mm × 1.6 mm with 1 mm pitch were printed as a fixed pattern set-up to carry out the electrical contact resistance study for each assembling test. Similarly, a fixed pattern consisting of two 5 mm × 3 mm stripes with 1 mm pitch was printed to estimate the strength stress tests. In both cases, the study was realized with 30 samples for each assembling method.

In order to join the SMD metallic pads with the printed pads, by means of the AgNP ink, the SMDs were manually located onto the printed pads, and a well-adapted pattern was printed afterwards with the high resolution drop jetting printer (Fig. 1).

In the case of silver epoxy and solder, the processing steps were manually operated. Before soldering, adopting the iron at 200 °C, a proper plating of component pads was applied. Afterwards, SMDs were soldered onto AgNP ink-printed pads. The three different mounting techniques under test onto the three chosen substrates are shown in Fig. 2.

The hybrid circuit tracks and pads were also previously printed on a paper substrate and heat treated as can be observed in Figure 3.

C. Characterization

Resistance measurements were performed by means of a Keithley 2400 source meter with the 4-probe method. In order to obtain an accurate value of the contact resistance, SMD resistors of nominally 0 Ω were measured to subtract

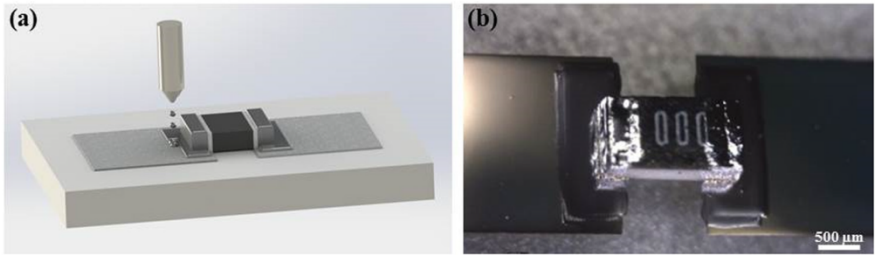

FIG. 1. (a) Illustration of the SMD AgNP ink assembling method. (b) SMD 0402 package of 0 Ω AgNP ink assembled.

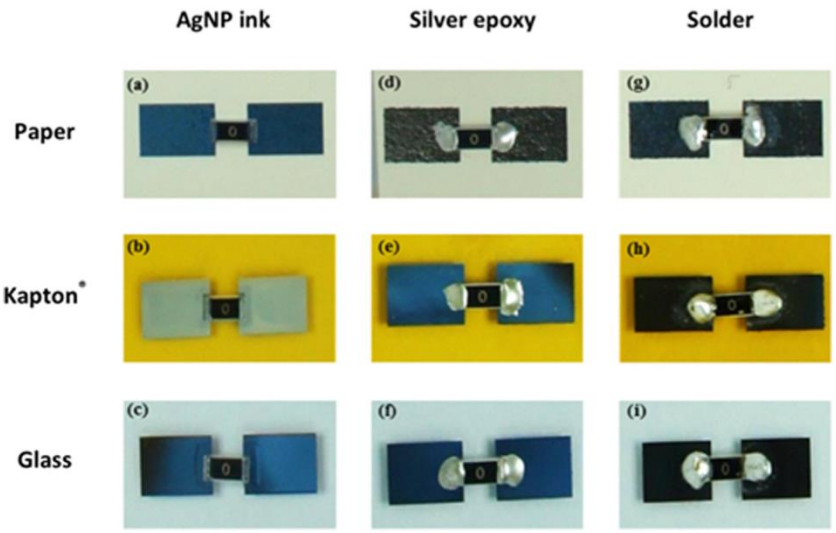

FIG. 2. Assembling SMDs on several substrates. (a)–(c) AgNP ink assembling method. (d)–(f) Silver epoxy assembling method. (g)–(i) Solder assembling method. The size of SMD devices is 3.2 mm × 1.6 mm.

their background contribution from the contact-SMD system. Each value was divided by the two contact junctions. For each assembling method and substrate used, an average contact resistance was determined.

The shear strength analysis was conducted by means of a Zwich/Roell ZMART.PRO with a load cell with a nominal force of 200 N. The evaluation test was done following the Japanese industrial standard for the mechanical tensile test called "Methods for shear strength of solder joints on chip components" (JIS Z 3198-7). The values of strength resistance, in MPa, were obtained from the breaking force and the joined surfaces in parallel to the applied force direction.

The morphology of different junctions related to each assembling technique was inspected by using a Field Emission-Scanning Electron Microscope (FEI Nova 200). In order to observe the interface of junctions, samples were embedded in resin and subsequently polished.

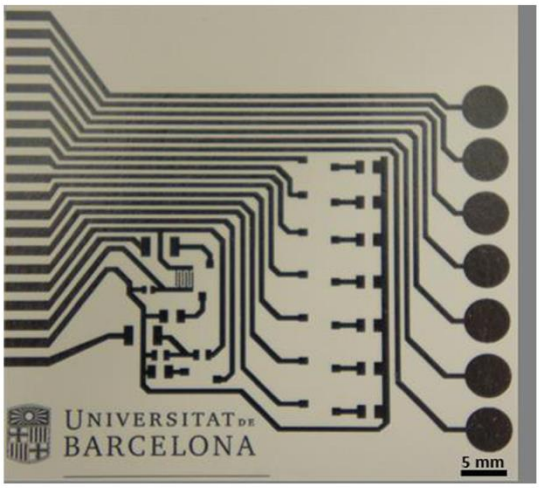

FIG. 3. Circuit pattern printed with AgNP ink on a paper substrate.

III. RESULTS AND DISCUSSION

The assembling performances were compared in terms of electrical, mechanical, and morphological properties in order to evaluate the reliability and feasibility of different techniques by an in-depth junction characterization.

Electrical contact resistance measurements were performed with the aim to demonstrate that a similar performance to benchmark materials can be achieved by the novel proposed assembling technique. The results are presented in Table II and Figure 4, taking into account the manufacturing failures. For each assembling method, all the badly attached components were considered as a failure and rejected. Then, considering the working devices (properly soldered), a contact resistance average value was estimated (a detailed example in the supplementary material, S3).

The roughness of the printed-paper surface plays an important role, impeding the interaction of the picoliter drop ink with the printed pad substrate and the SMD pad. The ink could not fill totally the interface between the inkjet-printed pad and the SMD pad, which would induce a weak junction. In order to solve this issue, the paper substrate that we selected is provided by a $CaCO_3$ precoating. Ohlund *et al.*[52,53] demonstrated that AgNP ink sintering could be impaired by the coating pore size but greatly enhanced by

TABLE II. Electrical contact resistance of assembled SMDs onto inkjet-printed pads depending on the attaching material and substrate.

Mounting method	Substrate	Contact resistance (Ω)	Failure (%)
AgNP ink	Paper[a]	0.27 ± 0.09	17
	Kapton	0.39 ± 0.15	17
	Glass	0.37 ± 0.10	23
Silver Epoxy	Paper	0.56 ± 0.07	10
	Kapton	0.39 ± 0.06	13
	Glass	0.39 ± 0.10	10
Solder	Paper	0.40 ± 0.11	3
	Kapton	0.12 ± 0.05	40
	Glass	0.47 ± 0.09	13

[a]SMDs assembled adding twice the material employed for Kapton and glass.

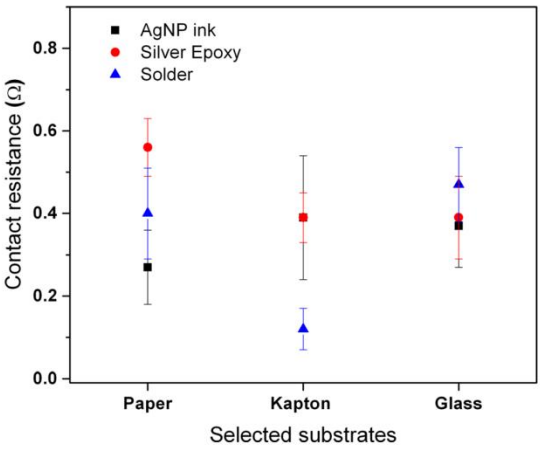

FIG. 4. Electrical contact resistance of assembled SMDs onto inkjet-printed pads depending on the attaching material and substrate.

using a porous $CaCO_3$ precoating. They proved that small concentrations of Cl and Ca are present on the surface of the paper with $CaCO_3$ precoating, and due to the presence of Cl in the AgNP ink, low temperature sintering with high conductivity values of printed pads can be facilitated by the presence of chloride.[52,53]

The precoating surface roughness and pore size, around 16–39 nm from the company datasheet, are small enough compared to the thickness of the printed layer ($\sim 1\,\mu$m). Therefore, in order to ensure the SMD assembling by AgNP ink, thick contacts were printed.

Regarding the smooth substrates glass and Kapton, high resolution drop size is ensured by a small value of contact-angle (using flash volatile solvents that evaporate during drop in-flight), but consequently, the system droplet would be more inclined to generate coffee rings[54] due to the non-uniform drying that leads to an excess of solute at the drop edges. The coffee ring effect was solved by the company, exploiting the Marangoni flow circulation in a drying drop, where, adding a proper co-solvent (triethylene glycol monoethyl ether) with a high boiling-point, a surface tension gradient is generated in order to reverse coffee-ring deposits.[55,56]

The best result for the electrical contact resistance was obtained on paper substrates with a value of $0.27 \pm 0.09\ \Omega$. In the case of a glass substrate, the roughness of the SMD pad and glass surfaces contributes to promoting the capillarity effect and then increasing the connected surface area. The measured high conductive contacts between printed pads and AgNP solder during electrical tests could be due to a re-dispersion of the solvents from the printed top contact to the bottom pads, where silver nanoparticles can generate an interlayer with high conductive performance after a new sintering process without forming a percolation network.[57] The other interlayer is promoted by the well-studied interaction between Ag nanoparticles and SMD Sn-plated.[58]

Similar electrical contact resistance values were obtained on a Kapton substrate, where the higher roughness of Kapton than that of glass seems to improve the junction reliability. In the case of a silver epoxy assembling material, the best results were achieved on Kapton and glass substrates. The electrical contact resistance exhibited equivalent and comparable values to AgNP ink in spite of the utilization of a large amount of silver epoxy that implies both the material waste and a difficult high resolution assembling process.

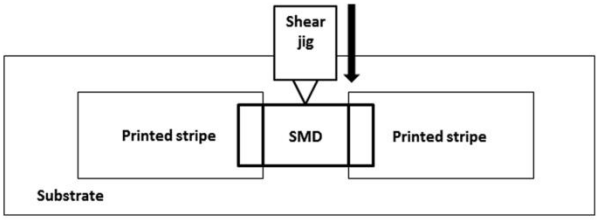

FIG. 5. Schematic of the tensile probe conducted according to the Japanese industrial standard JIS Z 3198-7.

Concerning the solder material, the best result was obtained on Kapton; however, the high number of failures showed lack of reliability. During the soldering process, degradation and displacement of the inkjet-printed pads due to the leaching effect were observed.[38] Similar phenomena appeared slightly on glass and paper substrates. Solder achieved, on paper substrates, the best process reliability and a suitable value for electrical contact resistance.

In summary, all the three different tested assembling techniques showed an equivalent electrical resistance value, which allows stating the feasibility of the proposed AgNP ink as an alternative straight forward and cost-efficient interconnecting material.

Andersson *et al.* determined the lowest electrical contact resistance of $0.4 \pm 0.15\,\Omega$ using a silver epoxy material to connect SMDs on inkjet-printed pads onto a paper substrate.[37] This value is equivalent and comparable to the proposed AgNP ink on all different selected substrates. In addition, due to the high resolution drop jetting control, the proposed novel attaching technique is also cost-effective, avoiding the wasted material during the assembling process.

Shear strength measurements were performed with the aim to demonstrate that comparable performance to benchmark materials can be achieved by the proposed assembling technique. As previously mentioned, the methodology to perform the mechanical test under the Japanese standard is conducted as the following scheme (Fig. 5). The calculated shear strength values for the assembled SMD using AgNP ink, silver epoxy, and solder are shown in Table III and Figure 6, taking into account the manufacturing failures. The shear strength value for each mounting method was estimated by

TABLE III. Shear strength resistance of the SMD assembled onto inkjet-printed pads depending on the attaching material and substrate.

Mounting method	Substrate	Shear strength (MPa)	Failure (%)
AgNP ink	Paper	2.51 ± 0.84	7
	Kapton	2.16 ± 0.79	10
	Glass	1.60 ± 0.16	13
Silver Epoxy	Paper	3.01 ± 0.62	3
	Kapton	1.87 ± 0.37	3
	Glass	3.52 ± 0.90	3
Solder	Paper	2.30 ± 0.61	3
	Kapton	1.03 ± 0.50	20
	Glass	0.55 ± 0.44	50

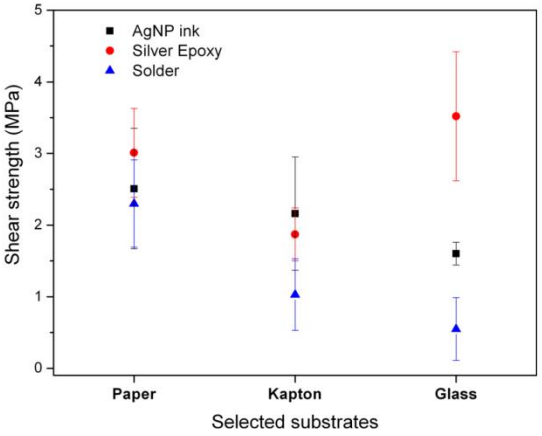

FIG. 6. Shear strength resistance of the SMD assembled onto inkjet-printed pads depending on the attaching material and substrate.

applying a similar modus operandi as done previously for the electrical measurements. Detailed information of characterization is presented in the supplementary material, S4.

With regard to the AgNP ink connecting material, the paper substrate showed the maximum shear strength value, followed by polyimide Kapton and glass substrates. Figure 7 presents evidence that the shear strength value is the result of two contributions: the interaction of the assembling material with printed pads and the adhesion strength of the printed pads onto the selected substrate. Indeed, the latter contribution is directly correlated with the roughness and porosity of the substrate.

With regard to the silver epoxy assembling material, the strongest adhesion was obtained on the glass substrate, and a comparable value was observed on the paper substrate.

The lowest shear strength, achieved with silver epoxy, was obtained with a Kapton substrate. The mechanical tests show greater epoxy remains on glass than on Kapton, demonstrating a better fixation between epoxy and printed pad on glass and justifying the higher shear strength reached (Figs. 8(b) and 8(d)). The adhesion results could be explained by different epoxy wettabilities onto each printed substrate. In the case of the solder connecting material, a general tendency to weaker shear strength than the previous assembling materials was observed in all the selected substrates. The strongest solder adhesion value was obtained on the paper substrate due to its considerable porosity and roughness that ensure a larger surface-area ratio than in the other substrates.

The mechanical test results confirmed that AgNP ink, exploiting the capillarity action in order to assemble the SMDs (Fig. 9(b)), performs as silver epoxy and is sturdier than solder. Fig. 9(b) shows how an isolated underlying contact point between the SMD pad and the inkjet-printed pad is produced by inkjet-printed AgNP ink. The electrical and mechanical study highlighted the AgNP ink as a promising alternative assembling material for SMDs.

To sum up, the proposed high resolution drop jetting technique sheds light on how, employing few picoliter drops, AgNP ink reveals comparable electrical and mechanical performances of benchmark assembling materials onto several inkjet-printed substrates.

Structural inspection of different junctions related to each assembling technique was performed to justify why the AgNP ink assembling technique exhibits competitive performances. Microscopic analyses of device cross-sections were performed by the FE-SEM technique, as shown in Fig. 10. The cross-sectional image of tin-plated SMD extremities displays the junction area between the surface device and inkjet-printed pad. Employing AgNP ink, the capillarity action moves the printed ink up to the underlying tin-plated SMD pads. Figures 10(b)–10(d) highlight the achieved

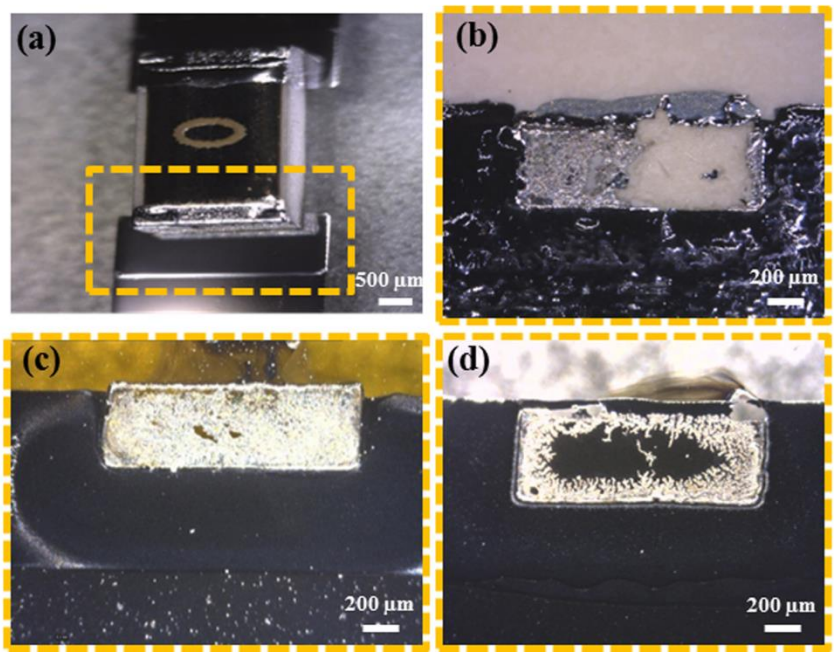

FIG. 7. (a) Image of SMD AgNP ink-connected on a glass substrate. (b)–(d) Pictures correspond to the substrate pad after removing SMD, AgNP ink-attached, from paper, Kapton, and glass, respectively. All the cases show partially removed inkjet-printed pads.

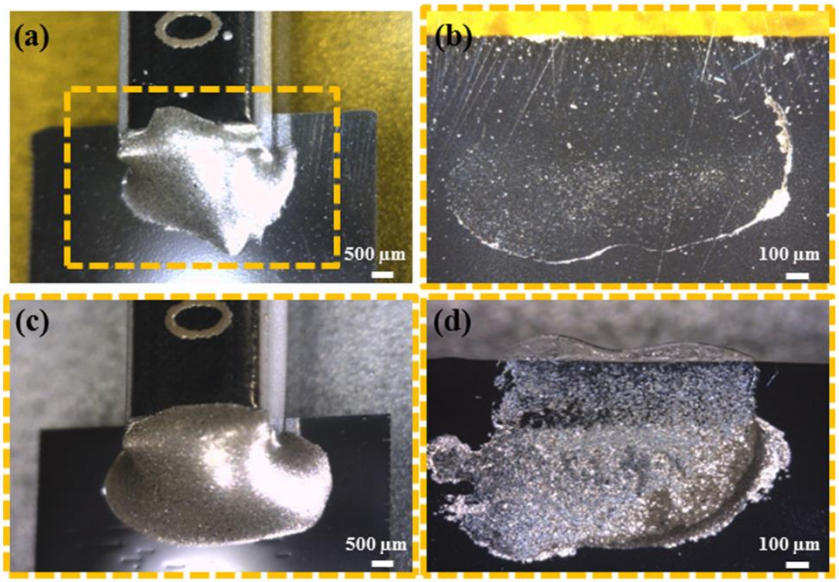

FIG. 8. (a) and (c) Optical images of the epoxy assembling before the shear strength test onto Kapton and glass, respectively. (b) and (d) Optical images of the epoxy assembling after the shear strength test onto Kapton and glass, respectively.

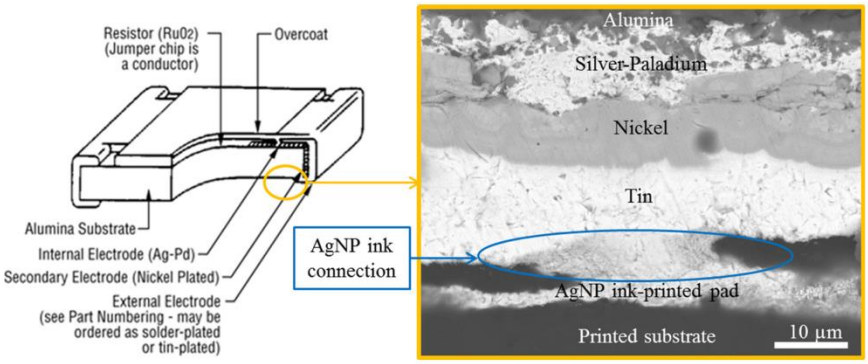

FIG. 9. (a) Schematic of the SMDs. (b) FE-SEM cross-sectional image of an isolated underlying contact area by AgNP ink between SMD tin-plated extremities and inkjet-printed solder pad. Furthermore, the description of the different layers is presented, proved by EDX analysis.

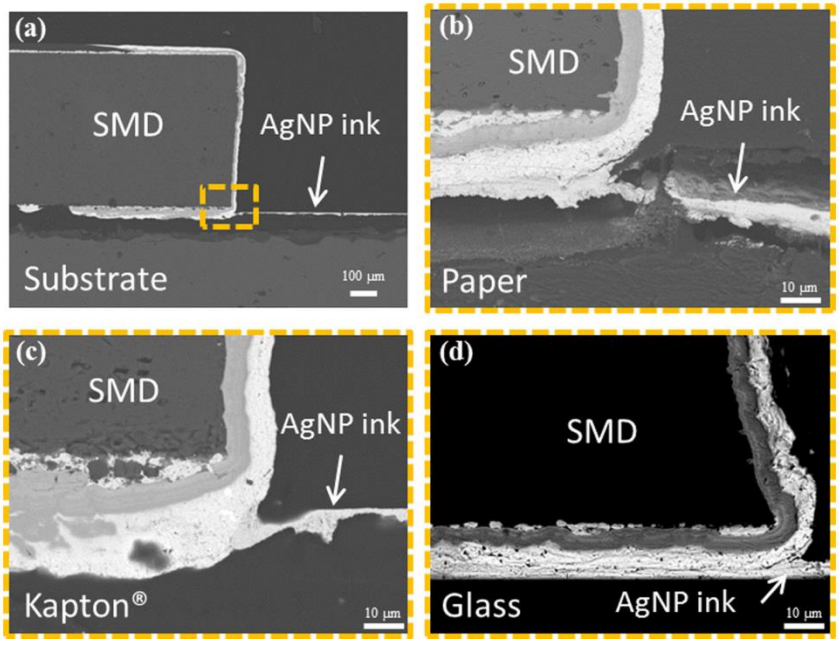

FIG. 10. (a) FESEM image of a cross-sectional view of one SMD pad AgNP ink-assembled on a printed pad. (b)–(d) FE-SEM images correspond to the details of the junction zone of the SMD Sn-plated pad, AgNP ink connector inkjet-printed, and AgNP ink inkjet-printed pad on paper, Kapton, and glass substrates, respectively.

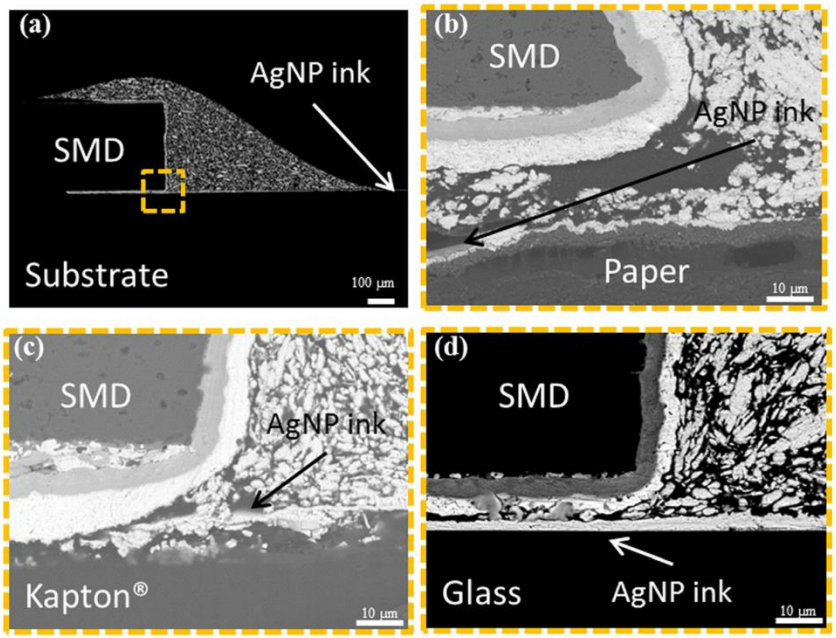

FIG. 11. (a) FE-SEM image of a cross-sectional view of an SMD pad silver epoxy-assembled on an inkjet-printed pad. (b)–(d) FE-SEM images correspond to the details of the junction zone of the SMD Sn-plated pad, silver epoxy connector, and AgNP inkjet-printed pad on paper, Kapton, and glass substrates, respectively.

excellent junction between printed connection and printed pad, which is proved by the indistinguishable bottom contact thickness contrast. The ink agglomerates almost uniformly down the edges of the SMD pads contributing to the high quality validated electrical contact and mechanical properties. In a different way than AgNP ink, devices connected by silver epoxy are not assisted by capillarity. Silver epoxy, manually applied, embeds the whole SMD pad area. However, the contact resistance measured is not better than with the AgNP ink assembling method. This is due to the existent adhesive filler mixed with the silver flakes in an approximately 50:50 ratio, as shown in Figs. 11(a)–11(d) by the dark zones between the bright silver particles. As previously reported about silver epoxy, in the same way, solder was manually deposited in order to assemble the SMD, as detailed in Fig. 12(a). Figs. 12(b)–12(d) point out a continuous junction interface between the soldering material and the inkjet-printed pad onto different selected substrates. As observed in the case of epoxy and due to lower conductivity than SNPI, an outwardly covered SMD pad does not ensure a better contact resistance.

Overall, FE-SEM images demonstrate that the assembling SMD technique by AgNP ink uniformly adapts and envelopes the Sn-plated SMD pads, without wasting unnecessary material

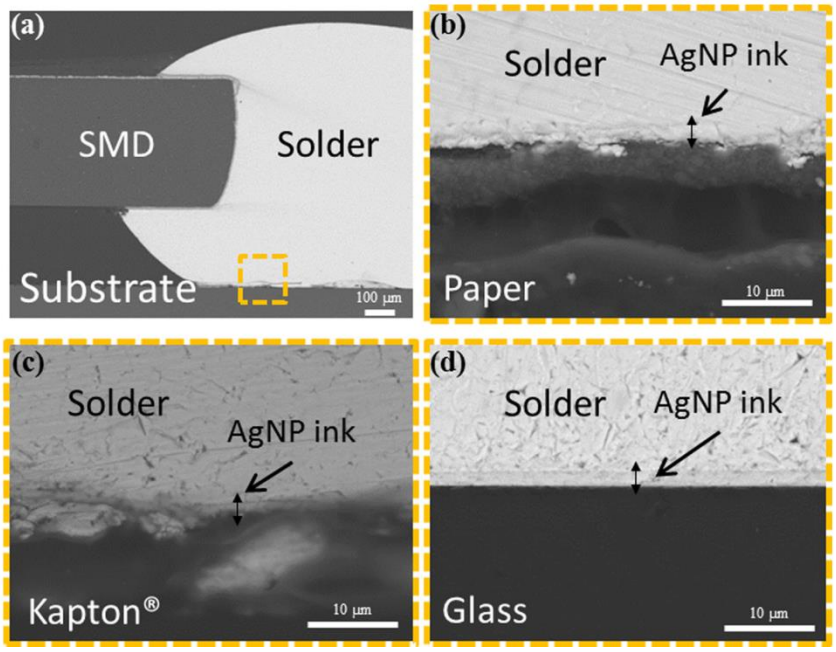

FIG. 12. (a) FESEM image of a cross-sectional view of one SMD pad Sn assembled. (b)–(d) FE-SEM images correspond to the details of the junction zone of the solder connector and AgNP inkjet-printed pad on paper, Kapton, and glass substrates, respectively.

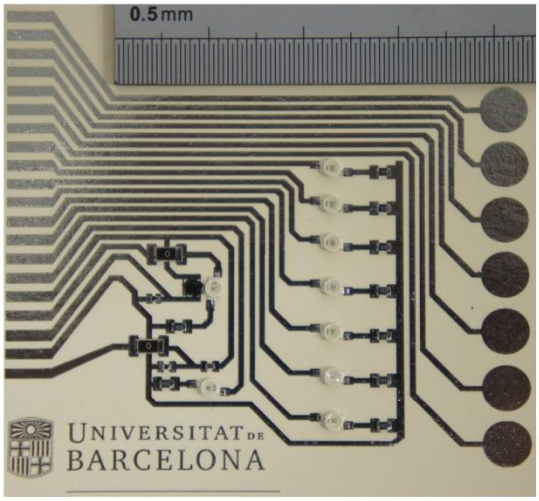

FIG. 13. Paper-based inkjet-printed electronic circuit with SMD AgNP ink-connected. (Multimedia view) [URL: http://dx.doi.org/10.1063/1.4977961.1]

surrounding the contact area as in the case of silver epoxy and solder methods. The structural characterization has shown that the morphology of the inkjet-printed silver connections evidences a solid and stable structure without detrimental fractures or pin-holes.

As practical demonstration of the proposed AgNP ink method, an inkjet-printed circuit with different families of assembled SMDs on paper is presented as shown in Fig. 13 and its associated video (Multimedia view).

The hybrid electronics circuit was controlled by Arduino One, which was programmed to monitor three different functional modes: capacitive touch control, temperature sensor, and humidity sensor. Each mode had a series of LEDs associated to easily visualize the information about the variation state. The supplementary material includes a demonstration video of the hybrid printed circuit and some complementary images (supplementary material, S5).

IV. CONCLUSIONS

SMDs have been assembled successfully onto an inkjet-printed flexible and rigid substrate by AgNP ink using high resolution inkjet printing technology. AgNP ink was selectively printed in order to reach a homogeneous junction between SMD pads and printed stripes followed by a low-temperature thermal treatment at $\sim$150 °C. Capillarity action of printed ink and coalescence sintering of silver nanoparticles ensures high quality soldering, promoted by 98% of interconnecting silver.

FE-SEM revealed the homogeneity and indiscernible contact between SMD and printed pads onto flexible substrates, paper, polyimide Kapton, and rigid glass substrate.

Electrical contact resistance and shear strength measurements proved drop-on-demand inkjet printing technology as a valid technique to incorporate on SMT, widening the applicability to stretchable and bendable substrates. In addition, high resolution and selective deposit of silver nanoparticles, exploiting the capillarity action, allows to avoid material waste (as in the case of silver epoxy and solder), thus maintaining high component density and fast assembling (6 m/s).

Taking advantage of the proposed method, an intelligent flexible hybrid circuit was successfully achieved on paper, where SMDs of different sizes have been assembled by AgNP ink, demonstrating the reliability and feasibility of the proposed method to be implemented in a roll-to-roll manufacturing process.

In light of the all above-mentioned studies, an inkjet printing connecting technique is demonstrated as a promising method that allows selectively assembling integrated devices, in a non-contact process, onto inkjet-printed flexible and rigid substrates for upcoming hybrid electronics.

SUPPLEMENTARY MATERIAL

See supplementary material for more details about the cleaning procedure of used substrates. Moreover, an example of different test characterizations and fully printed hybrid circuit on a paper substrate is presented.

ACKNOWLEDGMENTS

The authors acknowledge Julio Rivera, Arturo Peitivi, and Sergio Llorente from BSH Electrodomésticos España, S.A. for their fruitful support and enlightening discussions. A. Cirera acknowledges 2015 edition of BBVA Foundation Grants for Researchers and Cultural Creators.

[1]M. Berggren, D. Nilsson, and N. D. Robinson, Nat. Mater. **6**, 3 (2007).
[2]A. C. Siegel, S. T. Phillips, M. D. Dickey, N. Lu, Z. Suo, and G. M. Whitesides, Adv. Funct. Mater. **20**, 28 (2010).
[3]H. Yan, Z. Chen, Y. Zheng, C. Newman, J. R. Quinn, F. Dötz, M. Kastler, and A. Facchetti, Nature **457**, 679 (2009).
[4]F. C. Krebs, Sol. Energy Mater. Sol. Cells **93**, 394 (2009).
[5]M. Pudas, N. Halonen, P. Granat, and J. Vähäkangas, Prog. Org. Coatings **54**, 310 (2005).
[6]F. C. Krebs, M. Jørgensen, K. Norrman, O. Hagemann, J. Alstrup, T. D. Nielsen, J. Fyenbo, K. Larsen, and J. Kristensen, Sol. Energy Mater. Sol. Cells **93**, 422 (2009).
[7]C. López-Gándara, J. M. Fernández-Sanjuán, F. M. Ramos, and A. Cirera, Solid State Ionics **184**, 83 (2011).
[8]M. Colina, M. Duocastella, J. M. Fernández-Pradas, P. Serra, and J. L. Morenza, J. Appl. Phys. **99**, 084909 (2006).
[9]I. Clancy, G. Amarandei, C. Nash, and B. A. Glowacki, J. Appl. Phys. **119**, 054903 (2016).
[10]Y. Noda, H. Matsui, H. Minemawari, T. Yamada, and T. Hasegawa, J. Appl. Phys. **114**, 044905 (2013).
[11]S. Claramunt, O. Monereo, M. Boix, R. Leghrib, J. D. Prades, A. Cornet, P. Merino, C. Merino, and A. Cirera, Sens. Actuators, B **187**, 401 (2013).
[12]O. Monereo, S. Claramunt, M. M. De Marigorta, M. Boix, R. Leghrib, J. D. Prades, A. Cornet, P. Merino, C. Merino, and A. Cirera, Talanta **107**, 239 (2013).
[13]H. Sirringhaus, T. Kawase, R. H. Friend, T. Shimoda, M. Inbasekaran, W. Wu, and E. P. Woo, Science **290**, 2123 (2000).
[14]H. Minemawari, T. Yamada, H. Matsui, J. Tsutsumi, S. Haas, R. Chiba, R. Kumai, and T. Hasegawa, Nature **475**, 364 (2011).
[15]S. H. Ko, J. Chung, H. Pan, C. P. Grigoropoulos, and D. Poulikakos, Sens. Actuators, A **134**, 161 (2007).
[16]D. Tobjörk and R. Österbacka, Adv. Mater. **23**, 1935 (2011).
[17]S. Magdassi and S. Magdassi, Pigm. Resin Technol. **16**, 4 (1987), ISBN 9812818219.
[18]M. Singh, H. M. Haverinen, P. Dhagat, and G. E. Jabbour, Adv. Mater. **22**, 673 (2010).
[19]T. Sekitani, Y. Noguchi, U. Zschieschang, H. Klauk, and T. Someya, Proc. Natl. Acad. Sci. U. S. A. **105**, 4976 (2008).
[20]N. Zhao, M. Chiesa, H. Sirringhaus, Y. Li, Y. Wu, and B. Ong, J. Appl. Phys. **101**, 064513 (2007).

[21]H. Song, J. Spencer, A. Jander, J. Nielsen, J. Stasiak, V. Kasperchik, and P. Dhagat, J. Appl. Phys. **115**, 17E308 (2014).
[22]S. Jeong, H. C. Song, W. W. Lee, Y. Choi, and B. H. Ryu, J. Appl. Phys. **108**, 102805 (2010).
[23]A. Kamyshny and S. Magdassi, Small **10**, 3515 (2014).
[24]H. W. Choi, T. Zhou, M. Singh, and G. E. Jabbour, Nanoscale **7**, 3338 (2015).
[25]E. M. C. Fortunato, P. M. C. Barquinha, A. C. M. B. G. Pimentel, A. M. F. Gonçalves, A. J. S. Marques, L. M. N. Pereira, and R. F. P. Martins, Adv. Mater. **17**, 590 (2005).
[26]N. Stutzmann, R. H. Friend, and H. Sirringhaus, Science **299**, 1881 (2003).
[27]T. Y. Kim, M. Amani, G. H. Ahn, Y. Song, A. Javey, S. Chung, and T. Lee, ACS Nano **10**, 2819 (2016).
[28]F. Torrisi, T. Hasan, W. Wu, Z. Sun, A. Lombardo, T. S. Kulmala, G.-W. Hsieh, S. Jung, F. Bonaccorso, P. J. Paul, D. Chu, and A. C. Ferrari, ACS Nano **6**, 2992 (2012).
[29]C. Wang, J.-C. Chien, H. Fang, K. Takei, J. Nah, E. Plis, S. Krishna, A. M. Niknejad, and A. Javey, Nano Lett. **12**, 4140 (2012).
[30]L. Huang, Y. Huang, J. Liang, X. Wan, and Y. Chen, Nano Res. **4**, 675 (2011).
[31]G. Vescio, J. López-Vidrier, R. Leghrib, A. Cornet, and A. Cirera, J. Mater. Chem. C **4**, 1804 (2016).
[32]Y. Liu, T. Cui, and K. Varahramyan, Solid. State. Electron. **47**, 1543 (2003).
[33]S.-C. Chang, J. Liu, J. Bharathan, Y. Yang, J. Onohara, and J. Kido, Adv. Mater. **11**, 734 (1999).
[34]J. Jiang, B. Bao, M. Li, J. Sun, C. Zhang, Y. Li, F. Li, X. Yao, and Y. Song, Adv. Mater. **28**, 1420 (2016).
[35]S. E. Burns, P. Cain, J. Mills, J. Wang, and H. Sirringhaus, MRS Bull. **28**, 829 (2003).
[36]H. Andersson, J. Sidén, V. Skerved, X. Li, and L. Gyllner, IEEE Trans. Compon. Packag. Technol. **6**, 478 (2016).
[37]H. a Andersson, A. Manuilskiy, S. Haller, M. Hummelgård, J. Sidén, C. Hummelgård, H. Olin, and H.-E. Nilsson, Nanotechnology **25**, 094002 (2014).
[38]J. Niittynen, J. Kiilunen, J. Putaala, V. Pekkanen, M. Mäntysalo, H. Jantunen, and D. Lupo, Microelectron. Reliab. **52**, 2709 (2012).
[39]J. Putaala, J. Hannu, E. Kunnari, M. Mäntysalo, O. Nousiainen, and H. Jantunen, Microelectron. Reliab. **54**, 272 (2014).
[40]V. Pekkanen, M. Mäntysalo, K. Kaija, P. Mansikkamäki, E. Kunnari, K. Laine, J. Niittynen, S. Koskinen, E. Halonen, and U. Caglar, Microelectron. Eng. **87**, 2382 (2010).
[41]S. Xu, A. D. Pickel, A. Prasitthipayong, A. H. Habib, and M. E. McHenry, J. Appl. Phys. **113**, 2011 (2013).
[42]J. Rivera, A. Peitivi, S. Llorente, X. Arrese, L. Servera, and A. Cirera, Spain patent ES 2 564 760 A1 (2014).
[43]K.-S. Moon, H. Dong, R. Maric, S. Pothukuchi, A. Hunt, Y. Li, and C. P. Wong, J. Electron. Mater. **34**, 168 (2005).
[44]M. L. Allen, M. Aronniemi, T. Mattila, A. Alastalo, K. Ojanperä, M. Suhonen, and H. Seppä, Nanotechnology **19**, 175201 (2008).
[45]H.-H. Lee, K.-S. Chou, and K.-C. Huang, Nanotechnology **16**, 2436 (2005).
[46]S. Yan, D. Sun, Y. Gong, Y. Tan, X. Xing, G. Mo, Z. Chen, Q. Cai, Z. Li, H. Yu, and Z. Wu, J. Synchrotron Radiat. **23**, 718 (2016).
[47]J. Perelaer, B. J. De Gans, and U. S. Schubert, Adv. Mater. **18**, 2101 (2006).
[48]O. Monereo, S. Illera, A. Varea, M. Schmidt, T. Sauerwald, A. Schütze, A. Cirera, and J. D. Prades, Nanoscale **8**, 5082 (2016).
[49]O. Monereo, J. D. Prades, and A. Cirera, Sens. Actuators, B **211**, 489 (2015).
[50]O. Monereo, O. Casals, J. D. Prades, and A. Cirera, Sens. Actuators, B **226**, 254 (2016).
[51]B. J. Perelaer, A. W. M. de Laat, C. E. Hendriks, and U. S. Schubert, J. Mater. Chem. **18**, 3209 (2008).
[52]T. Öhlund, A. Schuppert, B. Andres, H. Andersson, S. Forsberg, W. Schmidt, H.-E. Nilsson, M. Andersson, R. Zhang, and H. Olin, RSC Adv. **5**, 64841 (2015).
[53]T. Öhlund, J. Örtegren, S. Forsberg, and H. E. Nilsson, Appl. Surf. Sci. **259**, 731 (2012).
[54]R. D. Deegan, O. Bakajin, T. F. Dupont, G. Huber, S. R. Nagel, and T. A. Witten, Nature **389**, 827 (1997).
[55]H. Hu and R. G. Larson, Langmuir **21**, 3972 (2005).
[56]H. Hu and R. G. Larson, J. Phys. Chem. B **110**, 7090 (2006).
[57]C. Nash, Y. Spiesschaert, G. Amarandei, Z. Stoeva, R. I. Tomov, and D. A. N. Tonchev, J. Electronic Mater. **44**, 497 (2015).
[58]B. F. Dyson, J. Appl. Phys. **37**, 2375 (1966).

Electronic Supplementary Information for Journal of Applied Physics

SUPPORTING INFORMATION

Flexible Hybrid Circuit Fully Inkjet-Printed: Surface Mount Devices Assembled by Silver Nanoparticles-Based Inkjet Ink.

Javier Arrese Carrasquer, Giovanni Vescio, Elena Xuriguera Martín, Beatriz Medina-Rodríguez, Albert Cornet Calveras, and Albert Cirera Hernandez

email: xarrese@el.ub.edu

This PDF file includes:

S1

Substrates cleaning procedures

The glass and kapton substrates were cleaned by means the following steps:

- 5 minutes ultrasonication in bath of acetone.
- 5 minutes ultrasonication in bath of isopropyl alcohol.
- 2 minutes ultrasonication in bath of deionized water.

Paper substrates were burn cleaned through a thermal process keeping the samples in an oven at 160 °C / 45 min. Thus, avoiding contamination of the silver printed pads in the sintering process"

S2

Definition of failures conditions during contact resistance test.

For each assembling method, all the badly-attached components were considered as a failure. Then, using the remaining devices, an initial contact resistance average value was estimated. All the devices with contact resistance values higher twice the average value were considered also as a failure. A final electrical contact resistance value was accurately recalculated with no failure devices.

Example:

First step

Sample	Contact resistance (Ω)	Sample considered	Initial Contact resistance Average value (Ω)
1	1,1	Correct	2,3
2	1,0	Correct	
3	1,3	Correct	
4	0,9	Correct	
5	1,0	Correct	
6	5,3	Correct	
7	Open circuit	Failure	
8	1,1	Correct	
9	7,0	Correct	
10	Open circuit	Failure	

Second step

Sample	Contact resistance (Ω)	Contact Resistance / Initial contact resistance average value	Sample considered	Contact resistance Average value (Ω)
1	1,1	0,48	Correct	0,91
2	1,0	0,43	Correct	
3	1,3	0,56	Correct	
4	0,9	0,39	Correct	
5	1,0	0,43	Correct	
6	5,3	2,30	Failure	
7	Open circuit	-	Failure	
8	1,1	0,48	Correct	
9	7,0	3,04	Failure	
10	Open circuit	-	Failure	

S3

Definition of failures conditions during shear strength test.

For each assembling method, all the badly-attached components were considered as a failure. Then, using the remaining devices, a shear strength value for each mounting method was estimated. All the devices with shear strength values smaller twice the average value were considered also as a failure. A final electrical contact resistance value was accurately recalculated with no failure devices.

Example

First step

Sample	Shear strength (MPa)	Sample considered	Initial Shear strength Average value (MPa)
1	2,0	Correct	1,9
2	2,1	Correct	
3	2,5	Correct	
4	1,9	Correct	
5	0,7	Correct	
6	1,8	Correct	
7	0,01	Failure	
8	2,2	Correct	
9	2,0	Correct	
10	0,01	Failure	

Second step

Sample	Shear strength (MPa)	Shear strength / Initial Shear strength average value	Sample considered	Shear strength Average value (MPa)
1	2,0	1,05	Correct	2,1
2	2,1	1,1	Correct	
3	2,5	1,3	Correct	
4	1,9	1	Correct	
5	0,7	0,37	Failure	
6	1,8	0,94	Correct	
7	0,01	-	Failure	
8	2,2	1,16	Correct	
9	2,0	1,05	Correct	
10	0,01	-	Failure	

This PDF file includes:

Figs. S1 to S2

Figure Supplementary 1. Inter-digit printed electrodes of the humidity sensor.

The hybrid printed circuit is composed by three functional modes: a capacitive detecting mode, a temperature and humidity sensing modes. Regarding on capacitive mode, seven capacitive detectors are designed with its corresponding LED, which are turned on when the corresponding capacitive detector are touched. For temperature and humidity modes, LEDs advising state on/off is attached. The software is programed for changing between modes keeping the capacitive detectors three and five touched for a few seconds. At the same time, when each sensor mode is running, the Arduino software is programed for turn on/off the same LEDs of the capacitive mode to show the sensor signal variations.

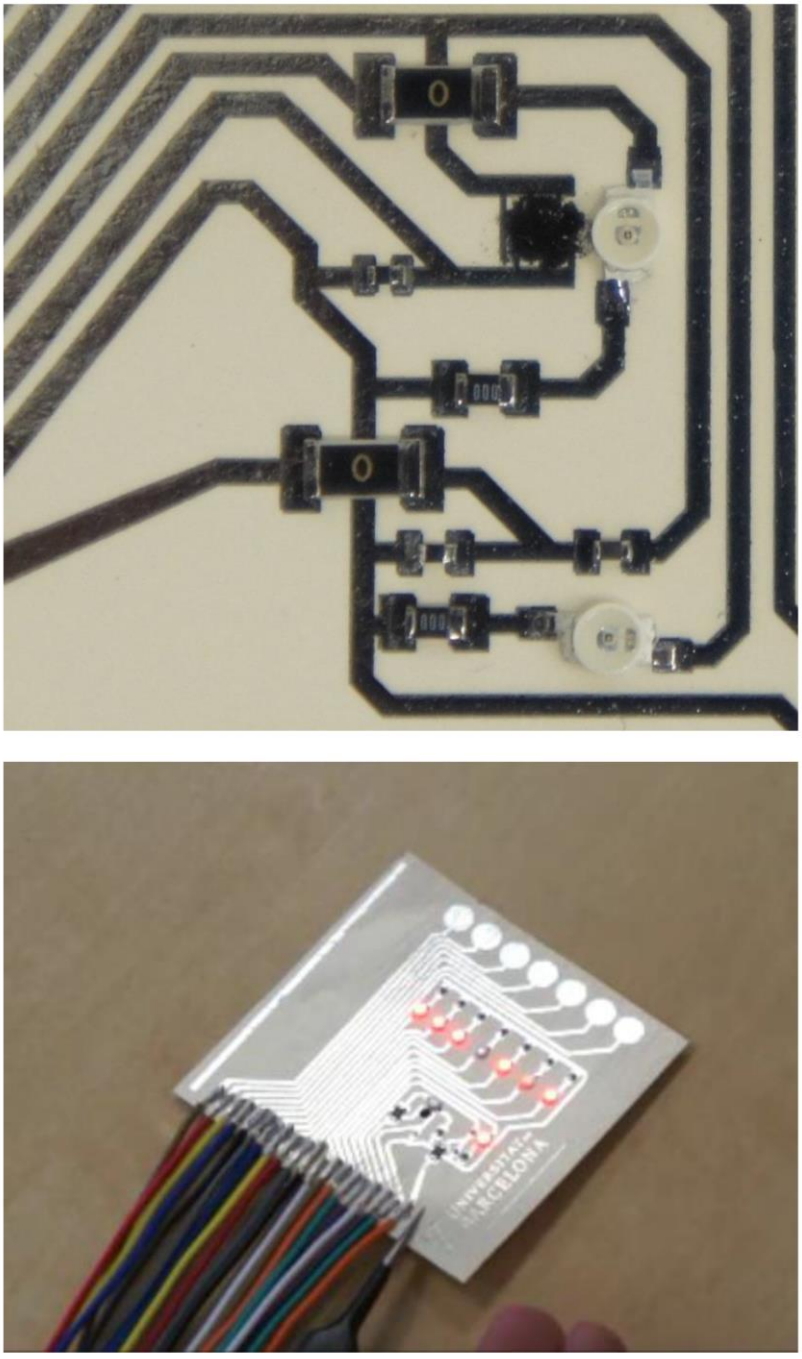

Figure Supplementary 2. Detailed image of SMDs SNPI-connected and hybrid circuit in temperature mode running.

References:

1. Izdebska, J., Thomas, S. & Soleimani-Gorgani, A. in *Printing on Polymers* (2016). doi:10.1016/B978-0-323-37468-2.00014-2
2. Shlomo Magdassi. *THE CHEMISTRY OF INKJET INKS*. **I,** (2010).
3. Derby, B. Inkjet Printing of Functional and Structural Materials: Fluid Property Requirements, Feature Stability, and Resolution. *Annu. Rev. Mater. Res.* (2010). doi:10.1146/annurev-matsci-070909-104502
4. Calvert, P. Inkjet Printing for Materials and Devices. *Chem. Mater.* **13,** 3299–3305 (2001).
5. Singh, M., Haverinen, H. M., Dhagat, P. & Jabbour, G. E. Inkjet printing-process and its applications. *Adv. Mater.* **22,** 673–685 (2010).
6. Morita, N. Thermal Inkjet. *Inkjet-based Micromanufacturing* (2012).
7. Bokor, J. Ultra-high-resolution monolithic thermal bubble inkjet print head. *J. Micro/Nanolithography, MEMS, MOEMS* (2007). doi:10.1117/1.2816449
8. Brünahl, J. & Grishin, A. M. Piezoelectric shear mode drop-on-demand inkjet actuator. *Sensors Actuators, A Phys.* (2002). doi:10.1016/S0924-4247(02)00212-1
9. Brunahl, J., Grishin, A. M., Khartsev, S. I. & Osterberg, C. Piezoelectric shear mode inkjet actuator. *Mater. Sci. Microelectromechanical Syst. Devices IV, Novemb. 25, 2001 - Novemb. 28, 2001* (2002). doi:10.1557/PROC-687-B1.4
10. Lee, M. J. Inkjet printing technology still in progress. *J. Korean Ceram. Soc.* (2011). doi:10.419/kcers.2011.48.6.543
11. Verkouteren, R. M. & Verkouteren, J. R. Inkjet metrology II: Resolved effects of ejection frequency, fluidic pressure, and droplet number on reproducible drop-on-demand dispensing. *Langmuir* **27,** 9644–9653 (2011).
12. www.fujifilmusa.com. Dimatix Fujifilm.
13. Shin, K.-Y., Lee, S.-H. & Oh, J. H. Solvent and substrate effects on inkjet-printed dots and lines of silver nanoparticle colloids. *J. Micromechanics Microengineering* (2011). doi:10.1088/0960-1317/21/4/045012
14. Kamyshny, A. & Magdassi, S. Inkjet Ink Formulations. *Inkjet-based Micromanufacturing* (2012). doi:10.1002/9783527647101.ch12
15. Soltman, D. & Subramanian, V. Inkjet-printed line morphologies and temperature control of the coffee ring effect. *Langmuir* **24,** 2224–2231 (2008).
16. Raje, P. V. & Murmu, N. C. A Review on Electrohydrodynamic-inkjet Printing Technology. *Ijetae.Com* (2014).
17. Rahman, K., Mustafa, M., Muhammad, N. M. & Choi, K. H. Electrohydrodynamic printed TiO2 flexible memory device – fabrication and characterisation. *Electron. Lett.* **48,** 1261 (2012).
18. Mashayekhi, M. *et al.* Evaluation of Aerosol, Superfine Inkjet, and Photolithography Printing

Techniques for Metallization of Application Specific Printed Electronic Circuits. *IEEE Trans. Electron Devices* **63,** 1246–1253 (2016).

19. Jang, D., Kim, D. & Moon, J. Influence of fluid physical properties on ink-jet printability. *Langmuir* **25,** 2629–2635 (2009).
20. Van Osch, T. H. J., Perelaer, J., De Laat, A. W. M. & Schubert, U. S. Inkjet printing of narrow conductive tracks on untreated polymeric substrates. *Adv. Mater.* **20,** 343–345 (2008).
21. Shlomo Magdassi & Magdassi, S. Ink jet printing — Post Office project. *Pigment Resin Technol.* **16,** 4–10 (1987).
22. Capasso, a. *et al.* Ink-jet printing of graphene for flexible electronics: An environmentally-friendly approach. *Solid State Commun.* **224,** 53–63 (2015).
23. Bonaccorso, F. *et al.* Production and processing of graphene and 2d crystals. *Mater. Today* **15,** 564–589 (2012).
24. Lu, J. High dielectric constant polymer nanocomposites for embedded capacitor applications. (2008). at <http://smartech.gatech.edu/jspui/handle/1853/26666%5Cnhttp://smartech.gatech.edu/xmlui/bitstream/1853/26666/1/Lu_Jiongxin_200812_phd.pdf>
25. Coleman, J. N. Liquid-phase exfoliation of nanotubes and graphene. *Adv. Funct. Mater.* **19,** 3680–3695 (2009).
26. Kamyshny, A. & Magdassi, S. Conductive nanomaterials for printed electronics. *Small* **10,** 3515–3535 (2014).
27. www.harima.co.jp. Harima NanoPaste NP Series: Metal paste for fine pattern formation.

Chapter 4: Inkjet-printed High-k HfO_2 for Capacitor and Memristor

In this Chapter, inkjet-printed high-*k* materials are studied. In particular, the dielectric properties of these materials have been tested as gate oxide and active layer in capacitor and memristor systems, respectively. Overall, the suitability of inkjet-printing process as a functional deposition method for this kind of materials and device structures is demonstrated.

4.1 Moore's Law

During the last 40 years, and based on the *golden rule* of device scaling well-known as Moore's law,[1] which states that the number of transistors in a dense integrated circuit doubles approximately every two years, the electronics industry has been continuously developed towards the reduction of electronic component dimensions (Figure 4.1). According to the International Technology Roadmap for Semiconductors (ITRS),[2] shrinking the main device size, i.e., the metal-oxide-semiconductor field effect transistor (MOSFET), cost production and power consumption are reduced while simultaneously enhancing the density and the operation speed performance of the integrated circuits. In addition, increasing the integrated circuit density promotes the significant expansion of both the memory capacity and the electronic circuit functionalities. To date, the most powerful processor is the Intel Core M, built with the 14-nm technology and made up of 1.3 billion transistors. In addition, during 2017, a commercial release of the 10-nm devices is expected by the leading company Samsung.

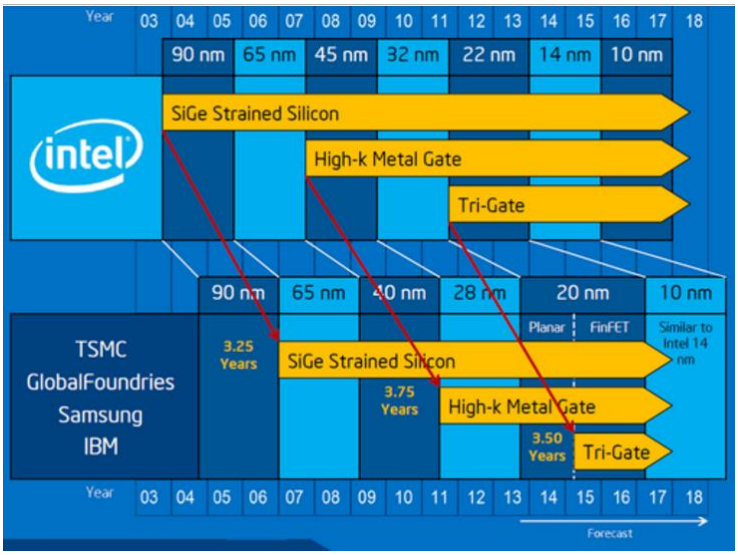

Fig. 4.1 *Intel is committed to Moore's law in reducing the transistor cost by increasing the process density in a near linear fashion.* [2]

The ITRS roadmap defines all the technical requirements that the integrated circuit must follow, such as the circuit speed, the static (off-state) power consumption, and the ranges of the power supply and output voltages.[3] On the basis of the final application area (from space exploration to water purification, and from displays to automotive batteries), the requirements differ according to the properties and the limitations of the elemental materials selected for the manufacturing process. The novel properties of printed thin-films, using inkjet printing technology in our case, can facilitate the fabrication of flexible electronic devices where low weight, mechanical flexibility and durability, simple device integration, along with low-cost and large-area manufacturing allow them to be utilized in a wealth of applications.

4.2 Device Scaling

The procedure for device scaling is based on the optimization of the main electronic device, the MOSFET, to increase the drain-source current saturation that ensures high speed and low power consumption. There are three fundamental approaches: i) source-drain channel length reduction, ii) selection of an ideally higher mobility channel semiconductor and iii) enlarging the gate MOS capacitance.[4,5] The saturation current I_{DSat} of the MOSFET can be described as:

$$I_{DSat} = \frac{W}{L}\frac{C_{ox}\mu}{2}(V_G - V_T)^2 \qquad \text{[eq. 2]}$$

where W and L are the width and length of the MOSFET channel, respectively, μ is the channel carrier effective mobility, C_{ox} is the gate oxide capacitance density, V_G is the gate voltage, and V_T is the threshold voltage. Acting on the shrinking of channel length by means of innovative solution during fabrication processes, selecting a material with higher channel carrier effective mobility μ and expanding the gate oxide capacitance density C_{ox} will result in an improved I_{DSat}.[4]
Among the three actions, the C_{ox} enlargement is essentially related to the device geometry and dielectric material properties, following the next expression for parallel plate capacitors:

$$Cox = \frac{A\varepsilon_0\varepsilon_r}{d} \qquad \text{[eq. 3]}$$

where ε_0 is the vacuum dielectric permittivity, ε_r is the relative dielectric constant, A is the device area and d is the gate oxide thickness. Obviously, decreasing the thickness of the gate oxide layer

and/or employing dielectric materials with a higher dielectric constant will promote the C_{ox} enlargement.[4]

4.3 Alternative Gate Dielectrics: High-k Materials

The further reduction in the thickness of the gate dielectric, silicon oxide (SiO_2) for the standard integrated circuits, in order to increase the gate dielectric capacitance is limited by several problems when the gate layer thickness goes below ~1 nm (the full band gap of SiO_2 is obtained only after 2 monolayers of SiO_2).[1,4] Above all, gate leakage current, due to the direct tunnelling of electrons through the thin layer, exceeds the maximum value allowed in order to contain the circuit power consumption (1 $A \cdot cm^{-2}$ at 1 V) dissipation, causing a degradation of the device reliability.[6] Therefore, alternative dielectric materials with higher permittivity than SiO_2, well-known as high-*k* dielectric material, are employed for *equivalent-scaling*, in order to obtain the equivalent C_{ox} with thicker layers, which solves the leakage problem while still allowing for device scaling.[4,6]
The electrical thickness of the high-*k* gate oxide is evaluated using the concept of *equivalent oxide thickness* (EOT), which is the required thickness for a high-*k* dielectric material to give an equal capacitance value than an equivalent thin of SiO_2 layer, [6] and which is defined by the following relation:

$$EOT = d_{high-k}\left(\frac{k_{SiO2}}{k_{high-k}}\right) \qquad \text{[eq. 4]}$$

4.4 High-k Dielectric Material Choice

The ITRS roadmap defines the main guidelines that a high-*k* material must accomplish in order to guarantee a contained gate leakage current while ensuring the MOSFET device reliable performance.[3] Taking into account the Clausius-Masotti relation,[7] which connects the dielectric constant value to the polarizability of the atoms constituting the dielectric material, an increase in permittivity results in a decrease of the related bandgap. Therefore, in order to attain a barrier height greater than 1.0 eV between the semiconductor and dielectric layers, which avoids the undesired thermal conduction and tunneling, a dielectric constant ranging from 8 to 30 and a bandgap superior to 5 eV are required. Furthermore, the selected gate dielectric material must adapt accurately to the

manufacturing process, thus showing high thermodynamic stability, interface quality, and film morphology.[8 6]

In the last decade, several dielectric materials have been explored and only few of them abide by the before mentioned ITRS requirements. In particular, dielectrics such as metal oxides (Al_2O_3, ZrO_2, HfO_2 and Ta_2O_5)[9,10] stand out as alternative gate dielectric. In addition, oxides of binary alloys such as $ZrAl_XO_Y$, which take advantage of the properties of both metal oxides, have been surveyed. As well, metal silicates such as Zr- and Hf-based silicates are also considered as promising materials because they exhibit high thermal stability. Amongst these potential materials, the best dielectric layer should ensure low oxygen diffusivity, low density of defects and a high thermal stability with the adjacent semiconductor in order to minimize the interfacial reactions and thus avoiding the formation of a new low-*k* dielectric. Contemplating all the restrictions and requirements, Al_2O_3, ZrO_2 and HfO_2 metal oxides are the most promising candidates. [8,12,11]

To sum up, the main requirements that a high-*k* dielectric material must accomplish in order to be an alternative gate oxide for MOSFET devices are summarized below:

- *High value of dielectric constant*: The actual dielectric constant of a high-*k* dielectric thin film varies according to the employed deposition technique, the deposition parameters, and the properties of the interfacial layer between the gate dielectric and the semiconductor.[8,10,11]

- *Minimum band gap:* Adequate band gap of the high-*k* dielectric material is necessary, in order to reduce the gate leakage current while simultaneously maintaining a suitable conduction band and valence band offsets between the high-*k* dielectric material and the semiconductor. Materials such as Al_2O_3, HfO_2 and ZrO_2 have large band gaps and band offsets, making them ideal candidates to replace SiO_2 in the semiconductor industry. [8,10,12,11]

- *Interfacial thermal stability between high-k and semiconductor:* Manufacturing deposition methods of the high-*k* materials could affect the crystallization temperature, which forms defects that in turn increase the gate leakage current. [8,10]

- *Low density of defects:* The interface traps at the interface between semiconductor and high-*k* dielectric decrease the charge carrier mobility due to the carrier scattering effect in the channel of transistors. [8,10,11]

Amongst the possible metal oxide high-*k* materials, HfO_2 is the most suitable alternative to SiO_2 that fulfils all the guidelines and requirements by exhibiting outstanding properties such as k~25 and bandgap energy of ~5.8 eV. Indeed, HfO_2 is commonly used as the fundamental high-*k* dielectric in the manufacture of integrated circuits since 2007, when Intel and IBM started using HfO_2 in their 45-nm technology. [12,13,11]

4.5 High-k Dielectric Material for ReRAM

4.5.1. Memory Scaling

Concurrently to MOSFETs, the Moore's law has been applied also to memory storage devices, which evolved in order to adapt to the technology guideline target, commonly defined as *node*, by means of a process of memory scaling.[2]

Nowadays, the 10-nm node has been presented by Samsung by the introduction of the Exynos 8895 processor Octa core of 64 bit (2.35 GHz Quad + 1.9 GHz Quad). In spite of the available outstanding processor, non-volatile memories (NVMs), which rely on a special transistor configuration well-known as flash-memory, have been developed and manufactured down to the 16-nm node. Therefore, memories must overcome several difficulties, comparable to MOSFETs, due to the required scaling process towards nanoscale resolution, where any defect or variation plays an important role by influencing the atomic scale processes.

Flash memories are MOSFETs with an extra floating gate (conductive element) incorporated into the metal-oxide interface, where the data storage programming is achieved by both electron tunnelling through the gate oxide and by hot electron injection into the floating gate.[14,15] The use of electron tunnelling mechanism causes a gradual degradation of the gate oxide, resulting in increasing high leakage currents that provoke data loss. Thus the mayor limitation of flash-memory is its endurance.[16,17] In the last decade, research has been focused on an emerging two-terminal non-volatile memory with 3D multilevel capability that increases the performance speed and provides higher density of data and lower power consumption, while maintaining its reliability. The new universal memory component is an easy alternative technological structure based on a crossbar architecture, where a matrix of arrays of capacitor cells, which are basically MIMs, allows controlling the continuous scaling process. This simple structure permits each MIM to be addressed

independently by a particular word (horizontal) and bit (vertical) line.[18,19] Several materials demonstrated resistive switching behaviour, such as organic insulators (like polymers)[20] and graphene oxide,[21] amorphous silicon,[22] chalcogenides (selenides and tellurides),[23] carbon nanotubes,[24] perovskite oxides,[25] and binary transition metal oxides[26]. This suggests a wide range of material selection as building blocks of devices for memory applications. The ReRAM devices were proved to overcome the general performance requirements and also showed high compatibility to the CMOS manufacturing technology.[27] Common critical parameter specifications are: switching write and read speeds, resistance ratio, low power consumption, endurance and data retention time.[28]

Table 2 summarizes the guideline requirements. ReRAMs based on metal-oxide exhibited fast read/write speeds, exceptional endurance, and very low power/energy consumption, all consistent with CMOS technology. Among the metal oxides, HfO_2 has been deeply studied and proved as a suitable material for ReRAM devices.[29–32] In this section, the physics of memristive switching and the details of the memristor devices are presented.

Table 2 : Requirements for ReRAM devices. [33]

	Min. Required	Best Projected	Demonstrated
Feature Size F	<65 nm	5 nm	30 nm, 9 nm
Cell Area	$8F^2$	$4F^2$	4F2, $8F^2$
Read Time	<15 ns	<10 ns	<50 ns
W/E Time	Application dependent	< 1 ns	0.3 ns
Retention Time	>10 years	>10 years	>10 years
Write Cycles	>1E5	>1E16	1E12
Write Voltage	Application dependent	<0.5 V	0.6 V/-0.2 V
Read Voltage	2.5	<0.2 V	0.15
Write Energy	Application dependent	1E-17 (J/bit)	1E-13 J/bit

4.5.2. Resistive Switching Mechanisms

Amongst the existing memories, especially after the discovery of the memristor non-volatile property by HP in 2008,[34] ReRAM is the most suitable and feasible printable component due to its simple vertical MIM-like structure. Moreover, the crossbar architectures usually used in these devices ensure high scalability and cost-efficient fabrication. The main feature of memristors is the resistive switching (RS) phenomenon, which consists in the successive controlled changes between two conductive states, a low-resistance state (LRS) and a high-resistance state (HRS). In the case of MIM structures, it is commonly accepted that this phenomenon is due to the creation of a conductive filament (CF) in the dielectric that can be opened or closed depending on the applied voltage to the electrodes of the device. [35]

There are only two possible RS behaviours, the unipolar and the bipolar RS (Figure 4.2). Generally, the type of behaviour is strongly related to the mechanism that provokes the CF formation by exploiting the properties of the employed insulating material. [22]
The pristine memristor device is commonly in HRS, and thus some stress is needed to provoke a controlled oxide soft breakdown, called *electroforming*, by means of a current compliance limit which is fixed to avoid destructive dielectric breakdown.

During the electroforming process, the soft breakdown causes a radical localized rearrangement of the insulator atomic structure by changing the density of defects such as the oxygen vacancies. Therefore, after the application of controlled voltages, when a critical value is reached, the material makes a transition to the LRS. [36]

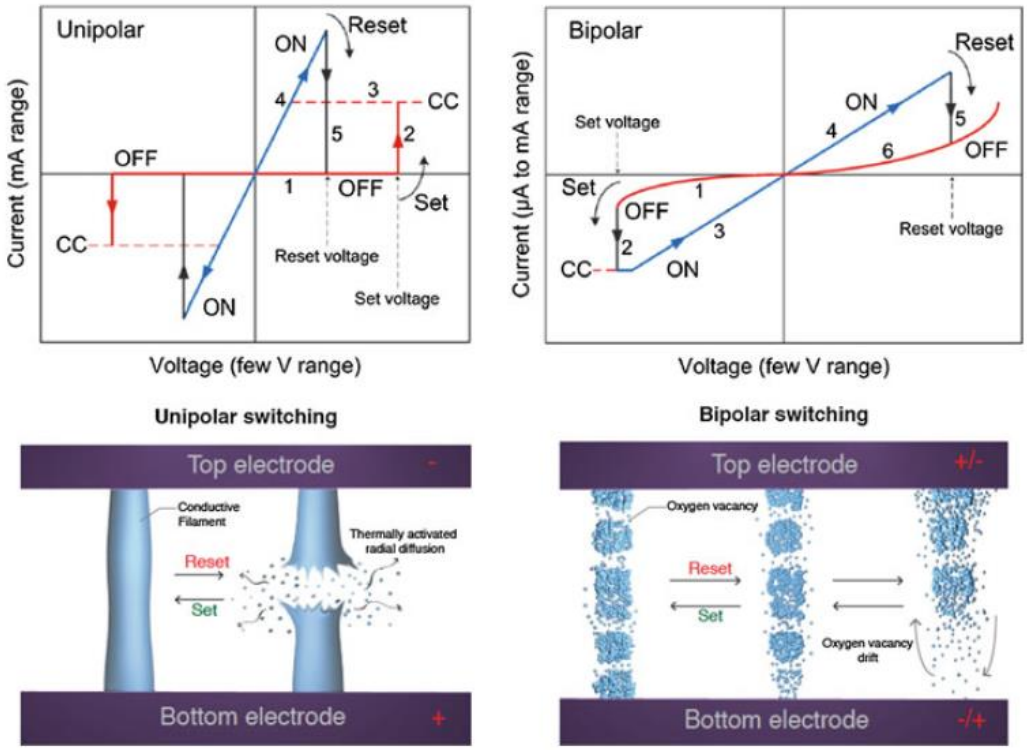

Fig. 4.2 *Typical hysteretic current-voltage curves for resistive switching. Top LHS Unipolar switching mode. An initial high resistance state (red line) switches to a low resistance state at a threshold voltage. A current compliance (limit: CC) is set to avoid destructive breakdown of the oxide. Removing the compliance limit and ramping the voltage (blue line) results in a transition back to the original high resistance state. Both transitions occur in the same polarity, and the current-voltage curves are shown as symmetric in this schematic. Top RHS Bipolar switching mode. In this case, the transitions from high resistance to low resistance and back again occur in opposite polarities. A current compliance limit is shown (CC) for the high-to-low resistance transition. In practice this is not always necessary. The two lower diagrams show schematics of the switching process. Bottom LHS Unipolar switching in which a highly conductive filament is formed by the application of a field and disrupted by Joule (Ohmic) heating. Bottom RHS Bipolar switching in which drift of oxygen vacancies under the application of an external field governs both set and reset processes.*[22]

In *bipolar* switching the LRS and the HRS are obtained on reversed bias voltage polarities. Consequently, when the device presents some kind of asymmetry, either promoted during the electroforming process or obtained by employing different electrode materials, it is expected that the CF rupture is achieved using an opposite voltage to the electroforming.

In the *unipolar* RS case, the CF dissolution is independent of the electrical polarity, so that the LRS and the HRS occur on the same bias voltage polarity, which facilitates a high current flow through the filaments that induces a large amount of Joule-effect heat within, consequently fusing the filaments. [36]

Amongst the several memristor structures, the memory effects can be induced by mechanical stress, by ferromagnetic domain polarization, by change in phase or by resistive switching mechanism (Figure 4.3). The latter, commonly defined as redox-reaction mechanisms, encloses three different

categories of switching dynamics: thermochemical (TCM), electrochemical metallization (ECM), and valence change (VCM) mechanism. [36]

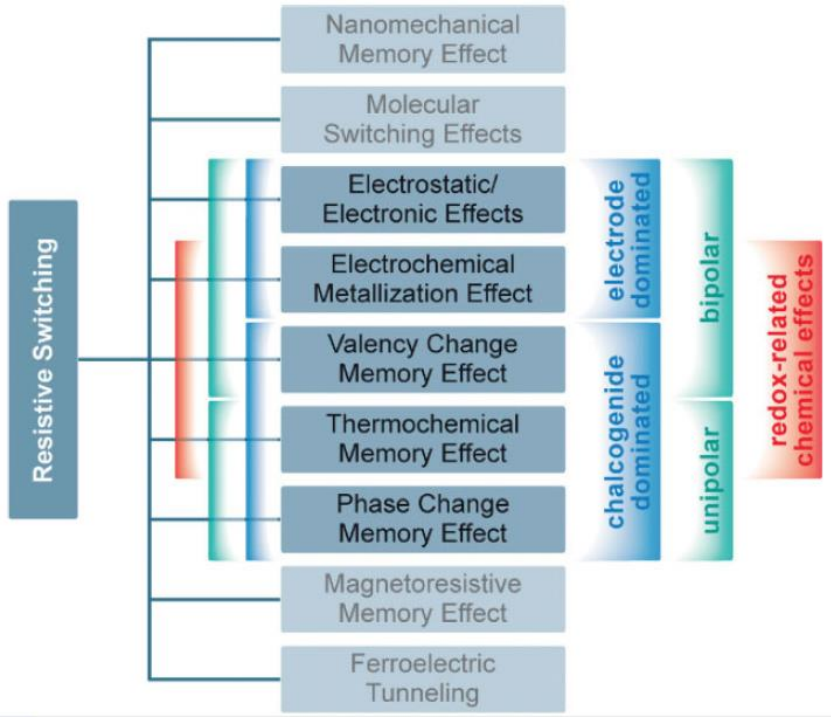

Fig. 4.3 *Classification of the resistive switching effects which are considered for non-volatile memory applications. The switching mechanisms based on thermal, chemical, and electronic/electrostatic effects (five classes in the center) are further described in the text. This review will cover the redox-related chemical switching effects (red bracket).*[36]

4.5.2.1. TCM

The thermochemical resistance change mechanism results from local Joule heating effects which occur in the insulator due to high current resulting from a voltage applied across the electrodes. If a large enough electric field is applied across the insulator, electrical breakdown, i.e., a shift to a conductive state, can take place. After breakdown, the insulator is in a low resistance state until it can be recovered in some way, e.g., by subsequent application of another voltage (unipolar RS). [35,36]

4.5.2.2. ECM

In the electrochemical resistive switching mechanism the system needs a specific MEM structure, which strictly requires a highly electrochemically-active top electrode (Ag, Cu, Ni, Al), and an

insulator commonly consisting of a derivate compound of the top electrode element, hence suitable for transporting metal ions. The formation of the CF (Figure 23) is obtained by the controlled electro-migration of metallic ions into the insulator and therefore the dissolution of the CF results when a higher current is applied in order to provoke a local Joule-effect heating (unipolar RS). [35,36]

4.5.2.3. VCM

The valence change mechanism or memory effect occurs in specific transition metal oxides and is triggered by a migration of anions, such as oxygen anions (typically described by the motion of the corresponding vacancies). A subsequent change of the stoichiometry leads to a redox reaction expressed by a valence change of the cation sub-lattice and a change in the electronic conductivity.[35,36] The formation of the CF is due to the oxygen vacancies into the metal-oxide insulator, which create a pathway from the inert bottom electrode to the top electrode (that could be slightly electrochemically active) with a consequent change of the resistance state to the LRS when a positive voltage is applied. Afterwards, the change to the HRS state occurs by the recombination of the oxygen anions with the unoccupied oxygen vacancies (Figure 4.4). [35,36]

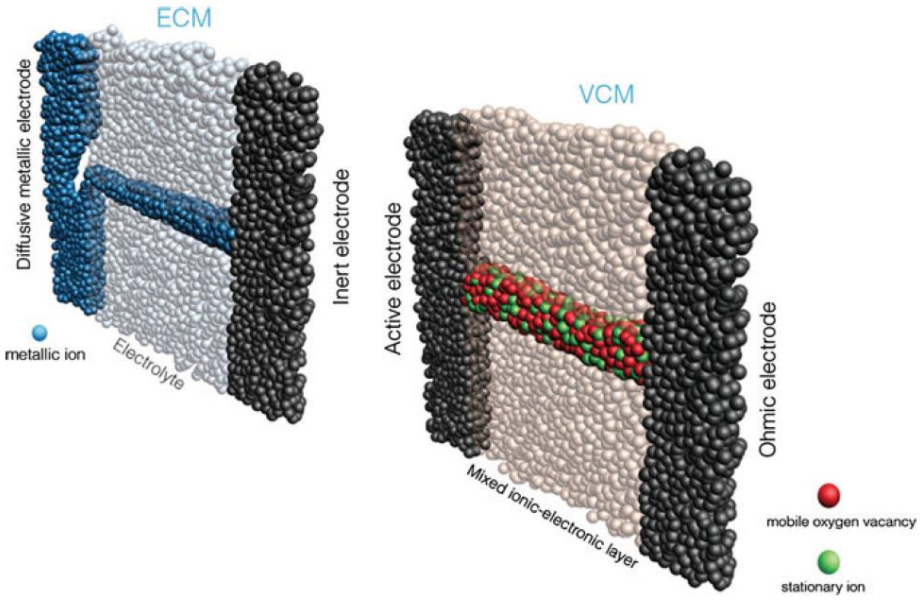

Fig. 4.4 *LHS In electrochemical memory (ECM) systems the conductive filament is a continuous metallic pathway formed by the drift of metal ions from an active electrode (for example, Ag) into the dielectric layer. RHS In the case of valence change memories (VCM), drift of oxygen vacancies and associated redox reactions within the dielectric layer result in a more mixed filament, typically with a higher resistivity than that of ECM systems. From* [37]

4.6 Inkjet-printed HfO2 Nanoparticle-based Ink

Printed electronics relies on a continuous development of new printable inks based on outstanding materials that can improve and fulfil the required high performance for flexible applications.

Amongst the metal-oxides as promising alternative to SiO_2, nanoparticles-based inorganic inks often require high thermal annealing post processing in order to ensure a reliable dielectric layer. Consequently, the main issue for the development of the flexible devices market is the metal-oxide sintering temperature, which inevitably reduces the amount of suitable flexible substrates. For instance, polymeric or paper substrates cannot bear temperatures above 300 °C.

Nowadays, hafnia (HfO_2) has been selected as the high-*k* insulating dielectric in the latest generations of MOSFETs and memristors due to its oxygen defects, which play an important role on the performance of transistors and on the resistive switching mechanism.

In this chapter, a fully-printed MIM capacitor with high homogeneity and good integrity is demonstrated on a flexible substrate, where the high-*k* monoclinic (HfO_2 was selected as the dielectric material and sintered at low temperature (240 °C). ***PAPER IV***

The high-*k* HfO_2 is further studied focusing on the ink properties, and his suitability as oxide for wearable electronic memory devices is assessed. In this chapter the development of inkjet-printed resistive random access memory (ReRAM) and its basic principles of general functionality are explored, and the memristive switching mechanism is exploited towards demonstrating data storage in these devices.

This work presents the characterization of two different HfO_2 nanoparticles-based ReRAM devices, illustrating some unique testing to show the working fundamentals of ReRAM devices, and yielding promising results. ***PAPER V and PAPER VI***

4.6.1. Inkjet-Printed HfO2 Capacitor

In ***Paper IV****: Flexible inkjet-printed high-k HfO_2-based MIM capacitors,* the following issues were disclosed and studied in detail:

(1) The manufacturing for the first time of fully-printed MIM capacitors with high resolution based on the high-*k* hafnium oxide as insulator by means of drop-on-demand inkjet technology onto flexible substrates.

(2) The observation of the deposition uniformity and the crystalline purity of the high-*k* HfO_2 thin film based on nanoparticles.

(3) The demonstration of the low contamination of the insulator due to the ink formulation, deposition by inkjet technology and low-temperature annealing processes for the fabrication of the MIMs devices.

(4) The evidence, by means of capacitance- and voltage-dependent measurements, that the MIMs work properly within the ITRS 2016 roadmap requirements.

The previously mentioned results are explained in terms of the HfO_2 dielectric properties: on one hand, the energy gap of the printed oxide that ensures the high barrier for electrons; on the other hand, the relative permittivity and the dielectric loss tangent that avoid charge carrier impurities conduction. Overall, the paper aims at the correlation between inkjet printing of a thin-film oxide and the electrical properties of devices based on high-*k* hafnium oxide (HfO_2), with different controlled resolution.

** Note that sections, equations and references numbering in the reproduced research article follow the ones of the published version. This statement applies to all Papers presented in this Thesis Dissertation.*

The article has been reproduced from Journal of Materials Chemistry C; vol. 4; G. Vescio, J. López-Vidrier, R. Leghrib, A. Cornet and A. Cirera , ― *Flexible inkjet printed high-k HfO_2-based MIM capacitors*‖; pp. 1804-1812; Copyright 2016; with permission from Royal Society of Chemistry.

Journal of
Materials Chemistry C

PAPER

Cite this: J. Mater. Chem. C, 2016, 4, 1804

Flexible inkjet printed high-k HfO_2-based MIM capacitors†

G. Vescio,*[a] J. López-Vidrier,[a] R. Leghrib,[b] A. Cornet[a] and A. Cirera[a]

Received 13th October 2015,
Accepted 25th January 2016

DOI: 10.1039/c5tc03307a

www.rsc.org/MaterialsC

The soaring global demand for flexible, wearable and transparent devices has created an urgent need for new fabrication technologies that are both cost-competitive and eco-friendly. Printed electronics holds the promise of enabling low-cost, scalable solutions exploiting the ability of innovative materials to be used as processed inks onto a large area substrate. In this article, we demonstrate the direct drop-on-demand inkjet printing technology as a viable method for the fabrication of fully-printed metal–insulator–metal capacitors on a flexible substrate (Kapton®), where the high-k hafnium oxide (HfO_2) was selected as the dielectric. After a low-temperature annealing process, the deposited nanoparticle (NP)-based ink of HfO_2 showed high homogeneity and good integrity of the printed thin film by microscopy and spectroscopy studies. The fully-printed capacitors were characterized by field-emission scanning and transmission electron microscopies. X-ray diffraction patterns, as well as Raman scattering and Fourier-transform infrared spectra, revealed the presence of a polycrystalline solid layer, without solvent organic ink remains. The bonding structure of the HfO_2 layer and the interface with the Ag electrode was studied by X-ray photoelectron spectroscopy. The good performance of the thin film was proved by its relative permittivity, k = 12.6, and dielectric loss tangent, $\tan\delta$ = 0.0125 at 1 MHz. Finally, the electrical current density–voltage and capacitance–voltage measurements have been studied in the frequency range from 10 kHz to 1 MHz. The obtained results indicate that MIM capacitors based on inkjet-printed flexible HfO_2 NPs work properly within the ITRS 2016 roadmap requirements.

1. Introduction

Recently, printed electronics on flexible supports has quickly gained interest as a low-cost, high-area, lightweight and bendable plastic alternative to Si technology.[1,2] Amongst all the existing printing technologies, drop-on-demand inkjet printing stands out as a quick, maskless, digital-pattern design, as well as being a non-contact technique.[1,3,4] In addition, the piezoelectric cartridges used in inkjet printers, well known for their high sturdiness (no clogging nozzle), allow to print innovative materials requiring only a few-picoliter amount of ink after an in-depth study of its rheology.[5,6]

Concerning the inkjet technique, drawbacks such as limited resolution and relatively large minimum thickness of the deposited layer need to be solved to obtain electronic devices with performance and reliability comparable to those based on Si technology. Therefore, complex and expensive techniques such as self-alignment printing[7,8] or femtoliter drop jetting[9] are used as advanced processes to overcome the current limitations of inkjet printing technology. In this regard, selecting and employing outstanding materials to be printed as insulators,[10,11] such as the high-k dielectric materials[12,13] (with a higher dielectric constant than the usual SiO_2), is imperative. Furthermore, flexible and transparent substrates, which limit the temperature of the post-deposition thermal treatments down to 180 °C (Kapton® is an exception, allowing for temperatures as high as 350 °C),[14] are the most promising and suitable materials for the fabrication of bendable devices.

One of the most limiting factors for a material to be a candidate for inkjet printing is the maintenance of the physical and chemical properties of the ink when subjected to the temperatures required for the printing process. As well, the effective lifetime of the printer head must be as long as possible. To meet these requirements (thus preventing effects such as evaporation of the ink while inkjet printing and damage to the printer head), the ink particle size must lie in the sub-micron scale (the ratio between the nanoparticle size and the printer nozzle orifice should ideally be 1/50). Nowadays, there exist very promising high-k oxides that guarantee this condition. However, for the particular application as a gate oxide in MIM capacitors, other conditions have to be accomplished (thermal and kinetic stabilities,

[a] MIND-IN2UB, Electronics Departament, Universitat de Barcelona, C. Martí i Franquès 1, 08028, Barcelona, Spain. E-mail: gvescio@el.ub.edu; Tel: +34-93-4024804
[b] Laboratoire d'Electronique, de Traitement du signal et de Modélisation Physique (LETSMP) Faculté des Sciences, Université Ibn Zohr, Agadir, Morocco

† Electronic supplementary information (ESI) available: Details of device fabrication, XPS HfO_2 survey, and C–V curves on different substrates. See DOI: 10.1039/c5tc03307a

band offsets, good metal/semiconductor interface quality and low bulk defect density) apart from high dielectric constants. Among the existing high-k materials, HfO_2 and Hf silicates have been found to well fit these characteristics.[15]

During the last decade, hafnium oxide (HfO_2) has become one of the most remarkable compounds to be employed as an alternative dielectric gate due to its physical properties, such as a relatively wide band gap of 5.8 eV[16] that ensures a barrier for electrical conduction at room temperature, and a higher dielectric constant (k = 20)[16] compared to SiO_2 (k = 3.9). Moreover, it is also appreciated for its hardness, high melting point, chemical resistance, resistance to impurity diffusion because of its high density (9.68 g cm^{-3}), and thermal stability up to 700 °C.[17,18] Finally, HfO_2 is one of the most studied materials to be implemented as optical components due to its transparency from the infrared to the ultraviolet range.[19] For these reasons, HfO_2 is an attractive high-k dielectric material for the future generation of metal–oxide–semiconductor field-effect transistors (MOSFETs), micro-electro-mechanical systems (MEMS), complementary metal–oxide–silicon (CMOS) transistors, highly-scaled memories, radio frequency circuits, and a variety of configurations in analogue integrated circuits.[20]

Various methods for preparing metal oxide films have been reported, such as sputtering,[21] atomic layer deposition (ALD),[22,23] physical vapour deposition (PVD),[24] metal organic chemical vapour deposition (MOCVD),[25,26] pulsed laser deposition (PLD),[27,28] thermal evaporation,[29] sol–gel spin-coating,[14] or by sonochemistry.[30] Alongside all these methods, inkjet printing appears as a disrupting new technology that allows us to selectively deposit smooth films of nanoparticles (NPs) in a non-contact process on flexible substrates for metal–insulator–metal (MIM) devices, at room temperature and ambient pressure. Consequently, lithography, etching, vacuum systems and high-temperature thermal processes are avoided.

In this study, we report the properties of HfO_2 NPs used as dielectric thin film of a fully-printed MIM capacitor. The films have been deposited on a flexible polyimide substrate by inkjet printing, followed by a low-temperature post-annealing process. To determine the insulator properties, the structure and the morphology of the film have been investigated. The morphology and the microscopic properties of the HfO_2 have been characterized by transmission electron microscopy (TEM), focused ion beam (FIB)-assisted field-emission scanning electron microscopy (FE-SEM), X-ray diffraction (XRD), Raman scattering and Fourier-transform infrared (FTIR) spectroscopies, X-ray photoelectron spectroscopy (XPS), and UV–visible absorption spectroscopy. Device performance and reliability were tested by capacitance–voltage (C–V), and the leakage current density–voltage (J–V) characteristic was evaluated.

2. Experimental

2.1 Materials and fabrication

Ag/HfO_2/Ag MIM capacitors were printed onto a polyamide Kapton® flexible substrate with a Xennia XenJet 4000 inkjet printing system, using Xaar cartridges (XJ126-50 series), with an ink droplet volume fixed at 50 pl. For the electrodes and the dielectric layer, Ag nanoparticle-based ink U5603 from Sun Chemical Corporation and HfO_2 NP ink from Torrecid S.A. were used, respectively.

Table 1 Hafnium oxide ink compounds

Component	wt%
HfO_2	45–50
Mixed aliphatic compounds	42–47
Organic hydroxy compounds	5–8
Polymeric amide derivatives	2–4
Polymethylsiloxane derivative	0.05–0.1
Modified amide derivative	0.1–0.3
Organic thixotropic agents	0.1–0.2

The HfO_2 NPs were synthesized by means of spray-pyrolysis from hafnium acetylacetonate dissolved in aliphatic compounds. The ink was prepared by dispersing HfO_2 nanoparticles in the liquid vehicle formed by solvents and other additives by using the approximate formula in Table 1.

Prior to the printing process, standard cleaning of the Kapton® surface substrate was carried out. A silver bottom electrode with a thickness of 300 nm was printed; afterwards, it was annealed at 220 °C for 20 minutes in order to remove the organic solvents and to achieve a resistivity of around 16 μΩ cm, which is among the best values found in the literature.[31]

For the HfO_2 deposition onto the bottom electrode, an ink ejection frequency of 7.5 kHz and a resolution of 450 drops per inch (DPI) between the ink droplets were used. During the HfO_2 layer printing, the substrate temperature was kept constant at 55 °C in order to attain a proper adhesion between the different layers. To reach a more homogeneous layer, which implies a better dielectric behaviour, post-deposition annealing at 250 °C for 180 minutes was performed, according to the results of thermogravimetric analysis (TGA) [see Fig. S1 in the ESI†] and differential scanning calorimetry (DSC) [Fig. S2, ESI†]. Subsequently, the silver NPs top electrode was deposited under the same printing conditions compared to the bottom electrode and annealed at 220 °C for 20 minutes. In order to enhance contrast resolution in FIB-processed FESEM-images, a bottom contact of sputtered Pt was used.

Finally, a layer of PMMA was deposited by drop coating on the fabricated devices to protect them from any environmental contamination. Fig. 1 shows the scheme and the photo of the printed MIM structure under study.

2.2 Structural and physicochemical characterization

Inkjet-printed HfO_2 thin films were characterized morphologically, structurally and chemically.

The morphology and structure of the inkjet-printed MIM Ag/HfO_2/Ag devices were studied by FE-SEM using an FEI Nova 200 instrument, and by TEM using a JEOL JEM 2100 microscope. FE-SEM cross-section samples were cut with FIB (FEI dual beam STRATA 235). The surface roughness was evaluated using an AFM Digital Instruments Nanoscope D-5000. The morphology of the sample surface was accurately observed by scanning the x–y plane, with a z-axis resolution limit of around ~1 nm.

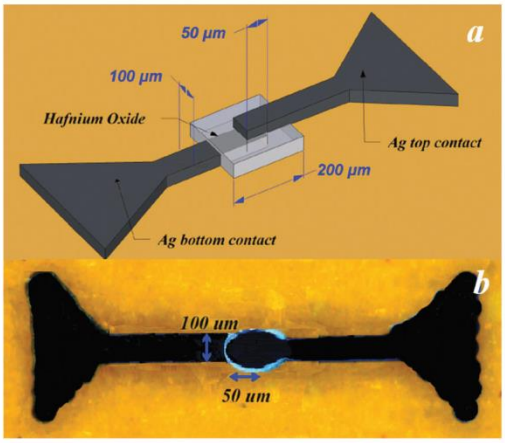

Fig. 1 (a) Scheme of the MIM structure under study. (b) Microscopy image of an Ag/HfO_2/Ag (MIM) capacitor, printed by the inkjet printing technique.

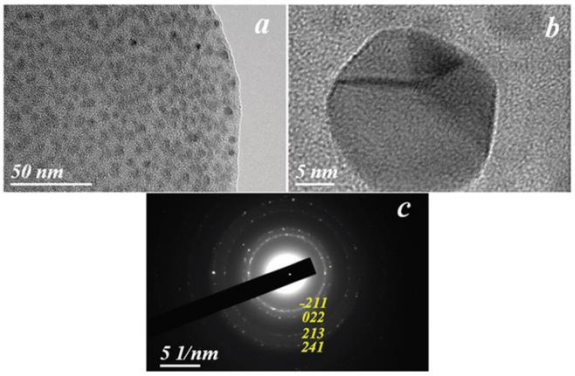

Fig. 2 (a and b) TEM images of HfO_2 thin film annealed at 250 °C for 3 h deposited on Ag bottom contact films. (c) Selected area electron diffraction showing pattern rings of the HfO_2 NPs.

The crystalline microstructure, orientation and size of the HfO_2 NPs were studied by XRD using a Japan Rigaku D/Max-IIA X-ray diffractometer using Cu K_α radiation, $\lambda = 1.5406$ Å, operating at 40 keV and 40 mA. A further study of the HfO_2 layer crystallinity and vibration properties was performed by means of Raman scattering, employing a Horiba Jobin-Yvon LabRam HR800 micro-Raman spectrometer operating at 20 mW laser power and an excitation wavelength of 532 nm (2nd harmonic of a Nd:YAG laser).

The analysis of the chemical composition of the HfO_2 thin film was performed using a PHI ESCA-5500 X-ray photoelectron spectrometer with a monochromatic Al K_α radiation ($E = 1486$ eV) at 350.0 W with the X-ray source and detector forming an angle of 45° with the normal of the sample, *i.e.* 90° between them. Additionally, a Thermo Scientific Systems NICOLET iN10 FT-IR spectrometer equipped with a DTGS detector for far-IR in the range from 4000 to 220 cm^{-1} was used to study the presence of the different remaining compounds adsorbed on the HfO_2 surface.

The thickness of the HfO_2 layers was estimated using the NanoSpec® 6100 Automated Film Thickness (AFT) Measurement System, whereas UV–vis spectroscopy analysis was carried out by means of a Hewlett Packard HP-8453 spectrophotometer to determine the optical properties of the material.

The current *versus* DC voltage characteristics were measured by means of a Keithley 4200-SCS Semiconductor Characterization System. The admittance *versus* voltage and admittance *versus* frequency curves were obtained using the same Keithley 4200-SCS with the integrated *C–V* (capacitance–voltage) instrument for frequencies from 10 kHz to 1 MHz and DC voltage biases in the range from −5 to +5 V.

3. Results

3.1 Thin film morphology

The morphology and shape of the as-printed dielectric layer were analyzed, thus the overall thin film structure was surveyed in depth. Fig. 2(a) shows a TEM image of the HfO_2 NPs film where the sample appears as a series of nanoparticles embedded within a polycrystalline matrix. We can observe how the HfO_2 NPs are sphere-shaped, being the estimated regular diameter of the NPs around 25 nm (Fig. 2(b)). Besides, the selected area electron diffraction analysis of the HfO_2 shows that NPs are polycrystalline with a lattice spacing of ~2.2 Å, in agreement with the monoclinic phase structure.[32]

In order to examine the surface of the printed layer, an AFM study was carried out. Fig. 3 presents a top-view AFM image of the HfO_2 film deposited by the inkjet technique process, after being sintered at 250 °C. The layer exhibits an RMS roughness value lower than 25 nm, which suggests compact NPs disposition into the layer, taking into account the grain size of these NPs.

As reported by other authors, a homogeneous and smooth surface is required for the fabrication of bottom-gate devices where even moderate interface roughness can adversely affect the material properties, such as carrier mobility.[33,34] In the case of the inkjet-printed MIM capacitors presented in this work, roughness is only related, in the best cases, to the NP size. However, a further drawback could appear considering the propagation

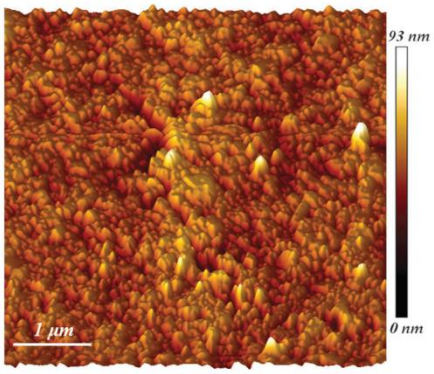

Fig. 3 HfO_2 films on Ag bottom contact on a Kapton® flexible substrate. The top-view AFM 3D image of an area of 5 × 5 μm^2.

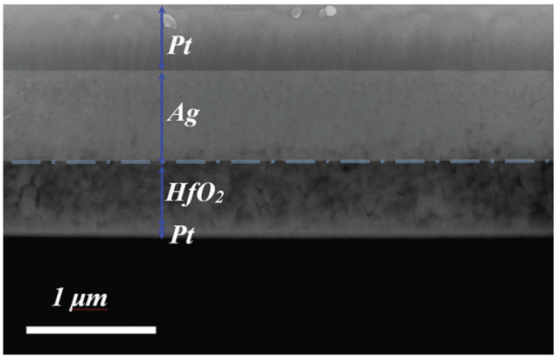

Fig. 4 Cross-section of the MIM capacitor by the FIB-assisted FE-SEM technique. The layers have a Pt bottom electrode thickness of 50 nm, 400 nm of HfO_2 and 700 nm of Ag top contact.

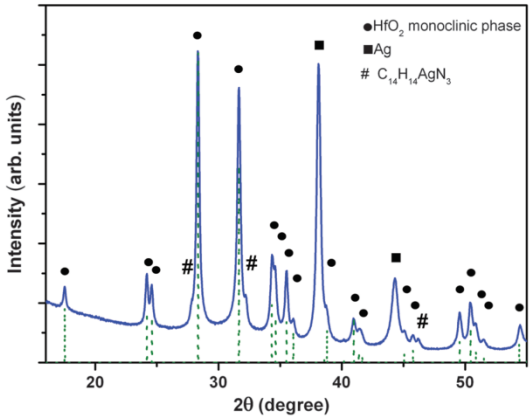

Fig. 5 XRD pattern of 120 nm thick HfO_2 annealed at 250 °C, deposited on an Ag bottom contact layer of 300 nm. Ag and main monoclinic HfO_2 peaks are labelled.

of surface defects (mainly pinholes) through the layer (in depth), which can induce a short circuit. For this purpose, we analyzed the device cross-section by FIB-assisted FE-SEM, as shown in Fig. 4. The section profile of the inkjet-printed HfO_2 film shows good homogeneity and the integrity of the layers, with a thickness of around 400 nm. Moreover, the whole MIM capacitor section on the substrate does not show any propagation of printing errors or large cavities among the layers. Additionally, the spectroscopic reflectometry results proved the fine control deposition achieved by a single printing process. The thickness of the HfO_2 thin film layer was measured to be around 100 nm, in agreement with the FIB cross-section image in Fig. S3 (ESI†).

Finally, the SEM cross-section image demonstrated that the film was grown quite uniformly over the metal film surface, following the roughness of the substrate surface. The possible porosity is still not well understood; therefore, further studies are required.

Overall, the structural characterization has shown that the morphology of the printed dielectric layer evidences a solid and stable structure without detrimental wrinkles, fractures or pin-holes.

3.2 Crystalline structure

The crystalline structure, size and orientation of the HfO_2 thin films were investigated by XRD, the results being shown in Fig. 5. The XRD pattern clearly shows the characteristic reflections of the HfO_2 monoclinic phase labelled by the circle symbols, as expected from the nature of the nanoparticles. The printed layer principally exhibited a polycrystalline monoclinic structure and mainly revealed ($\bar{1}11$) and (111) reflections (PDF#078-0049) at 28.16° and 31.85°, respectively.[35] The monoclinic HfO_2 phase is the most stable and well-studied structure according to the experimental and theoretical investigations in the previously reported studies at low temperature.[36,37] No other phases were observed, nor phenomena related to the nanoparticle recrystallization during the thermal annealing processes. In particular, the specimens evidenced the absence of the characteristic peak at 30.3° of metastable cubic, tetragonal, or orthorhombic phases of HfO_2.[38,39]

The XRD peaks centred at 2θ = 27.80°, 32.18°, and 46.26° indicate the presence of a crystalline phase of Ag–4,4′-dimethyldiazoaminobenzene ($C_{14}H_{14}AgN_3$).[40] In our case, $C_{14}H_{14}AgN_3$ forms from the Ag bottom contact; however, it does not affect the crystalline structure as proved by the clearly identifiable HfO_2 peaks (monoclinic phase) in the XRD patterns in Fig. 5.

The size of HfO_2 NPs was estimated from the full-width at half-maximum (FWHM) of the XRD reflection according to the Debye–Scherrer's equation (eqn (1)).[41] Considering the peak at different degrees, the average particle size, D, has been evaluated according to:

$$D = (0.9\lambda)/[B\cos(\theta)] \quad (1)$$

where λ = 0.15406 nm is the wavelength of X-ray radiation, B is the full-width at half-maximum (FWHM) and θ is the diffraction angle.

The average crystallite size of the as-prepared HfO_2 NPs was calculated to be around 25 nm, in agreement with the size calculated previously from TEM images, like in previous reports in the literature.[42,43]

The crystalline quality, uniformity and purity of HfO_2 NPs thin film were investigated also by micro-Raman analysis in Fig. 6. The Raman spectra were referenced to crystalline silicon main vibration at 521 cm^{-1}. The data were acquired in the spectral region from 100 to 800 cm^{-1}. The Raman spectrum of the HfO_2 oxide is shown in Fig. 6, where the monoclinic phase of HfO_2 exhibits two Raman-active in-phase vibration modes, A_g and B_g. Only 18 active vibration modes are expected in the Raman spectra of HfO_2 ($9A_g + 9B_g$), as confirmed from the spectra. These peaks are in good agreement with allowed phonon modes predicted for the HfO_2 monoclinic phase in the range from 100 to 800 cm^{-1}.[44,45]

The presence of remaining carbon contamination was analyzed by FT-IR. The acquired spectra are displayed in Fig. 7, where the peaks associated with the HfO_2 monoclinic phase (red line) are represented in the range from 4000 to 400 cm^{-1}. The main absorption bands in the infrared region are placed

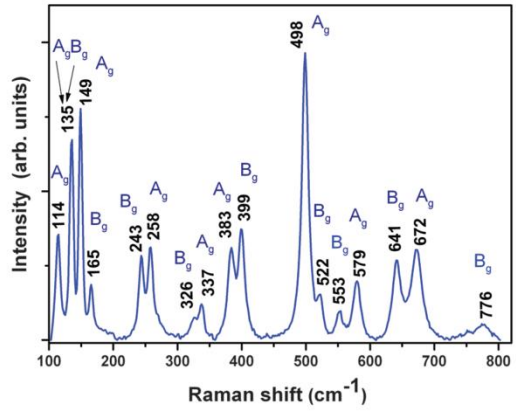

Fig. 6 Raman spectrum of the printed HfO_2. Monoclinic vibration modes of HfO_2 are labelled. The vibration modes are classified into A_g and B_g modes.

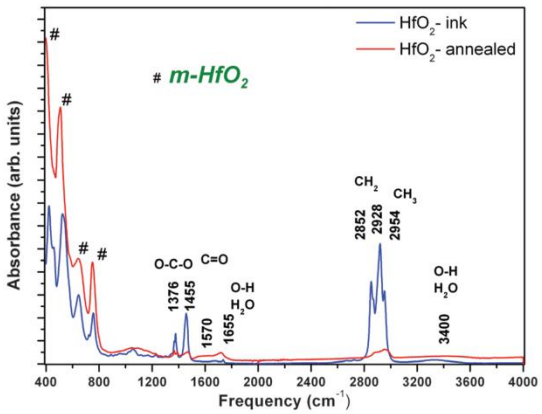

Fig. 7 FT-IR spectra comparison between the HfO_2 ink compound and HfO_2-annealed sample at 250 °C.

at 418, 514, 763 and 647 cm^{-1};[46,47] all of them are ascribed to the monoclinic hafnium oxide (m-HfO_2) phonon bands, in good agreement with previously reported values.[37,48–51] FT-IR measurements allowed us to identify any possible adsorbed contaminants by other absorption peaks in the range of 3400–1300 cm^{-1}, where the peaks are attributed to the H-bonded OH group of water, carbon bonding and to the bonding mode (H–O–H) of the water molecules.[46,48,52,53]

In fact, carbon compounds could be attributed to the inkjet process, and more precisely to an ink hydrocarbon vehicle. In Fig. 7 we show the characteristic FT-IR spectrum of the HfO_2 ink compound in the liquid phase (in blue) in comparison to the HfO_2 annealed layer (in red). Then, we can observe that the peaks of the vehicle fade out after the sintering process.

It should be noticed that residual organic carbon could affect the electrical properties of the insulator, which clearly seems to be one of the causes of the reduction of the expected dielectric constant of the material. Furthermore, this undesired residual carbon will probably enhance the conductivity of the layer by means of trapped charges into the high-*k* layer.

It is indispensable to explore and consider the stoichiometry of the HfO_2 and the relation of carbon compounds into the printed layer in order to watch over and guarantee an ideal insulator without trapped charges. For this purpose, Fig. 8(a) shows the XPS multiplex spectra of the HfO_2 layer. The wide energy survey spectrum exhibited the distinctive peaks of HfO_2 bonds, with their corresponding binding energies (BE). An analysis of these peaks revealed that 212.6 and 223.3 eV correspond to the $4d_{5/2}$ and $4d_{3/2}$ doublet of the Hf 4d spin–orbit doublet characteristic of HfO_2. The characteristic peak of the Hf 4p photoelectron line is located at the binding energy of 381.4 eV ($4p_{3/2}$), which corresponds to HfO_2.[54,55] The presence of the C 1s peak at 284.8 eV was attributed to the adsorbed carbon from the environment, the adventitious carbon[56–58] [Fig. S4, ESI†]. It should be mentioned that, at the interface of the structure HfO_2/Ag bottom contact [see Fig. S5, ESI†] a feeble carbon peak can be observed. Since the analysis of this contribution is not in the scope of the present study, its consequences on the electrical transport and charge trapping phenomena will be evaluated in a future work.

Details of the Hf 4f spectrum are shown in Fig. 8(b). The asymmetric shape of the spectrum suggests the presence of smaller doublet peaks, each with a 1.68 eV separation, towards lower BE for the expected Hf–O bonds. Therefore the Hf 4f energy level region can be deconvolved into three spin–orbit doublet peaks with the corresponding $4f_{7/2}$ binding energies at 15.4, 15.8, and 17.1 eV. In accordance to previous studies, the first two doublets exhibit larger widths than 0.9 eV and can accordingly be assigned to a Hf^{x+} suboxide, whereas the last one can be ascribed to the fully oxidized hafnium (Hf^{4+}).[17,59–61]

The formation of the suboxide probably depends on the substrate temperature and the depositing conditions that may induce bond structures such as HfOC,[62] or $HfC_xN_yO_z$,[63,64] as indicated by the O 1s spectra in Fig. 8(c). The peak placed at 530.7 eV (O 1s) is attributed to (metal–oxygen) Hf–O bonds, whereas the peaks at 529.1 and 532.5 eV indicate bond structures such as CO_x (adventitious carbon)[56] or $C_xH_yO_z$.[59,65,66] Nevertheless, their low relative intensity suggests a low concentration of these bonds, as confirmed by the FT-IR study.

In conclusion, the effective stoichiometry O:Hf could be estimated to be around 1.85, a good value that confirms, despite the dielectric thickness, how reliable the inkjet technology is in terms of purity in comparison to other well-known small-area and expensive technologies such as sputtering, ALD or CVD.[21,25,26,67]

3.3 Optical and electrical properties

The absorption spectrum of the HfO_2 NPs ink was acquired within the UV–vis range to evaluate the optical properties of the dielectric. The absorbance spectra recorded in the region from 190 to 1100 nm (see the inset in Fig. 9) allowed us to estimate the energy band gap (E_g) value of the HfO_2 NPs. This was achieved considering the Tauc law, able to fit the absorption coefficient in both direct and indirect band gap semiconductors[68] by plotting $(\gamma h\nu)^2$ *versus* photon energy ($h\nu$), using (eqn (2)):

$$(\gamma h\nu)^2 = A(h\nu - E_g) \quad (2)$$

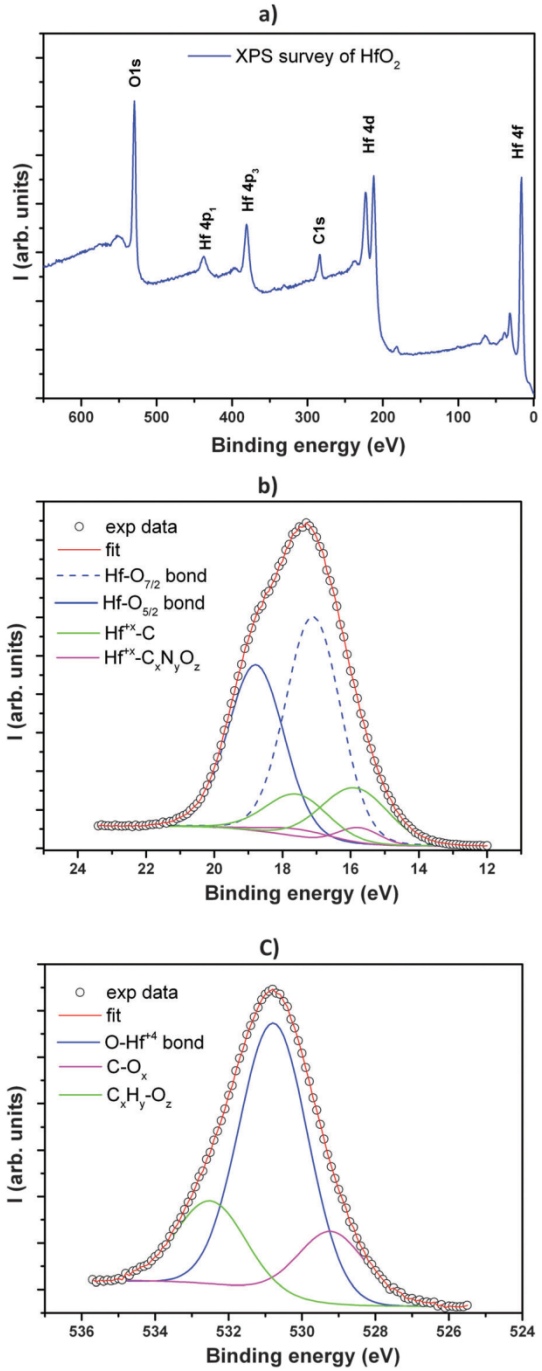

Fig. 8 (a) XPS binding energy survey and (b and c) high-resolution XPS spectra of Hf and O in annealed HfO_2 thin film at 250 °C for 3 h, deposited on Ag bottom contact. The curves represent the experimental data with the fit of the corresponding peaks.

where γ is the absorption coefficient, A is a constant, and E_g is the optical band gap of the NP-based material. Looking at the fit in Fig. 9, we can conclude that the film presents a direct

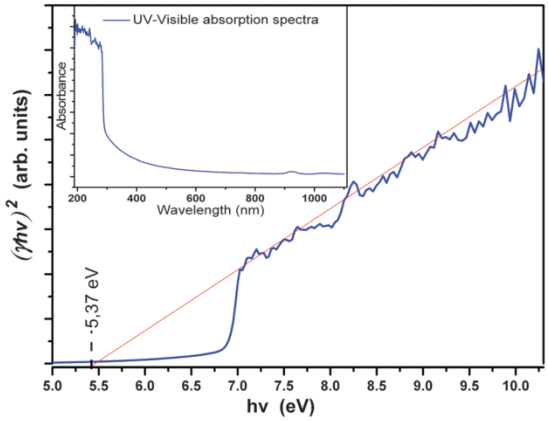

Fig. 9 Tauc plot fit corresponding to the UV–visible absorbance spectra of HfO_2 films which is displayed in the inset.

band gap, whose energy value can be obtained from the fit intersection with the photon energy axis. The image shows the derived value of the energy band gap, being E_g = 5.37 eV, which is found to be close to the previously reported value for polycrystalline HfO_2 NPs film.[69,70]

In order to characterize the electrical properties of the high-k HfO_2 NPs thin film, C–V measurements were carried out in the frequency range from 10 kHz to 1 MHz [Fig. S6, ESI†]. From the voltage dependence of the capacitance characteristic, the voltage coefficients of capacitance (VCCs) have been evaluated, which can be fitted by means of the following polynomial relation (eqn (3)):[71]

$$C_p = C_0(\alpha \cdot V^2 + \beta \cdot V + 1) \quad (3)$$

where C_0 is the capacitance value at zero bias voltage, and α and β are the quadratic and linear voltage dependences, respectively.[71] According to the ITRS roadmap up to 2016,[72] the quadratic coefficient of capacitance α might be smaller than 100 ppm V^{-2}, whereas β should lie below ±1000 ppm V^{-1}, for frequencies above 100 kHz. The obtained VCC values from the C–V measurements are shown in Table 2. It can be seen that the smallest α and β values are measured at higher frequencies, which can be explained as a result of the slow time constant of traps within the HfO_2-related dielectrics.[73]

In order to understand the behaviour of α and β with frequency, we can consider that for analogue-circuit applications the α parameter is the most important value, as the β value can be compensated by custom circuit design. Therefore, the interest is focused on the nonlinear behaviour of the standard C–V curves.

Table 2 Quadratic and linear voltage coefficients of capacitance (VCCs) at different frequencies, corresponding to a 400 nm thick MIM capacitor

HfO_2 MIM capacitor 400 nm thick		
Frequency	α (ppm V^{-2})	β (ppm V^{-1})
10 kHz	452	−6490
100 kHz	109	−920
1 MHz	18	146

The quadratic voltage characteristic is attributed to the following relation (eqn (4)):[74,75]

$$\alpha = 2(n_2 \cdot n_0)/(d^2 \cdot k_{lin}) \quad (4)$$

where n_0 is the linear refractive index, k_{lin} is the linear dielectric constant, n_2 is the nonlinear refractive index that contemplates the elastic properties of the oxide, and d the thickness of the dielectric layer. The high-k MIM capacitors exhibit a strong positive parabola [Fig. S6, ESI†], probably due to a high degree of electric field polarization and carrier injection.[24,76,77] The quadratic voltage coefficient of capacitance decreases with the applied frequency due to the change in relaxation time with different carrier mobility within the insulator, and correlates with the dielectric composition and thickness, which is an intrinsic property owing to the electric field polarization.[28,74]

From capacitance values, assuming plane-parallel electrodes, the obtained relative permittivity was $k = 12.6 \pm 0.8$ at 1 MHz [see Fig. S7 and S8, ESI†]. This value is perfectly comparable to the value of previous studies,[16] thus demonstrating that inkjet printing of high-k HfO_2 is a reliable technology towards high-quality device fabrication. Fig. 10 shows the capacitance density at different frequencies, exhibiting a constant value in the range around ± 3 V.

The plot in Fig. 11 shows the leakage current density–voltage characteristics of the HfO_2 MIM capacitor for a 400 nm-thick oxide film. The J–V characteristic was measured from an area of 2×10^{-4} cm^2 for all samples. Particularly, lower leakage currents of $\sim 3 \times 10^{-7}$ A cm^{-2} at ± 3 V were obtained.

Finally, the loss tangent value ($1/Q$ factor) was determined as a function of frequency for the HfO_2 dielectric MIM capacitors. Fig. 12 shows a similar trend in the loss tangent values for all the samples, exhibiting a value of around 0.0125 at a frequency of 1 MHz,[72] well below the ITRS roadmap scheduled data for 2016 (horizontal dotted line).

In light of the all above-mentioned studies, inkjet printing is demonstrated as a promising technology that allows selectively depositing, in a non-contact process and at ambient pressure, reliable thin films of the outstanding high-k dielectric HfO_2 on flexible substrates for MIM devices.

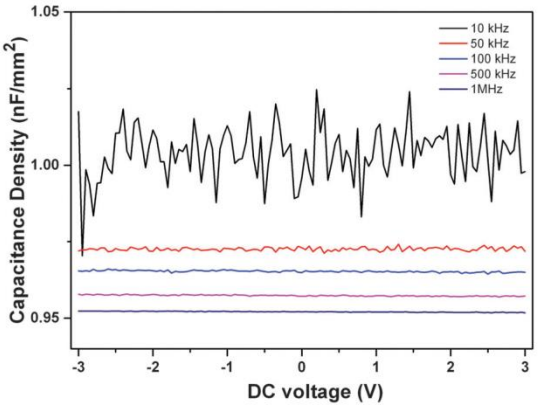

Fig. 10 Capacitance density at different frequencies.

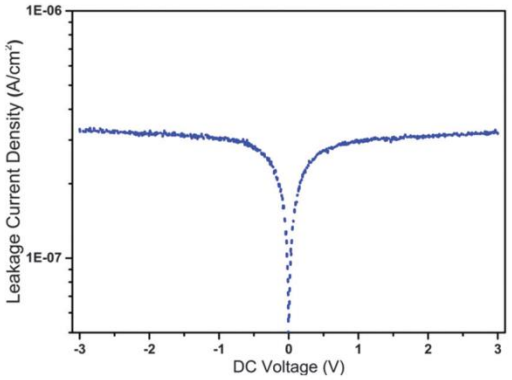

Fig. 11 Leakage current density–voltage characteristics of the MIM capacitor formed by an inkjet-printed 400 nm-thick HfO_2 thin film.

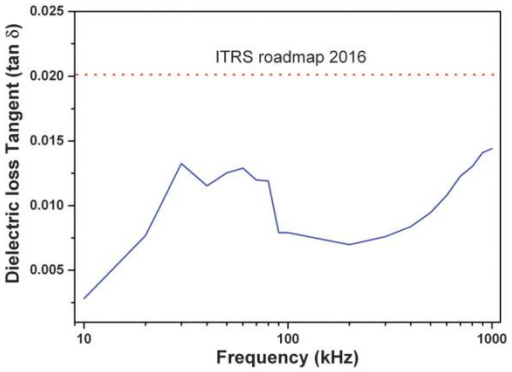

Fig. 12 Plot of the dielectric loss tangent value of a MIM capacitor (Ag/HfO_2/Ag structure) deposited by the inkjet printing technique.

4. Conclusions

Fully-printed flexible HfO_2-based MIM capacitors were fabricated by inkjet printing followed by a low-temperature thermal treatment. Ag ink was printed to form both top and bottom electrodes, whereas HfO_2 NPs ink was used to print the high-k dielectric thin film. FE-SEM and TEM images revealed the homogeneity of the insulating layer with spherical-shaped NPs of 25 nm diameter. A uniform polycrystalline structure with good purity was confirmed from XRD, FTIR and Raman scattering studies. The optical band gap energy was determined to be 5.37 eV by UV–vis absorption spectroscopy.

The HfO_2 thin film exhibits relative permittivity and dielectric loss tangent of $k = 12.6$ and $\tan\delta = 0.0125$ at 1 MHz, respectively. Below breakdown voltages, the leakage current did not exceed 6×10^{-8} A cm^{-2} at +3 V and $\sim 3 \times 10^{-7}$ A cm^{-2} at -3 V. The general stability and repeatability of the dielectric properties were confirmed by the VCCs coefficients (α and β), which behave as established by the ITRS roadmap, even at frequencies as high as 1 MHz.

Further work is required to reduce HfO_2 layer thickness in order to be comparable to those of silicon- and glass-based capacitor devices in the near future.

To sum up, all the parameters obtained from the structural, optical and electrical studies carried out in this work indicate that inkjet-printed flexible HfO_2 NPs-based MIM capacitors are suitable candidates to become possible alternatives to Si-based devices in the near future. Simultaneously, the demand for an innovative transparent, flexible and reliable technology is increasing due to the possibility of being employed in emerging fields such as biological sensors and flexible systems. For such applications, low-cost production and device integration are the key requirements, which can be provided by the promising inkjet printing technology.

Acknowledgements

G. Vescio acknowledges the Spanish Government for his PhD grant in the FPU program. A. Cirera acknowledges support from the 2015 edition of BBVA Foundation Grants for Researchers and Cultural Creators.

References

1 H. Y. Tseng and V. Subramanian, *Org. Electron.*, 2011, **12**, 249–256.
2 M. Caironi, E. Gili, T. Sakanoue, X. Cheng and H. Sirringhaus, *ACS Nano*, 2010, **4**, 1451–1456.
3 R. M. Verkouteren and J. R. Verkouteren, *Langmuir*, 2011, **27**, 9644–9653.
4 H. Sirringhaus, T. Kawase, R. H. Friend, T. Shimoda, M. Inbasekaran, W. Wu and E. P. Woo, *Science*, 2000, **290**, 2123–2126.
5 S. Magdassi and S. Magdassi, *Pigm. Resin Technol.*, 1987, **16**, 4–10.
6 H. Minemawari, T. Yamada, H. Matsui, J. Tsutsumi, S. Haas, R. Chiba, R. Kumai and T. Hasegawa, *Nature*, 2011, **475**, 364–367.
7 C. Wang, J.-C. Chien, H. Fang, K. Takei, J. Nah, E. Plis, S. Krishna, A. M. Niknejad and A. Javey, *Nano Lett.*, 2012, **12**, 4140–4145.
8 N. Zhao, M. Chiesa, H. Sirringhaus, Y. Li, Y. Wu and B. Ong, *J. Appl. Phys.*, 2007, **101**, 064513.
9 T. Sekitani, Y. Noguchi, U. Zschieschang, H. Klauk and T. Someya, *Proc. Natl. Acad. Sci. U. S. A.*, 2008, **105**, 4976–4980.
10 C. Mariotti, S. Member, B. S. Cook, L. Roselli, S. Member and M. M. Tentzeris, *Ieee Microw. Wirel. Components Lett.*, 2015, **25**, 13–15.
11 B. S. Cook, J. R. Cooper and M. M. Tentzeris, *IEEE Microw. Wirel. Components Lett.*, 2013, **23**, 353–355.
12 B. Miao, R. Mahapatra, N. Wright and A. Horsfall, *J. Appl. Phys.*, 2008, **104**, 054510.
13 S.-J. Ding, C. Zhu, M.-F. Li and D. W. Zhang, *Appl. Phys. Lett.*, 2005, **87**, 053501.
14 J. S. Meena, M.-C. Chu, S.-W. Kuo, F.-C. Chang and F.-H. Ko, *Phys. Chem. Chem. Phys.*, 2010, **12**, 2582–2589.
15 J. Robertson and R. M. Wallace, *Mater. Sci. Eng., R*, 2015, **88**, 1–41.
16 J. Robertson, *Eur. Phys. J.: Appl. Phys.*, 2004, **291**, 265–291.
17 S. Suzer, S. Sayan, M. M. Banaszak Holl, E. Garfunkel, Z. Hussain and N. M. Hamdan, *J. Vac. Sci. Technol., A*, 2003, **21**, 106.
18 O. Khaldi, P. Gonon, C. Mannequin, C. Vallée, F. Jomni and A. Sylvestre, *ECS Solid State Lett.*, 2013, **2**, N15–N17.
19 T. Tan, Z. Liu, H. Lu, W. Liu and H. Tian, *Opt. Mater.*, 2010, **32**, 432–435.
20 J. Y. Soon and Y. Roh, *IEEE Nanotechnol. Mater. Devices Conf.*, 2006, 546–547.
21 F. L. Martínez, M. Toledano-Luque, J. J. Gandía, J. Cárabe, W. Bohne, J. Röhrich, E. Strub and I. Mártil, *J. Phys. D: Appl. Phys.*, 2007, **40**, 5256–5265.
22 K. Kukli, T. Aaltonen, J. Aarik, J. Lu, M. Ritala, S. Ferrari, A. Hårsta and M. Leskelä, *J. Electrochem. Soc.*, 2005, **152**, F75.
23 X. Yu, C. Zhu, H. Hu and A. Chin, *IEEE Electron Device Lett.*, 2003, **24**, 63–65.
24 S. J. Kim, B. J. Cho, M. F. Li, X. Yu, C. Zhu, A. Chin and D. Kwong, *IEEE Electron Device Lett.*, 2003, **24**, 387–389.
25 N. V. Nguyen, A. V. Davydov, D. Chandler-Horowitz and M. M. Frank, *Appl. Phys. Lett.*, 2005, **87**, 192903.
26 J. Park, B. K. Park, M. Cho, C. S. Hwang, K. Oh and D. Y. Yang, *J. Electrochem. Soc.*, 2002, **149**, G89–G94.
27 M. Ratzke, D. Wolfframm, M. Kappa, S. Kouteva-Arguirova and J. Reif, *Appl. Surf. Sci.*, 2005, **247**, 128–133.
28 H. Hu, C. Zhu, Y. F. Lu, Y. H. Wu, T. Liew, M. F. Li, B. J. Cho, W. K. Choi and N. Yakovlev, *J. Appl. Phys.*, 2003, **94**, 551.
29 R. Garg, N. A. Chowdhury, M. Bhaskaran, P. K. Swain and D. Misra, *J. Electrochem. Soc.*, 2004, **151**, F215.
30 A. Ramadoss and S. J. Kim, *J. Alloys Compd.*, 2012, **544**, 115–119.
31 B. J. Perelaer, A. W. M. de Laat, C. E. Hendriks and U. S. Schubert, *J. Mater. Chem.*, 2008, **18**, 3209.
32 A. Mukhopadhyay, J. Sanz and C. Musgrave, *Phys. Rev. B: Condens. Matter Mater. Phys.*, 2006, **73**, 115330.
33 J. R. Williams, T. Low, M. S. Lundstrom and C. M. Marcus, *Nat. Nanotechnol.*, 2011, **6**, 222–225.
34 K. Everaerts, J. D. Emery, D. Jariwala, H. J. Karmel, V. K. Sangwan, P. L. Prabhumirashi, M. L. Geier, J. J. McMorrow, M. J. Bedzyk, A. Facchetti, M. C. Hersam and T. J. Marks, *J. Am. Chem. Soc.*, 2013, **135**, 8926–8939.
35 R. E. Hann, P. R. Suitch and J. L. Pentecost, *J. Am. Ceram. Soc.*, 1985, **68**, C-285–C-286.
36 K.-C. Tsai, W.-F. Wu, C.-G. Chao and C.-P. Kuan, *J. Electrochem. Soc.*, 2006, **153**, G492.
37 B. Zhou, H. Shi, X. D. Zhang, Q. Su and Z. Y. Jiang, *J. Phys. D: Appl. Phys.*, 2014, **47**, 115502.
38 G. Scarel, S. Spiga, C. Wiemer, G. Tallarida, S. Ferrari and M. Fanciulli, *Mater. Sci. Eng., B*, 2004, **109**, 11–16.
39 D. Min, N. Hoivik, G. U. Jensen, F. Tyholdt, C. Haavik and U. Hanke, *Appl. Phys. A: Mater. Sci. Process.*, 2011, **105**, 867–874.
40 R. Mendoza-Reséndez, N. Núñez, E. Barriga-Castro and C. Luna, *RSC Adv.*, 2013, **3**, 20765.
41 S. J. S. Qazi, A. R. Rennie, J. K. Cockcroft and M. Vickers, *J. Colloid Interface Sci.*, 2009, **338**, 105–110.

42 Z. M. Rittersma, F. Roozeboom, M. A. Verheijen, J. G. M. van Berkum, T. Dao, J. H. M. Snijders, E. Vainonen-Ahlgren, E. Tois, M. Tuominen and S. Haukka, *J. Electrochem. Soc.*, 2004, **151**, C716.

43 J. Yota, H. Shen and R. Ramanathan, *J. Vac. Sci. Technol., A*, 2013, **31**, 01A134.

44 R. Wu, B. Zhou, Q. Li, Z. Jiang, W. Wang, W. Ma and X. Zhang, *J. Phys. D: Appl. Phys.*, 2012, **45**, 125304.

45 B.-K. Kim and H. Hamaguchi, *Mater. Res. Bull.*, 1997, **32**, 1367–1370.

46 M. M. Frank, S. Sayan, S. Dörmann, T. J. Emge, L. S. Wielunski, E. Garfunkel and Y. J. Chabal, *Mater. Sci. Eng., B*, 2004, **109**, 6–10.

47 K. Tomida, K. Kita and A. Toriumi, *Appl. Phys. Lett.*, 2006, **89**, 142902.

48 D. A. Neumayer and E. Cartier, *J. Appl. Phys.*, 2001, **90**, 1801.

49 T. Hirata, *Phys. Rev. B: Condens. Matter Mater. Phys.*, 1994, **50**, 2874–2879.

50 M. Modreanu, J. Sancho-Parramon, O. Durand, B. Servet, M. Stchakovsky, C. Eypert, C. Naudin, A. Knowles, F. Bridou and M.-F. Ravet, *Appl. Surf. Sci.*, 2006, **253**, 328–334.

51 D. Ceresoli and D. Vanderbilt, *Phys. Rev. B: Condens. Matter Mater. Phys.*, 2006, **74**, 125108.

52 X. Zhao and D. Vanderbilt, *Phys. Rev. B: Condens. Matter Mater. Phys.*, 2002, **65**, 233106.

53 L. Koltunski and R. A. B. Devine, *Appl. Phys. Lett.*, 2001, **79**, 320.

54 R. Nyholm, A. Berndtsson and N. Martensson, *J. Phys. C: Solid State Phys.*, 1980, **13**, 1091.

55 D. D. Sarma and C. N. R. Rao, *J. Electron Spectrosc. Relat. Phenom.*, 1980, **20**, 25–45.

56 L. Ramqvist, K. Hamrin, G. Johansson, A. Fahlman and C. Nordling, *Solid State Commun.*, 1969, **7**, v–vi.

57 T. L. Barr, *J. Vac. Sci. Technol., A*, 1995, **13**, 1239.

58 D. J. Miller, M. C. Biesinger and N. S. McIntyre, *Surf. Interface Anal.*, 2002, **33**, 299–305.

59 M. Engelhard, J. Herman, R. Wallace and D. Baer, *Surf. Sci. Spectra*, 2011, **18**, 46–57.

60 P. Dudek, R. Schmidt, M. Lukosius, G. Lupina, C. Wenger, A. Abrutis, M. Albert, K. Xu and A. Devi, *Thin Solid Films*, 2011, **519**, 5796–5799.

61 T.-C. Tien, L.-C. Lin, L.-S. Lee, C.-J. Hwang, S. Maikap and Y. M. Shulga, *J. Mater. Sci.: Mater. Electron.*, 2009, **21**, 475–480.

62 J. P. Lehan, Y. Mao, B. G. Bovard and H. A. Macleod, *Thin Solid Films*, 1991, **203**, 227–250.

63 R. Smart, S. Mcintyre and I. Bello, *Surf. Sci.*, 2011, **6**, 86.

64 P. Steiner, H. Höchst, J. Schneider, S. Hüfner and C. Politis, *Z. Phys. B: Condens. Matter Quanta*, 1979, **33**, 241–250.

65 Y. B. Yoo, J. H. Park, K. H. Lee, H. W. Lee, K. M. Song, S. J. Lee and H. K. Baik, *J. Mater. Chem. C*, 2013, **1**, 1651.

66 P. Steiner and S. Hüfner, *Solid State Commun.*, 1982, **44**, 1305–1307.

67 D. Barreca, A. Milanov, R. A. Fischer, A. Devi and E. Tondello, *Surf. Sci. Spectra*, 2007, **14**, 34.

68 J. Aarik, H. Mändar, M. Kirm and L. Pung, *Thin Solid Films*, 2004, **466**, 41–47.

69 T. Tan, Z. Liu, H. Lu, W. Liu, F. Yan and W. Zhang, *Appl. Phys. A: Mater. Sci. Process.*, 2009, **97**, 475–479.

70 Y. Xie, Z. Ma, Y. Su, Y. Liu, L. Liu, H. Zhao, J. Zhou, Z. Zhang, J. Li and E. Xie, *J. Mater. Res.*, 2011, **26**, 50–54.

71 C. Jorel, C. Vallée, P. Gonon, E. Gourvest, C. Dubarry and E. Defay, *Appl. Phys. Lett.*, 2009, **94**, 253502.

72 A. Allan, *et al.*, *International technology roadmap for semiconductors (ITRS)*, 2012.

73 M. Lukosius, C. B. Kaynak, S. Rushworth and C. Wenger, *J. Electrochem. Soc.*, 2011, **158**, G119.

74 C. Wenger, G. Lupina, M. Lukosius, O. Seifarth, H.-J. Müssig, S. Pasko and C. Lohe, *J. Appl. Phys.*, 2008, **103**, 104103.

75 C. Wenger, M. Lukosius, G. Weidner, H.-J. Müssig, S. Pasko and C. Lohe, *Thin Solid Films*, 2009, **517**, 6334–6336.

76 C. Zhu, H. Hu, X. Yu, S. J. Kim, A. Chin, M. F. Li, B. J. Cho and D. L. Kwong, *IEDM*, 2003, **36**, 879–882.

77 J. Robertson, *Appl. Surf. Sci.*, 2002, **190**, 2–10.

Electronic Supplementary Information for JMCC

SUPPORTING INFORMATION

Flexible Inkjet Printed high-k HfO_2-Based MIM Capacitors

G. Vescio,[a] J. López-Vidrier,[a] R. Leghrib,[b] A. Cornet [a] and A. Cirera [a]

MIND/IN2UB Electronics Department, Universitat de Barcelona, c/ Martí i Franquès 1, Planta 2, 08028, Barcelona, Spain.

email: gvescio@el.ub.edu

This PDF file includes:

Figs. S1 to S08

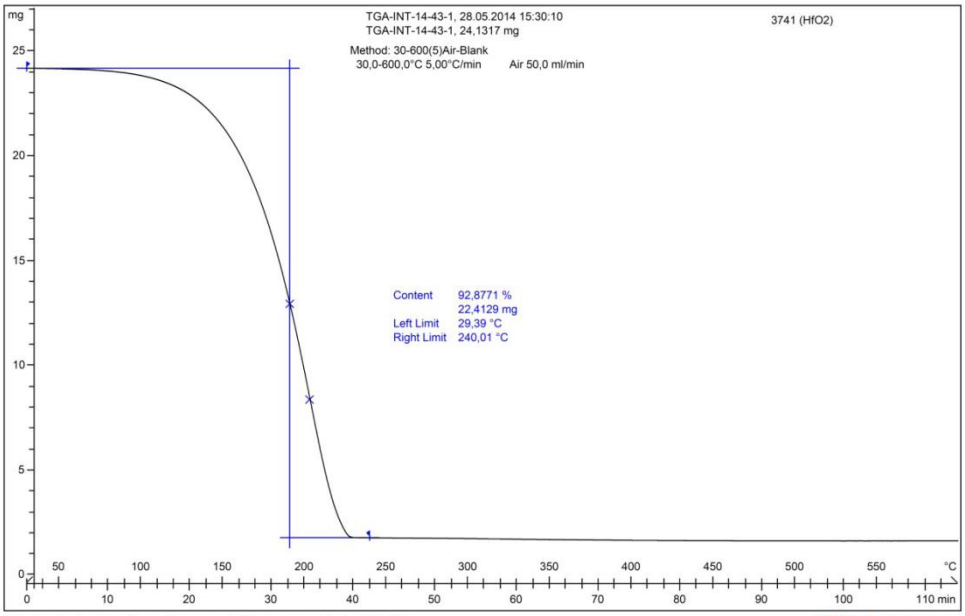

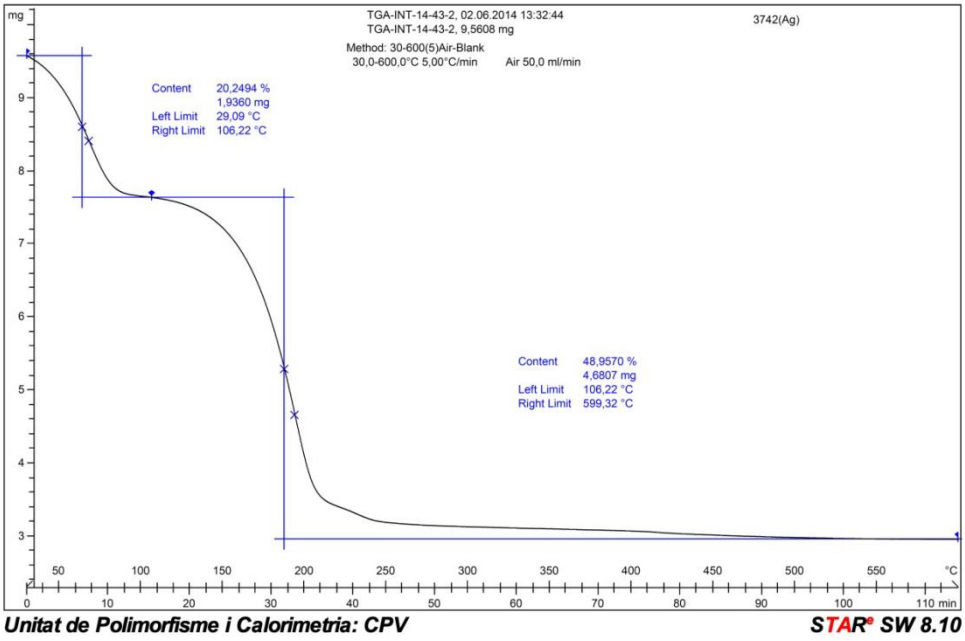

Fig. S1 Thermogravity analysis (TGA) of HfO_2 and Ag inks.

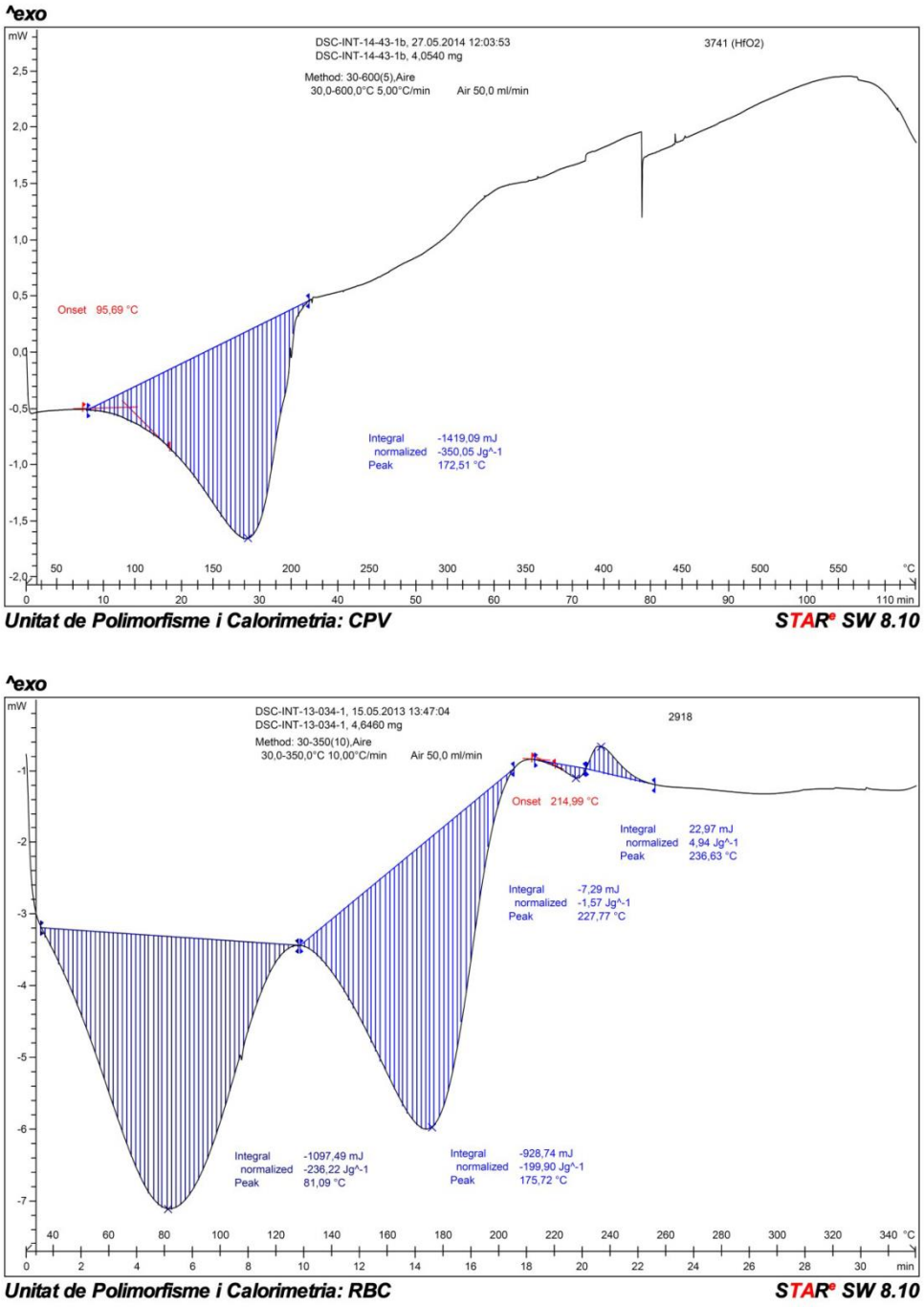

Fig. S2 Differential scanning calorimetry (DSC) measurement of HfO_2 and Ag inks.

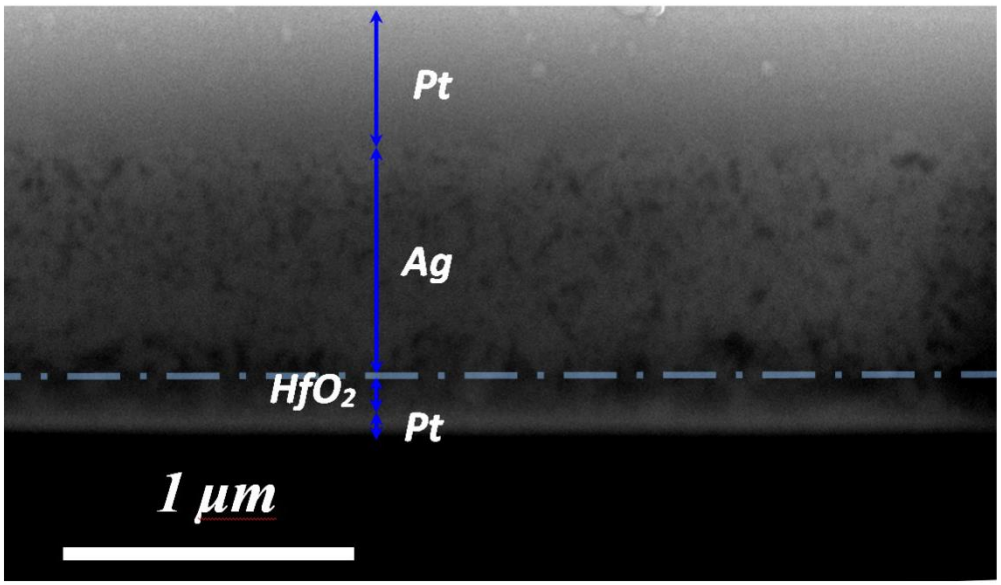

Fig. S3 Cross-section of MIM capacitor by FIB-assisted FE-SEM technique. The as-deposited layers have a Pt bottom electrode thickness of 50 nm, 120 nm for HfO_2 and 700 nm of Ag top contact.

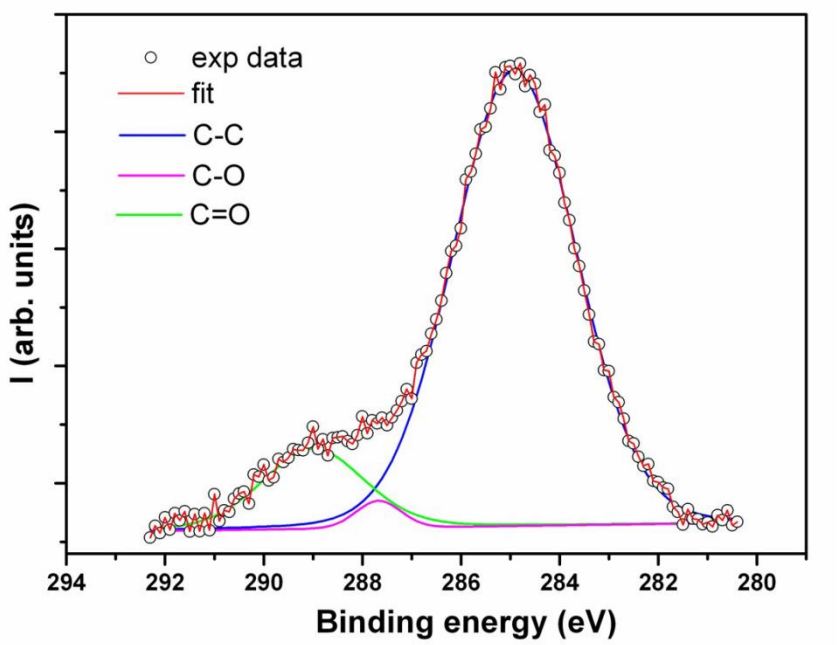

Fig. S4 XPS Binding Energy High-Resolution spectra of C in annealed HfO_2 thin film at 250 °C for 2 h, deposited on Ag bottom contact. The curve represents the experimental data with the corresponding peaks fitting.

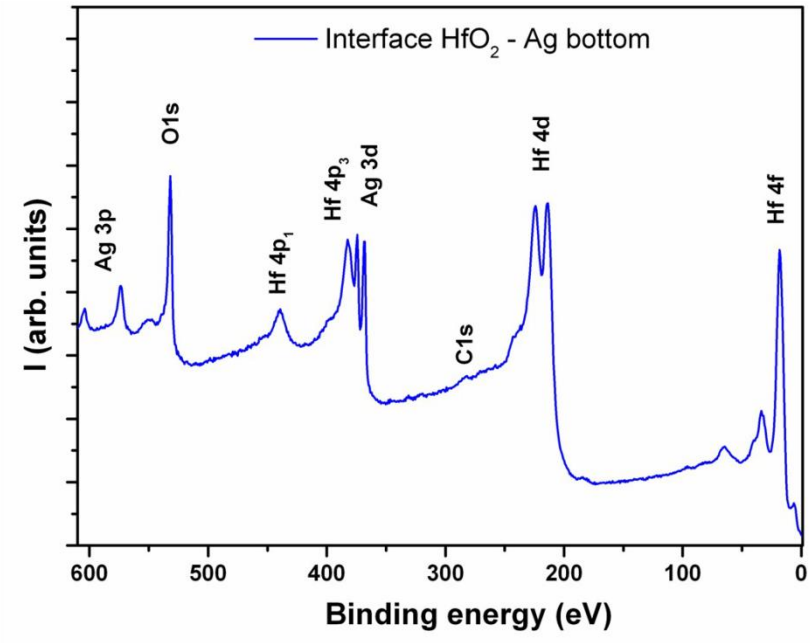

Fig. S5 XPS Binding Energy Survey spectra at the interface of the structure HfO_2/Ag bottom contact.

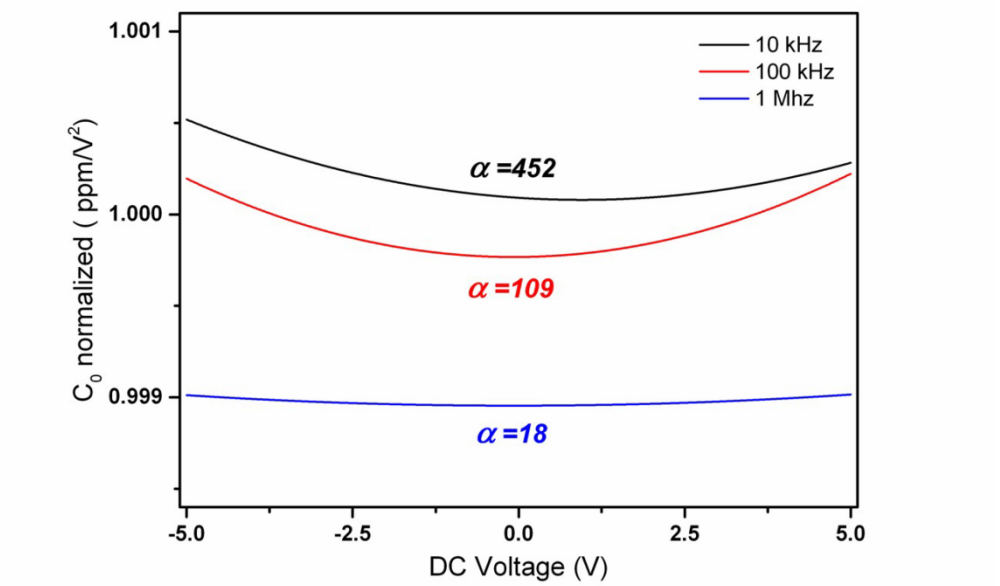

Fig. S6 Normalized capacitance-frequency dependence of an inkjet-printed Ag/HfO_2/Ag MIM capacitor.

a)

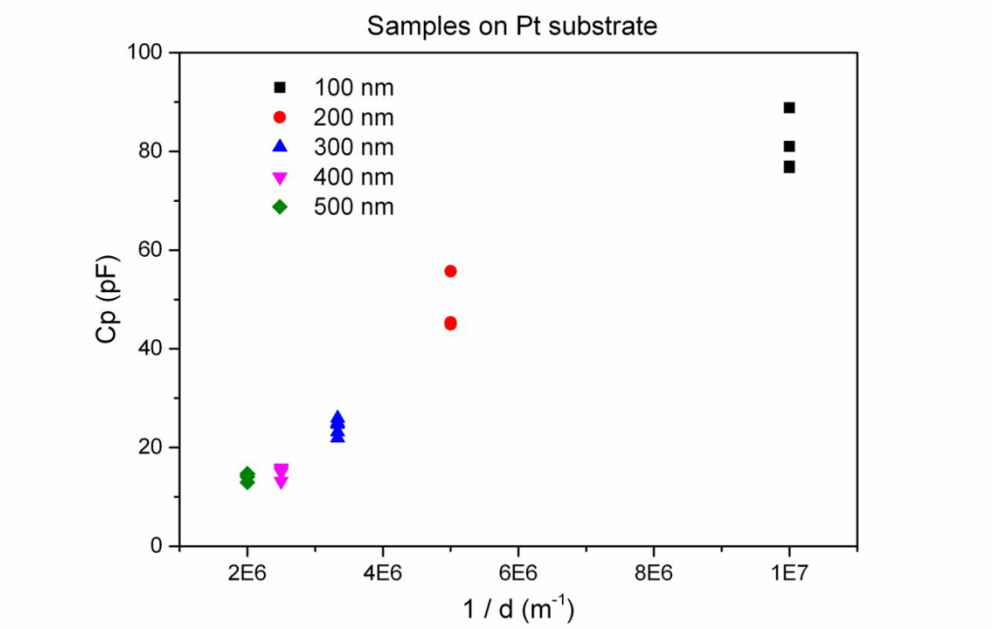

b)

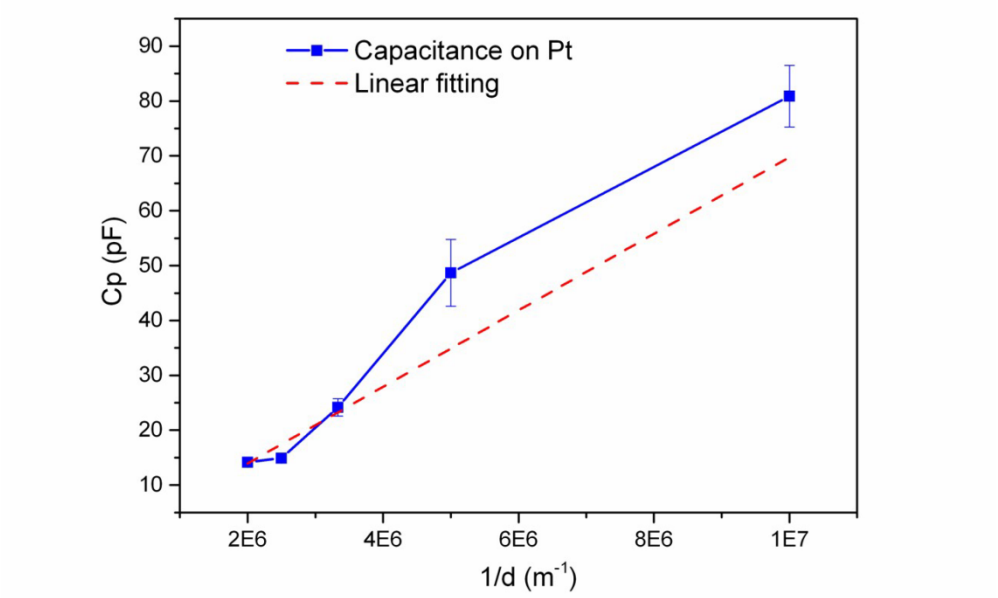

Fig. S7 **(a)** MIM capacitors structure Ag / HfO_2 / Pt with different thickness. **(b)** Linear fitting and curve regression for evaluation of dielectric constant.

a)

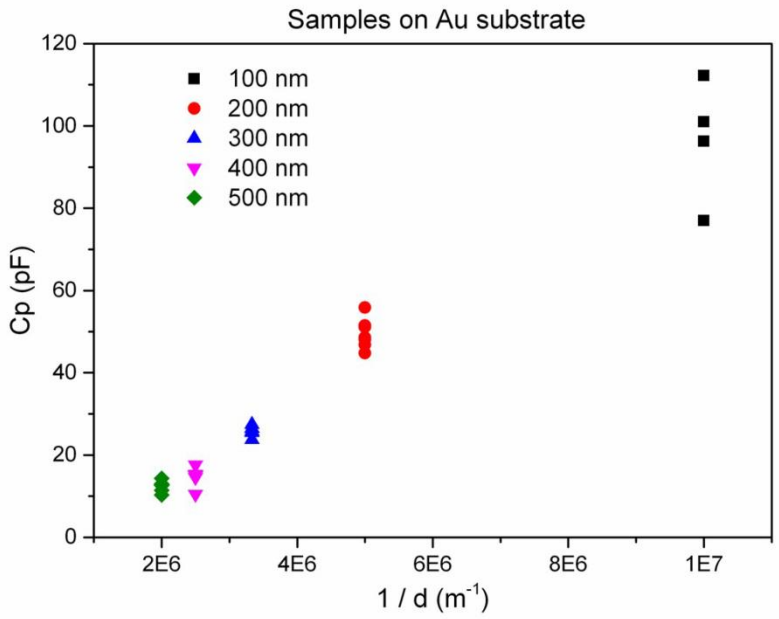

b)

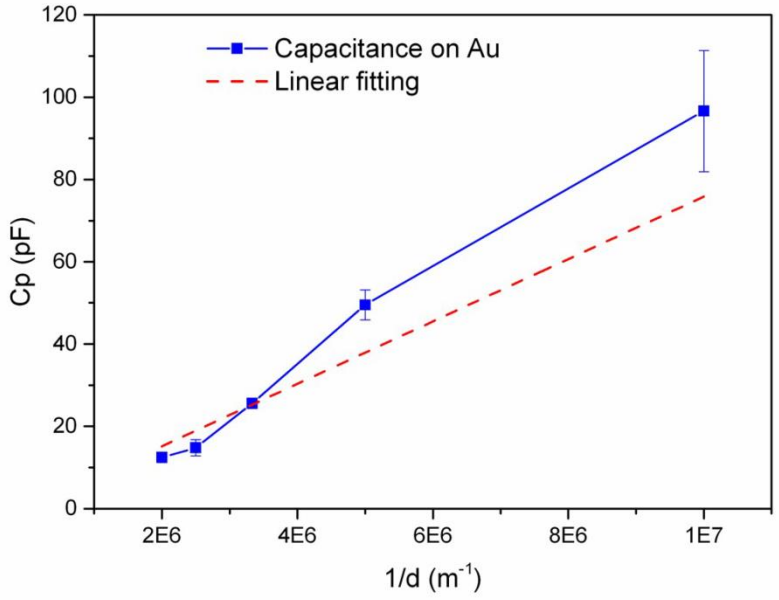

Fig. S08 **(a)** MIM capacitors structure Ag / HfO_2 / Au with different thickness. **(b)** Linear fitting and curve regression for evaluation of dielectric constant.

4.6.2. Inkjet-Printed HfO2-Based Memristor Au/HfO2/Ag

In ***Paper V****: Inkjet Printed HfO_2 -Based ReRAMs: First Demonstration and Performance Characterization,* the following issues were addressed in detail:

(1) The manufacturing for the first time of a memristor component with simple MIM structure, Au/HfO_2/Ag, based on the high-*k* hafnium oxide as flexible insulator, by means of drop-on-demand inkjet-printing technology.

(2) The observation of a bipolar resistive switching phenomenon, where the successive controlled changes between two conductive states, LRS and HRS, are obtained by applying positive SET (forming process) and negative RESET voltages.

(3) The demonstration of high-performance features such as I_{ON}/I_{OFF} ratio of three orders of magnitude and low switching operating voltages around 0.2V, thus allowing for a consumption reduction. These parameters are comparable to those achieved by conventional CMOS technologies.

(4) The evidence, by means of cyclic current-voltage measurements, that the HfO_2-based ReRAM devices work properly, reaching more than 128 Resistive Switching cycles.

The previously mentioned results are explained in terms of the forming process into the inkjet-printed thin-film dielectric layer, which creates a switchable conductive filament. Firstly, a SET process is characterized by a very low tunneling current (1 pA at 1 V). Afterwards, the high current values, measured after SET, suggest that conduction during LRS is controlled by a conductive filament created inside the printed HfO_2 layer. Consequently, measured currents after RESET indicate that the conductive filament is not completely closed, thus implying that conduction during HRS is, possibly, also controlled by the same conductive filament, which is weaker because it is partially closed. The paper aims at the demonstration of inkjet-printing technology as alternative method to deposit thin-film high-*k* HfO_2 nanoparticle-based ink for the manufacturing of ReRAM devices.

** Note that sections, equations and references numbering in the reproduced research article follow the ones of the published version. This statement applies to all Papers presented in this Thesis Dissertation.*

Inkjet Printed HfO_2-Based ReRAMs: First Demonstration and Performance Characterization

G. Vescio, A. Crespo-Yepes, D. Alonso, S. Claramunt, M. Porti, R. Rodriguez, A. Cornet, A. Cirera, M. Nafria, and X. Aymerich

***Abstract*— In this letter we demonstrate for the first time, the implementation of inkjet-printed high-performance ReRAM devices based on the high-k HfO_2 dielectric. Features such as high on/off current ratio and low switching voltages pave the way for low power applications. These characteristics, along with the known flexible properties of the inkjet-printed dielectric layer, make this kind of ReRAMs suitable for portable devices that do not require large integration density i.e. low density nonvolatile memories or reconfigurable analog circuits.**

***Index Terms*— Inkjet printed technology, resistive switching, ReRAM, low power applications, flexible devices, cost-competitive technology.**

I. Introduction

THE rising appeal for flexible, transparent, lightweight and cheap circuits or devices for current applications on medicine, sensing or IoT, is driving the development of emerging technologies into the field of printed electronics as an alternative to the Silicon technologies [1]. Despite the micrometric area resolution, printing technologies provide many advantages for several applications where Integrated Circuits are not strictly needed, reducing extremely the fabrication cost and the ecological impact. Up to now, bendable OLED displays [2], RFID antennas [3], solar cells [4], sensors [5] and transistors [6] have been developed by means of different printing technologies. In order to increase the benefits of these printed devices, many efforts are being spent on fulfilling the demands of small-size, low consumption and simple memories.

Manuscript received January 20, 2017; accepted February 8, 2017. Date of publication February 14, 2017; date of current version March 22, 2017. The work of G. Vescio was supported by the Spanish Government under a Ph.D. Grant in the FPU program. The work of A. Crespo-Yepes, D. Alonso, S. Claramunt, M. Porti, R. Rodriguez, M. Nafria, and X. Aymerich was supported in part by the Spanish MINECO and ERDF under Grant TEC2013-45638-C3-1-R and in part by the Generalitat de Catalunya under Grant 2014SGR-384. The work of A. Cirera was supported by the 2015 edition of BBVA Foundation Grants for Researchers and Cultural Creators. The review of this letter was arranged by Editor L. Selmi.

G. Vescio, A. Cornet, and A. Cirera are with MIND-IN2UB, Electronics Engineering Department, Universitat de Barcelona, 08007 Barcelona, Spain.

A. Crespo-Yepes, D. Alonso, S. Claramunt, M. Porti, R. Rodriguez, M. Nafria, and X. Aymerich are with the Electronic Engineering Department, Universitat Autònoma de Barcelona, 08193 Barcelona, Spain (e-mail: albert.crespo@uab.es).

Color versions of one or more of the figures in this letter are available online at http://ieeexplore.ieee.org.

Digital Object Identifier 10.1109/LED.2017.2668599

Amongst the existing memories, especially after the discovery of the memristor non-volatile property by HP team in 2008 [7], resistive random access memory (ReRAM) is the most suitable and feasible printable component due to its simple vertical structure (Metal-Insulator-Metal, MIM). Moreover, the crossbar architectures usually used in these devices ensure high scalability and cost-efficient fabrication. Memristors main feature is the resistive switching phenomenon (RS) which consists in the successive controlled changes between two conductive states, a low resistance state (LRS) and a high resistance state (HRS). In the case of MIM structures, it is commonly accepted that this phenomenon is due to the creation of a conductive filament in the dielectric that can be opened or closed depending on the applied voltage to the structure [8]. Parameters as retention time, stability and endurance, switching speed and low power consumption are key values for good quality memristors [9], [10]. Several materials demonstrated resistive switching behavior, such as organic insulators [11], amorphous silicon [12], chalcogenides [13], carbon nanotubes [14], perovskite oxides [15] and binary transition metal oxides [16], [17], [18]. Among the metal oxides, HfO_2 has been deeply studied and proved as good material for memory devices [10], [19].

A variety of manufacturing processes are available for memristors fabrication, including atomic layer deposition [20], sputtering [21], sol–gel method [16], anodization [22], screen printing and inkjet printing technology [23], [24]. Among these additive bottom-up processes, drop-on-demand inkjet printing stands out as a versatile, maskless, cost-efficient and non-contact digital designing method [25], [26], permitting to deposit in ambient room conditions and at relatively low temperature few picoliters amount of ink material in a non-contact process. Zou et al. [24] presented a compelling solution, where inkjet printed silver electrodes are exploited, by electroplating process, in order to achieve a flexible inexpensive Cu/CuxO/Ag memory cell working at low-voltage operation. Nevertheless, low resolution and lack of available inks compounds, due to the change of the physical and chemical properties of the ink when submitted to the printing process, are drawbacks that are limiting the fabrication development of high-performing and reliable devices. On the other hand, in our previous work, [27] HfO_2 has been demonstrated as very promising oxides for MIM devices guaranteeing the reliability and feasibility of the inkjet printing method paving the way for fully inkjet-printed electronic circuits.

In this work, we focus on the application of inkjet-printed HfO_2 as flexible thin film dielectric layer for HfO_2-based ReRAM devices. The promising results, shown in this article, demonstrate that it is possible to implement low-cost and high-performance non-volatile memories by the inkjet printing technique, achieving comparable features than conventional CMOS-compatible ReRAM devices.

II. Samples and Experimental

The samples used were MIM structures based on Au/HfO_2/Ag stacks that were fabricated onto silicon substrate. Firstly, an Au thin film (50nm) bottom electrode was deposited by sputtering. Then, using a Dimatix printer (2831, Fujifilm, Japan), a HfO_2 nanoparticles-based ink (Torrecid S.L.) is printed selectively over the bottom electrode covering an area of 0.1mm^2 keeping the substrate temperature constant at 30°C. A post-deposition annealing process of 3 hours at 240°C in a vacuum oven is needed for the elimination of solvents, further details about inkjet printing of HfO_2 where published elsewhere [26]. Finally, a silver top electrode with a thickness of 700 nm was printed onto the insulator layer using a commercial available silver ink (DGP-HR, ANP). Afterwards, it was again annealed in vacuum at 200 °C for 20 minutes in order to remove the organic solvents from the new layer and to achieve the expected resistivity around 16$\mu\Omega$·cm. Printing resolution with a drop spacing of 20μm (1270 drop-per-inch) was used in order to achieve the minimum thickness for each printing step avoiding pin-holes defects. Thus, inkjet-printed HfO_2-based MIM devices with a dielectric layer of 200nm have been successfully obtained. The layers thicknesses of the manufactured samples were measured by Focused Ion Beam (FIB) processed Field Emission Scanning Electron Microscopy (FESEM) image, using a Zeiss CrossBeam 1560XB equipment. The electrical characteristics of the resulting devices were studied with a Keithley 4200 Semiconductor Parameter Analyzer. Figure 1 shows the 3D structure (Top figure) and the FIB-processed FESEM image (Bottom figure). In the bottom figure silicon substrate (Dark grey region), bottom electrode formed by 50nm Au layer (grey thin region over the silicon substrate), 200nm of HfO2 dielectric layer (nanoparticles-based region atop the bottom electrode layer), and top electrode formed by 700nm of Ag are shown.

III. Results

In order to carry out the experiments, ramp voltages were applied to the several manufactured samples to trigger both, the Set and Reset processes that will open (LRS) or close (HRS) the conductive filament. A current limitation was used during the Set process to control the forming process in the dielectric and create a switchable conductive filament. A representative example of the observed Resistive Switching phenomenology is shown in Figure 2. Red and blue curves correspond to the I-V characteristics where the Set and Reset processes are observed, respectively, on five random-selected cycles on the same sample. Black line shows the first Set process (forming process) of the same device, characterized before forming by a very low tunneling current (1pA at 1V). After the forming process, during subsequent cycles, HRS

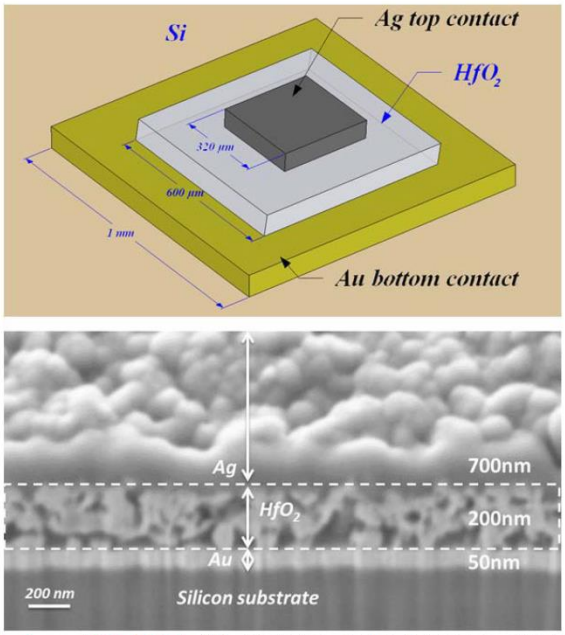

Fig. 1. (Top figure) 3D rendering of the fabricated structure. (Bottom figure) Cross-section image of the MIM capacitor obtained by FIB-assisted FESEM technique. The devices have an Au bottom electrode thickness of 50nm (grey region), 200nm of HfO_2 (framing region) and 700nm of Ag top contact.

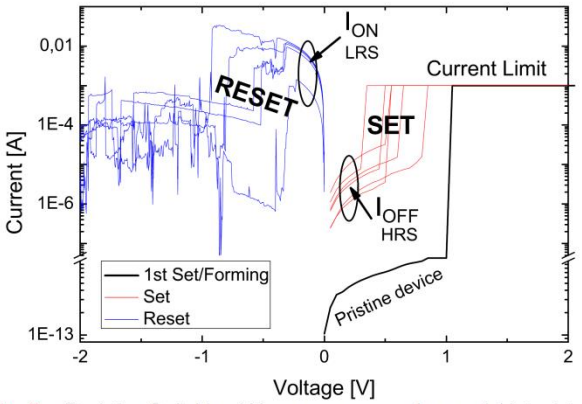

Fig. 2. Resistive Switching I-V curves measured on an inkjet printed ReRAM device. The current was limited at 1mA to avoid detrimental effects in the dielectric during Set process. In this case, measurement was stopped after 128 RS cycles. Stable switching behavior is observed in these samples. Pristine-HfO_2 device Set process is presented in black for reference.

(red lines until Set) is characterized by low currents (I_{OFF}), whereas LRS (blue lines until Reset) by large currents (I_{ON}).

Bipolar Resistive Switching (positive voltage bias for the Set and negative voltage bias for the Reset) is required to promote the memory switching. In order to verify the non-unipolar behaviour of the memory device, voltage bias larger than the value required for the Reset switching were applied (over |1V|). No trace of possible Set switching occurred at negative voltage bias up to −2V, confirming the bipolar switching behaviour of the Au/HfO_2/Ag where only positive voltage bias and negative voltage bias allow respectively Set and Reset switching. This phenomenology has been observed repeatedly in these samples.

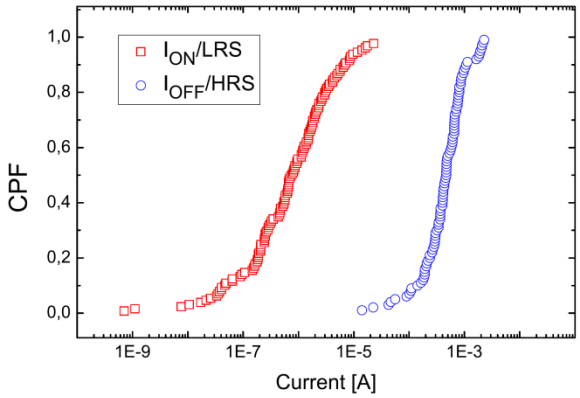

Fig. 3. Cumulative probability distributions of I_{ON} and I_{OFF} currents (blue circles and red squares respectively) measured at 50mV on the sample where the curves in Figure 2 were recorded (Au-based bottom electrode and 200nm HfO_2 thick). A three orders of magnitude I_{ON}/I_{OFF} ratio is achieved in most of cycles.

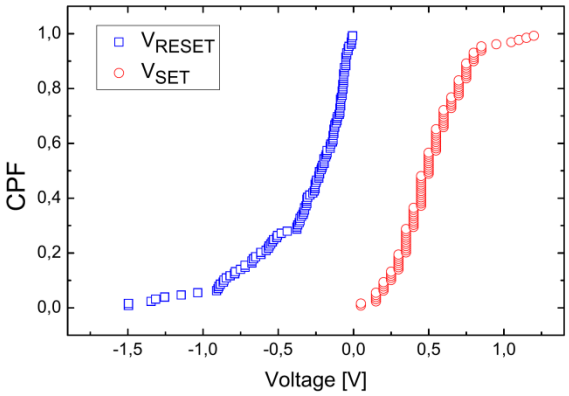

Fig. 4. Cumulative probability distributions of the Set and Reset voltages (red circles and blue squares respectively) obtained from the curves of the same sample (curves in Figure 2). Mean Set voltage is 0.5V while mean Reset voltages is 0.2V, approximately. Low dispersion is observed in both cases; however initial cycles introduce large tails in the Set and Reset voltage distributions, until 1V in the case of Set, and −1.5V in the case of Reset voltages.

In order to analyze in detail the I_{ON}/I_{OFF} currents and the Set/Reset voltages, the statistical distributions of these parameters have been analyzed. Figure 3 shows the cumulative probability distributions of the I_{ON} (blue circles) and I_{OFF} (red squares) currents measured at ±50mV on the same device during cycling. A large separation between both currents, around 3 orders of magnitude, is observed. One order of magnitude of dispersion is observed for I_{ON}, but larger dispersion is obtained for I_{OFF}, reaching three orders of magnitude. This result is similar to the dispersion observed in conventional Silicon-based Resistive RAMs due to the statistical nature of the reset process when the filament is closed [28]. Besides, the high current values measured after Set suggest that conduction during LRS is controlled by a conductive filament created inside the HfO_2 layer [29]. On the other hand, I_{OFF} currents are larger than the one through of the pristine-HfO_2 device (black line in figure 2), which suggests that the conductive filament is not completely closed. This observation seems to indicate that some damage remains in the dielectric layer during HRS, allowing the controlled Resistive Switching phenomenon. Since the analysis of this contribution is not in the scope of the present study, its consequences on the electrical transport will be evaluated in a future work.

Set and reset voltages distributions, obtained after successive RS cycles in the same sample, are represented in Figure 4 (red circles and blue squares respectively). As can be observed, both distributions present large dispersion, in a |1V| to 0V range, especially the Reset voltages distribution that goes beyond −1V. For the Set voltage distribution (red circles) it is possible to observe the values corresponding to the initial cycles in the upper tail. The mean value for the Set voltage distributions is around 0.5V, while for the Reset voltage distribution it is around −0.25V. The low switching voltage values obtained along with the thick dielectric layer suggest that filament formation and destruction occur more easily in these samples than in other technologies such as CMOS. Then, it highlights the perspective/chance for low power applications. However, at the same time, it could be a trouble in memory applications because it forces to build up the reading window within a |0.1V| voltage range under, to avoid non desirable programming events during reading operations.

Low voltage switching behaviour could be explained by the porosity conformation due to the oxide nanoparticles-based ink demonstrated by SEM cross-sectional images (Fig. 1). Although the porosity could be a tough trouble for thin film (few nanometres thick), the thickness resolution of inkjet printing technology is around ∼100nm due to the minimum drop volume (1 pL) that could be ejected-printed. Therefore, for devices with unconventional thickness of 200nm as our HfO_2-based memory devices, the porosity structure of the printed layer promotes and enables the inkjet printed memory devices working at very low voltage bias maintaining a stable and reliable resistive switching.

The proper selection of the printing parameters, related to the rheology of the ink formulation, and annealing temperature process, based on thermogravimetric analysis (TGA) and differential scanning calorimetry (DSC) results, ensure the reliability and reproducibility of uniform and crystalline high-k thin film HfO_2 based on nanoparticles.

IV. Conclusion

This article demonstrates that it is possible to implement ReRAM devices by inkjet printing technique, achieving high-performance features such as high ON/OFF ratio or low operating voltages, and using a low-cost technology at the same time. A forming process is required for fresh devices to create the filament for the first time. The observed Resistive Switching phenomenology is only possible by applying positive Sets and negative Resets meaning that it is a Bipolar Switching. Moreover, despite the similar absolute values of Set/Reset voltages, no Set events are observed at negative bias below −2V, avoiding the possibility of a new Set during the Reset ramp for the applied voltages. Larger currents during HRS (when compared to the pristine one) seem to indicate that conduction is also controlled by the conductive filament created during Set, which is partially closed during Reset. The I_{ON}/I_{OFF} ratio is around three orders of magnitude in most of cycles, which is similar to the features achieved by conventional technologies such as CMOS devices.

REFERENCES

[1] J. Jiang, B. Bao, M. Li, J. Sun, C. Zhang, Y. Li, F. Li, X. Yao, and Y. Song, "Fabrication of transparent multilayer circuits by inkjet printing," *Adv. Mater.*, vol. 28, no. 7, pp. 1420–1426, Feb. 2016.

[2] S.-C. Chang, J. Liu, J. Bharathan, Y. Yang, J. Onohara, and J. Kido, "Multicolor organic light-emitting diodes processed by hybrid inkjet printing," *Adv. Mater.*, vol. 11, no. 9, pp. 734–737, 1999.

[3] C. Rutherglen, D. Jain, and P. Burke, "Nanotube electronics for radiofrequency applications," *Nature Nanotechnol.*, vol. 4, no. 12, pp. 811–819, Dec. 2009.

[4] M. Kaltenbrunner, M. S. White, E. D. Głowacki, T. Sekitani, T. Someya, N. S. Sariciftci, and S. Bauer, "Ultrathin and lightweight organic solar cells with high flexibility," *Nature Commun.*, vol. 3, Apr. 2012, Art. no. 770.

[5] K. Takei, T. Takahashi, J. C. Ho, H. Ko, A. G. Gillies, P. W. Leu, R. S. Fearing, and A. Javey, "Nanowire active-matrix circuitry for low-voltage macroscale artificial skin," *Nature Mater.*, vol. 9, no. 10, pp. 821–826, 2010.

[6] E. M. C. Fortunato, P. M. C. Barquinha, A. C. M. B. G. Pimentel, A. M. F. Gonçalves, A. J. S. Marques, L. M. N. Pereira, and R. F. P. Martins, "Fully transparent ZnO thin-film transistor produced at room temperature," *Adv. Mater.*, vol. 17, no. 5, pp. 590–594, 2005.

[7] D. B. Strukov, G. S. Snider, D. R. Stewart, and R. S. Williams, "The missing memristor found," *Nature*, vol. 453, no. 7191, pp. 80–83, 2008.

[8] R. Waser, R. Dittmann, G. Staikov, and K. Szot, "Redox-based resistive switching memories—Nanoionic mechanisms, prospects, and challenges," *Adv. Mater.*, vol. 21, nos. 25–26, pp. 2632–2663, Jul. 2009.

[9] Y. C. Yang, F. Pan, Q. Liu, M. Liu, and F. Zeng, "Fully room-temperature-fabricated nonvolatile resistive memory for ultrafast and high-density memory application," *Nano Lett.*, vol. 9, no. 4, pp. 1636–1643, Feb. 2009.

[10] H. Y. Lee, P. S. Chen, T. Y. Wu, Y. S. Chen, C. C. Wang, P. J. Tzeng, C. H. Lin, F. Chen, C. H. Lien, and M.-J. Tsai, "Low power and high speed bipolar switching with a thin reactive ti buffer layer in robust HfO_2 based RRAM," in *IEDM Tech. Dig.*, 2008, pp. 3–6.

[11] J. Song, Y. Zhang, C. Xu, W. Wu, and Z. L. Wang, "Polar charges induced electric hysteresis of ZnO nano/microwire for fast data storage," *Nano Lett.*, vol. 11, no. 7, pp. 2829–2834, 2011.

[12] S. H. Jo, K.-H. Kim, and W. Lu, "High-density crossbar arrays based on a Si memristive system," *Nano Lett.*, vol. 9, no. 2, pp. 870–874, Jan. 2009.

[13] A. Redaelli, A. Pirovano, F. Pellizzer, A. L. Lacaita, D. Ielmini, and R. Bez, "Electronic switching effect and phase-change transition in chalcogenide materials," *IEEE Electron Device Lett.*, vol. 25, no. 10, pp. 684–686, Oct. 2004.

[14] A. D. Liao, P. T. Araujo, R. Xu, and M. S. Dresselhaus, "Carbon nanotube network-silicon oxide non-volatile switches," *Nature Commun.*, vol. 5, Dec. 2014, Art. no. 5673.

[15] K. Szot, W. Speier, G. Bihlmayer, and R. Waser, "Switching the electrical resistance of individual dislocations in single-crystalline $SrTiO_3$," *Nature Mater.*, vol. 5, no. 4, pp. 312–320, 2006.

[16] N. Gergel-Hackett *et al.*, "A flexible solution-processed memristor," *IEEE Electron Device Lett.*, vol. 30, no. 7, pp. 706–708, Jul. 2009.

[17] H. Y. Jeong, J. Y. Lee, and S.-Y. Choi, "Interface-engineered amorphous TiO_2-based resistive memory devices," *Adv. Funct. Mater.*, vol. 20, no. 22, pp. 3912–3917, 2010.

[18] J. Zhang, H. Yang, Q.-L. Zhang, S. Dong, and J. K. Luo, "Bipolar resistive switching characteristics of low temperature grown ZnO thin films by plasma-enhanced atomic layer deposition," *Appl. Phys. Lett.*, vol. 102, no. 1, p. 012113, 2013.

[19] R. C. Fang, L. H. Wang, W. Yang, Q. Q. Sun, P. Zhou, P. F. Wang, S. J. Ding, and D. W. Zhang, "Resistive switching of HfO_2 based flexible memories fabricated by low temperature atomic layer deposition," *J. Vac. Sci. Technol. B, Microelectron. Process. Phenom.*, vol. 30, no. 2, p. 020602, 2012.

[20] B. J. Choi, D. S. Jeong, S. K. Kim, C. Rohde, S. Choi, J. H. Oh, H. J. Kim, C. S. Hwang, K. Szot, R. Waser, B. Reichenberg, and S. Tiedke, "Resistive switching mechanism of TiO_2 thin films grown by atomic-layer deposition," *J. Appl. Phys.*, vol. 98, no. 3, p. 033715, 2005.

[21] J. J. Yang, F. Miao, M. D. Pickett, D. A. A. Ohlberg, D. R. Stewart, C. N. Lau, and R. S. Williams, "The mechanism of electroforming of metal oxide memristive switches," *Nanotechnology*, vol. 20, no. 21, p. 215201, 2009.

[22] K. Miller, K. S. Nalwa, A. Bergerud, N. M. Neihart, and S. Chaudhary, "Memristive behavior in thin anodic Titania," *IEEE Electron Device Lett.*, vol. 31, no. 7, pp. 737–739, Jul. 2010.

[23] D.-H. Lien, Z.-K. Kao, T.-H. Huang, Y.-C. Liao, S.-C. Lee, and J.-H. He, "All-printed paper memory," *ACS Nano*, vol. 8, no. 8, pp. 7613–7619, Aug. 2014.

[24] S. Zou and C. Michael, "Flexible non-volatile $Cu/Cu_xO/Ag$ ReRAM memory devices fabricated using ink-jet printing technology," in *Proc. IEEE 64th Electron. Compon. Technol. Conf. (ECTC)*, May 2014, pp. 441–446.

[25] M. Singh, H. M. Haverinen, P. Dhagat, and G. E. Jabbour, "Inkjet printing—Process and its applications," *Adv. Mater.*, vol. 22, no. 6, pp. 673–685, Feb. 2010.

[26] S. Magdassi and S. Magdassi, "Ink jet printing—Post office project," *Pigment Resin Technol.*, vol. 16, no. 5, pp. 4–10, May 1987.

[27] G. Vescio, J. López-Vidrier, R. Leghrib, A. Cornet, and A. Cirera, "Flexible inkjet printed high-k HfO_2-based MIM capacitors," *J. Mater. Chem. C*, vol. 4, no. 9, pp. 1804–1812, 2016.

[28] A. Crespo-Yepes, J. Martin-Martinez, I. Rama, M. Maestro, R. Rodriguez, M. Nafria, X. Aymerich, M. B. Gonzalez, and F. Campabadal, "Intra-device statistical parameters in variability-aware modelling of resistive switching devices," in *Proc. Joint Int. EUROSOI Workshop Int. Conf. Ultimate Integr. Silicon (EUROSOI-ULIS)*, Jan. 2016, pp. 84–87.

[29] M. Maestro, A. Crespo-Yepes, J. Martin-Martinez, S. Claramunt, R. Rodriguez, M. Nafria, and X. Aymerich, "Distinguishing conductive filament and non-localized gate conduction in resistive switching devices," in *Proc. 10th Spanish Conf. Electron Devices (CDE)*, 2015, pp. 1–4.

4.6.3. Inkjet-Printed HfO_2-Based Memristor Pt / HfO_2 / Ag

In ***Paper VI****: Low-Power High-Performance Low-Cost Non-Volatile Inkjet Printed HfO_2-based ReRAM: from nanoscale to device characterization*, the following issues were addressed in detail:

(1) The manufacturing of a memristor component with simple MIM structure, Pt/HfO_2/Ag, on SiO2/Si substrates are investigated and compared to the Au/HfO_2/Ag structures in order to study the bottom electrode interaction with the HfO_2 dielectric layer and the resulting effects on the resistive switching phenomena.

(2) The observation of a bipolar resistive switching phenomenon obtained by applying positive SET (forming process) and negative RESET voltages. The current-voltage measurements showed that the Pt bottom electrode enhances the memory window and increases the endurance of SET and RESET operations, ~10^3 cycles. In addition, the devices showed low SET and RESET voltages and relatively low switching current (~1 μA), which are comparable to the characteristics of current commercial CMOS memories.

(3) The demonstration of high-performance features such as I_{ON}/I_{OFF} ratio of more than six orders of magnitude and low switching operating voltages around 0.2V, thus allowing for a consumption reduction.

The previously mentioned results are explained in terms of the forming process into the inkjet-printed thin-film dielectric layer, which creates a switchable conductive filament. Physical characterizations are carried out to understand the resistive switching mechanisms by high-resolution transmission electron microscopy (HR-TEM) and focused ion beam (FIB)-assisted field-emission scanning electron microscopy (FE-SEM). The analyses of the cross-sectional images showed asymmetric oxygen accumulation in the oxide layer under ramped electrical bias. EELS inspections proved in both structures the absence of possible silver electromigration effect, resulting that the resistive switching mechanism is due to the formation of a vacancy oxygen conductive filament into the HfO_2 layer.

** Note that sections, equations and references numbering in the reproduced research article follow the ones of the published version. This statement applies to all Papers presented in this Thesis Dissertation.*

The article has been SUBMITTED to Advanced Materials; G. Vescio*, G. Martín, A. Crespo-Yepes, S. Claramunt, D. Alonso, J. López-Vidrier, S. Estradé, M. Porti, R. Rodriguez, F. Peiró A. Cornet, A. Cirera, M. Nafría. **—** *Low-Power High-Performance Low-Cost Non-Volatile Inkjet Printed HfO_2-based ReRAM: from nanoscale to device characterization.*

Low-Power High-Performance Low-Cost Non-Volatile Inkjet Printed HfO2-based ReRAM: from nanoscale to device characterization.

G. Vescio, G. Martín, A. Crespo-Yepes, S. Claramunt, D. Alonso, J. López-Vidrier, S. Estradé, M. Porti, R. Rodriguez, F. Peiró A. Cornet, A. Cirera, M. Nafría.*

MIND-IN2UB, Engineering Department: Electronics, Universitat de Barcelona, 08028, Spain.

Electronic Engineering Department, Universitat Autònoma de Barcelona, 08193, Spain.

E-mail: ((gvescio@el.ub.edu))

Keywords: (Inkjet Printed ReRAM, high-k HfO_2, cost-efficient technology, high-performance Resistive Switching, TEM)

Abstract:

Low-power high-performance metal-insulator-metal (MIM) non-volatile resistive memories based on high-k dielectric HfO_2 are fabricated using drop-on-demand inkjet printing technique as low-cost and eco-friendly method. The characteristics of resistive switching of Pt/HfO_2/Ag stacks on SiO2/Si substrates are investigated and compared to the Au/HfO_2/Ag structures in order to study the bottom electrode interaction with the HfO_2 dielectric layer and the resulting effects on the resistive switching phenomena. The current-voltage measurements showed that the Pt bottom electrode enhances the memory window and increases the endurance of SET and RESET operations, ~10^3 cycles. In addition, the devices showed low SET and RESET voltages and relatively low switching current (~1 μA), which are comparable to the characteristics of current commercial CMOS memories. Physical characterizations are carried out to understand the resistive switching mechanisms by high-resolution transmission electron microscopy (HR-TEM) and focused ion beam (FIB)-assisted field-emission scanning electron microscopy (FE-SEM). The analyses of the cross-sectional images showed asymmetric oxygen accumulation in the oxide layer under ramped electrical bias. EELS inspections proved in both structures the absence of possible silver electromigration effect, resulting that the resistive switching mechanism is due to the formation of a vacancy oxygen conductive filament into the HfO_{2-x} layer.

Introduction:

The increasing demand for flexible, wearable and transparent devices has been stimulated by the irruption of the Internet-of-Things (*IoT*), where electronic applications are, at anytime and everywhere, responsive to and communicating with the total environment by means of a wireless network. Considering the horizon of *IoT*, and the existing requirement for pervasive computing and sensing, the manufacturing of electronic objects that ensure low-power consumption and low-cost fabrication, assuring flexibility and/or wearability, can be achieved only by printing technologies. During the last decade, printed electronics holds the promise of enabling low-cost, scalable solutions by exploiting the ability of innovative fabrication technologies that are both cost-competitive and eco-friendly, using disrupting materials to be employed as processed inks onto a large-area flexible substrate. The strong development of rising technologies, like inkjet printing, is providing new opportunities to fabricate electronic devices and circuits cheaply, despite of the devices performance that are below the CMOS parameters. However, research has been focused on an emerging two-terminal non-volatile memory with 3D multilevel capability that increases the performance speed and provides higher density of data and lower power consumption, while maintaining its reliability. Several materials demonstrated resistive switching behaviour, such as organic insulators (like polymers)[1] and graphene oxide,[2] amorphous silicon,[3] chalcogenides (selenides and tellurides),[4] carbon nanotubes,[5] perovskite oxides,[6] and binary transition metal oxides[7]. This suggests a wide range of material selection as building blocks of devices for memory applications. The ReRAM devices were proved to overcome the general performance requirements and also showed high compatibility to the CMOS manufacturing technology.[8] Common critical parameter specifications are: switching write and read speeds, resistance ratio, low power consumption, endurance and data retention time.[9] Taking into account the guideline requirements,[10] ReRAMs based on metal-oxide exhibited fast read/write speeds, exceptional endurance, and very low power/energy consumption, all consistent with CMOS technology. Among the metal oxides, HfO_2 has been deeply studied and proved as a suitable material for ReRAM devices.[11–14]

In this article, an inkjet-printed HfO_2-based ReRAM, that exhibits very high-performance and very low-power consumption in addition to flexible and cost-efficient fabrication properties, is presented and characterized from nanoscale to device level. The switching mechanism and the effect of the electrode material and its implications on the device features are analysed in detail. These promising characteristics make these ReRAM devices a good candidate for portable and flexible systems, where large integration density is not strictly required i.e. low-density non-volatile memories or reconfigurable circuits.

Resultsand and Discussion:

Metal-insulator-metal (MIM) structures using Ag ink for the top electrodes and HfO_2 ink as dielectric layer have been inkjet-printed onto Pt bottom electrode, Pt/HfO_2/Ag. **Figure 1a** sketches the MIM structure and **Figure 1b** shows a cross-sectional images of the device used to assess the performance of the ReRAM based on inkjet-printed HfO_2 dielectric material. The procedure implemented to carry out the experiments consists on apply positive voltage ramps to provoke the Set and negative ramps to induce the Reset that will open (LRS) and closed (HRS) the conductive filament, respectively. During the Set process a current limitation is forced to avoid detrimental effects that make permanent dielectric breakdown during Set. The experimental sequence of consecutive Set and Reset processes has been applied in several samples with different HfO2 layer thickness (200nm and 300nm) to study the effect of the dielectric thickness on the switchable filament, and consequently in the device performance. Current limitation is also changed in order to study de Set process and the conductive filament formation.

Figure 1c shows two consecutive cycles of the typical Bipolar Resistive Switching I-V curves obtained in these samples where the current compliance is fixed at 1uA. Blue lines correspond to Set process applied as double sweep ramp. After reaching the current limit the current remains constant due the compliance of the current limitation. When the negative voltage ramp to provoke the Reset is applied a large current corresponding to the ON state (LRS) is registered (1mA at -0.05V approximately) in spite of the low current limitation applied during Set. When the Reset occurs at -0.1V a large current drop of 9 orders of magnitude is observed indicating that the sample has switched to the OFF state (HRS). After back to the OFF state, ramp is stopped at -0.2V to avoid new Set evens at negative bias and without current limit. The very low and stable currents registered indicates that the OFF state is similar than the fresh device being not possible to distinguish electrically between them, while the ON current is on the typical RS values [refs]. Besides, in contradistinction to CMOS based-ReRAMs, in these samples ultra-low programming voltages are observed (~100mV in absolute value). This phenomenology is widely and stably observed in these samples.

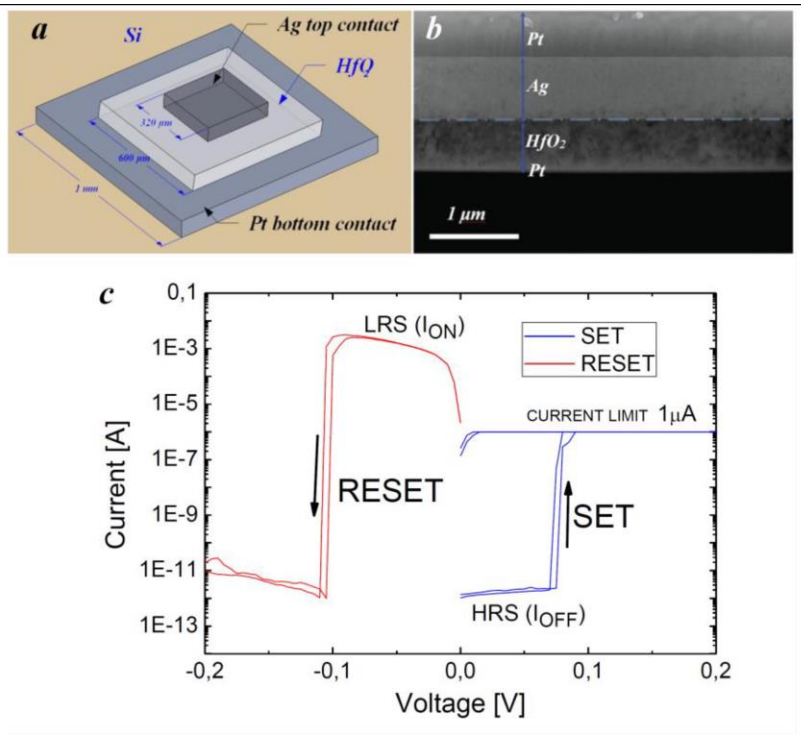

***Figure 1**: (**a**) 3D image of the MIM structure based-ReRAM fabricated. (**b**) Cross-section image obtained by FIB-assisted FE-SEM technique. The structure is compost by a Pt layer bottom electrode thickness of 50nm over a silicon substrate, 400nm of high-k based-HfO2 layer and a 700nm top electrode layer of Ag. An extra Pt layer is deposited above the structure because the FIB technique. (**c**) Representative Bipolar Resistive Switching I-V curves of two consecutive cycles measured on a inkjet printed ReRAM capacitor. The current limitation is established at 1uA to ensure limiting the damage inside the dielectric. Blue and red lines correpond to the Set and Reset processes respectively. In this example, measurement is stopped after 128 RS cycles.*

In order to study the ON/OFF current ratio and the Set/Reset voltages, distributions of the I_{ON}-I_{OFF} and the V_{SET}-V_{RESET} parameters are analysed in detail. **Figure 2a** shows the cumulative probability distribution of the ON (black solid squares) and OFF (red solid circles) currents measured at 0.01V (absolute value) during 128 cycles in a sample with 200nm HfO2 layer. As can be observed, both ON and OFF distributions are extremely stable being the relative dispersion lower than one order of magnitude, even for the OFF state. Moreover, ON current distribution presents higher relative dispersion than the OFF state, in opposition of the typical RS current distributions [refs] where HRS variability is larger than for the LRS. This slope changing for the ON distribution also seems to indicate that two breakdown (Set) modes are coexisting in the dielectric, Hard and Soft. Hard BD contributes to the high stability for current values upper than 100uA, whereas the Soft BD mode produces a slope reduction in the distribution for lower current values.

In order to analyse the dielectric thickness effect on the observed RS, the measured current obtained after 128 cycles in another sample with 300nm of HfO2 layer is also plotted in **Figure 2a**. As observed before, both ON (empty black squares) and OFF (empty red circles) states present very stable values and the OFF state is closely similar for both samples. However, the mean value of the ON state distribution is one order of magnitude higher for sample of 300nm dielectric layer than for sample of 200nm. Additionally, no significant tail is observed provoking a straight distribution with even more stable values than the previous sample, suggesting that the Hard mode is driving the LRS. This significant change on the mean value of the distribution indicates that the conductive filament created in the dielectric becomes more relevant the higher the thickness.

Figure 2b shows the Set (black squares) and Reset (red circles) voltage distributions obtained from the previous samples. As can be observed in the figure, in both cases the programming voltages are ranged from 0 to 0.2Volts in absolute values leading to low power switching in comparison to other ReRAM technologies [refs..]. For Set voltage distribution, both samples take values from 0.05 to 0.2 Volts without regarding the tails closed to 0V. However, for the sample of 200nm Reset voltage distributions presents larger dispersion ultra-low values closed to -0.01Volts while the sample of 300nm presents more stable values around -0.1Volts.

In order to study the effect of the current limitation, after 50 cycles the current compliance of the equipment is increased from 1uA to 1mA. During the first 50 cycles current jump is stopped because current limit (black squares in **Figure 2c**). However, when the compliance is increased at 1mA during the Set process and the sample is switched from the OFF to the ON state current across the filament doesn't reach the current limitation (black lines). Surprisingly, after the Set without current limit a new Reset process is observed (red lines) being possible apply new iterations of the sequence without the current compliance of the equipment, 85 cycles in this measurement. This observation suggests that once the conductive filament is formed during the first cycles with current limitation, it is no longer necessary to observe the switchable behaviour of the sample. Moreover, both ON and OFF states take similar values being extremely similar for the OFF state where curves overlap each other.

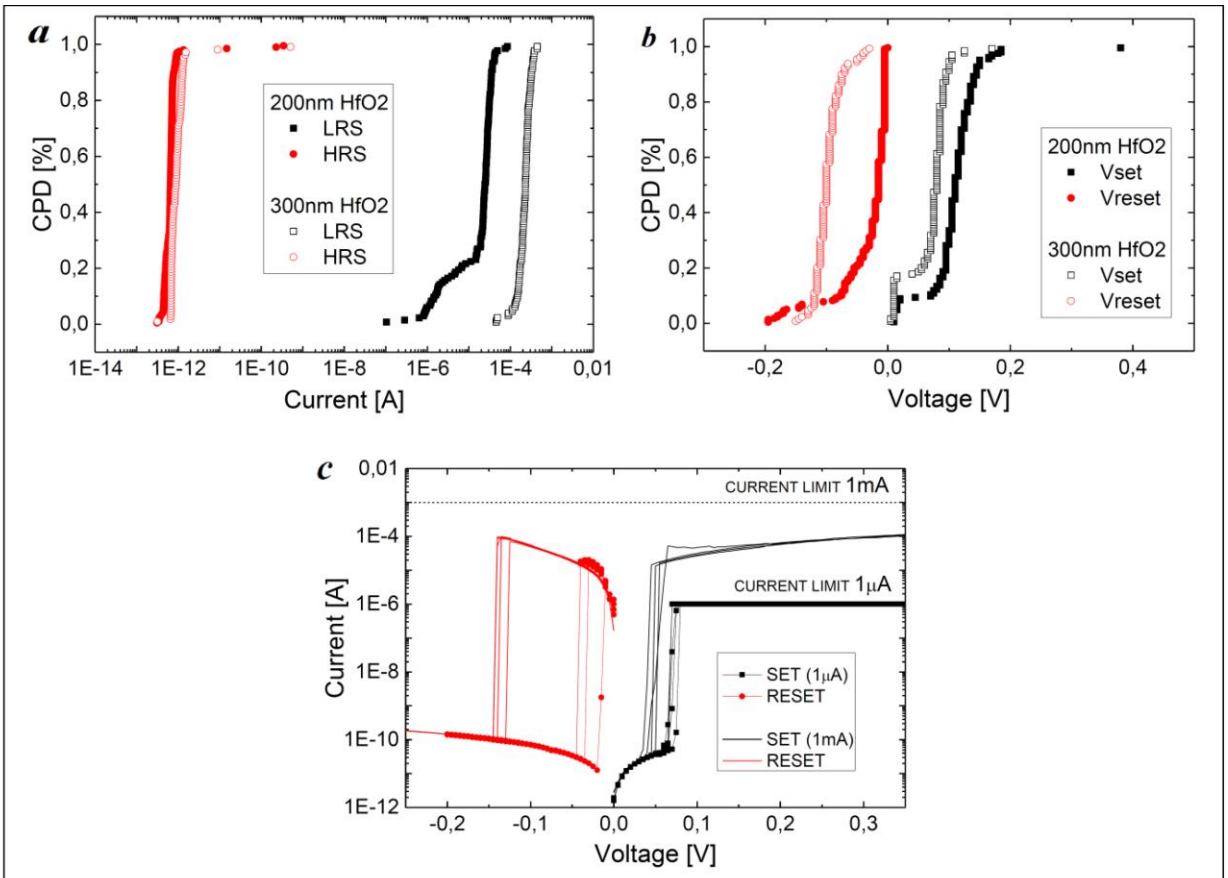

Figure 2: ***(a)*** *LRS (black square symbols) and HRS (red circle symbols) current distributions for a samples with 200nm (empty symbols) and 300nm (solid symbols) of HfO2 dielectric layer. The OFF (HRS) and the ON (LRS) states present high stability in both cases. However, while the OFF current distributions take similar values for both samples, the ON current distribution of the thicker sample is one order of magnitude lower than the thinner sample, suggesting a thickness dependence on the LRS state.* ***(b)*** *Set (black squares) and Reset (red circles) voltage distributions for the samples of figure 3, one with 200nm (solid symbols) and the other with 300nm (empty symbols) of HfO2. In both cases, programming voltage distributions are ranged below 0.2Volts in absolute value.* ***(c)*** *I-V curves of the Resistive Switching observed in a sample of 100nm HfO2 where the current limitation is increased from 1uA to 1mA after 50 cycles, and 85 cycles are applied next. 4 consecutive cycles of the last 85 cycles (lines) are plotted together with other 4 consecutive cycles of the previous 50 cycles (solid symbols).*

Detection y characterization of CF is a challenging task due to the nanoscale size of the filaments and their randomicity. A possible approach to visualize and analyse the ReRAM devices is by TEM that permit to go insight the structures to obtain a comprehensive characterization of local areas. High resolution TEM images allow detecting possible CF images, and energy dispersive X-ray (EDX) spectroscopy and electron energy-loss spectroscopy (EELS) inspections can be further employed to validate the composition of the structure area under characterization, which permit to analyse the switching mechanism and the effect of the electrode material and its implications on the device features (**Figure 3**).

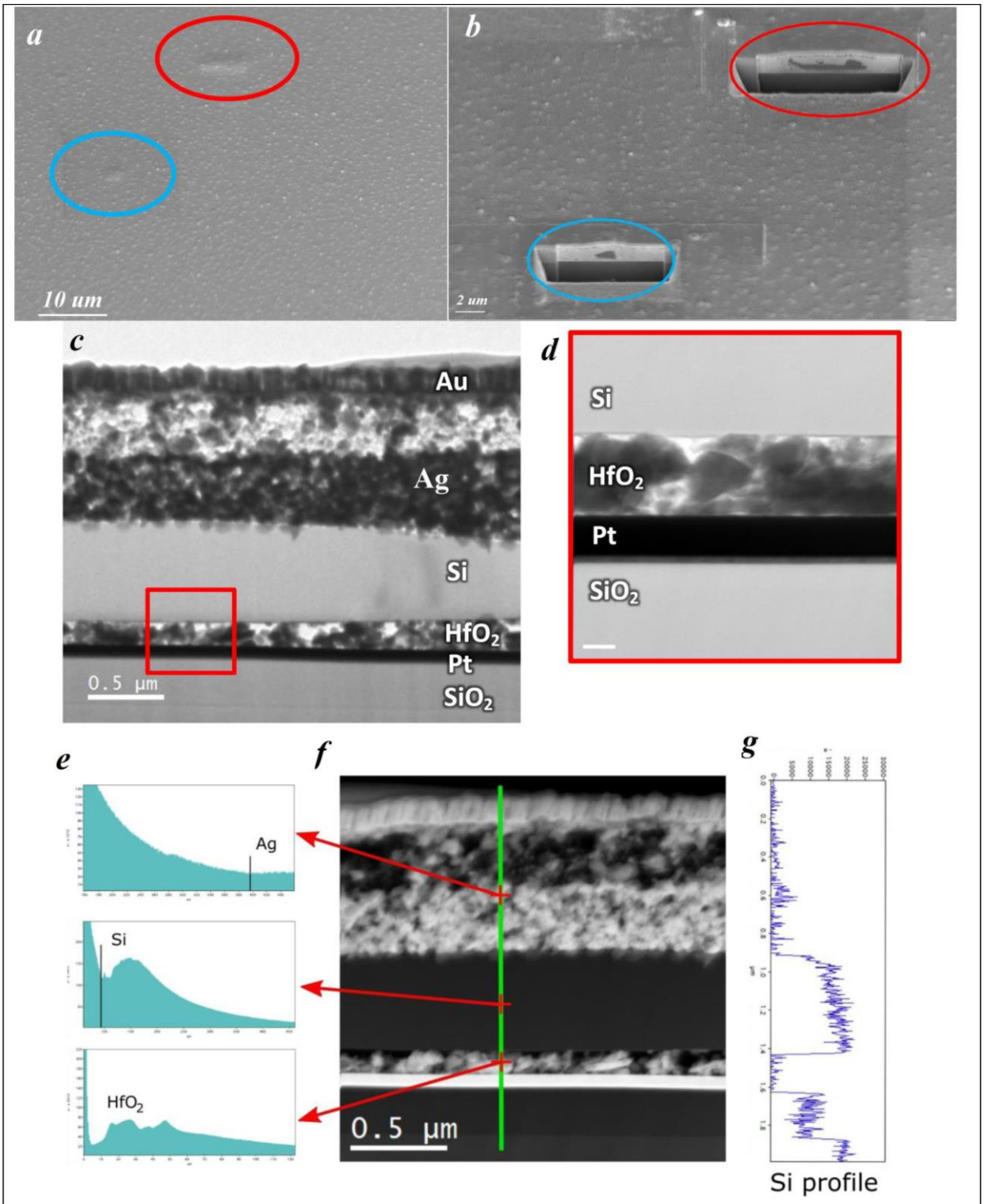

Figure 3: ***(a)*** *Top view image before the FIB cross section;* ***(b)*** *cross-sectional image of the insight view of the detected bubbles.* ***(c,d)*** *TEM images of the biased sample with Pt bottom electrode.* ***(e,f, g)*** *STEM image of the biased sample with Pt electrode (f) together with the EELS data acquired along the highlighted line. (e): single spectra from the Ag layer, the Si precipitate and the HfO2 layer, as indicated with red arrows. (g): Si intensity profile along the highlighted line.*

Figure 3a and Figure 3b show a top view and cross-sectional images using FE-SEM, and the same device was analysed by dark field STEM (Figure 3c, 3f). The images of a device demonstrated clear bubble-like features randomly disposed with diameters of 1 um due to the formation of a void between the HfO2 and Ag top electrode layers. The formation of precipitates of Si, that cause the bubbles, due to a migration from the substrate far away from a tip scratch (contact for the electrical measurements) is observed (Figure 3e). The dependences of switching voltages, resistances as well as device yield on electrode imply the importance of electrode plays in the RS behaviours, and may provide guidelines for devices electrode material selection. For the device with Au electrode appears to be less stable and can be ascribed to the much large ionic radius of Au atom as well as gold's chemical inertness which makes it hard to diffuse into the film. Therefore, appropriate design on bottom electrode (or cathode) structure can also be used to improve the RS behaviours. In this case, the Pt bottom electrode allows the diffusion of Si from the substrate that permit to the ReRAM device to reach a high-stability.

Experimental

A Fujifilm Dimatix DMP 2831 inkjet printer was employed, equipped with cartridges with droplet volume of 1 pL (for conductive ink) and of 10 pL (for 2d materials). Two types of inks were used for inkjet print the final MIM structure: a conductive Ag-nanoparticles (NPs)-based ink and HfO2 NP ink as high-k dielectric from Torrecid S.A were used, respectively. Contact leads were printed using Ag NPs-based ink from Advanced Nano Product (DGP-HR, 30% w/w). The HfO2 NPs ink formulation is explained elsewhere.[15]

ReRAM MIM structure: Firstly, a Pt thin film (50nm) bottom electrode was deposited by sputtering on Ti layer (15 nm). Then, using a Dimatix printer (2831, Fujifilm, Japan), a HfO2 nanoparticles-based ink (Torrecid S.L.) is printed selectively over the bottom electrode covering an area of 0.1 mm^2 keeping the substrate temperature constant at 30 ºC. A post-deposition annealing process of 3 hours at 240ºC in a vacuum oven is needed for the elimination of solvents, further details about inkjet printing of HfO2 where published elsewhere.[15] Finally, a silver top electrode with a thickness of 300 nm was printed

Thin films were deposited by inkjet printing on Si/SiO_2 substrate in order to fabricate ReRAM devices. FE-SEM and TEM cross-section of the fully-printed devices were cut with focus ion-beam (FIB,FIB CrossBeam 1560XB, Zeiss). After FIB cross-section cut, the samples were analysed by high-resolution field-emission variable-pressure (VP) scanning electron microscope (SEM) Zeiss 1555 VP-FESEM. X–ray microanalyses have been performed using an Oxford Instruments X-Max 80 silicon drift EDS system with AZtec and INCA software. TEM images and EELS spectra of the devices cross-sections were obtained in a JEOL J2010F microscope, coupled to a Gatan GIF spectrometer.

Electrical measurements: The current versus DC voltage characteristics were measured by a B1500-A Semiconductor Device Analyzer (Agilent). For the acquisition of transport data, the devices characterisation was carried out at room temperature (~24 °C) using a four-probes configuration.

Bibliography:

1. Erokhin, V. Organic memristors: Basic principles. *ISCAS 2010 - 2010 IEEE Int. Symp. Circuits Syst. Nano-Bio Circuit Fabr. Syst.* 5–8 (2010). doi:10.1109/ISCAS.2010.5537145

2. Porro, S. & Ricciardi, C. Memristive behaviour in inkjet printed graphene oxide thin layers. *RSC Adv.* **5,** 68565–68570 (2015).

3. Mehonic, a & Kenyon, a J. Defects at Oxide Surfaces. **58,** 401–428 (2015).

4. Redaelli, A. *et al.* Electronic switching effect and phase-change transition in chalcogenide materials. *IEEE Electron Device Lett.* **25,** 684–686 (2004).

5. Liao, A. D., Araujo, P. T., Xu, R. & Dresselhaus, M. S. Carbon nanotube network-silicon oxide non-volatile switches. *Nat. Commun.* **5,** 5673 (2014).

6. Jeong, D. S. *et al.* Emerging memories: resistive switching mechanisms and current status. *Reports Prog. Phys.* **75,** 76502 (2012).

7. Sawa, A. Resistive switching in transition metal oxides. *Mater. Today* **11,** 28–36 (2008).

8. Jo, S. H., Kim, K. H. & Lu, W. High-density crossbar arrays based on a Si memristive system. *Nano Lett.* **9,** 870–874 (2009).

9. Ye, C. *et al.* Physical Mechanism and Performance Factors of Metal Oxide Based Resistive Switching Memory: A Review. *J. Mater. Sci. Technol.* **32,** 1–11 (2016).

10. Itrs. International Technology Roadmap for Semiconductors 2.0: Executive Report. *Int. Technol. roadmap Semicond.* (2015). at <http://www.semiconductors.org/main/2015_international_technology_roadmap_for_semiconductors_itrs/>

11. Privitera, S. *et al.* Microscopy study of the conductive filament in HfO2 resistive switching memory devices. *Microelectron. Eng.* **109,** 75–78 (2013).

12. Puglisi, F. M., Qafa, A. & Pavan, P. Temperature impact on the reset operation in HfO2 RRAM. *IEEE Electron Device Lett.* **36,** 244–246 (2015).

13. Wang, Z. *et al.* Transport properties of HfO 2-x based resistive-switching memories. *Phys. Rev. B - Condens. Matter Mater. Phys.* **85,** 1–10 (2012).

14. Puglisi, F. M., Pavan, P., Larcher, L. & Padovani, A. Statistical analysis of random telegraph noise in HfO2-based RRAM devices in LRS. *Solid. State. Electron.* **113,** 132–137 (2015).

15. Vescio, G., López-Vidrier, J., Leghrib, R., Cornet, A. & Cirera, A. Flexible inkjet printed high-k HfO 2 - based MIM capacitors. *J. Mater. Chem. C* **4,** 1804–1812 (2016).

References:

1. Moore, G. E. Understanding Moore's Law: Four Decades of Innovation. *Underst. Moore's Law Four Decad. Innov.* (2006). doi:10.1086/529346
2. Association, S. I. 2015 ITRS Section 5: More Moore. 1–52 (2015).
3. Itrs. International Technology Roadmap for Semiconductors 2.0: Executive Report. *Int. Technol. roadmap Semicond.* (2015).
4. Antoniadis, D. a. *et al.* Continuous MOSFET performance increase with device scaling: The role of strain and channel material innovations. *IBM J. Res. Dev.* (2006). doi:10.1147/rd.504.0363
5. Wang, C. *et al.* Self-aligned, extremely high frequency III-V metal-oxide-semiconductor field-effect transistors on rigid and flexible substrates. *Nano Lett.* **12,** 4140–5 (2012).
6. Colombo, L., Chambers, J. J. & Niimi, H. Gate Dielectric Process Technology for the Sub-1 nm Equivalent Oxide Thickness (EOT) Era. *Interface* (2007).
7. Iwamatsu, M. The Clausius-Mossotti relation for insulators. *J. Phys. C Solid State Phys.* (1985). doi:10.1088/0022-3719/18/15/015
8. Robertson, J. Band structures and band offsets of high K dielectrics on Si. *Appl. Surf. Sci.* **190,** 2–10 (2002).
9. Wang, X., Shahidi, G., Oldiges, P. & Khare, M. Device scaling of high performance MOSFET with metal gate high-K at 32nm technology node and beyond. in *International Conference on Simulation of Semiconductor Processes and Devices, SISPAD* (2008). doi:10.1109/SISPAD.2008.4648299
10. Ritala, M. *High k Gate Dielectrics*. *High k Gate Dielectrics* (2003).
11. Robertson, J. & Wallace, R. M. High-K materials and metal gates for CMOS applications. *Mater. Sci. Eng. R* **88,** 1–41 (2015).
12. Tan, T. *et al.* Band structure and valence-band offset of HfO2 thin film on Si substrate from photoemission spectroscopy. *Appl. Phys. A* **97,** 475–479 (2009).
13. Ceresoli, D. & Vanderbilt, D. Structural and dielectric properties of amorphous ZrO2 and HfO2. *Physical Review B* **74,** 125108–6 (2006).
14. Molas, G. & de Salvo, B. New modules, materials and architectures for Flash Memory scaling. *2006 IEEE Int. Conf. IC Des. Technol.* (2006). doi:10.1109/ICICDT.2006.220836
15. She, M. Semiconductor Flash Memory Scaling. *Thesis* (2003).
16. Wakai, H. *et al.* Ultrahigh-density HfO2 nanodots for flash memory scaling. *Japanese J. Appl. Physics, Part 1 Regul. Pap. Short Notes Rev. Pap.* (2006). doi:10.1143/JJAP.45.2459
17. Hou, T. H., Lee, J., Shaw, J. T. & Kan, E. C. Flash memory scaling: From material selection to performance improvement. *Mater. Sci. Technol. Nonvolatile Memories* (2008).
18. Ielmini, D. Resistive switching memories based on metal oxides: mechanisms, reliability and scaling. *Semicond. Sci. Technol.* **31,** 063002– (2016).
19. Russo, U., Cagli, C., Spiga, S., Cianci, E. & Ielmini, D. Impact of electrode materials on resistive-

switching memory programming. *IEEE Electron Device Lett.* **30,** 817–819 (2009).

20. Erokhin, V. Organic memristors: Basic principles. *ISCAS 2010 - 2010 IEEE Int. Symp. Circuits Syst. Nano-Bio Circuit Fabr. Syst.* 5–8 (2010). doi:10.1109/ISCAS.2010.5537145
21. Porro, S. & Ricciardi, C. Memristive behaviour in inkjet printed graphene oxide thin layers. *RSC Adv.* **5,** 68565–68570 (2015).
22. Mehonic, a & Kenyon, a J. Defects at Oxide Surfaces. **58,** 401–428 (2015).
23. Redaelli, A. *et al.* Electronic switching effect and phase-change transition in chalcogenide materials. *IEEE Electron Device Lett.* **25,** 684–686 (2004).
24. Liao, A. D., Araujo, P. T., Xu, R. & Dresselhaus, M. S. Carbon nanotube network-silicon oxide non-volatile switches. *Nat. Commun.* **5,** 5673 (2014).
25. Jeong, D. S. *et al.* Emerging memories: resistive switching mechanisms and current status. *Reports Prog. Phys.* **75,** 76502 (2012).
26. Sawa, A. Resistive switching in transition metal oxides. *Mater. Today* **11,** 28–36 (2008).
27. Jo, S. H., Kim, K. H. & Lu, W. High-density crossbar arrays based on a Si memristive system. *Nano Lett.* **9,** 870–874 (2009).
28. Ye, C. *et al.* Physical Mechanism and Performance Factors of Metal Oxide Based Resistive Switching Memory: A Review. *J. Mater. Sci. Technol.* **32,** 1–11 (2016).
29. Privitera, S. *et al.* Microscopy study of the conductive filament in HfO2 resistive switching memory devices. *Microelectron. Eng.* **109,** 75–78 (2013).
30. Puglisi, F. M., Qafa, A. & Pavan, P. Temperature impact on the reset operation in HfO2 RRAM. *IEEE Electron Device Lett.* **36,** 244–246 (2015).
31. Wang, Z. *et al.* Transport properties of HfO 2-x based resistive-switching memories. *Phys. Rev. B - Condens. Matter Mater. Phys.* **85,** 1–10 (2012).
32. Puglisi, F. M., Pavan, P., Larcher, L. & Padovani, A. Statistical analysis of random telegraph noise in HfO2-based RRAM devices in LRS. *Solid. State. Electron.* **113,** 132–137 (2015).
33. Akinaga, H. & Shima, H. Resistive Random Access Memory (ReRAM) Based on Metal Oxides. *Proc. IEEE* **98,** 2237–2251 (2010).
34. Strukov, D. B., Snider, G. S., Stewart, D. R. & Williams, R. S. The missing memristor found. *Nature* **453,** 80–3 (2008).
35. Waser, R. & Aono, M. Nanoionics-based resistive switching memories. *Nat. Mater.* **6,** 833–40 (2007).
36. Waser, R., Dittmann, R., Staikov, G. & Szot, K. Redox-Based Resistive Switching Memories - Nanoionic Mechanisms, Prospects, and Challenges. *Adv. Mater.* **21,** 2632–2663 (2009).
37. Mehonic, a *et al.* Quantum Conductance in Silicon Oxide Resistive Memory Devices. *Sci. Rep.* (2013). doi:10.1038/srep02708

Chapter 5: Inkjet-printed Gr/h-BN heterostructure

5.1 h-BN Dielectric

High integration, low-cost production and low-power consumption are the key parameters which moved the electronics industry to architecture solutions such as device scaling and 3D vertical structures (fin field-effect transistor, FIN-FETs), plus the introduction of high-*k* dielectric such as HfO_2. Although these strategies obtained the expected performance for electronic systems up to the 10-nm node presented by Samsung in 2017 (which recently announced 8-nm and 6-nm nodes) in order to accomplish the Moore's law, the traditional aggressive approach of scaling device is reaching the reliability fundamental limit of existing materials.

For this reason, the ITRS[1] and OE-A[2] roadmaps, which delineate the electronics manufacturing industry guidelines for the next-generation of MOSFETs and related electronic devices for rigid (ITRS) and flexible (OE-A) devices, considered and predicted the use of new materials such as graphene[3–5] (Figure 5.1) and related materials (GRMs) [5,6,7], that is, hexagonal boron-nitride (h-BN) [5,6,7] and transition metal dichalcogenides (MoS_2, $MoSe_2$, Bi_2Se_3, $BiTe_3$). [5,6,7]

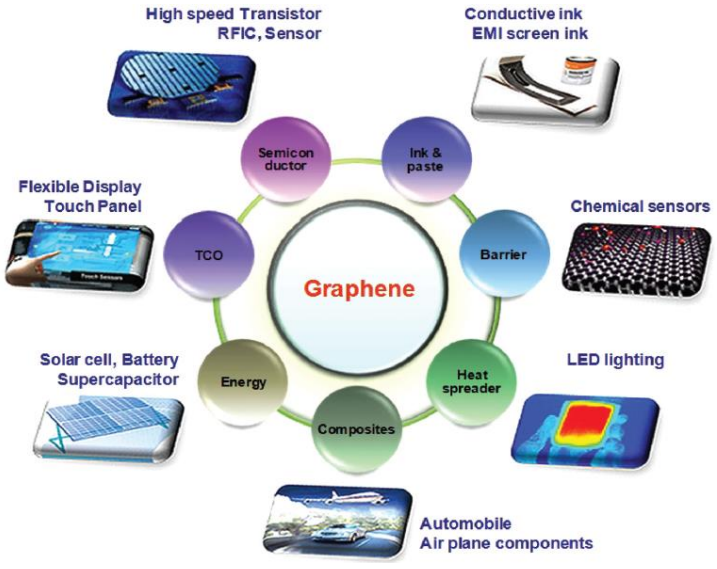

Fig. 5.1 *Overview of Applications of Graphene in different sectors ranging from conductive ink to chemical sensors, light emitting devices, composites, energy, touch panels and high frequency electronics.* [7]

Several studies demonstrated GRMs as the perfect replacement of silicon technology for the flexible electronics industry due to their excellent mechanical properties. In addition, the large amount of existing GRMs permits to adapt and tune the device properties in order to obtain the

highest charge transport mobility and the strongest flexible structure, ensuring at the same time low power consumption and higher working frequency.[8,9] Therefore, advances and development of new methods for large production of GRMs allow emerging the interest in outstanding flexible electronic devices. In recent years, printed electronics on flexible supports has quickly gained interest as a low-cost, high-area, light-weight and bendable plastic alternative to Si technology. [10] [11] [12] [13] [14]

To date, different printing technologies, such as gravure,[15] screen,[16] flexographic[17,18] and inkjet printing[19,20] have been employed to fabricate flexible organic light-emitting diode (OLED) displays,[21,22] radio-frequency identification (RFID) antennas[23], solar cells,[24,25,26] sensors[27] and thin-film transistors (TFTs).[28,29,30] Amongst the current printing technologies, drop-on-demand inkjet printing stands out as a cost-efficient technique, fast (up to 15 m/s), digital-pattern design (fast prototyping), and mask-less (non-contact process), which guarantees controlled selective deposition of few picoliters (1 pL each single drop) of novel nanomaterials-based inks for large-area manufacturing.

Concerning the inkjet technique, drawbacks such as limited resolution and relatively large minimum thickness of the deposited layer need to be solved to obtain electronic devices with performance and reliability comparable to those based on Si technology.[20,31,32] Therefore, some groups tried complex and expensive techniques such as self-alignment printing[33,34] or femtoliter drop jetting (EHD printing)[35] as advanced processes to overcome the current limitations of the inkjet printing technology. In this regard, selecting and employing outstanding materials to be printed such as GRMs, is imperative.

One of the most limiting factors for a material to be a candidate for inkjet printing is the maintenance of the physical and chemical properties of the ink when submitted to the thermal and mechanical stresses required by the printing process. To meet these requirements (i.e., preventing effects such as evaporation of the ink while inkjet-printing and damage to the printer head or undesired conglomerate), the ink–filler size must lie in the sub-micron scale (the ratio between the nanofiller size and the printer nozzle orifice should ideally be 1:50). [36\] In Chapter 4, very promising nanoparticles-based HfO_2 high-*k* oxide has been demonstrated that satisfies the requirements for fully-printed devices (capacitors and memristors), but the NPs dimension will limit, due to the dielectric vertical thickness, the scaling device and hence the possible final applications. In this regard, the possibility of printing GRMs such as graphene,[37–40] which is a one-atom-thick planar layer of carbon atoms that are self-assembled into a honeycomb-type 2D lattice,[5] has attracted substantial interest due to its outstanding properties. This opened the world to the ink formulation of other numerous 2D materials such as h-BN[41–45] and transition metal dichalcogenides such as MoS_2,

which exhibit, complementary to graphene, interesting properties and offer a wealth of applications in electronics, biosciences, etc. During the last decade, h-BN has become one of the most remarkable compounds to be employed as dielectric gate due to its physical properties, such as a relatively wide band gap of 5.8-6.0 eV[46,47,] that ensures a barrier for electrical conduction at room temperature, and its higher dielectric constant (k = 5 - 6)[46,48,49] compared to SiO_2 (k = 3.9). In addition, h-BN is also appreciated for its hardness, high melting point, chemical resistance, [50,51] resistance to impurity diffusion because of its high density (2.1 gcm^{-3}), and thermal stability up to ~400 $Wm^{-1}k^{-1}$. [52,53] In particular, hexagonal boron nitride (h-BN) is an attractive material due to its similar structural properties to graphite and its well-known allotrope, graphene. [47,48,49,54,55] However, the h-BN consists of hexagonal layers of covalently-bonded B–N rings on adjustment layers, whereas these layers are weakly held together by Van der Waals forces with an interlayer spacing of 3.3 Å. [50,51,52,54,55] The exceptional 2D crystal structures called boron nitride nanosheets (BNNSs) make h-BN an electronically insulating material, a particularly appealing material for future applications in various fields such as electronic, polymeric composite, and high-temperature stable device.[54,55,56] Indeed, h-BN is one of the most studied materials to be implemented as gate oxide for 2D graphene-based transistors devices due to their structures compatibility. For these reasons, h-BN ink is an attractive material for the future generation of 2D printed devices in the fields of transistors, composite fillers, solid lubricants, topological insulators, energy storage, thermal conductors, and ultraviolet-light emitters. [54,55,56]

At present, several methods have been proposed to prepare BNNSs, generally divided between growth and exfoliation methods. Chemical-vapour deposition (CVD) [48,49] is a very well-known growth method able to produce large and high-quality (low-defect, single atomic layer of BNNSs) sheets of BNNSs. Nevertheless, it requires high temperature and vacuum systems that enhance complexity, cost and difficulties when aiming at large-scale production. Various methods for the BNNSs dispersion have been reported, but the synthesis of BNNSs with specific structures and controlled properties still remains a significant challenge. The exfoliation of h-BN is more difficult compared to that of graphite because of the weak ionic bonding between BN layers and the fact that many scalable methods for graphene, such as the widely-used Hummer's and related graphene oxide methods, cannot be directly applied to h-BN.[44,57] Some techniques, comprising micromechanical cleavage, [5,58] ball milling, [42] wet-chemical exfoliation (liquid-phase exfoliation, LPE), [41,42,44,45] hydrodynamics, [59] and unzipping of BN nanotubes[55] were recently employed to produce BNNSs at small scales, always limited by the drawback of high-energy and time-consuming processes.[45]

Alongside all these methods, high-pressure microfluidation (microfluidic exfoliation) appears as a disrupting large-scale, efficient, high-yield, and high-throughput method that allows exfoliation from raw material to high-quality 2D BNNSs flakes using a high-pressure process, conducted via high-shear fluid processor.[45,60] Successful solvents for the dispersion of GRMs are those with surface tension of ~40 mJ m^{-2},[61] thus matching the surface energy of the 2D materials. Although water has a surface tension of ~72 mJ m^{-2},[62] exfoliation of flakes can be stabilized against reaggregation by Coulomb repulsion using linear-chain monomeric surfactants[63] [i.e., bile salts (SC)[64] or sodium-deoxycholate (SDC)[65]], or by steric repulsion employing polymeric stabilizers[66] in aqueous systems. In addition, the dispersion method, which utilizes greener solvents (water-based solutions), can enable cost-effective large-scale production processes that minimize or eliminate the need for properly disposing potentially-harmful chemicals. In particular, biopolymer-based h-BN nanocomposites, such as chitosan,[67] starch,[68] hydroxyl ethyl cellulose[69] and methyl cellulose,[69] showed, in addition to nontoxicity and biodegradability, high improvement on the thermal, mechanical, electrical, and biocompatibility properties. High-*k* thin-film layers based on biopolymers like cellulose derivatives for low voltage TFTs were demonstrated by Petriz *et al.*,[70,71] which proved the excellent properties of the gate dielectric with their limitation on the final engineering application.

In this chapter, the formulation of a nanocomposite dielectric, based on the combination of the BNNSs with carboxymethylcellulose (CMC),[72] is added to the list of high-*k* gate dielectric materials. The biopolymer CMC has diverse and interesting properties, including biocompatibility, nontoxicity, biodegradability, and film-forming ability.[73–75] These properties make CMC one of the most important cellulose derivatives. CMC, mainly derived from wood and with diameters and lengths in the nanoscale, is considered to be a low-cost, green and inexhaustible material. Owing to its impressive mechanical and thermal properties, CMC has been extensively studied as a building block for films and membranes separator for batteries. [75,76] The presence of polar –OH groups enables hydrophilicity, whereas the exposure of hydrophobic –CH moieties causes hydrophobic faces. The existence of both hydrophilic and hydrophobic faces allows CMC to be used as a biosolvent. In water, the mechanisms for the dispersion of 2D materials are the CMC presence, which attaches to the flakes through the interaction between its hydrophobic sites (–CH) and the hydrophobic plane of the flakes (B–N), as well as hydrogen bonding between the CMC hydroxyl groups (–OH) and the defective edges of the 2D materials. The flakes are stabilized due to steric hindrance and the electrostatic repulsive forces generated by the charged carboxylmethyl groups ($–CH_2–COO^-$).[72,77,78]

5.1.1. Flexible Fully Inkjet-Printed Gr/h-BN TFT

In ***Paper VII****: Flexible fully inkjet-printed Gr/h-BN thin film transistor*, the following issues were studied and discussed in detail:

(1) The design of a water-based h-BN ink (water/CMC solution) with high concentration of exfoliated BNNSs obtained using a microfluidic processor to perform the LPE process. The developed dispersions showed good stability and the microscopy characterization of the h-BN flakes confirmed nanometric thickness and lateral size of the BNNSs.

(2) The inkjet-printing of the h-BN ink in order to achieve controlled dielectric thin films in MIM-structured devices on flexible PET substrate. In addition, the validated h-BN dielectric has shown high-*k* characteristics, with ε_{hBN} ~6.92.

(3) The fabrication of flexible fully inkjet-printed graphene/h-BN TFT devices, resulting in hole carrier mobility of graphene up to 110 $cm^2V^{-1}s^{-1}$ while maintaining the distinctive electrical properties, in either normal mechanical conditions or under bending stress.

In this paper, we selected high-pressure microfluidization as an efficient, cost-effective and mass-production technique for LPE of bulk h-BN flakes down to few nm-thick h-BN nanosheets dispersed in water. CMC was selected to stabilize the flakes in solution. We demonstrated that the method results in high-concentrated BNNs dispersions that are suitable for drop-on-demand inkjet-printing technology. To determine the insulator properties of the h-BN layer, both the structure and the morphology of the inkjet-printed thin film have been studied. By selectively depositing smooth films of BNNSs in a non-contact process we present MIM devices and, consequently, we erect multilayered heterostructures in which BNNSs and exfoliated graphene flakes are alternatively stacked to form a fully-printed graphene-based transistor onto PET flexible substrate, at room temperature and ambient pressure.

We then inkjet print uniform pinholes-free thin-films of h-BN (50 nm per layer), and demonstrate fully-printed Ag/h-BN/Ag MIM capacitors with a dielectric constant value of ε_r = 6.92, achieving a capacitance per unit area of 1 nF mm^{-2}. Finally, we inkjet print 2D-materials based TFTs using h-BN and graphene ink as dielectric and channel layers, respectively. The reproducibility of the

graphene/h-BN TFTs is confirmed by a statistics over 20 devices, reporting a record mobility of up to 110 $cm^2 V^{-1} s^{-1}$, onto PET flexible substrates, at room temperature and ambient pressure.
Overall, this work has shown for the first time that exfoliated h-BN nanosheets constitute an adequate high-*k* dielectric material (high capacitance for low-voltage operation) to act as gate oxide and thus complement with graphene in fully inkjet-printed 2D-based flexible microelectronics at low-temperature(~100 °C, suitable for the selected PET substrate).

** Note that sections, equations and references numbering in the reproduced research article follow the ones of the published version.*

The article has been SUBMITTED to the Journal NATURE COMMUNICATIONS; Vescio G., Lombardi L., López-Vidrier J., Martín G., López-Conesa L., Estradé S., Karagiannidis P., Hodge S., Peiró F., Cornet A., Ferrari A. C., Cirera A., Torrisi F. ― *Flexible fully inkjet-printed Gr/h-BN thin film transistor* ‖; Copyright 2017; with permission from NATURE COMMUNICATIONS.

Flexible fully inkjet-printed hBN–Graphene thin film transistor

Vescio G.,[1*] Lombardi L.,[2] López-Vidrier J.,[3] Martín G.,[1] López-Conesa L.,[1] Estradé S.,[1] Karagiannidis P.,[2] Hodge S.,[2] Peiró F.,[1] Cornet A.,[1] Ferrari A. C.,[2] Cirera A.[1], Torrisi F. [2*]

[1] *MIND-IN2UB, Engineering Department: Electronics, Universitat de Barcelona, Martí i Franquès 1, Barcelona 08028, Spain*

[2] *Cambridge Graphene Centre, University of Cambridge, 9 JJ Thomson Avenue, Cambridge CB3 0FA, United Kingdom*

[3] *IMTEK, Faculty of Engineering, Albert-Ludwigs-University Freiburg, Georges-Köhler-Allee 103, D–79110 Freiburg, Germany*

ABSTRACT

Flexible electronics is a rapidly emerging field. The new paradigm of heterostructures based on two-dimensional (2d) atomic crystals has already led to the demonstration of novel physical phenomena and creation of new flexible electronic devices. Mechanically stacking layers of different 2d crystals allows unprecedented control over the electronic and optical properties of the resulting devices. Inks and dispersions made from 2d crystals have extended such new exciting properties to printed and flexible electronics. For 2d crystal based inks, the major challenges with current printing techniques are the lack of control over the quality of such structures, the 2d-2dinterface and the formation of pin-hole free 2d material-based thin film dielectrics. In this work we demonstrate fully inkjet printed 2d material-based heterostructures stacking films of graphene and h-BN films. We achieve a dielectric constant of the pin-hole free h-BN film up to ε_r ~ 6.96 and a capacitance per unit area of ~1 nF mm^{-2}, when embedded into a metal-insulator-metal capacitor structure. Finally, we demonstrate a flexible all-inkjet printed graphene/h-BN Thin Film Transistor achieving a reproducible mobility of up to 110 cm^2 V^{-1} s^{-1}.

INTRODUCTION

To date, different printing technologies, such as gravure [15], screen [16], flexographic [17 18] and inkjet printing [19 20] have been employed to fabricate flexible electronics, [10 11 12 13 14] including organic light-emitting diode (OLED) displays [21 22], radio-frequency identification (RFID) antennas [23], solar cells [24 25 26], sensors [27] and thin-film transistors (TFTs) [28 29 30] . Although flexible substrate (polymeric plastic or paper) allows for properties such as transparency and/or resistance to mechanical deformation, printed devices also must fulfil current electrical requirements.[79] Because of this, electrical mobility (μ) and relative permittivity (ε) are the most critical parameters in printed electronics due to the liquid dispersion status of semiconductors and insulators inks, respectively, in comparison to the well-established silicon technology,.

On one hand, several approaches aim at improving the channel mobility of printed TFTs by the formulation of conjugated organic semiconductor polymers (i.e. poly(3,4-ethylenedioxythiophene) polystyrene sulfonate PEDOT:PSS or pentacene, up to μ~1.2 $cm^2V^{-1}s^{-1}$)[80,81], using carbon nanotube (CNT) coatings (up to μ~9 $cm^2V^{-1}s^{-1}$)[82,83] or by means of metal-oxide materials as semiconductor (i.e. indium-gallium-zinc-oxide IGZO, up to μ~10 $cm^2V^{-1}s^{-1}$)[84,85]. On the other hand, printable commercial dielectric inks are demonstrated as reliable insulators with low permittivity values ranging from ε~3 for poly(methyl methacrylate) PMMA[86 87], ε~4 for SU-8[88 89 88 90] to ε~5 for polyvinylpyrrolidone (PVP) [91 92] (printed layers thicker than ~1 μm are usually required). Dielectric coatings are formulated as nanoparticle-based high-*k* inks, [93,94,95] where sintering temperatures higher than 150 °C (damaging for several polymeric substrates such as polyethylene naphthalate (PEN) and polyethylene terephthalate (PET), are required.

Amongst the current printing technologies, drop-on-demand inkjet printing stands out as a cost-efficient technique, fast (up to 15 m/s), digital-pattern design (fast prototyping), maskless (non-contact) process, which guarantees controlled selective deposition of a few picoliters per drop of novel nanomaterial inks for large-area manufacturing.

In this context, inkjet-printable inks based on graphene and other 2d crystals [96] have attracted large interest in printed electronics as they offer a rich scalable platform for the creation of printed heterostructures of conducting, semiconducting and insulating thin films due to their outstanding and complementary mechanical, electrical, optical, and chemical properties.[97 98 99 100 101 102] Graphene as conductor, hexagonal BN (h-BN) as insulator and transition metal dichalcogenides (TMDs) as semiconductors are the building blocks that, combined within a vertical stack, allow for the fabrication of several fundamental electronic devices such as LEDs,[103] resonators,[104] TFTs, [30 105 47] photodetectors,[96] metal-insulator-metal (MIMs)[96], etc. [47 106 103 107 108 109 6]

Among the existing 2d materials, h-BN has been demonstrated as an ideal insulator due to its low dielectric screening, large optical bandgap, and absence of dangling bonds. [47] [48] [49] [50] [51] [52] Currently, several methods, divided into bottom-up and top-down techniques [6], have been used to produce highly-crystalline single atomic monolayer h-BN. Chemical-vapour deposition (CVD) [48] [49] or growth on silicon carbide [110] [111] are suitable to produce h-BN layers for outstanding electronic applications [112] [113] [114], despite the expensive costs and complexity required for large-scale fabrication.

Not only monolayered but also multilayered h-BN has awaken interest as dielectric layer or mechanical membrane in numerous device applications such as batteries [115] [116], solar cells [117] and ink composites [45]. Indeed, BNNs, have been produced at lab scale by several techniques such as micromechanical cleavage [5] [58], ball milling [42], wet-chemical exfoliation [41] [42], hydrodynamics [59]and unzipping of BN nanotubes [55]. In order to accomplish large concentrations of suspended BNNs (BNNSs), liquid phase exfoliation (LPE) [45] [37] [62] [118] [38] [43] can be performed in pure deionized water, [114] [43] solvents [59] [119], surfactants, [45] or polymeric compounds[116]. In particular, biopolymer-based h-BN nanocomposites, such as chitosan,[67] starch,[68] hydroxyl ethyl cellulose[69] and methyl cellulose,[69] showed, in addition to nontoxicity and biodegradability, high improvement on the thermal, mechanical, electrical, and biocompatibility properties.

In this paper, we selected high-pressure microfluidization [119, 120] [60] as an efficient, cost-effective and mass-production technique for LPE of bulk h-BN flakes down to few nm-thick BNNs dispersed in water. Carboxymethyl cellulose (CMC) was selected to stabilize the flakes in solution due to the steric hindrance and the electrostatic repulsive forces generated by its charged groups ($-CH_2-COO^-$).

We then inkjet print uniform pinhole-free thin-films of h-BN (50 nm per layer), and demonstrate fully-printed MIM Ag/h-BN capacitors with a dielectric constant value of ε_r = 6.92, and achieving a capacitance per unit area of 1 nF mm^{-2}. Finally, we inkjet print 2d-material based TFTs using h-BN and graphene ink as dielectric and channel layers, respectively. The reproducibility of the graphene/h-BN TFTs is confirmed by a statistics over 20 devices reporting a record mobility of up to 110 $cm^2\ V^{-1}\ s^{-1}$, onto PET substrate, at room temperature and ambient pressure.

Results and discussion

Exfoliation process of h-BN and formulation of h-BN ink.

During the LPE process, the presence of a stabilizer that balances the solvent – h-BN interaction with the inter-sheet attractive forces is required in order to minimize the enthalpy of mixing (ΔH_{mix})[37 57]. Therefore, successful solvents for the dispersion of graphene and 2d related materials are those with surface tension of ~40 mJ/m^2[61], matching the surface energy of the 2d materials. Although water has a surface tension of ~72 mJ/m^2,[62] exfoliation of flakes can be stabilized against reaggregation by Coulomb repulsion using linear chain monomeric surfactants[63] [i.e. bile salts (SC)[64] or sodium-deoxycholate (SDC)[65]] or by steric repulsion employing polymeric stabilizers[66] in aqueous systems. In our work first of all we exfoliated h-BN powders in solvents with varying surface tensions (See Supplementary Figure S1) and using different exfoliation methods. The h-BN flakes stabilized in water by the CMC sodium salt, [121] showed good results for both microfluidic and sonication exfoliation with the amount of exfoliated nanosheetss maximized when the h-BN/CMC mixture is processed by a shear fluid processor. We formulate the h-BN ink using commercial h-BN powder as starting material, with particles size of ~10 μm (99%) to ensure the flow in the microchannel (~75 μm wide) of the microfluidizer, avoiding prejudicial blockages during processing (See Methods for materials and exfoliatiob process. We processed h-BN – water mixture with h-BN C (4 mg/mL) and 10mg/mL CMC in DI water over multiple cycles (10, 25, 50, 100), where one cycle is defined as a complete pass of the mixture through the interaction chamber[60] and purified the resulting dispersion by centrifugation (See Methods).

The resulting inks/dispersions are initially characterized by optical absorption spectroscopy (OAS) and zeta potential measurements. After measuring the optical properties of the h-BN ink by means of OAS, Fig. 1b, the concentration of the BNNs dispersion is calculated by exploiting the Beer-Lambert law $A = \alpha C l$, where A is the absorbance measured at 300 nm,[57] l is the path length, C is the concentration, and α the absorption coefficient (2367 mL mg^{-1} m^{-1} [62 57]). The estimation of the concentration is facilitated by the A/l linear behaviour varying the number of microfluidization cycles (inset in Fig. 1b). The contribution of high shear forces (up to 10^8 s^{-1}) inside the microfluidizer interaction chamber, (See Supplementary data for the Mechanism of exfoliation) promotes dispersion of multilayer BNNs up to C ~1 mg mL^{-1} after 100 process cycles (inset of Fig. 1b) with a yield by weight Y_W ~25%, where Y_W is defined as the ratio between the weight of dispersed material and that of the starting h-BN powder.[118] The reported value of concentration is in line with the highest reported for h-BN inks (1.6 mg mL^{-1})[96] employing sonication and sedimentation-based separation[45]. Zeta potential

measurements were performed to estimate the degree of steric-electrostatic repulsion and consequently the stability of the h-BN dispersion.

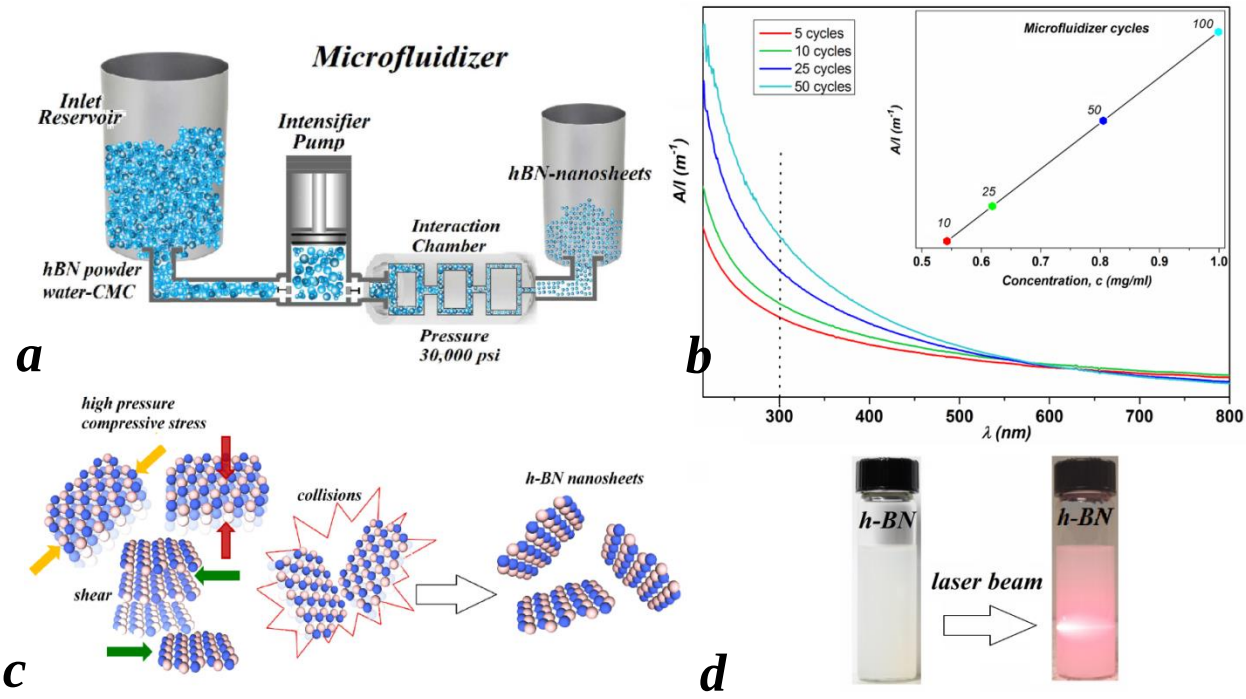

Figure 1 | Concentration of the h-BN ink. *Absorbance per unit length as a function of the incident wavelength, for h-BN inks obtained at different microfluidizer cycles. The inset….*

CMC is an ionic polymer which is expected to be adsorbed onto the BNNs and to impart an effective charge.[122] [123] The measured zeta potential for the h-BN/CMC dispersion is centred at -53 mV (Supplementary Fig. S2) and fits in the accepted range of |40 – 60| mV [124] [125] for excellent colloidal stability. The stability of the ink is also proved by the turbiscan index of ~5 (see Supplementary Fig. S3). The nanometric structure of the BNNs can be predicted irradiating the colloidal dispersions. Indeed, as shown in Fig. 1d, the path of a red laser is observed through the ink due to the light scattering because of the Tyndall effect (light scattering effect is visible when the colloidal nanoparticle size is below or near the wavelength of the excitation light, λ ~ 633 nm).

Characterization of h-BN nanosheets.

A combination of atomic force microscopy (AFM) and high-resolution transmission electron microscopy (TEM) are used to assess the thickness and average lateral size distribution of the BNNs in solution.

Thickness and shape of h-BN flakes are estimated from the topography profiles by AFM. The h-BN ink is deposited by inkjet on mica substrate and then washed in order to remove the CMC (See Methods for ink characterization). The AFM image of a typical BNNs, Fig. 2a, shows an average thickness of ~6.6 nm, thus indicating that the BNNs consistes of ~20 layers (assuming the lattice constant of h-BN is ~ 3.3 Å). AFM statistics of the flakes thickness, shown in Fig. 2b (Supplementary Fig. S4), show a prevalence of flakes of ~5.7 nm.

TEM analysis (Supplementary Fig.S5) confirms that h-BN ink conteins of multilayer flakes with lateral size in the range from 100 nm to 550 nm, with an average lateral size (calculated as $area^{1/2}$) around ~240 nm (Fig. 2c). Fig. 2d shows a TEM image of a thin BNNs deposited on a holey carbon copper grid. Furthermore, some small parts of fragmented flakes of tens of nanometres (20–50 nm) have also been observed. Finally, an HRTEM image of the same flake (Fig. 2e) with the corresponding Fast Fourier-Transform (FFT) of the red-squared area (Fig. 2f) allows assessing that the crystalline structure of the h-BN flakes is conserved after processing.

Electron Energy Loss Spectroscopy (EELS) analysis, performed on one single flake of h-BN, probes the chemical composition of the sample (Supplementary Fig. S6). The presence of B (K edge at ~188 eV) and N (K edge at ~400 eV) atoms was detected as expected, and C (K edge at ~283 eV) and O (K edge at ~532 eV) were also observed due to the presence of the organic CMC compound.

The quality of the h-BN flakes is also investigated by Raman spectroscopy (Fig. 2g). The Raman spectrum of the exfoliated h-BN shows a well-defined single peak at 1366 cm^{-1}, the in-phase vibration mode E_{2g} of h-BN, with a full-width-half-maximum (FWHM) of 14 cm^{-1}. These numbers are in good agreement with allowed phonon modes of multilayer h-BN. [126]

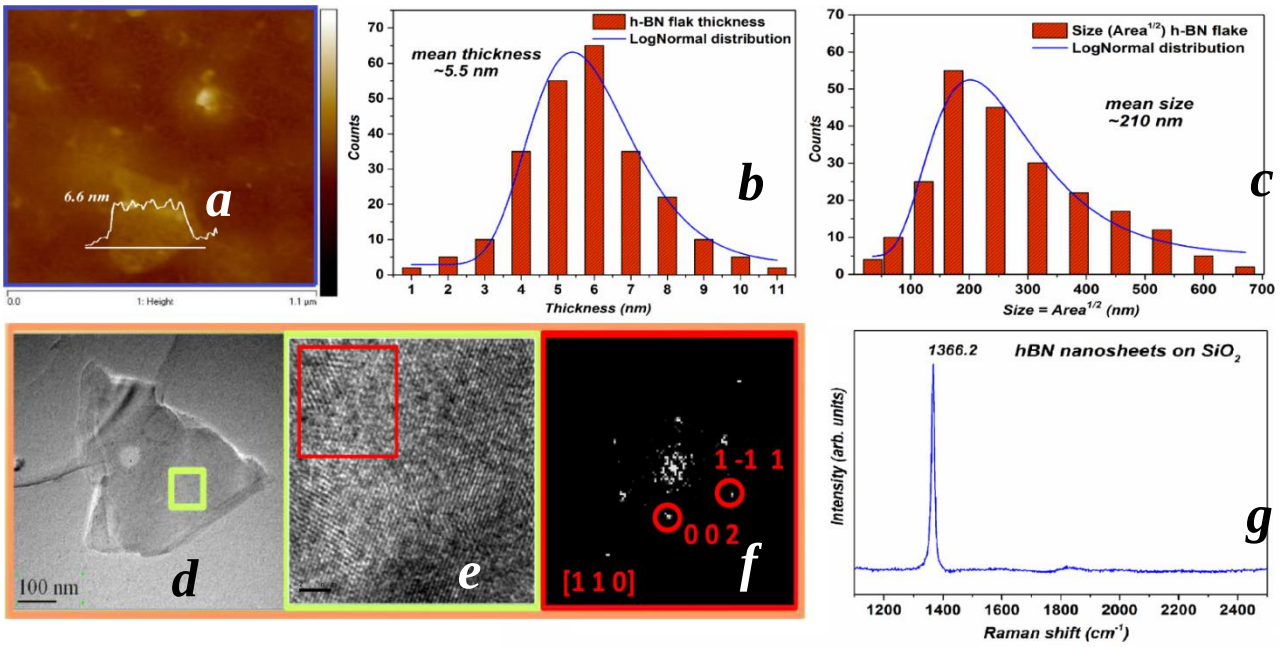

Figure 2 | Characterization of h-BN nanosheets. a, *AFM image of representative h-BNflake with height profile* ***b,*** *Histogram of the thickness obtained from different h-BN nanosheets probed by AFM. The data are fitted with a blue line following a Lorentzian-like distribution.* ***c****, Lateral size (area$^{1/2}$) histogram obtained from different h-BN flakes probed by TEM. The data are fitted with a blue line following a LogNormal-like distribution.* ***d,*** *TEM image of a h-BNsheet.* ***e****, HRTEM image obtained from the green region in figure* ***d****.* ***f,*** *FFT corresponding to the red-framed region in* ***e****.* ***g,*** *Raman spectrum of h-Bn flakes deposited on SiO_2 substrate.*

Characterization of the h-BN ink.

In order to prevent nozzle clogging when inks contain dispersed nanoparticles or nanosheets, the latter should be smaller than 1/50 the nozzle diameter,[36] δ, of the selected cartridge. The drop formation is influenced by the rheology parameters, such as density (ρ), viscosity (η) and surface tension (γ), which, take into account the inertial, viscous and surface tension forces, respectively. These parameters are required to estimate the quality of the ejected drop expressed by the correlated dimensionless figure of merit (FOM) Z number (eq. [1]) This is equivalent to the inverse of the Ohnesorge (Oh) parameter[127] (Supplementary table TS1), which is independent of fluid velocity: [127]

$$Z = \frac{1}{Oh} = \frac{\sqrt{\delta \cdot \rho \cdot \gamma}}{\eta} \qquad \text{[eq. 1]}$$

The calculated Z=12.11 (See Supplementary Fig. S7) predicts the formation of a stable drop, since the expected value lies on the range 1<Z<14[128]. As well, other quality factors such as printing resolution, homogeneity and adhesion to the substrate can be fulfilled adapting parameters such as frequency of injection, nozzle temperature, drops per inch, substrate temperature, etc. (Supplementary tableTS2).

AFM topography and field-emission scanning electron microscopy (FE-SEM) images (Supplementary Fig. S8) of inkjet-printed h-BN ink on mica substrate, without any post-

treatment washing, show the characteristic BNNs domains well-deposited and dispersed into the CMC matrix, with a horizontal preferential orientation to the substrate surface, being aligned through the compression direction.

Since chemical and structural modification of BNNs might occur during the printing process, compromising the expected electronic performance of the inkjet-printed films, their in-depth structural and chemical characterization is required. For this, X-Ray diffraction (XRD), X-ray photoelectron spectroscopy (XPS) and attenuated total reflectance Fourier transform infrared (ATR-FT-IR) spectroscopy are employed to investigate crystalline structure, elemental composition and chemical bonding, respectively.

Fig. 3a display the X-ray pattern acquired from the printed BNNs on Si. The spectrum exhibits two peaks at $2\theta = 26.70°$ and 55.10° corresponding to the signature of crystalline h-BN,[129] [130] which the JCPDS file number 01-073-2095 attributes to the {002} and {004} reflecting planes, respectively. By applying Bragg's law, the estimated interlayer distances are 3.33 and 1.1 Å, [131] respectively for each family of planes (See Methods for Chemical Characterization). These values are consistent with h-BN grown by CVD technique.[114] Indeed, both the intensity of the reflection in the preferential plane {002} and its narrow FWHM, ~0.42°, evidence the structural order and orientation of the inkjet-printed h-BN flakes. The band centred at $2\theta = 21.70°$, broad due to its amorphous structure, corresponds to the CMC phase[122] [123], whereas the peak centred at $2\theta = 28.50°$ results from the {111} family of planes from the Si substrate. The exfoliation of h-BN in the CMC matrix is not affected by the presence of the polymer incorporation as indicated by the structural ordering (confirmed by the preferential plane with narrow FWHM) of the h-BN nanosheets.

The ATR-FT-IR spectra are displayed in Fig. 3b. The blue curve shows the spectrum of inkjet-printed h-BN thin film, where the peaks positioned at 819 cm^{-1} and 1371 cm^{-1} are attributed to the h-BN flakes [131] and originate, respectively, from the B–N bending out-of-plane vibration (A2u mode) [131] and the B–N stretching in-plane vibration (E1u mode)[131]. This interpretation is also supported by the absence of these features in the FT-IR spectrum acquired on inkjet-printed water/CMC film (green line). The spectrum in this case exhibits the expected peaks for CMC positioned at 1584 cm^{-1} and 1053 cm^{-1}, respectively attributed to the -COO- asymmetric stretching and to the $–CH\text{-}O\text{-}CH_2$ stretching [122] [123]. Additional peaks centred around 2921 cm^{-1}, 1408 cm^{-1} and 1322 cm^{-1} are assigned to C–H stretching vibration, to $–CH_2$ scissoring and to –OH bending vibration, respectively. [122] [123] A wide absorption band is observed in the range 3.600- 3.000 cm^{-1}, due to the stretching frequency of the –OH group (details on the vibration modes of the typical functional groups in CMC can be found in Supplementary Table TS3).

It is important to note that the intensity of the asymmetric and symmetric stretching of OH hydroxyl group peaking at 1322 cm^{-1} and 3266 cm^{-1} increases in the spectrum of the

h-BN printed film (blue line) respect to the water/CMC one (green line). The same vibrations are also shifted and centred at 1325 cm^{-1} and 3255 cm^{-1}, respectively. The shift of the expected phonon band to lower frequencies in the h-BN film could be due to the creation of the bonds between CMC/water-bound molecules and BNNs by hydrogen-bonding into the h-BN ink (a sketch of the bonds whose vibration is revealed by ATR- FT-IR is drawn in Supplementary Fig. S9). Finally, there is no evidence of the undesired B-O bonding mode due to deformation from hydroxyl groups, since the spectrum does not show the characteristic peak at 1190 cm^{-1}.[42]

The B-N chemical bonds and their stoichiometry are verified by XPS, and the obtained multiplex survey for the inkjet-printed h-BN thin film layer is presented in Supplementary Fig. S10. The XPS spectrum exhibits the distinctive peaks of h-BN bonds, with their corresponding binding energies (BE) at 396.8 and 190.5 eV, respectively corresponding to N 1s and B1s single-orbit characteristics of h-BN.[59,43,130] High resolution spectra of printed BNNs are shown in Fig. 3(c,d). The symmetric shapes of the fitted spectra of N 1s and B 1s prove that covalent bonds are predominantly in B-N molecules [132] with an effective stoichiometry ratio (B:N) of 1:1 (See Supplementary table TS4). Details of the B 1s deconvolution spectrum shown in Fig. 3(d) suggest the presence of a smaller peak towards lower BE for the expected B 1s bonds centred at 189.1 eV. In accordance to previous ATR-FT-IR study , the chemical bond can accordingly be assigned to the B-H bonding due to the presence of hydrogen bonding between boron and water-CMC molecules.

The formation of hydrogen bonding probably depends on the hydroxyl groups of water/CMC base as indicated by the O 1s spectra in Fig. S11. The peaks placed at 533.5 and 536.1 eV indicate bond structures such as B-H-O and H_x-O. However, the relative intensity that can be estimated (Supplementary TS4) suggests the presence of adsorbed bound water[133] (~ 5%) and hydrogen bonds[133] (~4%), as confirmed from the FT-IR study.

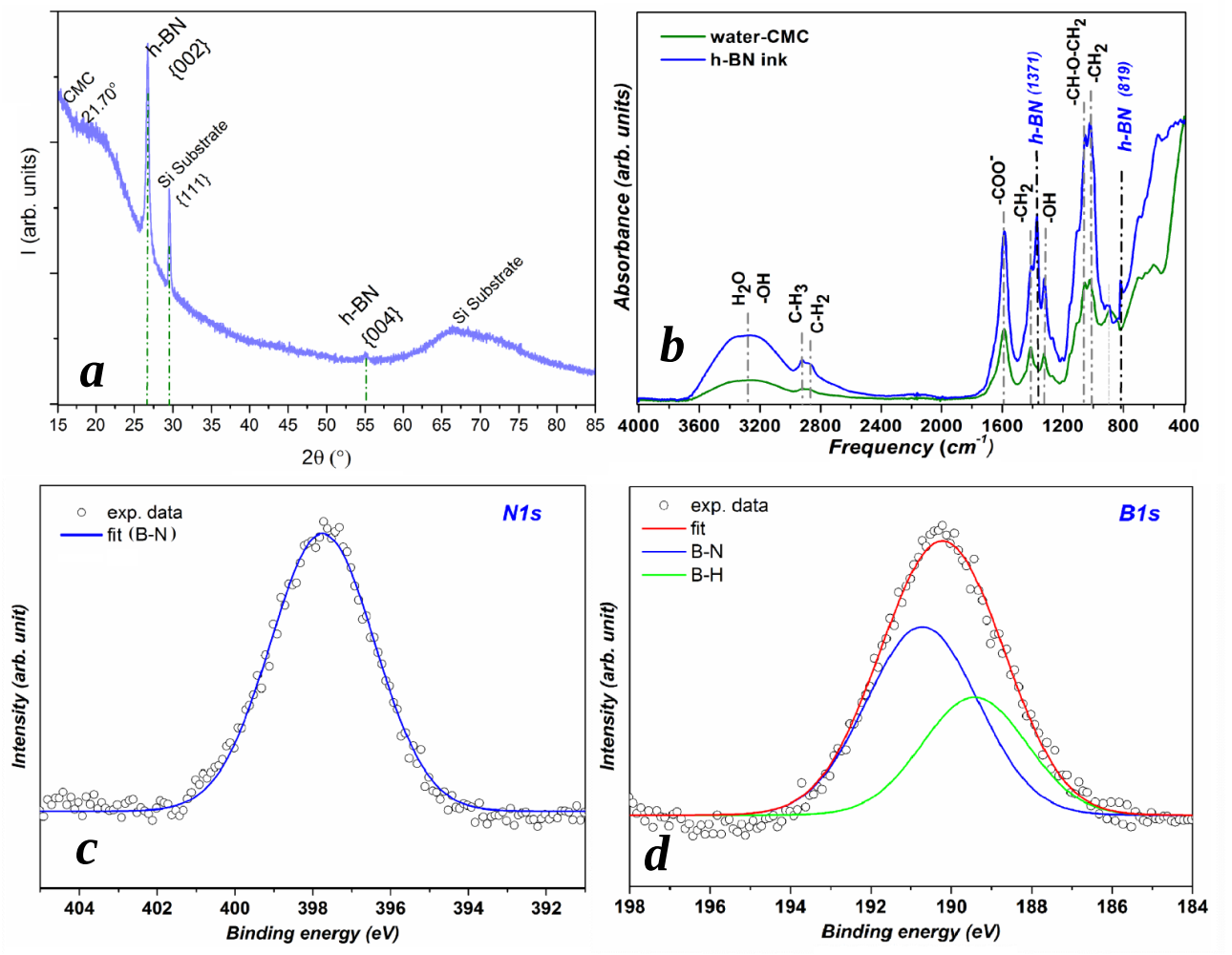

Figure 3 **|** ***Chemical analysis ofthe h-BN nanosheets. a,*** *XRD pattern from h-BNprinted on Si.* ***b,*** *FT-IR spectra corresponding to a thin h-BN film (in blue) and a reference water-CMC solution (in green).* ***c, d,*** *XPS spectra corresponding to the N1s (**c**) and B1s (**d**) bonds.*

Inkjet printing process and dielectric properties of h-BN films as dielectric layer for flexible capacitors (MIMs).

Metal-insulator-metal (MIM) structures using Ag ink fot the metal electrodes and h-BN ink as dielectric layer have been inkjet-printed onto polyethylene terephthalate (PET) and glass substrates (see the Methods). Fig. 4a sketches the Ag/h-BN/Ag MIM structure and Fig. 4b shows a top view of the device used to assessthe performance of the h-BN as dielectric material. The thickness (*d*) of the inkjet-printed h-BN layer ranges from ~100 nm to ~300 nm to investigte the effect of *d* on the dielectric properties and on the morphology of the film. The different thicknesses have been achieved by multiple inkjet printing passes (where *n* is the number of printing passes) following the *d* vs *n* curve shown in Fig. S12. Cross-sectional SEM analysis of the FIB-sectioned MIMs, Fig. 4(c,d) , is used to accurately determine *d* (Supplementary Fig. S13). As can be observed by the SEM cross-section images, each single printing step deposits ~50 nm of pinholes-free h-BNfilm ..

Temperature dependence of the dielectric constant is verified by choosing two different post-processing annealing temperatures. Due to the flexible PET frailty, the inkjet printed capacitors (batch of 315 deivces) are annealed at 100 °C in vacuum chambre to promote the complete evaporation of the solvent, whereas the thermal treatment is 180 °C for MIMs devices on glass sustrate (batch of 315 devices). Capacitance measurements of MIM devices containing dielectric layers with thickness ranging from 100 to 300 nm, , are presented in Fig. 4e. A capacitance density of up to ~1 nF mm^{-2} at 1 MHz is measured over a constant value in the range ± 3 V (see Methods). The inset in Fig. 4e shows the leakage current density (J) as a function of the applied electric field (E) for a 100-nm-thick h-BN MIM capacitor. J–E characteristic curve, measured over an area of 0.1 mm^2 shows a leakage current lower than ~5×10^{-5} A cm^{-2} at ± 0.3 MV cm^{-1} for all the samples, which matches the one reported for CVD-grown h-BN flakes (~10^{-5} A cm^{-2})[114], instead the average value of the breakdown electric field (E_{Bd}), around ± 0.5-1 MV cm^{-1}, is lower than the one of CVD h-BN (2–4 MV cm^{-1}).[114]

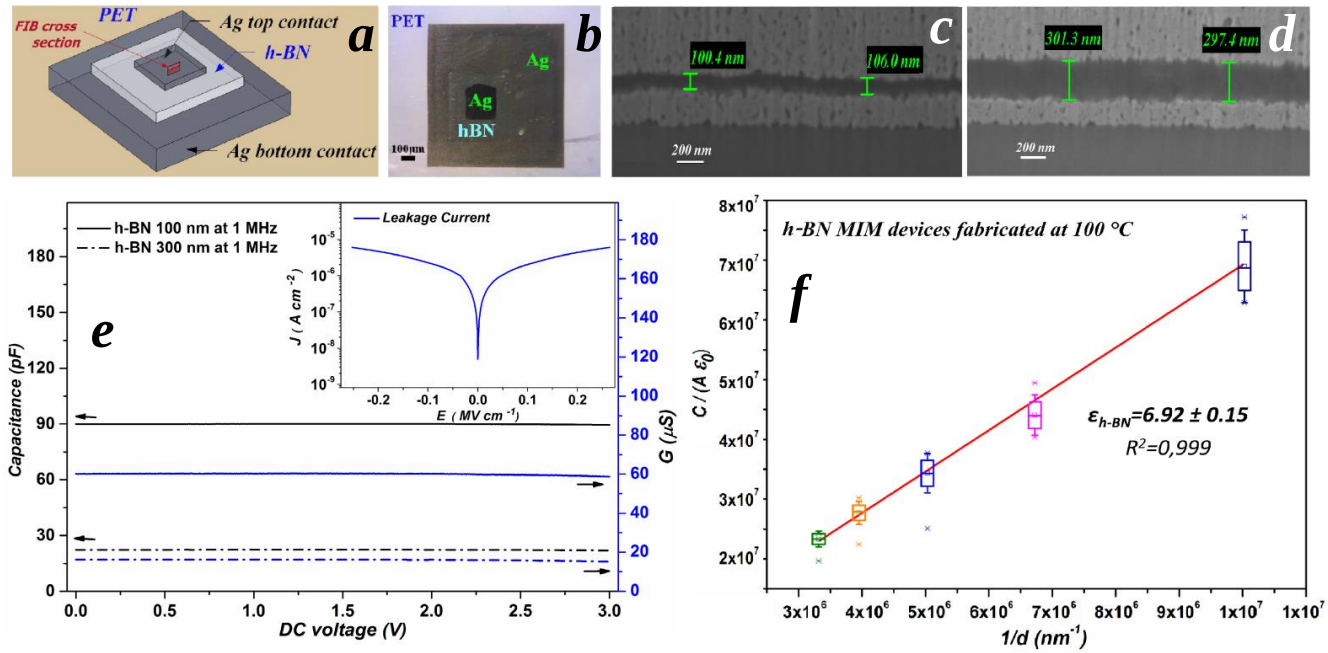

Figure 4 | Dielectric properties of inkjet-printed h-BN films. a, *3D schematic of the fabricated Ag / h-BN /Ag MIM capacitors on PET substrate. The red plane indicates the FIB cross section cut.* ***b,*** *Top view of one capacitor obtained by conventional optical microscopy.* ***c, d,*** *Cross-section FE-SEM images from MIMs containing h-BN layers with nominal thicknesses of 100 nm (**c**) and 300 nm(**d**).* ***e,*** *Capacitance (black) and conductance (blue) as a function of DC voltage for two samples with different h-BN thickness. The inset shows the leakage current density vs. electric field for a MIM device containing a 100-nm-thick insulator layer.* ***f,*** *C / (A ε_0) vs. 1/d plot from several devices fabricated at 100 °C on PET with different h-BN thickness. The value of ε_{h-BN} found by linear regression of the data is indicated in the graph.*

Using the expression of the capacitance for a parallel plate capacitor $C_{meas} = \varepsilon_0 \varepsilon_r A/d$, where ε_0 is the vacuum dielectric permittivity, ε_r is the relative dielectric constant, A is the device area and d is the insulator thickness, we extract the relative dielectric constants by linear fitting the regression curve. A relative dielectric constant of ε_{PET}=6.92 (Fig. 4f) is carried out for h-BN-based MIMs printed on PET substrate, and of ε_{glass}=6.96 (Supplementary Fig. S14) for h-BN-based MIMs printed on glass substrate. Flexible h-BN capacitors shows comparable dielectric constant and better reliability (R^2=0.999) than devices on rigid substrate (R^2=0.991), thus demonstrating the feasibility of flexible inkjet-printed h-BN MIMs (Supplementary Figs. S15 and S16). These values are higher than the one of other fully-printed (mixing inkjet and spray techniques) MIM devices where ε_{h-BN} is ~2.5 (with a minimum thickness required of 1.65 μm),[134] or where LPE h-BN is desposited via drop casting showing a permittivity ~1.5 (minimum thickness required of 600 nm)[96] [135]. Moreover, h-BN dielectric ink exhibits better permittivity than typical polymeric insulator inks (ε_{PMMA} ~3,[86] [87] ε_{SU-8} ~4, [88] [89] [88] [90] ε_{PVP} ~5 [91] [92]).

Our inkjet-printed h-BN dielectric ink shows the best design trade-off resulting in concurrent advances in several dielectric promising performance due to parameters such as high dielectric constant value (ε_{h-BN}=6.92), low temperature sintering (100 °C), pinholes-free printed thin film (~100 nm) and biocompatibility behaviour.

Printed and flexible graphene/h-BN TFT structure characterization.

Once the feasibility and reproducibility of the inkjet-printed h-BN thin film as a reliable insulator were demonstrated, building heterostructures combining the h-BN with other 2d materials, such as graphene, is imperative for the introduction of this fabrication technique in the state-of-the-art of research and technology. Therefore, in this section we fully-inkjet print a flexible graphene/h-BN (Gr/h-BN) TFT where graphene ink is the channel, h-BN ink the gate dielectric and Ag ink used as source/drain and top-gate electrodes onto PET substrate (details in Methods for Printed devices). Fig. 5a shows a 3d sketch of the inkjet-printed TFT (for a more generic scheme see Supplementary Fig. 17a), and Fig. 5b shows the device cross-section acquired by SEM.

FE-SEM and related energy dispersive X-ray (EDX) spectroscopy analysis (shown in Supplementary Fig. S17b) of inkjet-printed TFT structure confirms the chemical composition of h-BN layer, being the effective B:N stoichiometry estimated around 1.05, which is in line with XPS results. In addition, the FE-SEM cross-section images give no evidence of structure anomalies (grains clustering) or defect-generated (pinholes-free) on the h-BN insulator printed on the graphene layer (see Supplementary Fig. S17 c).

Fig. 5c plots the Raman spectrum of the printed graphene (Gr)h-BN heterostructure (black curve). Besides the G, D', 2D and D+D' peaks, which are fingerprints of LPE graphene

inks[38], it shows a peak centred at ~ 1370 cm^{-1} which originates from the convolution of the D peak of graphene with the E_{2g} peak of h-BN. This is further evidenced by subtracting the Raman spectrum of the pristine graphene ink (red curve) to that of Gr/h-BN, after normalization at the G peak. The resulting spectrum (blue curve) shows only one peak at ~1370 cm^{-1}, corresponding to the characteristic E_{2g} vibrational mode of exfoliated h-BN (green curve).[136] The G, D and 2D peaks in LPE graphene spectrum correspond to the high frequency E_{2g} phonon at Γ, to the TO phonons around the Brillouin zone corner K and to the D-peak overtone, respectively. The D peak requires a defect for its activation by double resonance (DR) and it is strongly dispersive with the excitation energy due to Kohn anomaly at K.[137] DR can also happen intravalley, i.e., connecting two points belonging to the same cone around K or K'. This gives the D' peak. The 2D peak originates from a process where the momentum conservation is satisfied by two phonons with opposite wave vector so defects are not required for its activation and it is always present.[138] The line shape of the 2D peak in graphene NMP ink is a single Lorentzian with FWHM (2D) ~70 cm^{-1}. This value is larger than the one expected for single layer graphene and it is consistent with the presence of a multilayer flakes in which the layers are electronically decoupled and act as a collection of single layers.[139] For the same ink the D peak is activated by edges and an intrinsic doping of at least 10^{13} cm^{-2} has been reported.[38]
The composition of the h-BN layer is further investigated by electron energy loss spectroscopy (EELS) in scanning mode Transmission Electron Microscopy (STEM). The region used for EELS Spectrum Imaging (SI) is highlighted in blue in the FIB image shown in Fig. 5b. Fig. 5d shows the resulting elemental maps for C (K edge at ~283 eV) , B (K edge at ~188 eV), and N (K edge at ~400 eV) represented in red, green and blue respectively and the corresponding RGB composite map (see Supplementary Fig. S18c).

Fig. 5e shows a HRTEM image of the h-BN layer, showing two flakes embedded in the polymer. The intensity profile (inset) shows an interplanar distance of 3.3 Å for the h-BN layer, while the bottom layer of printed graphene appears uniformly bended, following the surface roughness of the PET substrate. The total thickness of the analysed BNNs is ~ 4 nm. HRTEM images of Supplementary Fig. S18(a,b) confirm that the BNNSs layer seems to adapt to the graphene one without any distortion. Supplementary Fig. S18c shows an EELS spectrum of the h-BN layer, where the signatures for the B, C and N k-edges can be clearly observed.

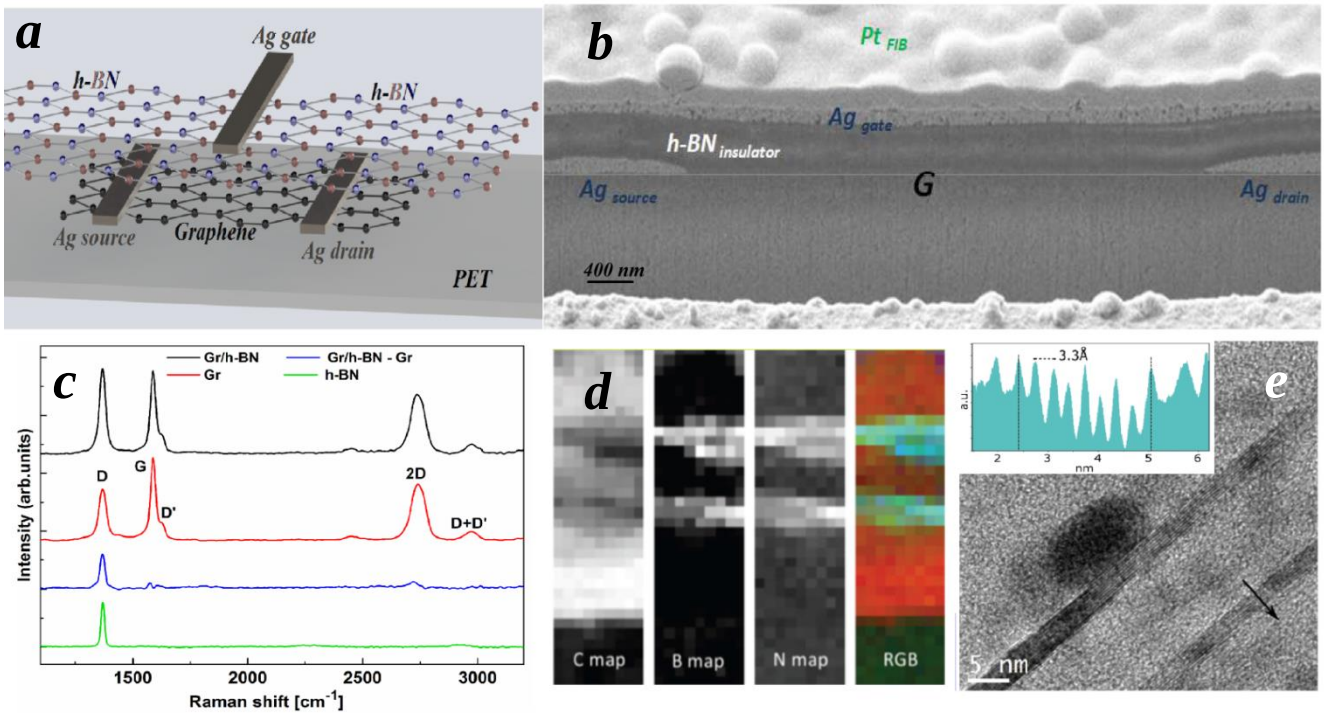

Figure 5 | Structural analysis of h-BN- and TFT graphene-based devices. a, *3D sketch of the fabricated TFT devices.* ***b,*** *FIB cross-section image of h-BN–Graphene printed TFT.* ***c,*** *Raman spectra of the graphene / h-BN stack (black), graphene ink (red), their subtraction (blue), and h-BN ink (green).* ***d,*** *Elemental distribution of C, B, and N (K edges), and the corresponding RGB composite image, obtained from STEM-EELS spectrum imaging in the dielectric layer.* ***e,*** *HRTEM image of a region of the heterostructure corresponding to the h-BN layer. The inset shows a contrast profile from the region indicated by the arrow.*

TFT graphene-based devices electrical characterization.

In order to characterise the inkjet-printed flexible Gr/h-BN TFT, we acquired the output and transfer characteristic curves from ~20 devices. Fig. 6a shows the output characteristic corresponding to devices with 400 nm thick h-BN dielectric layer, obtained at room temperature (~24 °C) and after the application of gate voltages ranging from -0.5 to 1.0 V. Despite the ON/OFF ratio of ~2, value expected for graphene-based transistors, high current intensity (~120 μA) has been achieved even at very low applied drain voltages (±1 V).

Figs. 6b shows the transfer characteristic curve of the same Gr/h-BN TFT measured at room temperature (~24 °C) and V_{DS}= 10 mV. The hole (μ_p) and electron (μ_n) field-effect carrier mobilities, in the linear range using the peak transconductance method, (see Methods for mobility extraction) are estimated up to μ_p = 110 cm^2 V^{-1} s^{-1} and μ_n = 75 cm^2 V^{-1} s^{-1}, respectively. Fig. S19 shows the device reliability, confirmed by mobility values extracted over ~20 devices ranging all from 35 cm^2 V^{-1} s^{-1} up to 110 cm^2 V^{-1} s^{-1}. The mobility variation of Gr/h-BN TFT on the PET could be attributed to the not ideal printing of the

metal electrode which causes a non-optimal contact resistance with graphene channel. [140 3] Moreover, imperfections of the flexible substrate (e.g. roughness, micro-fractures) could influence the device performance.

The excellent μ_n and μ_p values achieved in this work for a flexible fully printed Gr/h-BN TFT are comparable to mobility values (μ_p ~203 and μ_n ~91 $cm^2V^{-1}\cdot s^{-1}$)[141] for graphene transistor (CVD film) with printed ion gel dielectric on PET, to the extracted mobility (μ_p ~102 $cm^2V^{-1}\cdot s^{-1}$)[142] for graphene-based TFT (using dielectrophoresis) with yttrium oxide (high-k) on polyimide substrate, and higher than the symmetric evaluated mobilities ($\mu_{p,n}$ ~67 $cm^2V^{-1}\cdot s^{-1}$)[143] for a transparent-flexible graphene charge-trap memory device fabricated on polyethylene-naphthalate substrate. To date, to the best of our knowledge, we have first demonstrated flexible fully-inkjet printed graphene-based TFT,.

The electrical performances of the inkjet-printed Gr/h-BN TFTs are also tested upon mechanical bending. The devices are bent by attaching the flexible substrate on half-cylinders of various bending radii. The applied bending ranges from flat conditions (no bending) to strain up 1.5% (5 mm half-cylinders radius) (see Methods – bending extraction).

Transfer characteristics of one of the Gr/h-BN TFT with 400 nm of h-BN dielectric (flat condition μ_p = 74 $cm^2\ V^{-1}\ s^{-1}$ and electron mobility μ_n = 55 $cm^2\ V^{-1}\ s^{-1}$, Fig. S20) acquired at different bending radius are shown in Fig. 6c. During bending , the Gr/h-BN TFT still exhibits similar electrical curves, with a field-effect hole mobility of μ_p = 53 $cm^2\ V^{-1}\ s^{-1}$ and electron mobility of μ_n = 44 $cm^2\ V^{-1}\ s^{-1}$ under a strain up to 1.5%. Fig. 6d shows μ_p and μ_n values obtained under different bending strain conditions (see the inset in Fig. 6d), normalized to the unbend condition value (μ_0). Both the hole and electron mobilities decrease with bending with a variation less than 20%. A possible explanation for the different electrical performance during bending stress is the elongation of both the channel and the conductive electrodes resulting in an increase of the total resistance of the device. Consequently the decrease of the mobility does not dependent on the reduced performances of the h-BN dielectric film under bending.

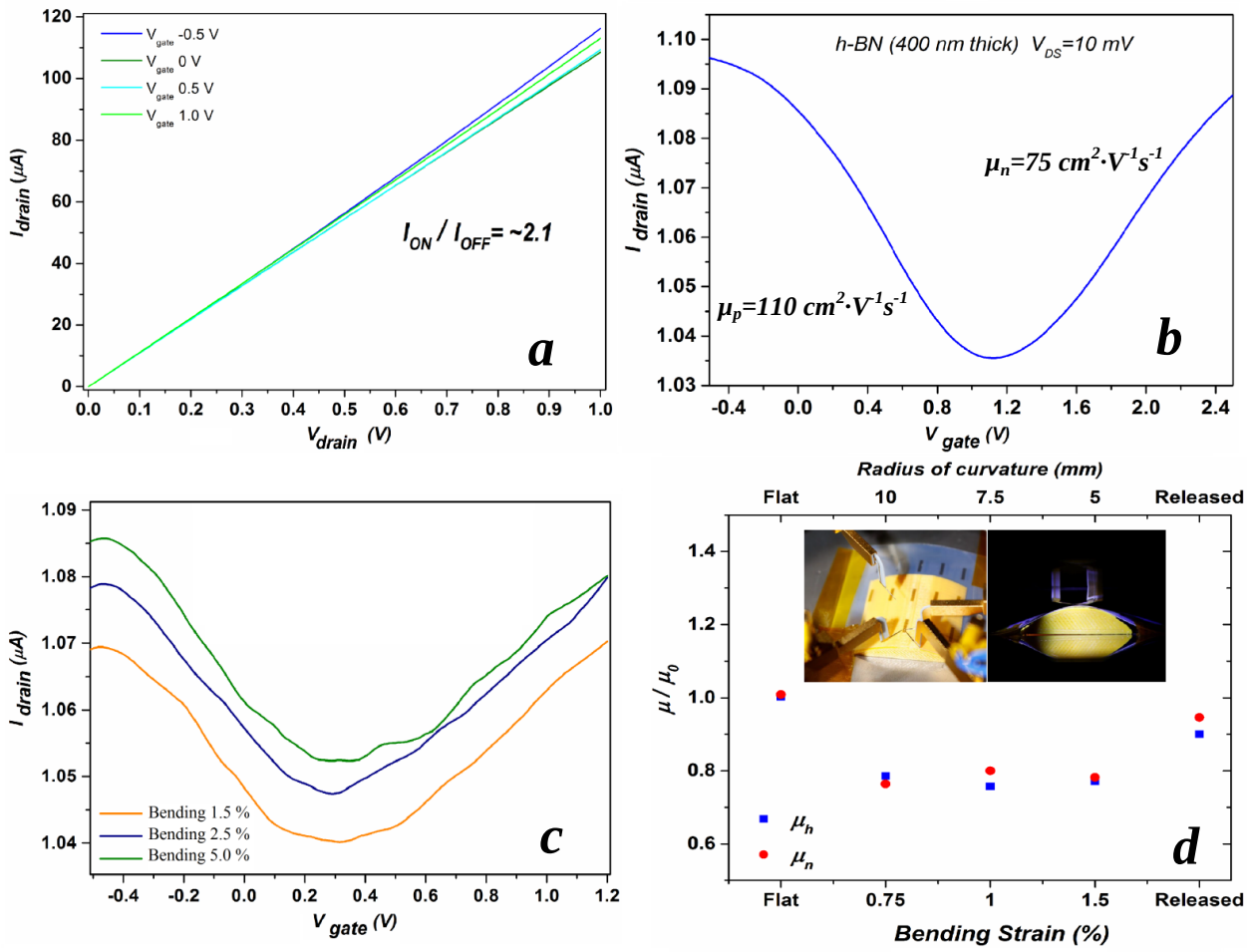

Figure 6 | ***a,*** *Transfer characteristics, measured at room temperature and under different gate voltages, of a TFTs with 400nm h-BN layer .* ***b,*** *Output characteristic, measured at room temperature and at Vds= 10mV of the same device showed in a. The obtained electron and hole mobility values from the peak transconductance method are reported in the the graph.* ***c,*** *Output characteristics, measured applied V_{DS}= 10 mV and different bending strain for a TFT with a h-BN thickness of 400 nm.* ***d,*** *Normalized hole mobility (with respect to the mobility valu ein flat conditions) as a function of bending radius. The inset shows photographs on how the mechanical bending was performed .*

Conclusion

We designed a water-based h-BN ink processed by microfluidics processor. The developed dispersions showed good stability and h-BN flakes with nanometric thickness (~5.7 nm) and lateral size (~240 nm). Inkjet printed h-BN layers with a thickness of ~100 nm in MIM-structured devices are demonstrated showing high-k characteristics ε_{hBN} ~6.92. Flexible fully-inkjet printed graphene/h-BN TFTs with state of the art mobility up to 110 $cm^2V^{-1}s^{-1}$ are reported demonstrating the distinctive dielectric properties of the h-BN ink both in flat and bended configuaration. In addition, low-temperature processability (~100 °C, suitable for flexible substrate), high capacitance for low-voltage operation reduced thickness to achieve pin-hole free films and good mechanical properties are clear advantages of the demonstrated h-BN dielectric ink.Overall, this work has shown for the first time that exfoliated h-BN nanosheets constitute an adequate high-k dielectric material to act as gate oxide and thus complement with graphene in fully inkjet-printed 2D-based flexible microelectronics.

Methods

Exfoliation of h-BN nanosheets

Microfluidization is a homogenization method that applies high pressure (up to 207 MPa) to a fluid forcing it to pass through a microchannel (diameter, *d*=75 μm), as shown in Fig. 1a. The key advantage over sonication and shear-mixing is that high shear rate, $\gamma > 10^6$ s^{-1} is applied to the whole fluid volume, and not just locally. Exfoliated h-BN nanosheets were prepared via LPE by a benchmark existing microfluidizer processor (M-110P, Microfludics Corp.). Its high pressure homogenization (up to 2069 bar/ 207 Pa/ 30000 Psi) promotes several forces into a well-designed interaction chamber (F-20Y-RT) based on micro channels (~75 μm), where the dispersion stream is constrained to pass through at velocities up to 400 $m \cdot s^{-1}$. In order to prepare a stable and high-concentrated h-BN ink, 4 $mg \cdot ml^{-1}$ sodium-carboxymethyl cellulose (CMC-Na Sigma Aldrich 700000) was dispersed in distilled water (100 ml) and stirred for 12 h to obtain homogeneous and stable solution. Then, an initial concentration of 10 mg/ml of commercial hexagonal BN powder (<10 um, 99.99%, Good-Fellow) was added (as received) to the dispersion and subjected to the high pressure of microfluidizer under a constant pressure (~2068 bar – 30000 Psi) up to 100 cycles (2 h), and kept at 25 °C through an external cooling equipment. The obtained h-BN nanosheets / water-CMC homogeneous mixture was ultra-centrifuged (10000 rpm for 20 min) to remove undesired residual large-size h-BN flakes. Finally, the supernatant (top two thirds of the centrifuged dispersion) was collected by pipette and the final solution was kept at an atmospheric condition (20 °C).

Dispersion properties and stability measurements

Toptical absorbance was measured by Perkin-Elmer Lamba 950 spectrometer with 1-nm resolution. To evaluate the dispersion stability, the zeta potential value was measured using a Zetasizer Nano ZS90 equipment with irradiation from a 633 nm He-Ne laser. The concentration of the h-BN / water-CMC ink for the zeta potential tests was ~1 mg/ml at a pH of 6.4 (Malvern Instruments, Worcestershire, UK).

The ink stability was assessed by Turbiscan LabExpert, connected to a cooling system TLab Cooler. The steady shear viscosity measurements were performed using a rotational Discovery Series Hybrid Rheometer (DHR-1) instrument equipped with an integrated magnetic cylinder geometry. The temperature range of measurements (from 10 to 100 °C) was regulated by a Peltier Plate temperature controller.

Structural and physicochemical characterization

The insulator h-BN /CMC ink was morphologically, structurally and chemically characterized, both as solution and after the printing process as inkjet-printed film.

The morphology and structure were studied by FE-SEM with a FEI Nova 200 instrument, and by TEM using a JEOL JEM 2100 (Japan) microscope, and a JEOL JEM 2010F equipped with a Tridiem Gatan imaging filter, both operating at 200 kV. Copper micro-grid covered with carbon film was used to deposit the h-BN on top. Additionally, the flake thickness were evaluated in a tapping mode by an AFM Digital Instruments Nanoscope D-5000. AFM scans were performed at 5 different locations on the substrate with each scan spanning an area of 20 μm × 20 μm. For each processing condition we measured 150 flakes. After depositing the printed ink solution onto the PET substrate and annealing at 100 °C, the morphology of the sample surface was accurately observed by scanning the x-y plane, with a z-axis resolution limit around ~1 nm at a scan rate of 0.5 Hz.

The crystalline microstructure, orientation and size of the h-BN nanosheets were studied by XRD using a Japan Rigaku D/Max-IIA X-ray diffractometer using Cu K_α radiation, λ = 1.5406 Å, operating at 40 keV and 40 mA. A further study of the h-BN nanosheets quality , both in solution and after the printing process in the heterostructure stack, was performed by Raman, employing a Horiba Jobin-Yvon LabRam HR800 micro-Raman spectrometer operating at 20 mW laser power and an excitation wavelength of 532 nm (2^{nd} harmonic of a Nd:YAG continuous-wave laser) in the visible range and 325 nm (He-Cd continuous-wave laser) in the UV range. Fourier Transform Infra-Red Spectroscopy (FTIR) spectra were acquired on a Thermo Scientific Systems NICOLET iN10 FT-IR spectrometer with a DTGS detector for far-IR in the spectral range from 4000 to 220 cm^{-1} to study the chemical interaction within the h-BN nanosheets / water-CMC solution, and to estimate the presence of the possible compounds adsorbed on the h-BN / water-CMC surface. The analysis of the chemical composition of the h-BN / water-CMC film was performed using a PHI ESCA-5500 X-ray photoelectron spectrometer (XPS) with a monochromatic Al K_α radiation (E = 1486 eV) at 350.0 W with the X-ray source and detector forming an angle of 45° with the normal of the sample, i.e., 90° between them. The binding energy was calibrated with reference to the C 1s energy (284.8 eV).
Thin films were deposited by inkjet printing on PET substrate in order to fabricate devices such as capacitors and transistors. FE-SEM and TEM cross-section of the fully-printed devices were cut with focus ion-beam (FIB,FIB CrossBeam 1560XB, Zeiss). After FIB cross-section cut, the sample wa analysed by high-resolution field-emission variable-pressure (VP) scanning electron microscope (SEM) Zeiss 1555 VP-FESEM. X–ray microanalyses have been performed using an Oxford Instruments X-Max 80 silicon drift EDS system with AZtec and INCA software. TEM images and EEL spectra of the devices cross-sections were obtained in a JEOL J2010F microscope, coupled to a Gatan GIF spectrometer.

Device fabrication using inkjet printing technology

A Fujifilm Dimatix DMP 2831 inkjet printer was employed equipped with cartridges with droplet volume of 1 pL (for conductive ink) and of 10 pL (for 2d materials). Three types of inks were used for inkjet print the final TFT heterostructure : a conductive Ag-nanoparticles (NPs)-based ink, a graphene solution[38] for the channel, and the formulated h-BN / water-CMC ink as high-k dielectric . Contact leads were printed using Ag NPs-based ink from Advanced Nano Product (DGP-HR, 30% w/w). Graphene ink, with a concentration of ~0.1 $g \cdot L^{-1}$, was produced by liquid phase exfoliation (LPE) of graphite in N-Methylpyrrolidone (NMP) using bath sonication, as already described in Ref. (torrisi, 78).

MIM capacitor: A silver bottom electrode with a thickness of 300 nm was printed onto glass substrate; afterwards, it was annealed in vacuum at 100 °C for 12 h in order to remove the organic solvents and to achieve the expected resistivity around 16 μΩ·cm.[144] The h-BN film on top was deposited by printing with ejection frequency of 2 kHz and a resolution of 20-μm drop-size were used in order to reach controlled nanometric thicknesses from 100 to 300 nm, with steps of 50 nm. During the printing of the h-BN layer, the temperature was kept constant at 30 °C while . A post-deposition annealing at 100 °C, for 12 h in a vacuum oven, was performed for the complete elimination of physisorbed water. Subsequently, the silver NPs top electrode was deposited and annealed under the same conditions of the bottom electrode.

Thin Film Transistor: Top gate configuration was selected as the best configuration for the fabrication of graphene-based transistors. Graphene ink [38] was used as active material to print micro patterns onto the PET substrate. The printed film, 50 printed-passes thick, was annealed at 100 °C in vacuum in order to remove the residual solvent. Silver electrodes were deposited onto the graphene layer by high-resolution drop jetting with a pad width of ~25 μm and a channel length of ~25 μm. Post-deposition annealing was performed in vacuum at 100 °C for 24 h in order to remove the organic solvents and to achieve the expected resistivity. High-k h-BN / water-CMC insulator ink was deposited as gate dielectric material and annealed at 100 °C in vacuum in order to remove the remaining solvent Finally, silver top gate electrode was printed and annealed under the same conditions than source and drain electrodes.

Electrical measurements

The current versus DC voltage characteristics were measured by a B1500-A Semiconductor Device Analyzer (Agilent). The admittance versus voltage and admittance versus frequency curves were obtained using the same Agilent B1500-A with an integrated capacitance-voltage (C–V) module suitable for operation frequencies ranging from 10 kHz to 1 MHz and DC voltage biases in the range from -5 to +5 V. For the acquisition of transport data, the devices characterisation was carried out at room temperature (~24 °C) using a four-probes configuration.

Mobility extraction: Taking into account the linear region of the output characteristic curve of a TFT in Ohmic mode, where V_{DS} is small enough in comparison to V_{GS}, both the field-effect hole and electron mobilities (μ_P and μ_n, respectively) were extracted from the following relation:

$$\mu_{h,e} = g_m \cdot \frac{L}{W} \cdot \frac{1}{C_{ox}} \cdot \frac{1}{V_{DS}} \ , \ g_m = \frac{\delta I_{drain}}{\delta V_{gate}}, \qquad \text{[eq. 4]}$$

where g_m is the transconductance, L is the channel length, W is the channel width, C_{ox} is the gate oxide capacitance per unit area of inkjet-printed h-BN dielectric, and V_{DS} the voltage applied in the linear region of the output characteristic curve.

Bending estimation: The bending tests were performed on all TFT devices attaching the PET substrate on cylinders with different radii. The induced bending strain was calculated via eq. 5, and the devices tested under linear increasing strain (0.5%, 0.75% and 1.5%):

$$Bending\ strain = \frac{\left(R+\frac{t}{2}\right)-R\cdot d\theta}{R\cdot d\theta} = \frac{t}{2\cdot R}, \qquad \text{[eq. 5]}$$

where $d\theta$ is the measured angle from the point of origin to the natural axis of the substrate.

References :

1. Itrs. International Technology Roadmap for Semiconductors 2.0: Executive Report. *Int. Technol. roadmap Semicond.* (2015). at <http://www.semiconductors.org/main/2015_international_technology_roadmap_for_semiconductors_itrs/>
2. www.oe-a.org. Roadmap for Organic and Printed Electronics Applications. (2015).

3. Geim, a K. & Novoselov, K. S. The rise of graphene. *Nat. Mater.* **6,** 183–91 (2007).

4. Novoselov, K. S. *et al.* A roadmap for graphene. *Nature* **490,** 192–200 (2012).

5. Novoselov, K. S. *et al.* Two-dimensional atomic crystals. *Proc. Natl. Acad. Sci. U. S. A.* **102,** 10451–3 (2005).

6. Novoselov, K. S., Mishchenko, A., Carvalho, A., Neto, A. H. C. & Road, O. 2D materials and van der Waals heterostructures. *Science (80-.).* **353,** aac9439 (2016).

7. Ferrari, A. C. *et al.* Science and technology roadmap for graphene, related two-dimensional crystals, and hybrid systems. *Nanoscale* **7,** 4598–4810 (2015).

8. Guo, Z. *et al.* Record maximum oscillation frequency in C-face epitaxial graphene transistors. *Nano Lett.* **13,** 942–7 (2013).

9. Wu, Y. *et al.* State-of-the-art graphene high-frequency electronics. *Nano Lett.* **12,** 3062–7 (2012).

10. Jiang, J. *et al.* Fabrication of Transparent Multilayer Circuits by Inkjet Printing. *Adv. Mater.* **28,** 1420–1426 (2016).

11. Tobjörk, D. & Österbacka, R. Paper Electronics. *Adv. Mater.* **23,** 1935–1961 (2011).

12. Berggren, M., Nilsson, D. & Robinson, N. D. Organic materials for printed electronics. *Nat. Mater.* **6,** 3–5 (2007).

13. Siegel, A. C. *et al.* Foldable printed circuit boards on paper substrates. *Adv. Funct. Mater.* **20,** 28–35 (2010).

14. Burns, S. E., Cain, P., Mills, J., Wang, J. & Sirringhaus, H. Inkjet Printing of Polymer Thin-Film Transistor Circuits. *MRS Bull.* **28,** 829–834 (2003).

15. Pudas, M., Halonen, N., Granat, P. & Vähäkangas, J. Gravure printing of conductive particulate polymer inks on flexible substrates. *Prog. Org. Coatings* **54,** 310–316 (2005).

16. Krebs, F. C. *et al.* A complete process for production of flexible large area polymer solar cells entirely using screen printing—First public demonstration. *Sol. Energy Mater. Sol. Cells* **93,** 422–441 (2009).

17. Søndergaard, R. R., Hösel, M. & Krebs, F. C. Roll-to-Roll fabrication of large area functional organic materials. *J. Polym. Sci. Part B Polym. Phys.* **51,** 16–34 (2013).

18. Choi, H. W., Zhou, T., Singh, M. & Jabbour, G. E. Recent developments and directions in printed nanomaterials. *Nanoscale* **7,** 3338–3355 (2014).

19. Calvert, P. Inkjet printing for materials and devices. *Chemistry of Materials* **13,** 3299–3305 (2001).

20. Singh, M., Haverinen, H. M., Dhagat, P. & Jabbour, G. E. Inkjet printing-process and its applications. *Adv. Mater.* **22,** 673–685 (2010).

21. Li, J. *et al.* Indium tin oxide modified transparent nanotube thin films as effective anodes for flexible organic light-emitting diodes. *Appl. Phys. Lett.* **93,** 83306 (2008).

22. Chang, S.-C. *et al.* Multicolor Organic Light-Emitting Diodes Processed by Hybrid Inkjet Printing. *Adv. Mater.* **11,** 734–737 (1999).

23. Rutherglen, C., Jain, D. & Burke, P. Nanotube electronics for radiofrequency applications. *Nat. Nanotechnol.* **4,** 811–819 (2009).

24. Kaltenbrunner, M. *et al.* Ultrathin and lightweight organic solar cells with high flexibility. *Nat.*

Commun. **3,** 770 (2012).

25. Galstyan, V. *et al.* Vertically Aligned TiO2 Nanotubes on Plastic Substrates for Flexible Solar Cells. *Small* **7,** 2437–42 (2011).

26. Krebs, F. C. Fabrication and processing of polymer solar cells: A review of printing and coating techniques. *Sol. Energy Mater. Sol. Cells* **93,** 394–412 (2009).

27. Takei, K. *et al.* Nanowire active-matrix circuitry for low-voltage macroscale artificial skin. *Nat. Mater.* **9,** 821–6 (2010).

28. Fortunato, E. M. C. *et al.* Fully transparent ZnO thin-film transistor produced at room temperature. *Adv. Mater.* **17,** 590–594 (2005).

29. Stutzmann, N., Friend, R. H. & Sirringhaus, H. Self-Aligned, Vertical-Channel, Polymer Field-Effect Transistors. *Science (80-.).* **299,** 1881–1884 (2003).

30. Kim, T. Y. *et al.* Electrical Properties of Synthesized Large-Area MoS2 Field-Effect Transistors Fabricated with Inkjet-Printed Contacts. *ACS Nano* **10,** 2819–2826 (2016).

31. Choi, H. W., Zhou, T., Singh, M. & Jabbour, G. E. Recent developments and directions in printed nanomaterials. *Nanoscale* **7,** 3338–3355 (2015).

32. Gao, M., Li, L. & Song, Y. Inkjet printing wearable electronic devices. *J. Mater. Chem. C* **5,** 2971–2993 (2017).

33. Wang, C. *et al.* Self-aligned, extremely high frequency III-V metal-oxide-semiconductor field-effect transistors on rigid and flexible substrates. *Nano Lett.* **12,** 4140–5 (2012).

34. Zhao, N. *et al.* Self-aligned inkjet printing of highly conducting gold electrodes with submicron resolution. *J. Appl. Phys.* **101,** 64513 (2007).

35. Sekitani, T., Noguchi, Y., Zschieschang, U., Klauk, H. & Someya, T. Organic transistors manufactured using inkjet technology with subfemtoliter accuracy. *Proc. Natl. Acad. Sci. U. S. A.* **105,** 4976–4980 (2008).

36. Van Osch, T. H. J., Perelaer, J., De Laat, A. W. M. & Schubert, U. S. Inkjet printing of narrow conductive tracks on untreated polymeric substrates. *Adv. Mater.* **20,** 343–345 (2008).

37. Hernandez, Y. *et al.* High yield production of graphene by liquid phase exfoliation of graphite. *Nat. Nanotechnol.* **3,** 563–8 (2008).

38. Torrisi, F. *et al.* Inkjet-printed graphene electronics. *ACS Nano* **6,** 2992–3006 (2012).

39. Capasso, a. *et al.* Ink-jet printing of graphene for flexible electronics: An environmentally-friendly approach. *Solid State Commun.* **224,** 53–63 (2015).

40. Nguyen, B. H. & Nguyen, V. H. Promising applications of graphene and graphene-based nanostructures. *Adv. Nat. Sci. Nanosci. Nanotechnol.* **7,** 23002 (2016).

41. Wang, Z. *et al.* Fabrication of Boron Nitride Nanosheets by Exfoliation. *Chem. Rec.* 1204–1215 (2016). doi:10.1002/tcr.201500302

42. Lee, D. *et al.* Scalable exfoliation process for highly soluble boron nitride nanoplatelets by hydroxide-assisted ball milling. *Nano Lett.* **15,** 1238–1244 (2015).

43. Kim, J. *et al.* Direct exfoliation and dispersion of two-dimensional materials in pure water via temperature control. *Nat. Commun.* **6,** 8294 (2015).

44. Backes, C. *et al.* Production of Highly Monolayer Enriched Dispersions of Liquid-Exfoliated Nanosheets by Liquid Cascade Centrifugation. *ACS Nano* acsnano.5b07228 (2016). doi:10.1021/acsnano.5b07228

45. Bonaccorso, F., Bartolotta, A., Coleman, J. N. & Backes, C. 2D-Crystal-Based Functional Inks. *Adv. Mater.* **28,** 6136–6166 (2016).

46. Robertson, J. High dielectric constant oxides. *Eur. Phys. J. Appl. Phys.* **291,** 265–291 (2004).

47. Lee, G.-H. *et al.* Flexible and Transparent MoS 2 Field-Effect Transistors on Hexagonal Boron Nitride-Graphene Heterostructures. *ACS Nano* **7,** 7931–7936 (2013).

48. Shi, Y. *et al.* Synthesis of few-layer hexagonal boron nitride thin film by chemical vapor deposition. *Nano Lett.* **10,** 4134–4139 (2010).

49. Kim, K. K. *et al.* Synthesis of Monolayer Boron Nitride on Cu Foil Using Chemical Vapor Deposition. *Nano Lett.* **xx,** xx (2011).

50. Kudin, K. N., Scuseria, G. E. & Yakobson, B. I. C2F, BN, and C nanoshell elasticity from ab initio computations. *Phys. Rev. B* **64,** 235406 (2001).

51. Cai, W. *et al.* Thermal transport in suspended and supported monolayer graphene grown by chemical vapor deposition. *Nano Lett.* **10,** 1645–1651 (2010).

52. Forster, F. *et al.* Dielectric screening of the Kohn anomaly of graphene on hexagonal boron nitride. *Phys. Rev. B - Condens. Matter Mater. Phys.* **88,** 1–7 (2013).

53. Yurdakul, H. *et al.* Nanoscopic characterization of two-dimensional (2D) boron nitride nanosheets (BNNSs) produced by microfluidization. *Ceram. Int.* **38,** 2187–2193 (2012).

54. Lin, Y. & Connell, J. W. Advances in 2D boron nitride nanostructures: nanosheets, nanoribbons, nanomeshes, and hybrids with graphene. *Nanoscale* **4,** 6908–39 (2012).

55. Yin, J. *et al.* Boron Nitride Nanostructures: Fabrication, Functionalization and Applications. *Small* 1–27 (2016). doi:10.1002/smll.201600053

56. Feng, P. *et al.* Fringe structures and tunable bandgap width of 2D boron nitride nanosheets. *Beilstein J. Nanotechnol.* **5,** 1186–92 (2014).

57. Coleman, J. N. *et al.* Two-dimensional nanosheets produced by liquid exfoliation of layered materials. *Science* **331,** 568–71 (2011).

58. Wang, Y. *et al.* Raman Studies of Monolayer Graphene : The Substrate Effect. *J. Phys. Chem. C* **112,** 10637–10640 (2008).

59. Yi, M. *et al.* Hydrodynamics-assisted scalable production of boron nitride nanosheets and their application in improving oxygen-atom erosion resistance of polymeric composites. *Nanoscale* **5,** 10660–7 (2013).

60. Karagiannidis, P. G. *et al.* Microfluidization of Graphite and Formulation of Graphene-Based Conductive Inks. *ACS Nano* **1,** acsnano.6b07735 (2017).

61. Bergin, S. D. *et al.* Towards solutions of single-walled carbon nanotubes in common solvents. *Adv. Mater.* **20,** 1876–1881 (2008).

62. Nicolosi, V., Chhowalla, M., Kanatzidis, M. G., Strano, M. S. & Coleman, J. N. Liquid Exfoliation of Layered Materials. *Science (80-.).* **340,** 1226419 (2013).

63. Paria, S. & Khilar, K. C. A review on experimental studies of surfactant adsorption at the hydrophilic solid-water interface. *Adv. Colloid Interface Sci.* **110,** 75–95 (2004).

64. Green, A. a & Hersam, M. C. Solution phase production of graphene with controlled thickness via density differentiation. *Nano Lett.* **9,** 4031–6 (2009).

65. Maragó, O. M. *et al.* Brownian motion of graphene. *ACS Nano* **4,** 7515–7523 (2010).

66. May, P., Khan, U., Hughes, J. M. & Coleman, J. N. Role of solubility parameters in understanding the steric stabilization of exfoliated two-dimensional nanosheets by adsorbed polymers. *J. Phys. Chem. C* **116,** 11393–11400 (2012).

67. Raddaha, N. S. *et al.* Electrophoretic deposition of chitosan/h-BN and chitosan/h-BN/TiO2 composite coatings on stainless steel (316L) substrates. *Materials (Basel).* **7,** 1814–1829 (2014).

68. Pradhan, G. C., Behera, L. & Swain, S. K. Effects of boron nitride nanopowder on thermal, chemical and gas barrier properties of starch. *Chinese J. Polym. Sci.* **32,** 1311–1318 (2014).

69. Bouville, F. & Deville, S. Dispersion of boron nitride powders in aqueous suspensions with cellulose. *J. Am. Ceram. Soc.* **97,** 394–398 (2014).

70. Petritz, A. *et al.* Cellulose as biodegradable high-k dielectric layer in organic complementary inverters. *Appl. Phys. Lett.* **103,** (2013).

71. Petritz, A. *et al.* Dielectrics: Cellulose-Derivative-Based Gate Dielectric for High-Performance Organic Complementary Inverters (Adv. Mater. 46/2015). *Adv. Mater.* **27,** 7485 (2015).

72. Yadav, M., Rhee, K. Y., Jung, I. H. & Park, S. J. Eco-friendly synthesis, characterization and properties of a sodium carboxymethyl cellulose/graphene oxide nanocomposite film. *Cellulose* **20,** 687–698 (2013).

73. K, U. & Hoffmann, H. Structure and solution properties of sodium carboxymethyl cellulose. **7757,** (1997).

74. Zhivkov, A. M. Electric Properties of Carboxymethyl Cellullose. *Cellul. Asp.* **10,** 197–226 (2013).

75. Samsudin, A. S., Lai, H. M. & Isa, M. I. N. Electrochimica Acta Biopolymer Materials Based Carboxymethyl Cellulose as a Proton Conducting Biopolymer Electrolyte for Application in Rechargeable Proton Battery. *Electrochim. Acta* **129,** 1–13 (2014).

76. Wei, L., Chen, C. & Wei, H. Poly (acrylic acid sodium) grafted carboxymethyl cellulose as a high performance polymer binder for silicon anode in lithium ion batteries.

77. Li, Y. *et al.* Nanocellulose as green dispersant for two-dimensional energy materials. *Nano Energy* **13,** 346–354 (2015).

78. Saake, B., Horner, S., Puls, J., Heinze, T. & Koch, W. A new approach in the analysis of the substituent distribution of carboxymethyl celluloses. *Cellulose* **8,** 59–67 (2001).

79. International Technology Roadmap for Semiconductors 2.0 2015 Edition, B. C. Beyond CMOS. 1–93 (2015). at <http://www.itrs2.net/itrs-reports.html>

80. Fukuda, K. *et al.* Fully-printed high-performance organic thin-film transistors and circuitry on one-micron-thick polymer films. *Nat. Commun.* **5,** 4147 (2014).

81. Yuan, Y. *et al.* Ultra-high mobility transparent organic thin film transistors grown by an off-centre spin-coating method. *Nat. Commun.* **5,** 3005 (2014).

82. Chen, K. *et al.* Printed Carbon Nanotube Electronics and Sensor Systems. *Adv. Mater.* **28,** 4397–4414 (2016).

83. Cao, C., Andrews, J. B., Kumar, A. & Franklin, A. D. Improving Contact Interfaces in Fully Printed Carbon Nanotube Thin-Film Transistors. *ACS Nano* **10,** 5221–5229 (2016).

84. Secor, E. B., Smith, J., Marks, T. J. & Hersam, M. C. High-Performance Inkjet-Printed Indium-Gallium-Zinc-Oxide Transistors Enabled by Embedded, Chemically Stable Graphene Electrodes. *ACS Appl. Mater. Interfaces* **8,** 17428–17434 (2016).

85. Choi, C.-H., Lin, L.-Y., Cheng, C.-C. & Chang, C. -h. Printed oxide thin film transistors: a mini review. *ECS J. Solid State Sci. Technol.* **4,** P3044–P3051 (2015).

86. Mikolajek, M. *et al.* Direct Inkjet Printing of Dielectric Ceramic/Polymer Composite Thick Films. *Adv. Eng. Mater.* **17,** 1294–1301 (2015).

87. Vaklev, N. L. *et al.* High-Performance Flexible Bottom-Gate Organic Field-Effect Transistors with Gravure Printed Thin Organic Dielectric. *Adv. Mater. Interfaces* **1,** 1–6 (2014).

88. Moya, A. *et al.* All-inkjet-printed dissolved oxygen sensors on flexible plastic substrates. *Org. Electron. physics, Mater. Appl.* **39,** 168–176 (2016).

89. Petritz, A. *et al.* High performance p-type organic thin film transistors with an intrinsically photopatternable, ultrathin polymer dielectric layer. *Org. Electron. physics, Mater. Appl.* **14,** 3070–3082 (2013).

90. Mariotti, C. *et al.* State-of-the-Art Inkjet-Printed Metal-Insulator-Metal (MIM) Capacitors on Silicon Substrate. *Ieee Microw. Wirel. Components Lett.* **25,** 13–15 (2015).

91. Ahmad, Z. in *Dielectric Material* 3–26 (InTech, 2012). doi:10.5772/50638

92. Hassinen, T., Ahn, B. & Ko, S. Printed polymer and carbon nanotube thin film transistors with high- k barium titanate insulator. *Jpn. J. Appl. Phys.* **53,** 05HB14 (2014).

93. Petritz, a. *et al.* Cellulose as biodegradable high-k dielectric layer in organic complementary inverters. *Appl. Phys. Lett.* **103,** (2013).

94. Vescio, G., López-Vidrier, J., Leghrib, R., Cornet, A. & Cirera, A. Flexible inkjet printed high-k HfO 2 - based MIM capacitors. *J. Mater. Chem. C* **4,** 1804–1812 (2016).

95. Sakai, Y., Futakuchi, T. & Adachi, M. Preparation of BaTiO3 thick films by inkjet printing on oxygen-plasma-modified substrates. *Japanese J. Appl. Physics, Part 1 Regul. Pap. Short Notes Rev. Pap.* **45,** 7247–7251 (2006).

96. McManus, D. *et al.* Water-based and biocompatible 2D crystal inks for all-inkjet-printed heterostructures. *Nat. Nanotechnol.* (2017). doi:10.1038/nnano.2016.281

97. Lee, Y. H. *et al.* Synthesis of large-area MoS 2 atomic layers with chemical vapor deposition. *Adv. Mater.* **24,** 2320–2325 (2012).

98. Li, X. *et al.* Large-area synthesis of high-quality and uniform graphene films on copper foils. *Science (80-.).* **324,** 1312–1314 (2009).

99. Song, L. *et al.* Large scale growth and characterization of atomic hexagonal boron nitride layers. *Nano Lett.* **10,** 3209–3215 (2010).

100. Li, X. *et al.* Large-Area Synthesis of High-Quality and Uniform Graphene Films on Copper Foils.

Science (80-.). **324,** 1312–1314 (2009).

101. Lee, J.-H. *et al.* Wafer-Scale Growth of Single-Crystal Monolayer Graphene on Reusable Hydrogen-Terminated Germanium. *Science (80-.).* **344,** 286–289 (2014).

102. Lee, C., Wei, X., Kysar, J. W. & Hone, J. Measurement of the Elastic Properties and Intrinsic Strength of Monolayer Graphene. *Science (80-.).* **321,** 385–388 (2008).

103. Withers, F. *et al.* Light-emitting diodes by band-structure engineering in van der Waals heterostructures. *Nat Mater* **14,** 301–306 (2015).

104. Castellanos-Gomez, A., Singh, V., van der Zant, H. S. J. & Steele, G. A. Mechanics of freely-suspended ultrathin layered materials. *Ann. Phys.* **527,** 27–44 (2015).

105. Radisavljevic, B., Radenovic, a, Brivio, J., Giacometti, V. & Kis, a. Single-layer MoS2 transistors. *Nat. Nanotechnol.* **6,** 147–50 (2011).

106. Li, M. Y., Chen, C. H., Shi, Y. & Li, L. J. Heterostructures based on two-dimensional layered materials and their potential applications. *Mater. Today* **19,** 322–335 (2015).

107. Li, X. Q. and Y. W. and W. L. and J. L. and J. *et al.* Modelling of stacked 2D materials and devices. *2D Mater.* **2,** 32003 (2015).

108. Sun, Z., Martinez, A. & Wang, F. Optical modulators with two-dimensional layered materials. *Nat. Photonics* **10,** 227–238 (2016).

109. Tien, D. H. *et al.* Study of Graphene-based 2D-Heterostructure Device Fabricated by All-Dry Transfer Process. *ACS Appl. Mater. Interfaces* **8,** 3072–3078 (2016).

110. Berger, C. *et al.* Ultrathin Epitaxial Graphite: 2D Electron Gas Properties and a Route toward Graphene-based Nanoelectronics. *J. Phys. Chem. B* **108,** 19912–19916 (2004).

111. Emtsev, K. V., Speck, F., Seyller, T., Ley, L. & Riley, J. D. Interaction, growth, and ordering of epitaxial graphene on SiC{0001} surfaces: A comparative photoelectron spectroscopy study. *Phys. Rev. B - Condens. Matter Mater. Phys.* **77,** 1–10 (2008).

112. Wang, Q. H., Kalantar-Zadeh, K., Kis, A., Coleman, J. N. & Strano, M. S. Electronics and optoelectronics of two-dimensional transition metal dichalcogenides. *Nat. Nanotechnol.* **7,** 699–712 (2012).

113. Fiori, G. *et al.* Electronics based on two-dimensional materials. *Nat. Nanotechnol.* **9,** 768–779 (2014).

114. Kim, S. M. *et al.* Synthesis of large-area multilayer hexagonal boron nitride for high material performance. *Nat. Commun.* **6,** 8662 (2015).

115. Bonaccorso, F. *et al.* 2D materials. Graphene, related two-dimensional crystals, and hybrid systems for energy conversion and storage. *Science (80-.).* **347,** 1246501 (2015).

116. Zhi, C., Bando, Y., Tang, C., Kuwahara, H. & Golberg, D. Large-scale fabrication of boron nitride nanosheets and their utilization in polymeric composites with improved thermal and mechanical properties. *Adv. Mater.* **21,** 2889–2893 (2009).

117. Shanmugam, M., Jacobs-Gedrim, R., Durcan, C. & Yu, B. 2D layered insulator hexagonal boron nitride enabled surface passivation in dye sensitized solar cells. *Nanoscale* **5,** 11275–82 (2013).

118. Bonaccorso, F. *et al.* Production and processing of graphene and 2d crystals. *Mater. Today* **15,** 564–589 (2012).

119. Yurdakul, H. *et al.* Nanoscopic characterization of two-dimensional (2D) boron nitride nanosheets (BNNSs) produced by microfluidization. *Ceram. Int.* **38,** 2187–2193 (2012).

120. Shang, J., Xue, F., Fan, C. & Ding, E. Preparation of few layers hexagonal boron nitride nanosheets via high-pressure homogenization. *Mater. Lett.* (2016). doi:10.1016/j.matlet.2016.05.154

121. Ummartyotin, S. & Manuspiya, H. A critical review on cellulose: From fundamental to an approach on sensor technology. *Renew. Sustain. Energy Rev.* **41,** 402–412 (2015).

122. Lopez, C. G., Rogers, S. E., Colby, R. H., Graham, P. & Cabral, J. T. Structure of sodium carboxymethyl cellulose aqueous solutions: A SANS and rheology study. *J. Polym. Sci. Part B Polym. Phys.* **53,** 492–501 (2015).

123. Cuba-Chiem, L. T., Huynh, L., Ralston, J. & Beattie, D. a. In situ particle film ATR FTIR spectroscopy of carboxymethyl cellulose adsorption on talc: Binding mechanism, pH effects, and adsorption kinetics. *Langmuir* **24,** 8036–8044 (2008).

124. Coleman, J. N. Liquid-phase exfoliation of nanotubes and graphene. *Adv. Funct. Mater.* **19,** 3680–3695 (2009).

125. Joni, I. M., Balgis, R., Ogi, T., Iwaki, T. & Okuyama, K. Surface functionalization for dispersing and stabilizing hexagonal boron nitride nanoparticle by bead milling. *Colloids Surfaces A Physicochem. Eng. Asp.* **388,** 49–58 (2011).

126. Gorbachev, R. V. *et al.* Hunting for monolayer boron nitride: Optical and raman signatures. *Small* **7,** 465–468 (2011).

127. Shlomo Magdassi & Magdassi, S. Ink jet printing — Post Office project. *Pigment Resin Technol.* **16,** 4–10 (1987).

128. Jang, D., Kim, D. & Moon, J. Influence of fluid physical properties on ink-jet printability. *Langmuir* **25,** 2629–2635 (2009).

129. Pease, R. S. Crystal Structure of Boron Nitride. *Nature* **165,** 722–723 (1950).

130. Yuan, S. *et al.* Pure &crystallized 2D Boron Nitride sheets synthesized via a novel process coupling both PDCs and SPS methods. *Sci. Rep.* **6,** 20388 (2016).

131. Thangasamy, P. & Sathish, M. Supercritical fluid processing: a rapid, one-pot exfoliation process for the production of surfactant-free hexagonal boron nitride nanosheets. *CrystEngComm* **17,** 5895–5899 (2015).

132. Bagus, P. S., Ilton, E. S. & Nelin, C. J. The interpretation of XPS spectra: Insights into materials properties. *Surf. Sci. Rep.* **68,** 273–304 (2013).

133. Pasqui, D., De Cagna, M. & Barbucci, R. Polysaccharide-based hydrogels: The key role of water in affecting mechanical properties. *Polymers (Basel).* **4,** 1517–1534 (2012).

134. Kelly, A. G., Finn, D., Harvey, A., Hallam, T. & Coleman, J. N. All-printed capacitors from graphene-BN-graphene nanosheet heterostructures. *Appl. Phys. Lett.* **109,** (2016).

135. Withers, F. *et al.* Heterostructures produced from nanosheet-based inks. *Nano Lett.* **14,** 3987–3992 (2014).

136. Geick, R., Perry, C. & Rupprecht, G. Normal Modes in Hexagonal Boron Nitride. *Phys. Rev.* **146,** 543–547 (1966).

137. Ferrari, a. & Robertson, J. Interpretation of Raman spectra of disordered and amorphous carbon. *Phys. Rev. B* **61,** 14095–14107 (2000).

138. Ferrari, A. C. & Basko, D. M. Raman spectroscopy as a versatile tool for studying the properties of graphene. *Nat. Nanotechnol.* **8,** 235–46 (2013).

139. Latil, S., Meunier, V. & Henrard, L. Massless fermions in multilayer graphitic systems with misoriented layers: Ab initio calculations and experimental fingerprints. *Phys. Rev. B - Condens. Matter Mater. Phys.* **76,** 1–4 (2007).

140. Xia, F., Perebeinos, V., Lin, Y., Wu, Y. & Avouris, P. The origins and limits of metal-graphene junction resistance. *Nat Nano* **6,** 179–184 (2011).

141. Kim, B. J. *et al.* High-performance flexible graphene field effect transistors with ion gel gate dielectrics. *Nano Lett.* **10,** 3464–6 (2010).

142. Sire, C. *et al.* Flexible gigahertz transistors derived from solution-based single-layer graphene. *Nano Lett.* **12,** 1184–1188 (2012).

143. Kim, S. M. *et al.* Transparent and flexible graphene charge-trap memory. *ACS Nano* **6,** 7879–7884 (2012).

144. Perelaer, J., De Gans, B. J. & Schubert, U. S. Ink-jet printing and microwave sintering of conductive silver tracks. *Adv. Mater.* **18,** 2101–2104 (2006).

145. Yeasmin, M. S. & Mondal, M. I. H. Synthesis of highly substituted carboxymethyl cellulose depending on cellulose particle size. *Int. J. Biol. Macromol.* **80,** 725–31 (2015).

Supplementary

Mechanism of exfoliation

Several techniques have been tested to exfoliate 2D h-BN nanosheets (Fig. S1). Among these methods, the most employed is the sonication technique (potentially bath and tip), which mainly exploits the generated liquid cavitation (a tensile stress wave as a result of the propagation of micro-jets and compressive shock stress waves) to exfoliate the selected material into different solvents, surfactants or polymeric dispersions. Other methods such as milling or shear fluidic film techniques take advantage of the rotating balls to generate shear force or lateral collision to exfoliate. In the light of all the above-mentioned techniques, microfluidization method induces high pressure release effect and Reynolds shear stress simultaneously to all the described exfoliation mechanisms.

Previous studies have shown that BNNSs could be attached to hydroxyl groups through edges and defects after LPE-assisted hydrolysis in water. Therefore, hydrogen bonding justifies the affinity of h-BN nanosheets with the hydrophilic CMC, which in turn encourages the use of the latter organic compound for our ink formulation. The electrostatic repulsive forces of the charged CMC carboxyl groups attached to h-BN flakes, as well as the steric hindrance formed by the CMC, prevent the dispersed flakes to re-aggregate. This leads to the formation of stable dispersions of h-BN nanosheets with the achieved high concentration up to ~1 mg/ml. In the work by Somsundaran *et al.* it was demonstrated that CMC polymer chains tend to be in a more stretched helical form in water and that the OH groups tend to stick out of the helix. CMC molecules choose a relatively flat conformation onto the h-BN nanosheets surface in order to allow their OH groups to be in contact with the flakes by hydrogen bonding.

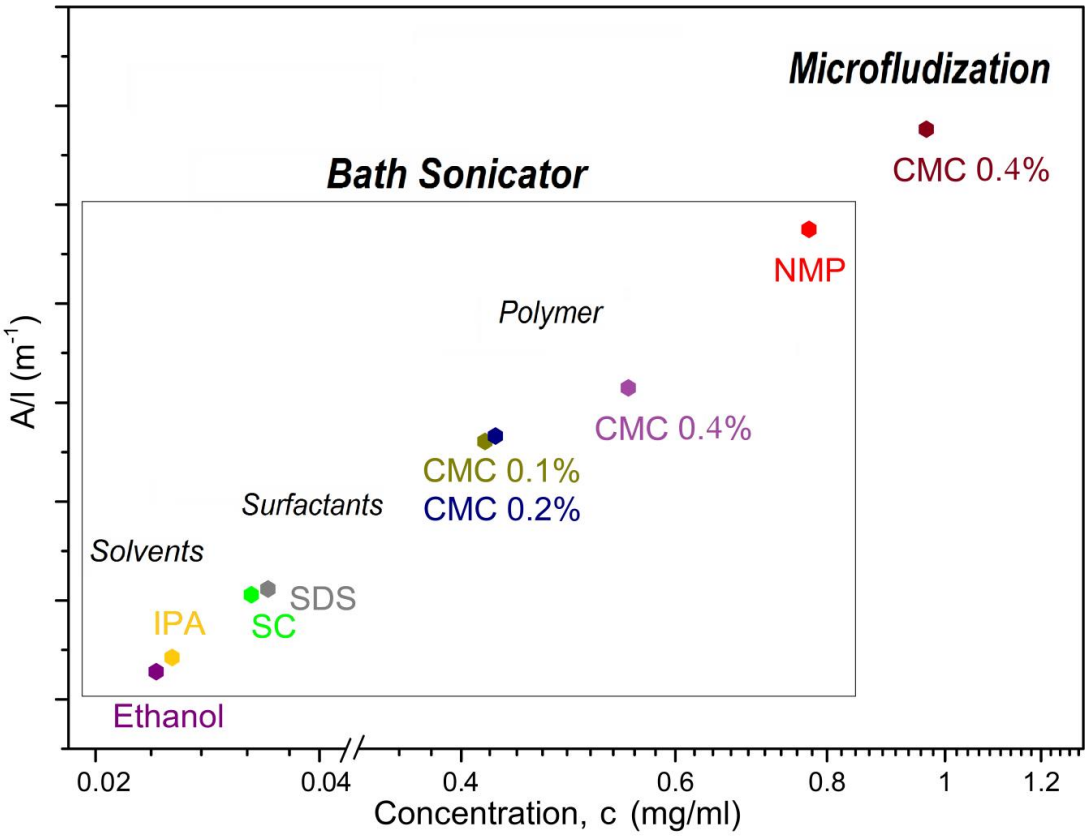

Figure S1 | h-BN exfoliation results after different solvents and techniques. Absorbance per unit length of h-BN nanosheets exfoliated into different solvents, surfactants and polymers, as a function of their concentration in solution. Results corresponding to bath sonicator and microfluidization techniques are reported.

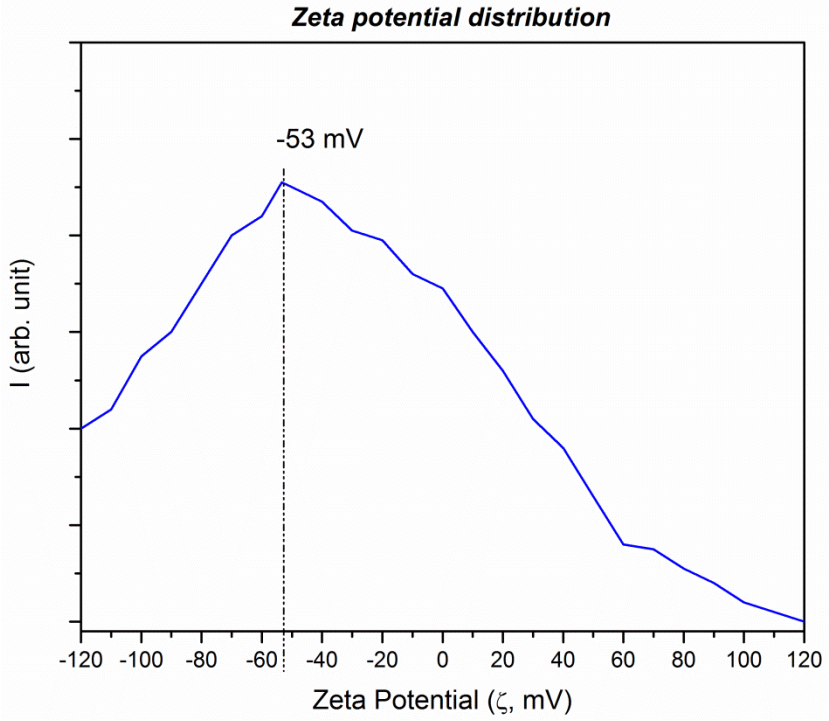

Figure S2 | Colloidal stability assessment. Zeta potential distribution corresponding to a h-BN/CMC colloidal dispersion, exhibiting a maximum intensity value at -53 mV.

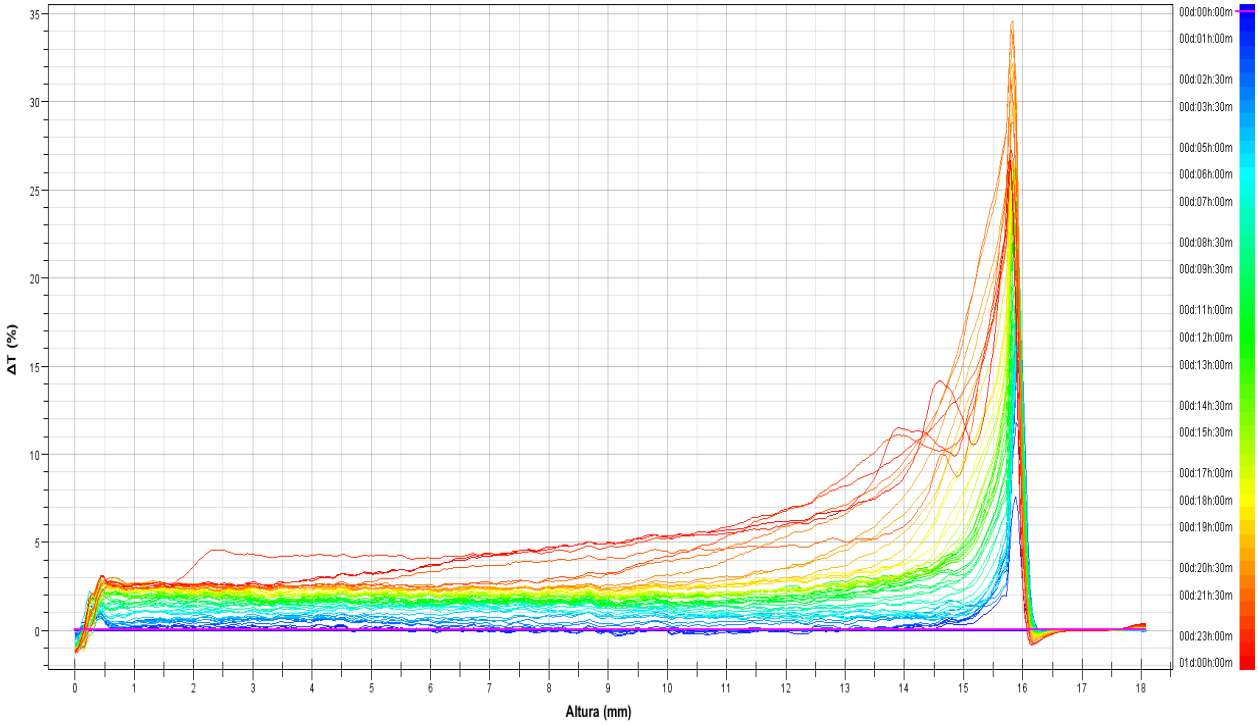

Figure S3 | Ink stability analysis. Turbiscan absorbance versus meassurement point height analyses of the h-BN ink under study (see Fig. 1d in the main text), obtained during 24 h after 6 months of ink storage.

For dispersion stability, turbidity data are taken for 24 h after 6 months of storage. Stability of h-BN Dispersions on Figure S3 shows the dispersion stability of h-BN ink in terms of turbiscan stability index (TSI), defined as follows in eq (1):

$$TSI = \sum_i \frac{\sum_h |scan_i(h) - scan_{i-1}(h)|}{H} \qquad \text{Eq [1]}$$

where *H* is the length of the sample, *h* is the height of the measure point, and *scani(h)* is the turbiscan intensity at height h. Based on the TSI value, aggregation, precipitation, or creaming of the dispersion can be evaluated. As the dispersion becomes less stable, the TSI value increases.

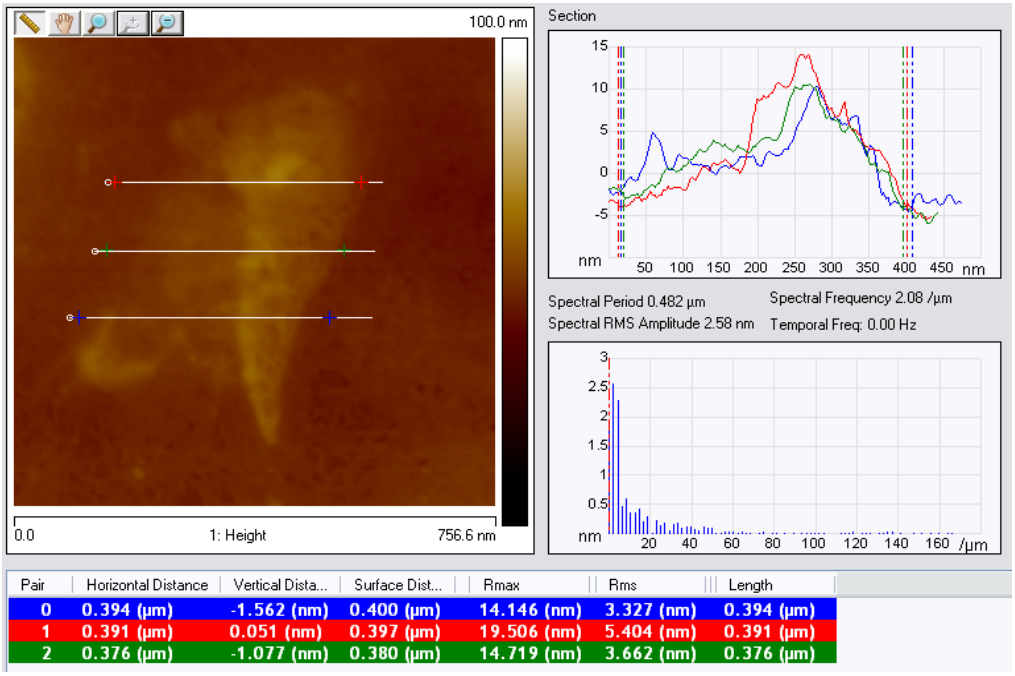

Figure S4 | AFM analysis on individual h-BN flakes. Example of topography and area analysis from an individual h-BN flake monitored by AFM.

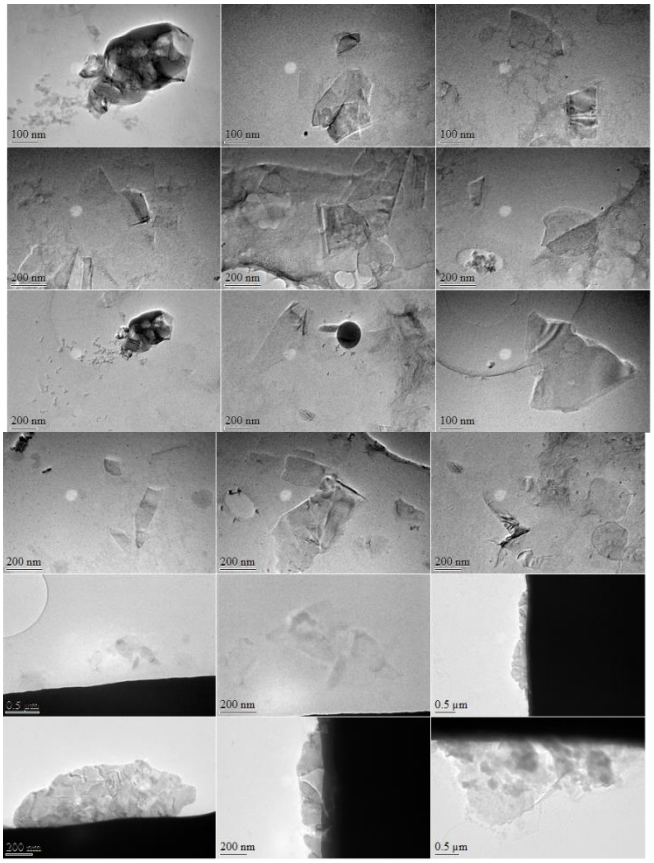

Figure S5 | TEM statistics on individual h-BN flakes. TEM images corresponding to several h-BN flakes within the ink. The lateral size statistics presented in Fig. 2c (main text) have been obtained from the TEM $(Area)^{1/2}$ measurements.

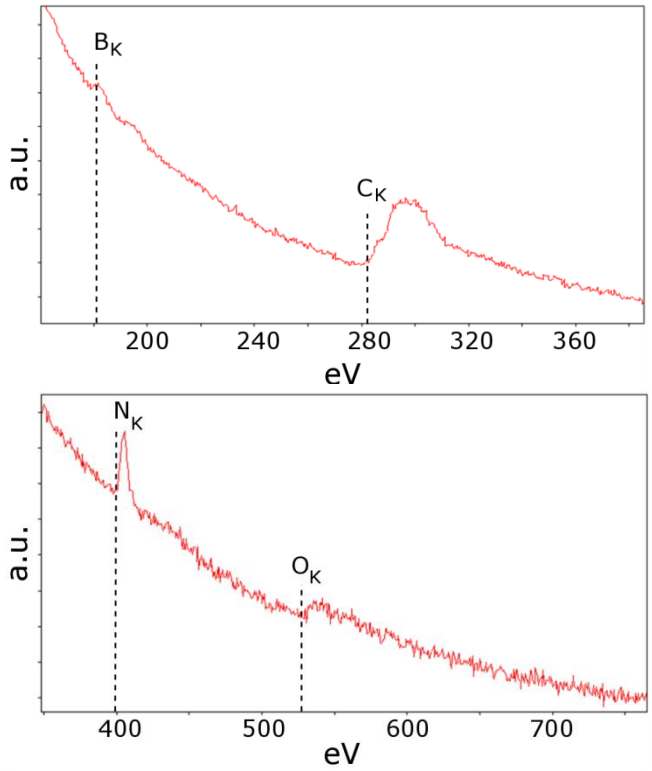

Figure S6 | Chemical composition analysis by EELS. EEL spectra from h-BN flake, displaying the k-edge signature corresponding to B and C, left panel, and N and O, right panel.

Table TS1 | Summary of ink rheology parameters. h-BN ink parameters as derived from the rheology study: viscosity, surface tension, density, nozzle diameter, velocity, and Reynolds (Re), Weber (We), Ohnesorge (Oh) and Z numbers. As well, the Re, We and Z values under different fluid velocity are also specified.

Ink parameters		
Viscosity (η)	(g/cm·s)	0,021
Surface tension (ϒ)	dynes/cm	28
Density (ρ)	g/cm3	1,1
Nozzle diameter (α)	cm	0,0021
Velocity (ν)	cm/s	175

Re	$(\rho \cdot v \cdot \alpha / \eta)$
We	$(\rho \cdot v^2 \cdot \alpha / \Upsilon)$
Oh	$(\frac{\sqrt{We}}{Re} = \frac{\eta}{\sqrt{\alpha \rho \Upsilon}})$
Z	$(1/Oh = \frac{\sqrt{\alpha \rho \Upsilon}}{\eta})$

Velocity	***Re***	***We***	**Z**
50	5,5	0,20625	12,1106
200	22	3,3	12,1106
500	55	20,625	12,1106
700	77	40,425	12,1106
1000	110	82,5	12,1106
1500	165	185,625	12,1106
2000	220	330	12,1106
3000	330	742,5	12,1106
4000	440	1320	12,1106

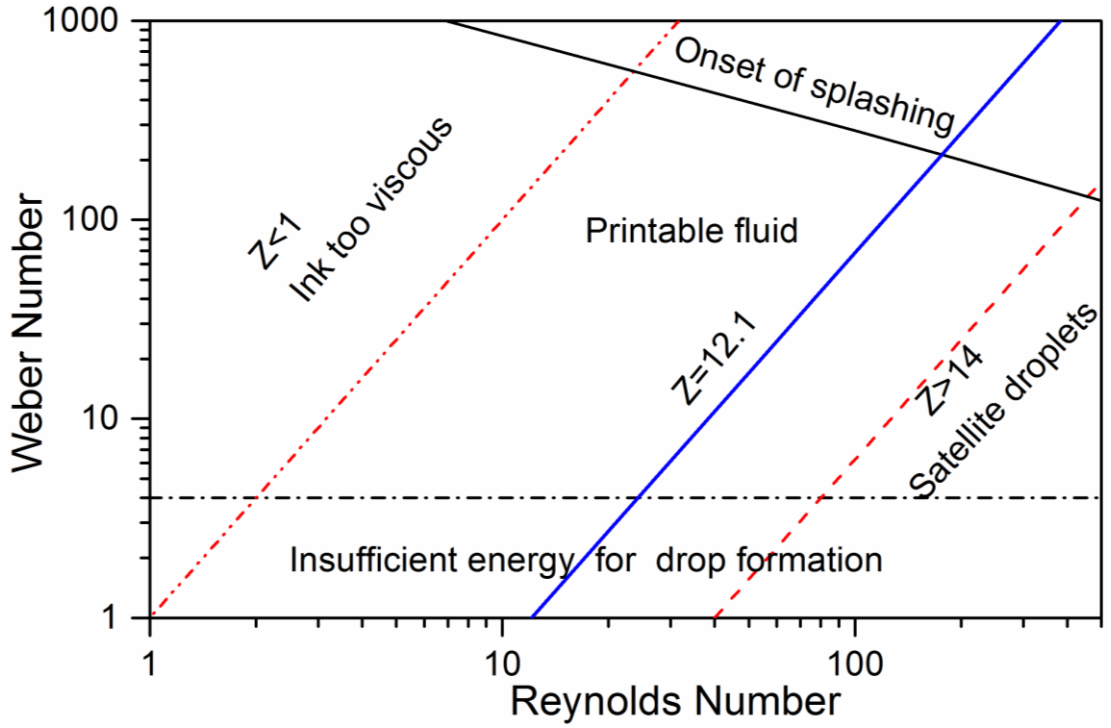

Figure S7 | Ink printability according to rheology parameters. Weber-Reynolds (Log-Log) chart representing the different quality regimes for an ink to be printable. Each phase characteristics are written down in the graph.

Table TS2 | Summary of ink quality parameters. Parameters employed for inkjet-printing the h-BN thin films under study in this work.

Parameters	Units	Value for h-BN ink
Voltage Amplitude	*V*	*20*
Drop Speed	*m/s*	*6*
Nozzle Temperature	^{o}C	*40*
Drop Spacing	*µm*	*20*
Printhead - Substrate	*µm*	*300*
Substrate Temperature	^{o}C	*40*

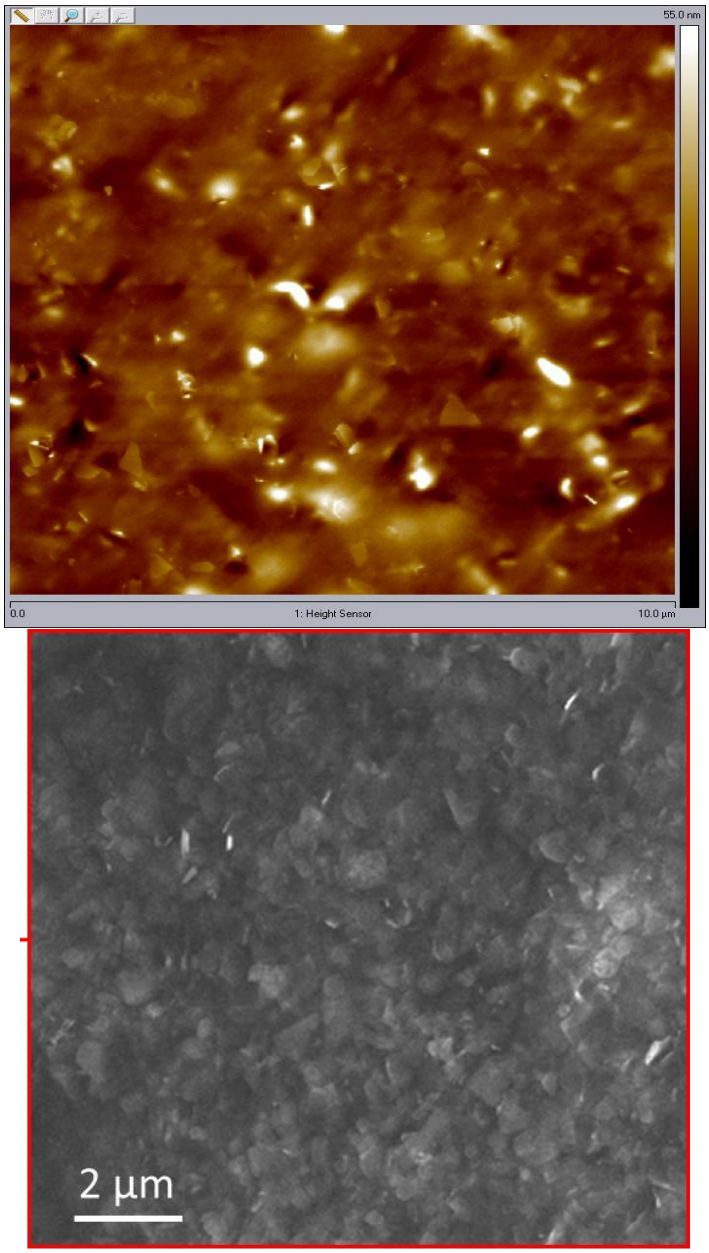

Figure S8 | AFM topography and field-emission SEM. a) AFM topography image corresponding to inkjet-printed h-BN layer on mica substrate. **b,** FESEM image corresponding to inkjet-printed h-BN layer on mica substrate.

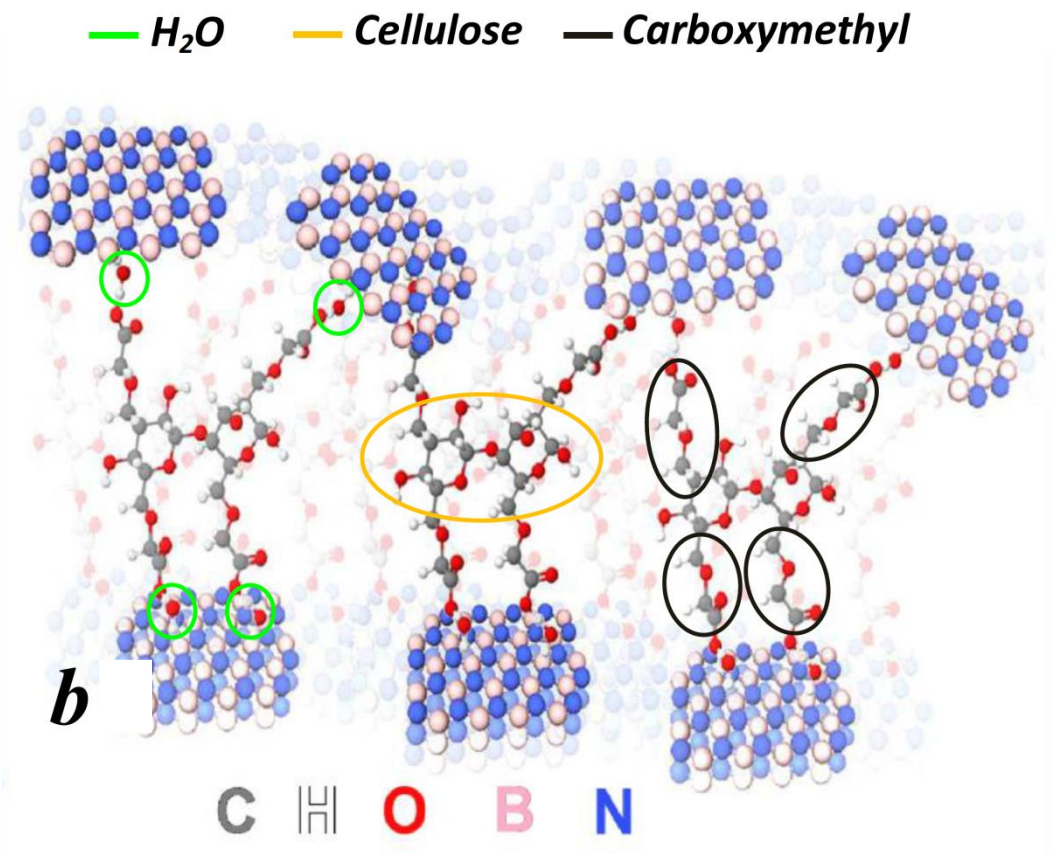

Figure S9 | h-BN chemical structure. 3D sketch of the different bonds found within the h-BN sample.

Table TS3 | FTIR vibration modes in CMC. FTIR absorption wavenumber corresponding to the different functional groups that can be found within the CMC polymer ink.

Wavenumber (cm^{-1})	***Functional group assignment*** [145]
3255	OH stretching
2908	-CH stretching -CH_2 and -CH_3 groups
1587	-C-O-O region (carboxylate symm. stretch)
1412	-CH_2 bonding and –C-O-O (carboxylate asymm. stretch)
1325	-OH in plane bending
1267	-C-O stretching
1106	-C-O and –C-C symmetry stretching
1053	-C-O-C bending
1020	-C-O bending
890	β-Glycoside linkage

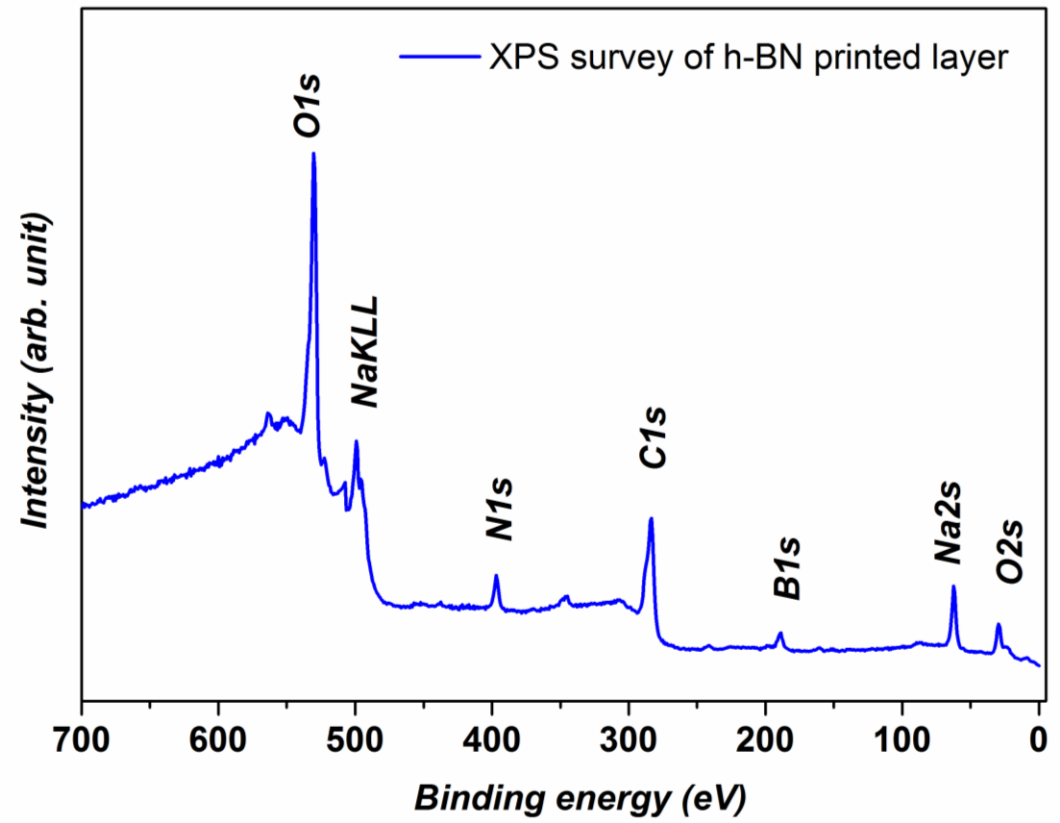

Figure S10 | h-BN bond determination. Multiplex XPS survey corresponding to a inkjet-printed h-BN film.

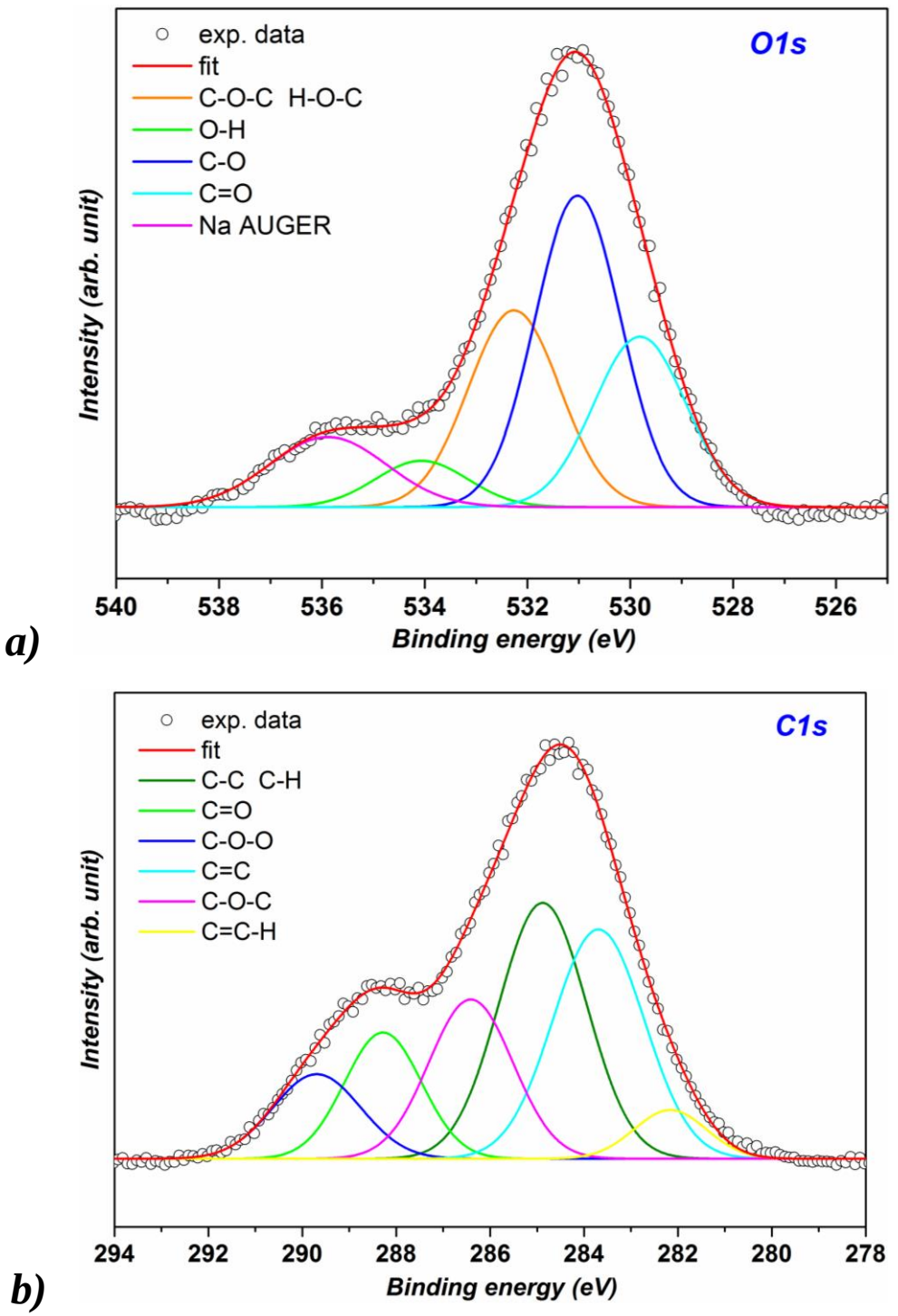

Figure S11 | XPS analysis of O1s and C1s bonds. XPS spectra from the O1s (**a**) and C 1s (**b**) bonds and their corresponding deconvolution into different functional groups contributions present in CMC.

C 1s and O 1s individual spectra, respectively presented in Figs. S13 and S14, display several deconvoluted peaks, ascribed to the CMC structure. As previously commented during the FT-IR spectra analysis, the hydroxyl group of trapped water (hydrolysis/degree of hydroxylation) is proved by the deconvoluted peak of O 1s spectra at 533.5 eV. Moreover, the carbon peak at 284.8 eV, attributed to the adsorbed carbon from the environment, the adventitious carbon, is very common in XPS measurements.

Table TS4 | XPS peaks statistics. Statistics corresponding to the analysis of the different bond contributions obtained after deconvolution of the XPS spectra as shown in Fig. 3(c,d) in the main text and Supplementary Fig. S11.

RSF (*Relative Sensitivity Factors*)	**C1 %**	**O1s %**	**B1s %**	**N1s %**	**Na1s %**
	0,314	**0,733**	**0,171**	**0,499**	**1,102**

C1 (eV)	**FWHM (eV)**	**Area**	**Area RSF**	**Area %**	**A.C %**	**A.C. (corrected) %**
C1s_1 ***284,88***	2.20	9285	29570,06	29,90	9,58	13,58
C1s_2 ***283,69***	2.29	8101	25799,36	26,09	8,36	11,85
C1s_3 ***286,41***	2.10	4775	15207,01	15,38	4,93	6,98
C1s_4 ***288,28***	1.93	3953	12589,17	12,73	4,08	5,78
C1s_5 ***289,69***	2.20	3283	10455,41	10,57	3,39	4,80
C1s_6 ***282,16***	1.81	1653	5264,33	5,32	1,71	2,42

O1s (eV)	**FWHM (eV)**	**Area**	**Area RSF**	**Area %**	**A.C %**	**A.C. (corrected) %**
O 1s_1 ***531,02***	1.96	25799	35196,45	35,69	11,40	16,16
O 1s_2 ***532,26***	2.10	17401	23739,43	24,07	7,69	10,90
O 1s_3 ***529,81***	2.11	15719	21444,75	21,75	6,95	9,85
O 1s_4 ***535,88 (Na AUGER)***	2.68	9125	12448,84	12,62	4,03	0,00
O 1s_5 ***534,06***	2.11	4235	5777,63	5,86	1,87	2,65

B1s_1 (eV)	**FWHM (eV)**	**Area**	**Area RSF**	**Area %**	**A.C %**	**A.C. (corrected) %**
B1s_1 ***190,37***	3.26	2173	12707,60	63,84	4,12	***5,83***
B-H ***188,5***	3.06	1231	7198,83	36,16	2,33	3,31

N1s (eV)	**FWHM (eV)**	**Area**	**Area RSF**	**Area %**	**A.C %**	**A.C. (corrected) %**
N1s_1 ***397,63***	3.16	6413	12851,70	100,00	4,16	***5,90***

Na1s (eV)	**FWHM (eV)**	**Area**	**Area RSF**	**Area %**	**A.C %**	**A.C. (corrected) %**
Na1s_1 ***1071,21***	2.50	100120	90852,99	100,00	1,00	**0.5**

B-

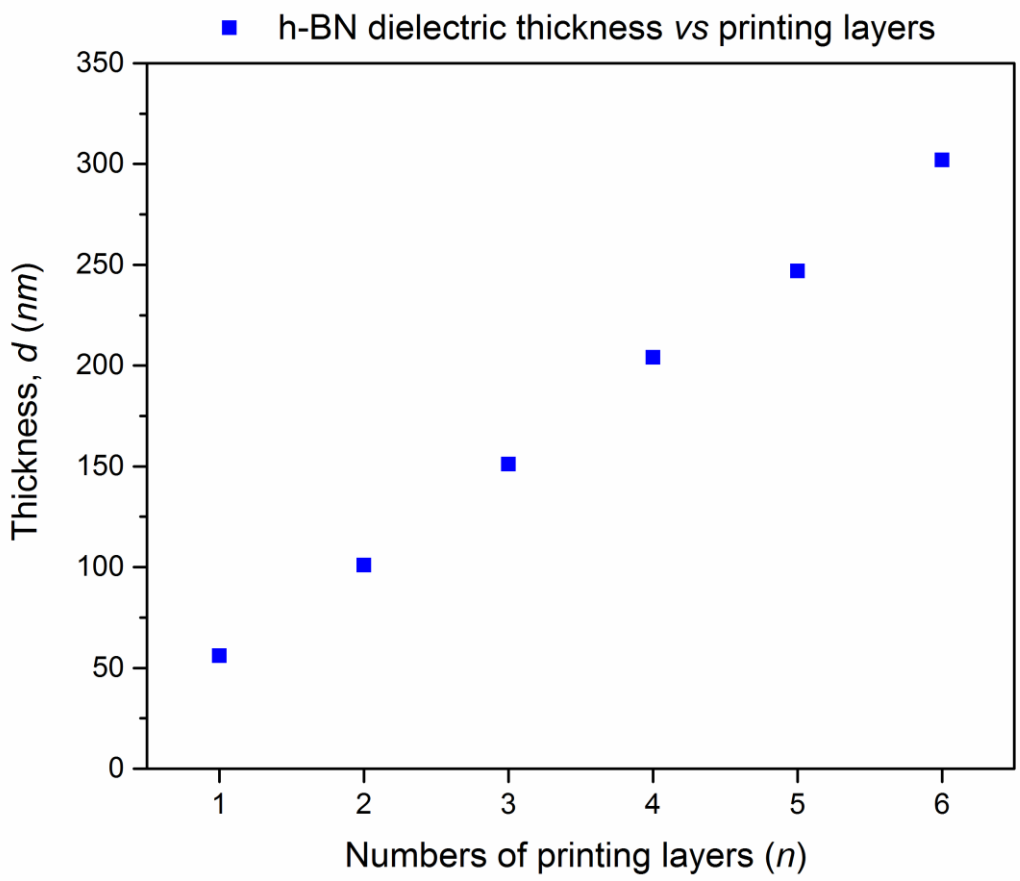

Figure S12 | Deposited h-BN layer thickness. Total h-BN layer thickness as a function of the number of printed layers.

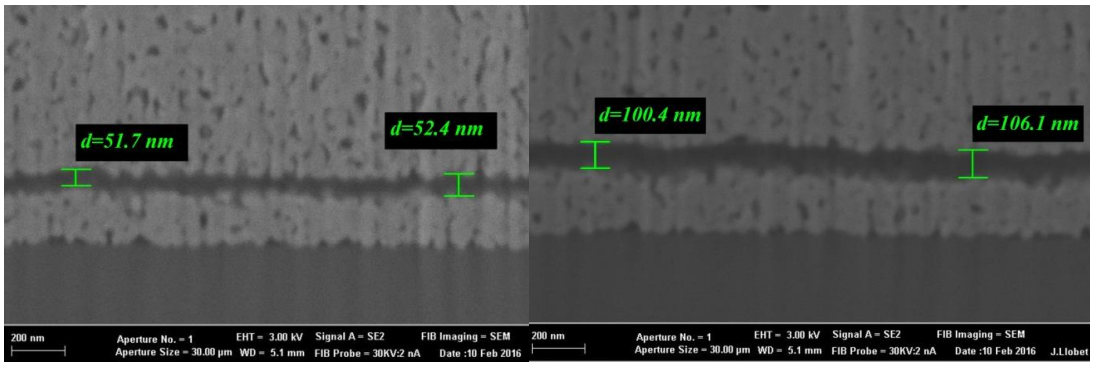

a) 0ne printing layer b) Two printing layers

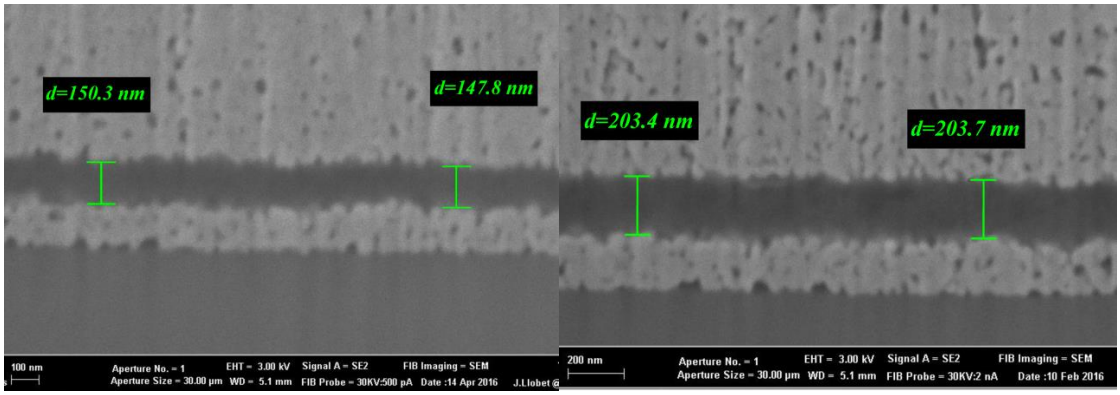

c) Three printing layers d) Four printing layers

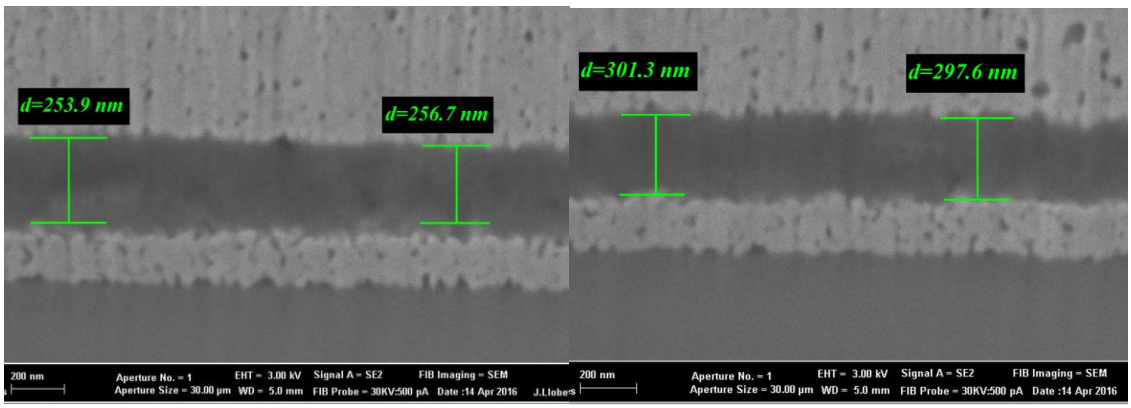

d) Five printing layers e) Six printing layers

Figure S13 | Experimental h-BN thickness after different number of printed layers. Cross-section SEM images of the FIB-sectioned MIMs under study (see Fig. 4a in the main text), where different number of inkjet-printed h-BN layers result in different total layer thickness.

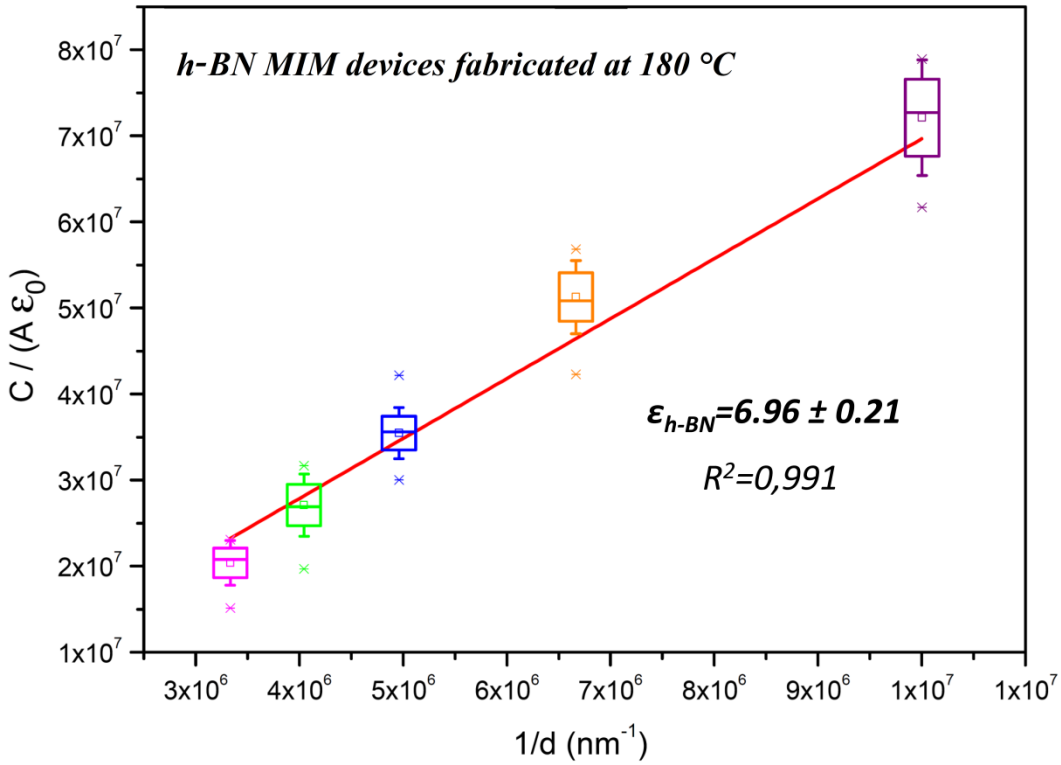

Figure S14 | h-BN-based MIM dielectric constant measurement on glass substrate. C / (A ε_0) vs. 1/d plot from several devices fabricated at 180 °C on glass substrate and presenting different h-BN insulator layer thickness. The value of ε_{h-BN} found by linear regression of the data is indicated in the graph.

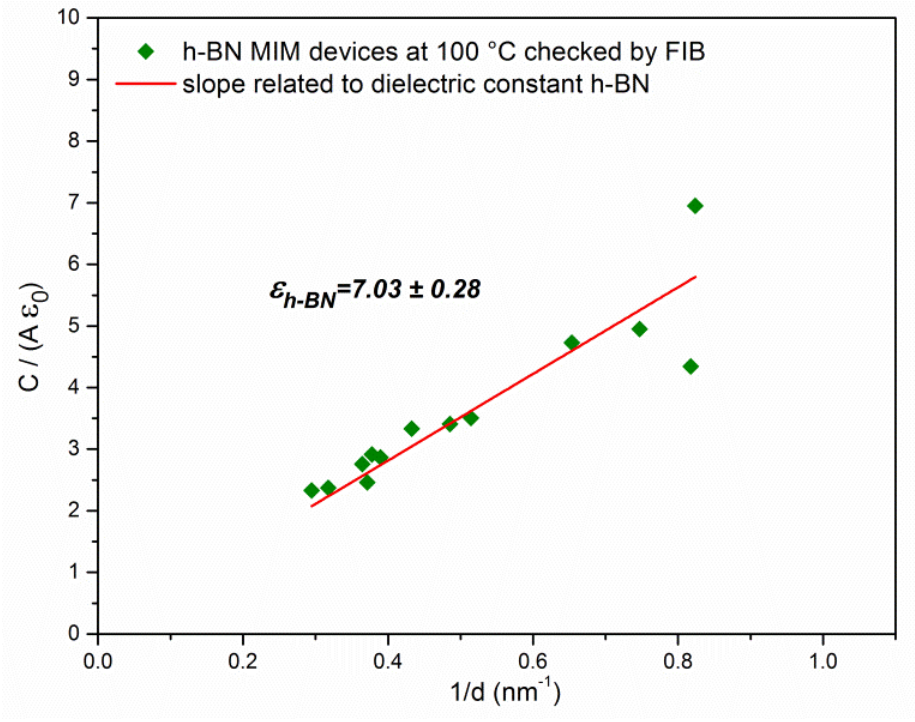

a)

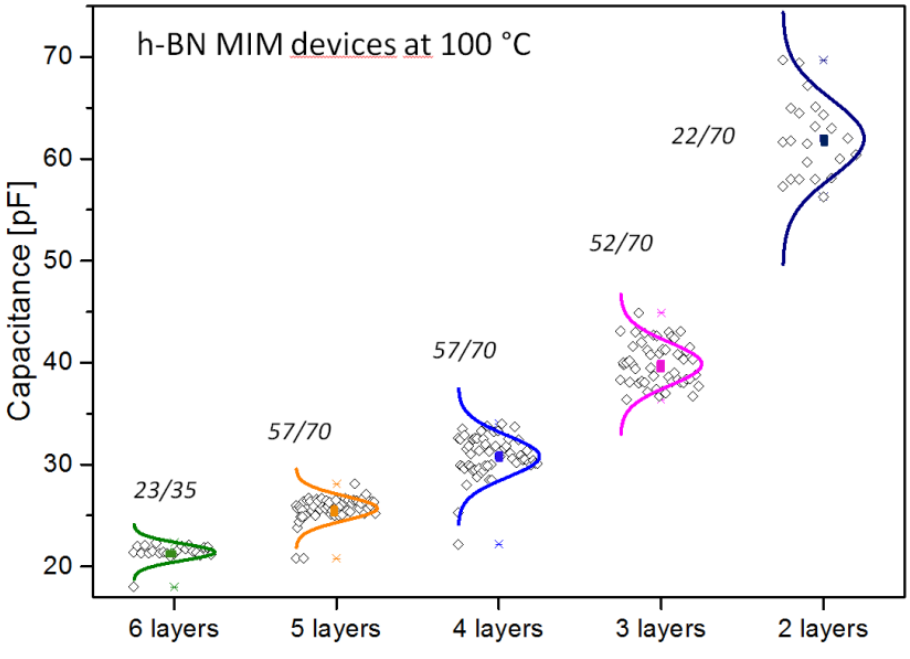

b)

Figure S15 | Numerous-devices statistics on the h-BN-based MIM dielectric characteristics on PET substrate. a, C / (A ε_0) vs. 1/d plot from several devices fabricated at 100 °C on PET substrate and presenting different h-BN insulator layer thickness. The value of ε_{h-BN} found by linear regression of the data is indicated in the graph. **b,** MIM capacitance as a function of the number of deposited h-BN layers, resulting from statistics over a large number of measured devices.

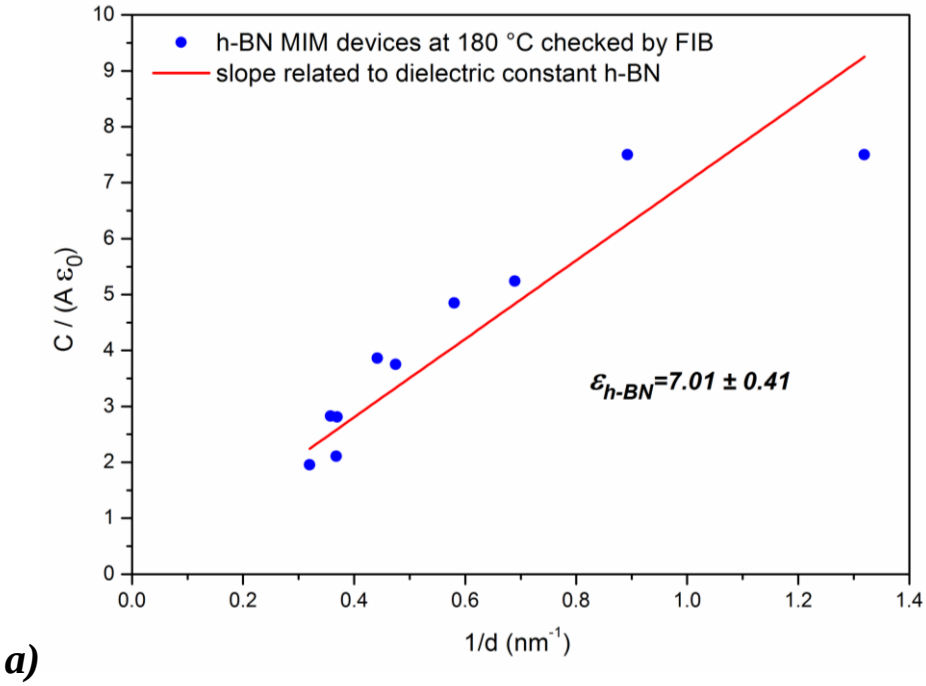

a)

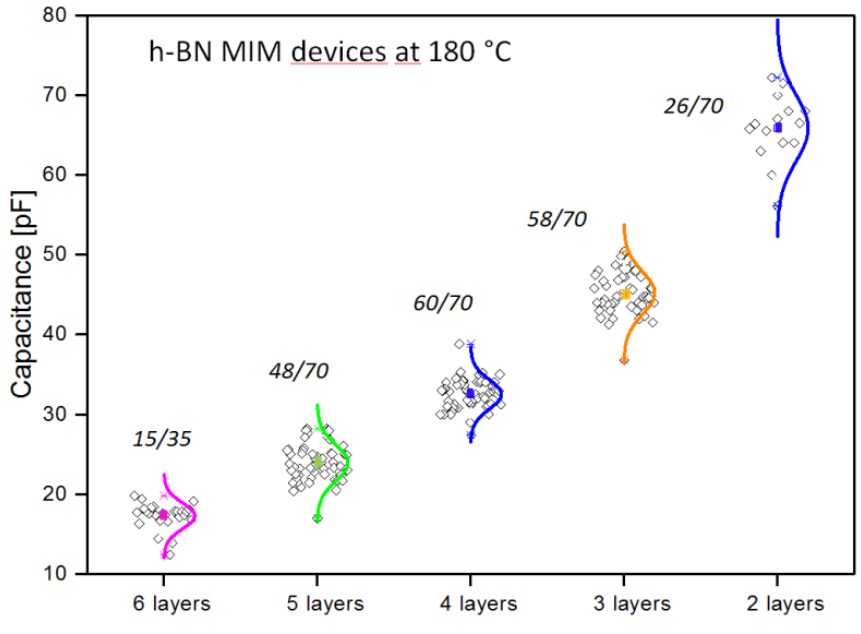

b)

Figure S16 | Numerous-devices statistics on the h-BN-based MIM dielectric characteristics on glass substrate. a, C / (A ε_0) vs. 1/d plot from several devices fabricated at 180 °C on glass substrate and presenting different h-BN insulator layer thickness. The value of ε_{h-BN} found by linear regression of the data is indicated in the graph. **b,** MIM capacitance as a function of the number of deposited h-BN layers, resulting from statistics over a large number of measured devices.

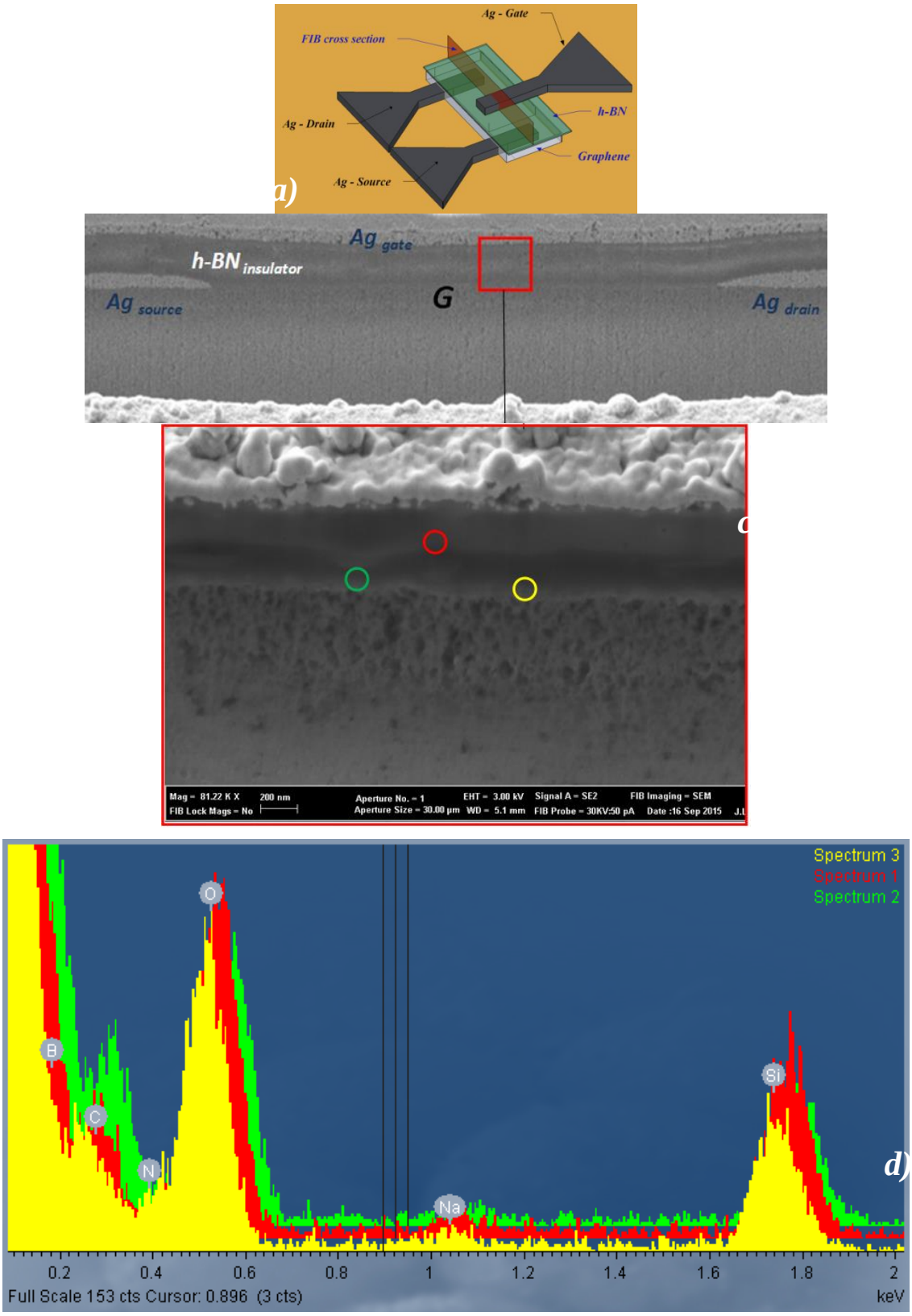

Figure S17 | TEM inspection of the TFT devices under study. a, 3D schematics of the fabricated TFT. **b,** FIB cross/section (according to red plane in **a**) image corresponding to one of the TFT devices under study. **c,** Zoom-in of the framed region in **b**. **d,** EDX spectra acquired on the highlighted regions in **c**.

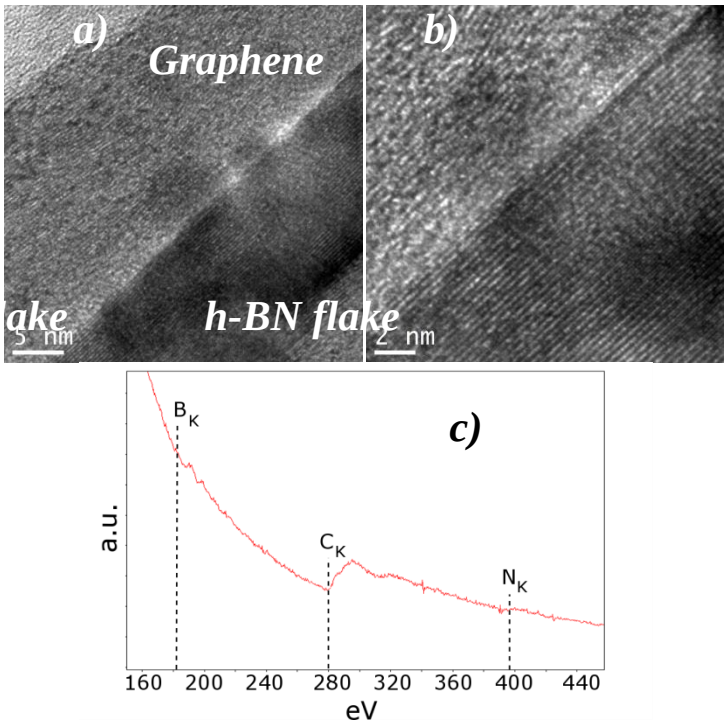

Figure S18 | Composition analyisis of TFT decvices. a, b, HRTEM images of the h-BN nanosheets-graphene heterostructure. **c,** EELS spectrum of the h-BN layer.

From the HRTEM images, Figs. S21(a,b), after the electronic measurements of the devices, the perfect matching of the BNNSs-graphene heterostructure is proved and confirmed. BNNSs layer seems to adapt onto graphene without any distortion with an interlayer distance of 3.3 Å, while the bottom layer of printed graphene flakes appears uniformly bended, as imposed by the PET substrate surface roughness.

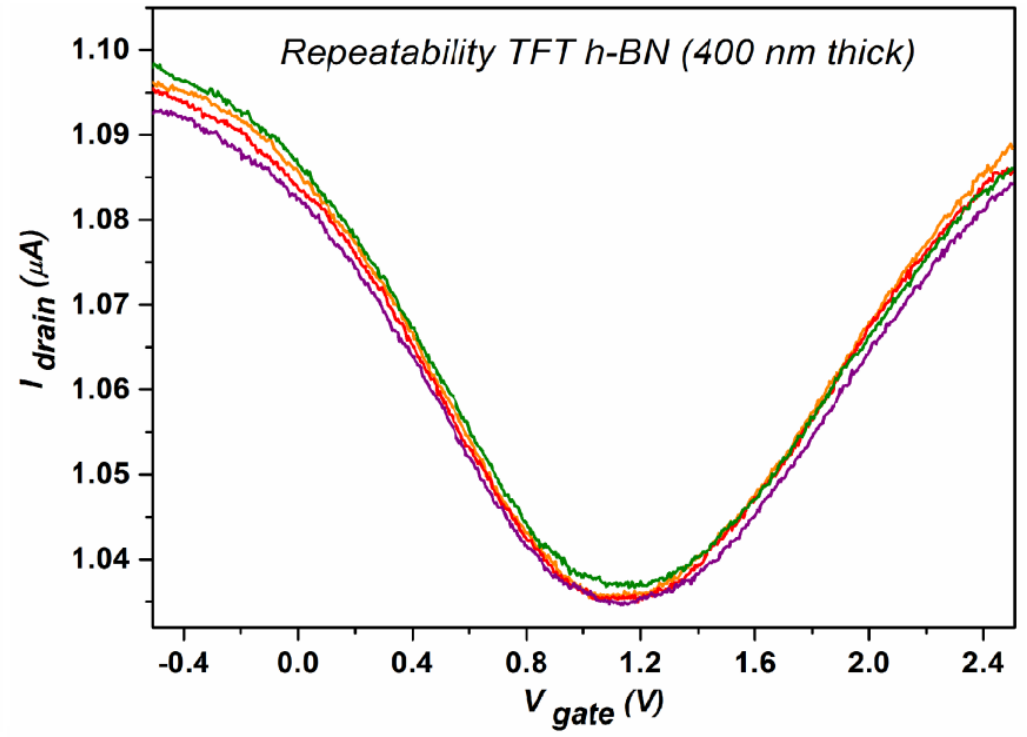

Figure S19 | Reproducibility of electrical characteristics of G-BN TFT devices. Drain current vs. gate voltage characteristic at room temperature and after the application of a drain-source voltage of V_{DS}= 10 mV, for a h-BN layer thickness of 400 nm. Different devices were measured that exhibit almost identical curves.

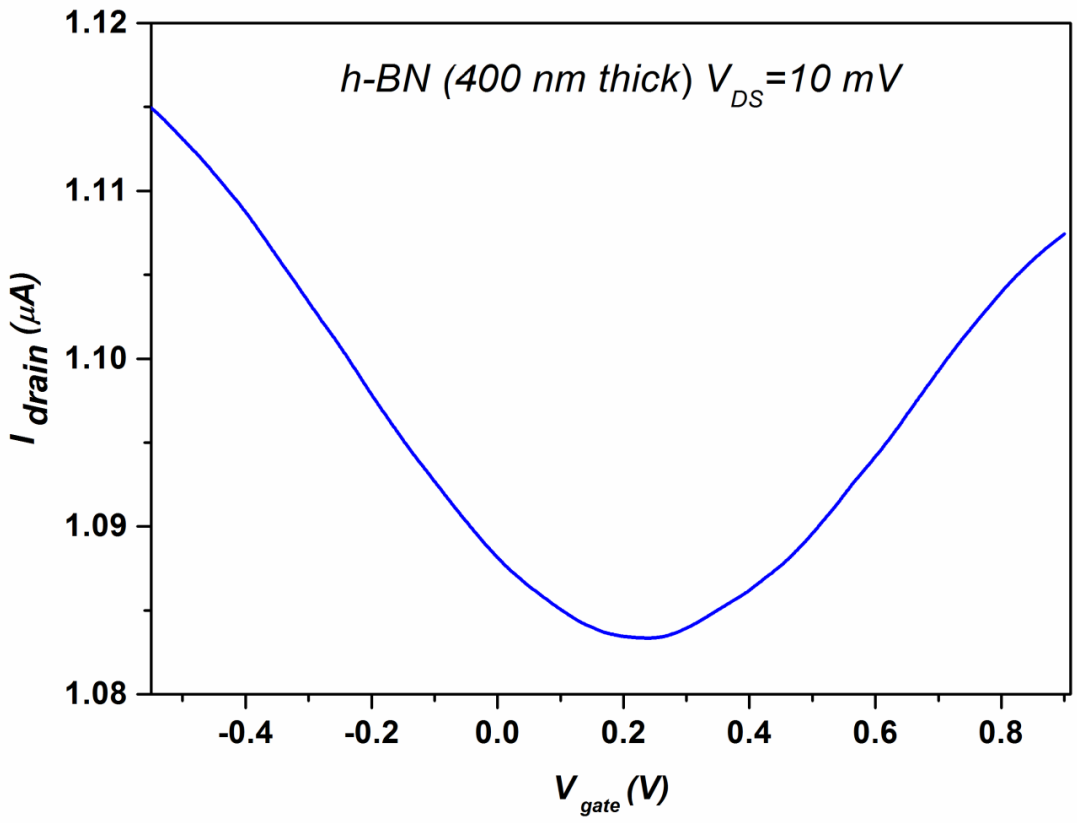

Figure S20 | Electrical characteristics of G-BN TFT devices. Drain current vs. gate voltage characteristic at room temperature and after the application of a drain-source voltage of V_{DS}= 10 mV, for a h-BN layer thickness of 400 nm.

References:

1. Itrs. International Technology Roadmap for Semiconductors 2.0: Executive Report. *Int. Technol. roadmap Semicond.* (2015). at <http://www.semiconductors.org/main/2015_international_technology_roadmap_for_semiconductors_itrs/>
2. www.oe-a.org. Roadmap for Organic and Printed Electronics Applications. (2015).
3. Geim, a K. & Novoselov, K. S. The rise of graphene. *Nat. Mater.* **6,** 183–91 (2007).
4. Novoselov, K. S. *et al.* A roadmap for graphene. *Nature* **490,** 192–200 (2012).
5. Novoselov, K. S. *et al.* Two-dimensional atomic crystals. *Proc. Natl. Acad. Sci. U. S. A.* **102,** 10451–3 (2005).
6. Novoselov, K. S., Mishchenko, A., Carvalho, A., Neto, A. H. C. & Road, O. 2D materials and van der Waals heterostructures. *Science (80-.).* **353,** aac9439 (2016).
7. Ferrari, A. C. *et al.* Science and technology roadmap for graphene, related two-dimensional crystals, and hybrid systems. *Nanoscale* **7,** 4598–4810 (2015).
8. Guo, Z. *et al.* Record maximum oscillation frequency in C-face epitaxial graphene transistors. *Nano Lett.* **13,** 942–7 (2013).
9. Wu, Y. *et al.* State-of-the-art graphene high-frequency electronics. *Nano Lett.* **12,** 3062–7 (2012).
10. Jiang, J. *et al.* Fabrication of Transparent Multilayer Circuits by Inkjet Printing. *Adv. Mater.* **28,** 1420–1426 (2016).
11. Tobjörk, D. & Österbacka, R. Paper Electronics. *Adv. Mater.* **23,** 1935–1961 (2011).
12. Berggren, M., Nilsson, D. & Robinson, N. D. Organic materials for printed electronics. *Nat. Mater.* **6,** 3–5 (2007).
13. Siegel, A. C. *et al.* Foldable printed circuit boards on paper substrates. *Adv. Funct. Mater.* **20,** 28–35 (2010).
14. Burns, S. E., Cain, P., Mills, J., Wang, J. & Sirringhaus, H. Inkjet Printing of Polymer Thin-Film Transistor Circuits. *MRS Bull.* **28,** 829–834 (2003).
15. Pudas, M., Halonen, N., Granat, P. & Vähäkangas, J. Gravure printing of conductive particulate polymer inks on flexible substrates. *Prog. Org. Coatings* **54,** 310–316 (2005).
16. Krebs, F. C. *et al.* A complete process for production of flexible large area polymer solar cells entirely using screen printing—First public demonstration. *Sol. Energy Mater. Sol. Cells* **93,** 422–441 (2009).
17. Søndergaard, R. R., Hösel, M. & Krebs, F. C. Roll-to-Roll fabrication of large area functional organic materials. *J. Polym. Sci. Part B Polym. Phys.* **51,** 16–34 (2013).
18. Choi, H. W., Zhou, T., Singh, M. & Jabbour, G. E. Recent developments and directions in printed nanomaterials. *Nanoscale* **7,** 3338–3355 (2014).
19. Calvert, P. Inkjet printing for materials and devices. *Chemistry of Materials* **13,** 3299–3305 (2001).
20. Singh, M., Haverinen, H. M., Dhagat, P. & Jabbour, G. E. Inkjet printing-process and its applications. *Adv. Mater.* **22,** 673–685 (2010).
21. Li, J. *et al.* Indium tin oxide modified transparent nanotube thin films as effective anodes for flexible organic light-emitting diodes. *Appl. Phys. Lett.* **93,** 83306 (2008).
22. Chang, S.-C. *et al.* Multicolor Organic Light-Emitting Diodes Processed by Hybrid Inkjet Printing. *Adv. Mater.* **11,** 734–737 (1999).
23. Rutherglen, C., Jain, D. & Burke, P. Nanotube electronics for radiofrequency applications. *Nat. Nanotechnol.* **4,** 811–819 (2009).
24. Kaltenbrunner, M. *et al.* Ultrathin and lightweight organic solar cells with high flexibility. *Nat. Commun.* **3,** 770 (2012).
25. Galstyan, V. *et al.* Vertically Aligned TiO2 Nanotubes on Plastic Substrates for Flexible Solar Cells. *Small* **7,** 2437–42 (2011).
26. Krebs, F. C. Fabrication and processing of polymer solar cells: A review of printing and coating techniques. *Sol. Energy Mater. Sol. Cells* **93,** 394–412 (2009).
27. Takei, K. *et al.* Nanowire active-matrix circuitry for low-voltage macroscale artificial skin. *Nat. Mater.* **9,** 821–6 (2010).

28. Fortunato, E. M. C. *et al.* Fully transparent ZnO thin-film transistor produced at room temperature. *Adv. Mater.* **17,** 590–594 (2005).

29. Stutzmann, N., Friend, R. H. & Sirringhaus, H. Self-Aligned, Vertical-Channel, Polymer Field-Effect Transistors. *Science (80-.).* **299,** 1881–1884 (2003).

30. Kim, T. Y. *et al.* Electrical Properties of Synthesized Large-Area MoS2 Field-Effect Transistors Fabricated with Inkjet-Printed Contacts. *ACS Nano* **10,** 2819–2826 (2016).

31. Choi, H. W., Zhou, T., Singh, M. & Jabbour, G. E. Recent developments and directions in printed nanomaterials. *Nanoscale* **7,** 3338–3355 (2015).

32. Gao, M., Li, L. & Song, Y. Inkjet printing wearable electronic devices. *J. Mater. Chem. C* **5,** 2971–2993 (2017).

33. Wang, C. *et al.* Self-aligned, extremely high frequency III-V metal-oxide-semiconductor field-effect transistors on rigid and flexible substrates. *Nano Lett.* **12,** 4140–5 (2012).

34. Zhao, N. *et al.* Self-aligned inkjet printing of highly conducting gold electrodes with submicron resolution. *J. Appl. Phys.* **101,** 64513 (2007).

35. Sekitani, T., Noguchi, Y., Zschieschang, U., Klauk, H. & Someya, T. Organic transistors manufactured using inkjet technology with subfemtoliter accuracy. *Proc. Natl. Acad. Sci. U. S. A.* **105,** 4976–4980 (2008).

36. Van Osch, T. H. J., Perelaer, J., De Laat, A. W. M. & Schubert, U. S. Inkjet printing of narrow conductive tracks on untreated polymeric substrates. *Adv. Mater.* **20,** 343–345 (2008).

37. Hernandez, Y. *et al.* High yield production of graphene by liquid phase exfoliation of graphite. *Nat. Nanotechnol.* **3,** 563–8 (2008).

38. Torrisi, F. *et al.* Inkjet-printed graphene electronics. *ACS Nano* **6,** 2992–3006 (2012).

39. Capasso, a. *et al.* Ink-jet printing of graphene for flexible electronics: An environmentally-friendly approach. *Solid State Commun.* **224,** 53–63 (2015).

40. Nguyen, B. H. & Nguyen, V. H. Promising applications of graphene and graphene-based nanostructures. *Adv. Nat. Sci. Nanosci. Nanotechnol.* **7,** 23002 (2016).

41. Wang, Z. *et al.* Fabrication of Boron Nitride Nanosheets by Exfoliation. *Chem. Rec.* 1204–1215 (2016). doi:10.1002/tcr.201500302

42. Lee, D. *et al.* Scalable exfoliation process for highly soluble boron nitride nanoplatelets by hydroxide-assisted ball milling. *Nano Lett.* **15,** 1238–1244 (2015).

43. Kim, J. *et al.* Direct exfoliation and dispersion of two-dimensional materials in pure water via temperature control. *Nat. Commun.* **6,** 8294 (2015).

44. Backes, C. *et al.* Production of Highly Monolayer Enriched Dispersions of Liquid-Exfoliated Nanosheets by Liquid Cascade Centrifugation. *ACS Nano* acsnano.5b07228 (2016). doi:10.1021/acsnano.5b07228

45. Bonaccorso, F., Bartolotta, A., Coleman, J. N. & Backes, C. 2D-Crystal-Based Functional Inks. *Adv. Mater.* **28,** 6136–6166 (2016).

46. Robertson, J. High dielectric constant oxides. *Eur. Phys. J. Appl. Phys.* **291,** 265–291 (2004).

47. Lee, G.-H. *et al.* Flexible and Transparent MoS 2 Field-Effect Transistors on Hexagonal Boron Nitride-Graphene Heterostructures. *ACS Nano* **7,** 7931–7936 (2013).

48. Shi, Y. *et al.* Synthesis of few-layer hexagonal boron nitride thin film by chemical vapor deposition. *Nano Lett.* **10,** 4134–4139 (2010).

49. Kim, K. K. *et al.* Synthesis of Monolayer Boron Nitride on Cu Foil Using Chemical Vapor Deposition. *Nano Lett.* **xx,** xx (2011).

50. Kudin, K. N., Scuseria, G. E. & Yakobson, B. I. C2F, BN, and C nanoshell elasticity from ab initio computations. *Phys. Rev. B* **64,** 235406 (2001).

51. Cai, W. *et al.* Thermal transport in suspended and supported monolayer graphene grown by chemical vapor deposition. *Nano Lett.* **10,** 1645–1651 (2010).

52. Forster, F. *et al.* Dielectric screening of the Kohn anomaly of graphene on hexagonal boron nitride. *Phys. Rev. B - Condens. Matter Mater. Phys.* **88,** 1–7 (2013).

53. Yurdakul, H. *et al.* Nanoscopic characterization of two-dimensional (2D) boron nitride nanosheets (BNNSs) produced by microfluidization. *Ceram. Int.* **38,** 2187–2193 (2012).

54. Lin, Y. & Connell, J. W. Advances in 2D boron nitride nanostructures: nanosheets, nanoribbons, nanomeshes,

and hybrids with graphene. *Nanoscale* **4,** 6908–39 (2012).

55. Yin, J. *et al.* Boron Nitride Nanostructures: Fabrication, Functionalization and Applications. *Small* 1–27 (2016). doi:10.1002/smll.201600053

56. Feng, P. *et al.* Fringe structures and tunable bandgap width of 2D boron nitride nanosheets. *Beilstein J. Nanotechnol.* **5,** 1186–92 (2014).

57. Coleman, J. N. *et al.* Two-dimensional nanosheets produced by liquid exfoliation of layered materials. *Science* **331,** 568–71 (2011).

58. Wang, Y. *et al.* Raman Studies of Monolayer Graphene : The Substrate Effect. *J. Phys. Chem. C* **112,** 10637–10640 (2008).

59. Yi, M. *et al.* Hydrodynamics-assisted scalable production of boron nitride nanosheets and their application in improving oxygen-atom erosion resistance of polymeric composites. *Nanoscale* **5,** 10660–7 (2013).

60. Karagiannidis, P. G. *et al.* Microfluidization of Graphite and Formulation of Graphene-Based Conductive Inks. *ACS Nano* **1,** acsnano.6b07735 (2017).

61. Bergin, S. D. *et al.* Towards solutions of single-walled carbon nanotubes in common solvents. *Adv. Mater.* **20,** 1876–1881 (2008).

62. Nicolosi, V., Chhowalla, M., Kanatzidis, M. G., Strano, M. S. & Coleman, J. N. Liquid Exfoliation of Layered Materials. *Science (80-.).* **340,** 1226419 (2013).

63. Paria, S. & Khilar, K. C. A review on experimental studies of surfactant adsorption at the hydrophilic solid-water interface. *Adv. Colloid Interface Sci.* **110,** 75–95 (2004).

64. Green, A. a & Hersam, M. C. Solution phase production of graphene with controlled thickness via density differentiation. *Nano Lett.* **9,** 4031–6 (2009).

65. Maragó, O. M. *et al.* Brownian motion of graphene. *ACS Nano* **4,** 7515–7523 (2010).

66. May, P., Khan, U., Hughes, J. M. & Coleman, J. N. Role of solubility parameters in understanding the steric stabilization of exfoliated two-dimensional nanosheets by adsorbed polymers. *J. Phys. Chem. C* **116,** 11393–11400 (2012).

67. Raddaha, N. S. *et al.* Electrophoretic deposition of chitosan/h-BN and chitosan/h-BN/TiO2 composite coatings on stainless steel (316L) substrates. *Materials (Basel).* **7,** 1814–1829 (2014).

68. Pradhan, G. C., Behera, L. & Swain, S. K. Effects of boron nitride nanopowder on thermal, chemical and gas barrier properties of starch. *Chinese J. Polym. Sci.* **32,** 1311–1318 (2014).

69. Bouville, F. & Deville, S. Dispersion of boron nitride powders in aqueous suspensions with cellulose. *J. Am. Ceram. Soc.* **97,** 394–398 (2014).

70. Petritz, A. *et al.* Cellulose as biodegradable high-k dielectric layer in organic complementary inverters. *Appl. Phys. Lett.* **103,** (2013).

71. Petritz, A. *et al.* Dielectrics: Cellulose-Derivative-Based Gate Dielectric for High-Performance Organic Complementary Inverters (Adv. Mater. 46/2015). *Adv. Mater.* **27,** 7485 (2015).

72. Yadav, M., Rhee, K. Y., Jung, I. H. & Park, S. J. Eco-friendly synthesis, characterization and properties of a sodium carboxymethyl cellulose/graphene oxide nanocomposite film. *Cellulose* **20,** 687–698 (2013).

73. K, U. & Hoffmann, H. Structure and solution properties of sodium carboxymethyl cellulose. **7757,** (1997).

74. Zhivkov, A. M. Electric Properties of Carboxymethyl Cellullose. *Cellul. Asp.* **10,** 197–226 (2013).

75. Samsudin, A. S., Lai, H. M. & Isa, M. I. N. Electrochimica Acta Biopolymer Materials Based Carboxymethyl Cellulose as a Proton Conducting Biopolymer Electrolyte for Application in Rechargeable Proton Battery. *Electrochim. Acta* **129,** 1–13 (2014).

76. Wei, L., Chen, C. & Wei, H. Poly (acrylic acid sodium) grafted carboxymethyl cellulose as a high performance polymer binder for silicon anode in lithium ion batteries.

77. Li, Y. *et al.* Nanocellulose as green dispersant for two-dimensional energy materials. *Nano Energy* **13,** 346–354 (2015).

78. Saake, B., Horner, S., Puls, J., Heinze, T. & Koch, W. A new approach in the analysis of the substituent distribution of carboxymethyl celluloses. *Cellulose* **8,** 59–67 (2001).

Chapter 6: Conclusions

In this section, the main conclusions of this Thesis are presented. The overall purpose of the work achieved along the whole dissertation will be exposed, including the detailed results obtained from each specific developed subject.

6.1 General Conclusions

In this thesis, inkjet printing technology is demonstrated as a versatile method for the manufacturing of different robust applications (flexible sensors and hybrid circuitry), and especially as a complement and alternative to standard fabrication silicon technology for the development of high-quality flexible fully inkjet-printed devices based on novel outstanding functional nanomaterials, from the high-*k* dielectric HfO_2 nanoparticle-based (3D) ink to the high-*k* dielectric composite of h-BN (2D).

The main objective of this Thesis was evidencing inkjet printing technology as a powerful tool for the oncoming flexible printed electronics development. Basically, the investigation of new promising application areas where inkjet-printing technology could contribute solving traditional issues and improving the manufacturing processes has been addressed.

First of all, we demonstrated the feasibility of inkjet printing as promising technique in comparison to the other current printing methods for the fabrication of robust gas sensor circuitry platforms and as alternative method to surface mount-technology (SMT), in order to assemble surface mount-devices (SMDs) onto previous inkjet-printed circuitry for flexible electronic applications.
Once the inkjet printing has been proved as a suitable technique for robust, low-cost and large-scale production, the second main topic of this work was the implementation of new solutions to chase and follow the guidelines of ITRS and iNEMA roadmaps for the next generation of flexible electronics applications by the ink formulation of novel dielectric inks that allow manufacturing excellent fully inkjet-printed electronic devices.
Primarily, the study was focused on the high-*k* HfO_2 dielectric ink and devoted to the investigation of the physical and chemical properties of the inkjet-printed insulator. Afterwards, the dielectric material was demonstrated, for the first time in literature, as a suitable high-*k* material to achieve flexible fully-inkjet printed electronic devices such as MIM capacitors (by established capacitance-

and voltage-dependent measurements) and ReRAM devices (by controlled cyclic current-voltage measurements).

Finally, despite the proved excellent properties of the HfO_2 nanoparticles-based ink, and due to the incompatibility with the available graphene ink (formulated by the CGC group at the University of Cambridge), the research objectives moved to the formulation of an eco-friendly water-based h-BN ink, specially designed to be printed as dielectric material. The dielectric h-BN ink confirmed the expected high-*k* dielectric constant value (ε_{hBN} ~ 6.9) by means of an in-depth characterization of flexible fully inkjet-printed MIMs.

Finally, the inkjet-printed h-BN was demonstrated as suitable gate oxide for flexible fully-inkjet printed graphene/h-BN heterostructures for TFT devices. Distinctive electrical properties, achieving a hole carrier mobility of graphene up to 110 $cm^2V^{-1}s^{-1}$ in normal mechanical conditions, and only a 20% reduction when under bending, were achieved, to the best of our knowledge, for the first time in literature.

6.2 Specific Conclusions

6.2.1. Results Concerning Inkjet-Printed Silver

- The fabrication of versatile, low-cost, flexible and reliable inkjet-printed gas sensor platforms for resistive sensors. The designed sensor platforms were compared with screen-printed equivalent platforms after life test and aging test analyses. Although inkjet-printed devices showed failure by hot spot phenomenon when a current bottleneck is promoted (excess of current allowed by the printed stripe in terms of thickness and width), no chemical degradation was observed, in contrast to screen-printed platforms.

- The feasibility of flexible inkjet-printed gas sensor platforms for the manufacturing of metal oxide titanium sub-oxide (TiO_{2-x}) by atmospheric plasma spray. Despite the high temperatures involved in APS (~300 °C), the inkjet-printed platform was not degraded during the process, thus obtaining a well-bonded titanium sub-oxide coating. Finally, the sensing behaviour of the metal oxide layer was tested by means of NH_3 (hazardous gas), proving positive results on NH_3 concentrations ranging from 10 to 100 ppm.

- The demonstration of scalability and reliability, for the first time, of fully inkjet-printed junctions

employing silver nanoparticle-based inket ink as high conductive interconnecting material for assembling surface-mount devices onto previous inkjet-printed circuitry. The observation of homogeneous assembling contact (~1-µm thick) between SMDs and printed pads onto printed substrates confirms inkjet printing technology as alternative method to standard surface-mount technology.

6.2.2. Inkjet-Printed High-k HfO_2 for Capacitor and Memristor devices

- The suitability of high-*k* dielectric (HfO_2) ink for inkjet printing technology demonstrated by in-depth chemical, physical and rheological studies. The characteristics and the electrical properties of the inkjet-printed HfO_2 high-*k* dielectric are demonstrated for the first time in literature by the fabrication of flexible fully inkjet-printed electronic devices such as MIM devices. The electrical results are explained in terms of dielectric properties: on the one hand, the energy gap of the printed oxide (5.4 eV) that ensures the high barrier for electrons, on the other hand the relative permittivity (ε_{hBN} ~ 12.6) and the dielectric loss tangent (δ~0.015) that guarantee low phenomena of charge carrier impurities conduction.

- The manufacturing for the first time of a memristor component with simple MIM structure (Au/HfO_2/Ag) based on the high-*k* hafnium oxide using inkjet printing technology. The observation of a bipolar resistive switching phenomenon, where the successive controlled changes between two conductive states, a Low Resistance (and a High Resistance State, are obtained by applying positive SET and negative RESET voltages. The demonstration of the high-performance features such as I_{ON}/I_{OFF} ratio of three orders of magnitude and low switching operating voltages around 0.2 V, thus allowing for a reduced power consumption. These parameters are comparable to that achieved by CMOS conventional technologies. The evidence, by means of cyclic current-voltage measurements, that the HfO_2-based ReRAM devices work properly reaching more than 128 Resistive Switching cycles.

- The development of the MEM structure, where the bottom Au was replaced by Pt resulting in the final Pt/HfO_2/Ag structure, which showed noticeable improvements with respect to the previously mentioned results such as I_{ON}/I_{OFF} ratio of six orders of magnitude and more than 516 resistive switching cycles while maintaining the low switching operating voltages around 0.2 V. The results

are explained in terms of the forming process into the inkjet-printed thin-film dielectric layer that creates a switchable conductive filament deeply characterized by SEM and TEM images.

6.2.3. Inkjet-printed h-BN– Graphene Heterostructure

- The design of a water-based h-BN ink (water/CMC solution) with high concentration of exfoliated BNNSs obtained using a microfluidic processor to perform the LPE process. The developed dispersions showed good stability and the microscopy characterization of the h-BN flakes confirmed nanometric thickness and lateral size of the BNNSs.

- The inkjet-printing of the h-BN ink in order to achieve controlled dielectric thin film in MIM-structured devices on flexible PET substrate. In addition, the validated h-BN dielectric has shown high-*k* characteristics, with ε_{hBN} ~6.92.

- The fabrication of flexible fully inkjet-printed graphene/h-BN TFT devices, and the resulting hole carrier mobility of graphene up to 110 $cm^2V^{-1}s^{-1}$, maintaining the distinctive electrical properties, in normal mechanical conditions or under bending stress.

Appendix A. Printers

A.1 Dimatix 2831 Fujifilm

DIMATIX MATERIALS PRINTER

- **Laboratory benchtop digital ink jet printing system**
- **MEMS-based interchangeable cartridge**
- **Precision XYZ motion control**

FEATURES

- Printing area approximately 200 mm x 300 mm (8 in x 12 in) with an adjustable Z height
- Print any pattern at 5 - 254 µm dot pitch (100 - 5080 dpi)
- Wide fluid compatibility/capability
- Substrates up to 25 mm thick
- Repeatability ± 25 µm (± 0.001 in)
- Heated vacuum table for rigid or flexible substrates
- Pre-loaded patterns, cleaning cycles and jetting waveforms or create your own
- System footprint 673 mm x 584 mm x 419 mm (26 in x 23 in x 16 in)
- Weight approximately 43 kg (95 lbs)
- Power 100-120/200-240 VAC 50/60 Hz 375 W maximum
- Operating temperature range 15-40° C
- PC-user interface with monitor
- Software - driver and printer applications including software pattern generator and Bitmap file import
- Downloadable file format types (DXF, Gerber, GDSII and OASIS)

BENEFITS

- Self contained ready-to-go system
- Non-contact fluid deposition
- User-fillable up to 1.5 ml, interchangeable, disposable cartridge
- User-variable drop size and drop density

OPTIONS

- Fiducial camera for alignment and inspection

DIMATIX MATERIALS CARTRIDGE

- **Piezo drop-on-demand ink jet cartridge**
- **Novel silicon MEMS jetting technology**
- **Easily interchangeable**
- **Efficient use of expensive fluids**

FEATURES

- 1 and 10 picoliter nominal drop volume
- Easy snap-in cartridge
- 1.5 ml capacity syringe fillable cartridge
- 16 nozzles, 254 µm spacing
- Tunable jetting parameters for many solvents, aqueous solutions, UV curing fluids, etc.
- Fluid temperature control up to 70° C for controlled jetting of viscous fluids

BENEFITS

- Easy to use
- Fill with your own fluids
- Minimum material waste
- Excellent fluid compatibility

Materials Printer & Cartridges
DMP-2831 & DMC-11601/11610

Datasheet

System Description

- Flat substrate, xyz stage, "ink jet" deposition system
- Low cost, user-fillable piezo-based ink jet print cartridges
- Built-in drop jetting observation system
- Fiducial camera for substrate alignment and measurement
- Variable jetting resolution and pattern creation PC-controlled with Graphical User Interface (GUI) application software
- Capable of jetting a wide range of fluids
- Heated vacuum platen
- Cartridge cleaning station
- Includes PC, monitor, and software

Mechanical System

- Printable area
  - Substrate < 0.5 mm thickness: 210 mm x 315 mm (8.27 in x 12.4 in)
  - Substrate 0.5 - 25 mm thickness: 210 mm x 260 mm (8.27 in x 10.2 in)
- Repeatability: ± 25 µm (± 0.001 in)
- Substrate holder
  - Vacuum platen
  - Temperature adjustable; ambient to 60° C
- System Footprint: 673 mm x 584 mm x 419 mm (26 in x 23 in x 16 in)
- Weight approximately 43 kg (95 lbs)
- Power 100-120/200-240 VAC 50/60 Hz 375 W maximum
- Operating range 15-40° C at 5-80% RH non-condensing
- Altitude up to 2000 m
- Safety and EMC compliance
  - Safety: NRTL Certified to EN 61010-1, UL 61010-1, CSA 22.2 No. 61010-1
  - EMC: EN61326-1 Class A, FCC Part 15 Class A

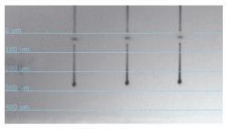

Drop Watcher View

Fiducial Camera

- Allows substrate alignment using reference marks
- Allows positioning a print origin or reference point to match substrate placement
- Provides measurement of features and locations
- Provides inspection and image capture of printed pattern or drops
- Provides cartridge alignment when using multiple cartridges
- Allows matching drop placement to previously patterned substrate

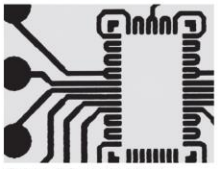

Fiducial Camera View

Cartridge

- Type: Piezo-driven jetting device with integrated reservoir and heater
- Usable Ink Capacity: Up to 1.5 ml (user-fillable)
- Materials Compatibility: Many water-based, solvent, acidic or basic fluids
- Number of Nozzles: 16 nozzles, 254 µm spacing, single row
- Drop Volume: 1 (DMC-11601) and 10 (DMC-11610) picoliter nominal

Control PC and Application Software

- Pre-loaded patterned templates
- Pattern preview
- Editors: Pattern, piezo drive waveform, cleaning cycle, substrate setting
- Bitmap (1 bit) files accepted
- DXF, Gerber, GDSII and OASIS file conversion to Bitmap

Replaceable Items

- Print cartridge with one-time user-fillable reservoir
- Cleaning station nozzle blotting pad
- Drop watcher fluid absorbing pad

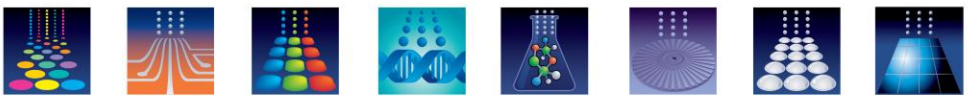

FUJIFILM Dimatix, Inc. • 2230 Martin Avenue • Santa Clara, CA 95050 • USA
Tel: (408) 565-9150 • Fax: (408) 565-9151
E-mail: infomdd@dimatix.com • URL: www.dimatix.com

DDS00017 Rev. 03 11/03/08

A.2 Xennia 4000

CARMINE
THE RANGE OF XENNIA DEVELOPMENT PRINTING SYSTEMS

XENNIA

Xennia Carnelian

Flexible inkjet development system

The Xennia Carnelian inkjet dispenser incorporates industrial printhead technology in a flexible, high precision 3-axis printer for fluid & process development, printhead evaluation and accurate fluid dispensing.

Ideal for fluid & process development

The Xennia Carnelian is the ultimate industrial fluid development and printhead evaluation tool for printed electronics, biotechnology/pharmaceutical or other fluid development applications, allowing developers to get to grips with industrial inkjet technology quickly and cost effectively. The Carnelian comes with a choice of industrial piezo printheads, and can even be fitted with two different types of printhead to allow technology comparison. The combined industrial and low volume syringe ink system allows evaluation of small quantities of fluid, while enabling scaling to a larger volume for extensive testing or pilot production.

Industrial-scale process development made simple

The Xennia Carnelian is a small-scale development tool built around industrial-scale printhead and fluid control technology, meaning that fluid development can be completed using the Carnelian and then ported onto a production printer using the same technology, without the need for reformulation.

Powerful performance with flexible options

The Carnelian uses a robust fully programmable XY motion stage with sub-micron resolution and repeatability of ±5 µm over an A4 printable area. An optional programmable Z axis allows print height to be easily adjusted for 3D substrates. The Carnelian is also available with an optional integrated vacuum table top and alignment camera system for advanced substrate handling and positioning, and with an optional integrated scanning UV lamp for inline pinning of UV fluids.

Intuitive printing with detailed control

Powerful XenJet print software is integrated into the Carnelian, allowing simple one click operation of the printer, or engineering level access to the detailed operation of the system if that is required. The software can also print fully variable data and process DXF/Gerber file formats with optional upgrades.

Application development support

Xennia offers a full application development and support service, including fluid formulation and process optimisation along with inkjet training, to help customers successfully implement inkjet technology into their production process.

- Functional materials dispensing
- Fluid testing and development
- Industrial printhead evaluation

Xennia Carnelian

Specifications

Fluid type	Wide range of aqueous, solvent and UV fluids
Printheads	Up to 2 (most types of industrial piezo printheads)
Printable area	229 mm x 305 mm (9 in x 12 in)
Motion resolution	0.25 µm (XY), 0.5 µm (Z)
Repeatability	±5 µm (XY)
Print speed	Up to 150 mm/s (6 in/s)
XY positioning	Stepper motors
Z positioning	Stepper motor (38 mm (1.5 in) travel)
Fluid control	Combined industrial and low volume syringe system (most printheads) Small volume recirculating ink management system (recirculating printheads)
Printhead maintenance	Manual purge and wipe
Software	XenJet print software with integrated user interface Variable data capability and DXF/Gerber capability available as an option.
Dimensions (WxDxH)	1.2 m x 0.75 m x 1.6 m (47 in x 30 in x 63 in) (approx)
Power supply	120/230V, 50-60Hz, single phase
Optional accessories	Integrated vacuum table top Alignment camera system Integrated scanning UV lamp Programmable Z axis Variable data capability DXF/Gerber file processing

Subject to technical modification without notice

Xennia Technology Ltd
Monroe House • Works Road • Letchworth • Hertfordshire SG6 1LN • UK
telephone: +44 (0) 1462 705220 • facsimile: +44 (0) 1462 705221 • email: enquiries@xennia.com
www.xennia.com

TENCATE
Xennia is part of Royal Ten Cate
www.tencate.com

Appendix B. Resumen en idioma oficial

B.1 Introducción

La impresión gráfica multicolor de ropa mediante la técnica de serigrafía, cuyo origen se estima en hace más de mil años, fue probablemente la primera explosión a gran escala de la creatividad humana. Desde entonces, la tecnología de impresión se desarrolló enormemente con la producción de los primeros periódicos y libros debido al inicio de la tipografía. Hoy en día, a pesar del aparición de los medios digitales, que redujeron la significativa notoriedad de la reproducción de impresiones en papel, se indujo un nuevo y atractivo proyecto de impresión de materiales funcionales sobre sustratos flexibles para impulsar la denominada electrónica "soft", es decir, circuitos mecánicamente deformables y por lo tanto adaptables a la ropa.

El uso de materiales funcionales convirtió disruptivamente la electrónica impresa en una tecnología establecida de bajo coste, en lo que hoy se conoce como electrónica flexible, cambiando el sistema estándar de fabricación de dispositivos electrónicos flexibles de gran área. Las técnicas electrónicas de impresión, que son métodos de fabricación aditivos, promueven el prototipado rápido de bajo coste y la producción de pequeños lotes debido a la reducción del desperdicio de material y la ausencia de procesos substractivos tales como la fotolitografía y el grabado.

Se han dedicado muchos esfuerzos en la formulación de una variedad de materiales compuestos innovadores para suministrar tintas funcionales conductoras, semiconductoras y aislantes. Hasta la fecha, varias tecnologías, generalmente utilizadas en la impresión gráfica tradicional, así como la impresión *gravure*, la *serigrafía*, la impresión *flexográfica* y la impresión por inyección de tinta (*inkjet*), han sido utilizadas para depositar componentes electrónicos basados en estructura de multicapa como dispositivos individuales o complejos para circuitos totalmente impresos. Recientemente, se han logrado varios avances interesantes en la electrónica impresa flexible mediante la fabricación sobre sustratos de plástico y papel de dispositivos tales como antenas de identificación por radiofrecuencia (RFID), diodos, condensadores (metal-aislante-metal, MIM), transistores de capa delgada (TFT), diodos emisores de luz orgánicos (OLED), células fotovoltaicas (células solares) y baterías. La integración de todos estos dispositivos abre el camino para las pantallas de visualización de información (hoy en día altamente flexibles), sistemas portátiles de recolección de energía como el etiquetado de identificación (energy-harvesting systems), sensores electrónicos distribuidos para robots como piel artificial, sensores biológicos para diagnóstico de salud e interfaz humana, etc.

Entre las tecnologías de impresión digital actuales, la selección de la técnica de impresión más adecuada está fuertemente relacionada con los requisitos geométricos, físicos y eléctricos del dispositivo a fabricar. Bajo estas condiciones, la impresión por inyección de tinta controlada se destaca como una técnica rentable, debido a características como un diseño de patrón digital rápido (hasta 15 m / s) (prototipado rápido), uso sin máscara (método de impresión sin contacto con el sustrato), y la garantía de una inyección controlada de gotas de pocos picolitros (hasta 1 pL por cada gota) de tintas basadas en novedosos nano-materiales. Además de minimizar el tamaño del dispositivo y el desperdicio de material, la impresión por inyección de tinta permite la fabricación de grandes áreas cuando se integra en un sistema de fabricación continua (*roll-to-roll*, R2R) que promueve nuevos mercados de electrónica escalable con beneficios rentables mediante la introducción de sustratos flexibles ecológicos y nano-materiales para aplicaciones en la vida cotidiana. Comprender la interacción entre el material funcional, el proceso de impresión y el sustrato ha sido (y sigue siendo) necesario para desarrollar sofisticados dispositivos electrónicos con éxito.

En este trabajo, se ha demostrado que la tecnología de impresión por inyección de tinta constituye un método versátil no solamente para la fabricación de diferentes aplicaciones de plataforma robusta (circuitería y sensores) sino también como complemento y alternativa al proceso de fabricación estándar para soldar un circuito híbrido flexible en circuitos previamente impresos por inyección de tinta.

Además, aunque el sustrato flexible (plástico polimérico o papel) permite propiedades tales como transparencia y / o resistencia a la deformación mecánica, los dispositivos totalmente impresos mediante esta técnica deben cumplir con los requisitos actuales establecidos por la hoja de ruta internacional para componentes electrónicos. La movilidad eléctrica (μ) y la constante dieléctrica (ε), que sirven de referencia para evaluar la calidad de los distintos materiales, dispositivos y procesos, son los parámetros más críticos en los dispositivos electrónicos impresos debido al estado de dispersión del líquido de las tintas semiconductoras y aislantes, respectivamente, en comparación con la bien establecida tecnología de silicio.

El trabajo principal de esta Tesis abarca temas que incluyen desde la completa caracterización de la tinta dieléctrica basadas en nanopartículas 3D de dióxido de hafnio (HfO_2) a la formulación de una nuevo compuesto aislante con elevada constante dieléctrica basada en láminas (*flakes-nanosheets*) 2D de nitruro de boro hexagonal (h-BN), teniendo como objetivo la fabricación de dispositivos totalmente impresos mediante inyección de tinta, así como condensadores, memorias y transistores, que se han fabricado sobre sustratos poliméricos flexibles.

B.2 Estructura del resumen

- En la sección *B.1 Introducción* se presenta la visión general de la Tesis, donde se introducen brevemente los aspectos más relevantes de esta memoria y su estructura (*B.2 Estructura del resumen*).

- Los objetivos que han guiado este trabajo de Tesis se resumen en el apartado *B.3 Objetivos de la tesis*.

- Los resultados de esta Tesis y su discusión (*B.4 Resultados y discusión*) están organizados en tres bloques, que corresponden a las diferentes temáticas desarrolladas por el autor durante el doctorado. Las áreas desarrolladas, y la contribución principal de esta Tesis en ellas, son las siguientes:

- En la primera etapa del Proyecto de Doctorado, el objetivo principal fue la investigación de nuevas áreas de aplicación prometedoras en las que la tecnología de impresión por inyección de tinta podría contribuir a resolver problemas tradicionales y mejorar los procesos de fabricación para dispositivos eléctricos flexibles. Como consecuencia, la impresión por inyección de tinta se utilizó como herramienta para la producción de plataformas de circuitos de sensores de gas (***Paper I***), siendo los mismos dispositivos posteriormente comparados con idénticos materiales pero fabricados a partir de la tecnología de serigrafía, más madura y consolidada (***Paper II***). Por último, se exploró la impresión mediante inyección de tinta, aprovechando la alta resolución de volumen de gota eyectada (unos10 pL por gota), para conectar y soldar dispositivos de montaje en superficie (SMD, de sus siglas en inglés) sobre circuitos previamente impresos por la misma máquina de inyección de tinta. Esto ha permitido generar un circuito híbrido sobre sustrato flexible completamente impreso (***Paper III***).

- En la segunda etapa de la Tesis, la investigación se centró en la caracterización de una solución comercial de dieléctrico con alta constante dieléctrica (*high-k* HfO_2), ajustando la reología para ser imprimible con alta resolución (10 pL por gota) mediante impresora de inyección de tinta. Por primera vez se ha reportado un estudio completo de caracterización de las propiedades eléctricas del dieléctrico HfO_2 a partir de la fabricación de dispositivos electrónicos flexibles totalmente impresos por inyección de tinta, tales como condensadores (***Paper IV***) y dispositivos de memoria (***Paper V*** y ***Paper VI***).

- Por último, pero no por ello menos importante, durante la tercera etapa de la Tesis, realizada principalmente en el *Cambridge Graphene Centre* de la Universidad de Cambridge (Inglaterra), los objetivos de investigación se trasladaron a la formulación de una tinta de h-

BN, biocompatible z basada en agua, diseñada para ser impresa como material dieléctrico con elevada constante dieléctrica. Se fabricaron por primera vez dispositivos transistores con estructura semiconductor / aislante de grafeno / h-BN, respectivamente. Los dispositivos han sido totalmente fabricados por inyección de tinta sobre sustratos flexibles, logrando una movilidad de huecos del canal semiconductor de grafeno de hasta 110 $cm^2V^{-1}s^{-1}$, y mostrando excelentes propiedades eléctricas en condiciones mecánicas normales (dispositivos planos) o bajo estrés mecánico (dispositivos bajo flexión) (***Paper VII***).

- En la sección B.5 *Conclusiones* se presentan las conclusiones más significativas de esta Tesis doctoral.
- Finalmente, los artículos científicos objeto de evaluación en esta Tesis doctoral se listan en la sección *B.6 Listado de artículos*.

B.3 Objetivos de la Tesis

Después de un analisis profundo que describe los antecedentes de la electrónica impresa, con una visión general de las técnicas de impresión actuales y de las aplicaciones electrónicas flexibles comunes, la tecnología de impresión de inyección de tinta se presenta como una herramienta de gran alcance en comparación con los procesos estándar de fabricación. Por otra parte, el tema principal es la revisión de los materiales funcionales de tinta existentes (conductores, semiconductores y aislantes) y la falta de nano-materiales en solución de tinta adecuados para cumplir con los requisitos para dispositivos electrónicos definidos en la hoja de ruta del ITRS.

Quisiera llamar la atención sobre las principales contribuciones de este trabajo y la importancia puede ser explicada por las siguientes razones:

- Comprobación de la robustez y la fiabilidad de la impresora de inyección de tinta para el desarollo de una plataforma electrónica funcional. Debido a la experiencia del grupo de investigación de la UB en sensores para la detección de gases, este campo ha sido seleccionado como referencia para la caracterización de la técnica de impresión por inyección de tinta, cuyos resultados se compararán con la tecnología de serigrafía, más madura y consolidada. Se analizarán los diferentes fenómenos de fallo existentes en las plataformas impresas para sensores de gases y se presentarán diferentes soluciones a dichos fallos. En consecuencia, se desarrollará la fabricación de plataformas de sensores de gases flexibles, robustas y fiables, utilizando la tecnología de impresión por inyección

de tinta para el desarrollo de una capa de óxido metálico (óxido de titanio, TiO_{2-x}) depositada sobre los circuitos impresos por inyección de plasma atmosférico (APS).

- Demostración de la tecnología de impresión por inyección de tinta como método alternativo a la tecnología de montaje en superficie (SMT, de sus siglas en inglés) para el ensamblaje (soldadura) de dispositivos de montaje en superficie (SMD) en circuitos previamente impresos por inyección de tinta sobre sustratos flexibles.

- Caracterización de un óxido de capa fina con elevada constante dieléctrica (HfO_2), impreso por medio de inyección de tinta, y estudio de sus propiedades eléctricas a partir de dispositivos capacitivos MIM. - Estudio en profundidad del fenómeno de conmutación resistiva bipolar de los memristores fabricados mediante técnica de inyección de tinta (ReRAMs) con una estructura MIM simple. El dieléctrico HfO_2 se seleccionará como material aislante, ya que está considerado como un oxido-metálico idóneo por sus defectos estequiométricos, formando así estructuras de Au / HfO_2 / Ag y Pt / HfO_2 / Ag. Las prestaciones de memristores impresos por medio del presente método serán comparadas con la tecnología convencional CMOS.

- Desarrollo de un proceso sistemático para la producción a gran escala de una tinta dieléctrica adecuada que pueda actuar como capa aislante en la electrónica basada en grafeno y materiales 2D relacionados. Se ha seleccionado el nitruro de boro hexagonal (h-BN) debido a sus propiedades dieléctricas (alta constante dieléctrica en el material masivo) y de biocompatibilidad. Además, la experiencia a largo plazo del grupo del CGC en la electrónica basada en grafeno y materiales 2D será fundamental para los logros previstos dentro de este Proyecto de Tesis.

B.4 Resultados y discusión

En esta sección se presentan y discuten los resultados obtenidos durante el desarollo de esta Tesis. Con este objetivo, se presentarán y resumirán los trabajos publicados más relevantes sobre estos resultados, así como los resultados no publicados o presentados recientemente que sean relevantes para el pleno logro de los objetivos de la Tesis. El trabajo total puede ser clasificado en tres bloques distintos.

Versatilidad de la tinta de plata impresa por técnica de inyección de tinta

- El primer bloque se centra en la versatilidad de la aplicación de la tinta a base de nanopartículas de plata (AgNP) mediante la técnica de impresión por inyección de tinta. Por un lado se emplea el material conductor como principal constituyente de la circuitería para plataformas de sensores de gas y para identificar las causas de posible fallo del dispositivo,

y se realiza una caracterización completa de las plataformas flexibles de circuitos impresos por inyección de tinta mediante una caracterización a largo plazo y pruebas de envejecimiento (***Paper I***). Una vez obtenida la optimización de las plataformas de sensores de gas, se implementan dispositivos de detección de gas mediante el desarrollo de una capa de óxido metálico (óxido de titanio, TiO_{2-x}) como capa activa depositada por inyección de plasma atmosférico sobre los circuitos previamente impresos por inyección de tinta (***Paper II***). Por otro lado se aplica el AgNP como material de soldadura para uniones completamente impresas por inyección de tinta en circuitos flexibles de electrónica híbrida. Se realizan caracterizaciones eléctricas, mecánicas y morfológicas para evaluar el rendimiento del nuevo método, que se compara con materiales de referencia comúnmente utilizados para soldadura (plata epoxi y estaño). Además, la fabricación de un circuito híbrido flexible, controlado por un micro-controlador Arduino, demuestra la aplicabilidad y escalabilidad del AgNP como material adecuado para la soldadura de componentes SMD sobre circuitos totalmente impresos por inyección de tinta. (***Paper III***)

Paper I : *Diseño y Fabricación de Plataformas de Sensores de Gas*

En el primer artículo que se presenta, ***Paper I***, se estudiaron y discutieron en detalle los siguientes puntos:

(1) La fabricación de plataformas de sensores versátiles, de bajo coste, flexibles y fiables para sensores resistivos. La plataforma de sensores diseñada consistió en una sistema de detección (en el lado superior del sustrato) y un calentador (en el lado inferior del sustrato).

(2) La calibración y caracterización de las plataformas de sensores de gas aplicando pulsos de tensión y monitoreando su temperatura para los ensayos de vida y envejecimiento. Posteriormente, se presentó una comparación con plataformas de sensor de gas equivalentes impresas mediante una técnica madura como la serigrafía.

(3) La mejora del diseño para evitar fallos en la plataforma y para reducir el consumo de energía debido al calentador.

El objetivo principal de este trabajo fue demostrar la viabilidad de plataformas flexibles de sensor de gas fabricadas con tecnología de impresión por inyección de tinta. Se realizaron ensayos de vida continua (manteniendo 120 °C durante el funcionamiento del calentador) y los resultados se compararon con plataformas de sensores de gas impresas por serigrafía. Se observó, en los

dispositivos de serigrafía, un fallo precoz del dispositivo causado por la degradación química, debido a la morfología en forma de escamas de las capas de plata de los depósitos. No se produjo ningún deterioro notable en las pistas conductoras de nanopartículas de plata impresas por inyección de tinta. Sin embargo, la película muy fina obtenida mediante el proceso de impresión promueve un fallo por fenómeno de punto caliente cuando se induce un exceso de corriente , aunque no se observó degradación química de las plataformas impresas. Además, el trabajo también demostró que la combinación sinérgica de sustratos poliméricos con electrónica impresa es una buena alternativa al silicio monolítico y a las tecnologías cerámicas.

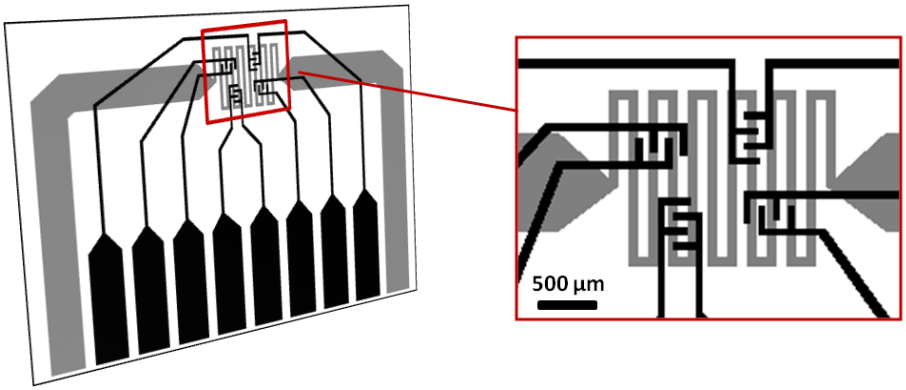

Fig.1 *Esquemade la parte de detección (en el lado superior del sustrato) y del calentador (en el lado inferior del sustrato).[Paper I]*

Paper II : *Aplicación en Plataformas de Sensores de Gas*

En el ***Paper II*** se presenta una ampliación evidente del trabajo presentado en el ***Paper I***, que trataba de los siguientes puntos:

(1) La viabilidad de plataformas flexibles de sensores de gas impresas por inyección de tinta para la fabricación de óxido metálico, óxido de titanio (TiO_{2-x}) en nuestro caso, por pulverización de plasma atmosférico (APS). A pesar de las altas temperaturas implicadas en el APS (~300 °C), las plataformas impresas por inyección de tinta no se degradaron durante el proceso, obteniendo así un revestimiento de óxido de titanio altamente uniforme.

(2) La caracterización de la respuesta del TiO_{2-x} al gas NH_3.

(3) La caracterización de la modulación de respuesta al NH_3 con la temperatura (de temperatura de ambiente hasta 220 °C), impulsada por el calentador.

En este trabajo, el objetivo principal fue la fabricación de un sensor de óxido metálico, óxido de titanio (TiO_{2-x}) en particular, por medio de APS, sobre una película delgada polimérica flexible. El dióxido de titanio es un material ampliamente utilizado en el campo de los sensores y actuadores.

Tanto su estabilidad química como su coste relativamente bajo lo hacen atractivo para aplicaciones industriales. Como consecuencia, el TiO_{2-x} ha sido seleccionado como materia prima en APS. A pesar de las altas temperaturas implicadas en APS, el sustrato polimérico no se degradó durante el proceso, obteniendo así un revestimiento de óxido de titanio altamente uniforme. Finalmente, se comprobó el comportamiento de detección de la capa de óxido metálico por medio de NH_3 (gas tóxico, demostrando resultados positivos en concentraciones de NH_3 comprendidas entre 10 y 100 ppm.

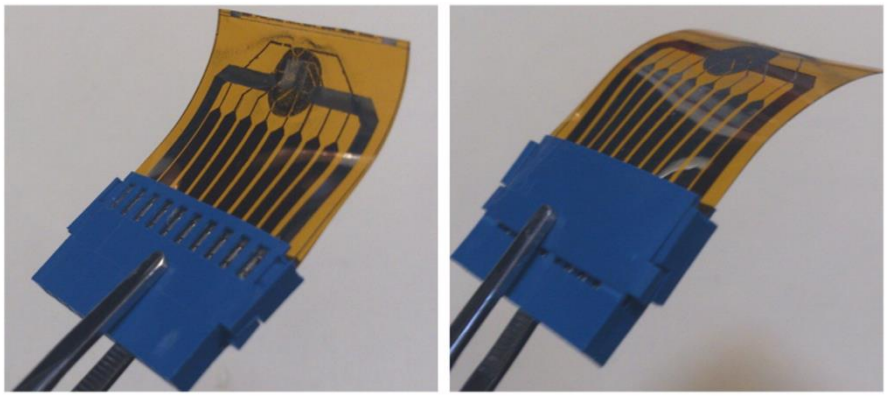

Fig.2 *Aplicación del dispositivo sensor de gas de NH_3. La capa activa de detección se basa en TiO_{2-x}.[Paper II]*

Paper III :*Soldadura por Inyección de Tinta*

En el ***Paper III*** se trataron en detalle los siguientes aspectos:

(1) La fabricación, por primera vez, de uniones completamente impresas mediante inyección de tinta que emplean inyección de alta resolución de tinta de plata a base de nanopartículas.

(2) La demostración de la viabilidad y la fiabilidad de las nanopartículas de plata como material de interconexión de alta conductividad para ensamblar dispositivos de montaje superficial (SMDs) sobre sustratos previos impresos por inyección de tinta mediante medidas de resistencia de contacto eléctrico y de resistencia al corte, comparando los resultados con materiales de ensamblaje de referencia (estaño y expoxy).

(3) La observación de un contacto de montaje homogéneo (~ 1 μm de espesor) entre el SMD y las pistas conductoras impresas sobre sustratos diferentes, confirmando así la reducción del consumo de material.

(4) La fabricación de un circuito híbrido flexible en papel para demostrar la aplicabilidad y escalabilidad de la técnica de ensamblaje propuesta, en la que sensores SMD, diferentes en forma y tamaño, están controlados a través de un micro-controlador Arduino.

El documento tiene como objetivo la demostración de la tecnología de impresión por inyección de tinta, como método alternativo a la tecnología de montaje en superficie (SMT), para ensamblar SMDs en sustratos previos impresos por inyección de tinta. Las aplicaciones y las implicaciones de este trabajo podrían ser de largo alcance. Creemos que nuestro trabajo mejorará las etiquetas RF existentes, potenciará y promoverá el empaquetado inteligente y mejorará la electrónica portátil, flexible y de papel.

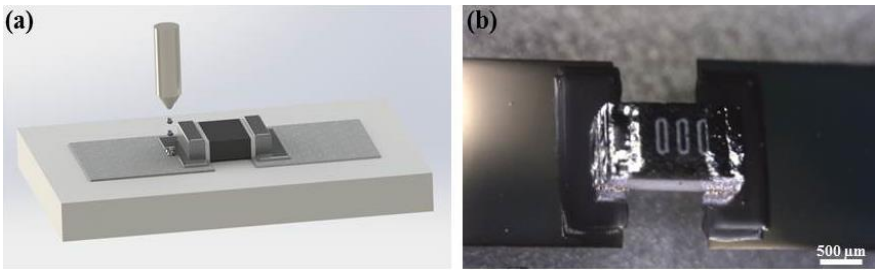

Fig. 3 *(a) Illustración de un SMD soldado por la tinta de AgNP mediante inyección de tinta. (b) SMD 0402 de 0 Ω conectado por medio de tinta AgNP sobre pista conductora también previamente impresa.[Paper III]*

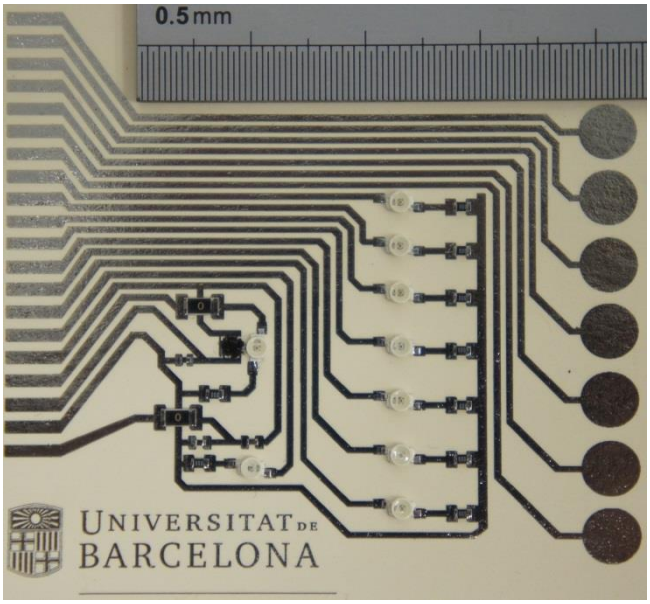

Fig.4 *Circuito impreso mediante inyección de tinta sobre sustrato de papel con SMDs basados en tinta de AgNPs interconectados. [Paper III]*

Impresiòn del aislante HfO_2 para dispositivos electrónicos: capacidades y memristores.

- El segundo bloque presenta el uso de la tinta dieléctrica a base de nanopartículas de alta constante dieléctrica, siendo HfO_2 el material seleccionado, para la fabricación de dispositivos flexibles totalmente impresos por inyección de tinta, en particular condensadores (MIM) (***Paper IV***) y memristores (MEMS) (***Paper V***), y se dedica al estudio de las propiedades físicas y químicas del aislante impreso. La caracterización eléctrica evidenció, a partir de medidas dependientes de la capacitancia y la tensión, que los MIMs funcionan adecuadamente dentro de los requerimientos de la hoja de ruta ITRS 2016 y que, a través de mediciones cíclicas de corriente y tensión, los dispositivos ReRAMs basados en HfO_2 funcionan adecuadamente alcanzando más de 516 ciclos de conmutación resistiva.

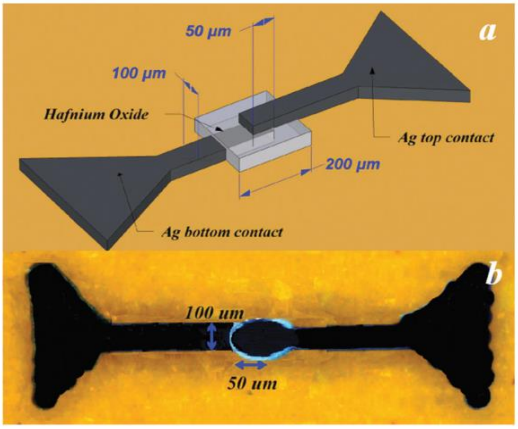

Fig. 5 *(a) Esquema de la estructura MIM Ag / HfO_2 / Ag. (b) Imagen de microscopio de un dispositivo condensador impreso sobre sustrato flexible mediante inyección de tinta. [Paper IV]*

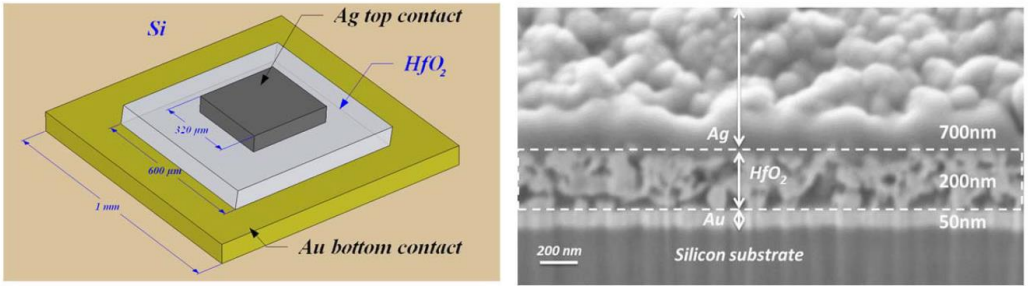

Fig. 6 *(a) Esquema de la estructura Au / HfO_2 / Ag para dispositivo memristor. (b) Imagen de microscopía de la sección transversal de un dispositivo memristivo impreso mediante técnica de inyección de tinta. [Paper V]*

Paper IV: *Condensador HfO_2 Impreso mediante Inyección de Tinta*

En el ***Paper IV*** se describieron y estudiaron los siguientes aspectos:
(1) La fabricación por primera vez de condensadores MIM totalmente impresos con alta resolución basada en el óxido de hafnio, de alta constante dieléctrica, como aislante, por medio de la tecnología de inyección de tinta sobre sustratos flexibles.
(2) La observación de la uniformidad del depósito y la pureza cristalina de la capa fina impresa del dieléctrico HfO_2 basado en nanopartículas.
(3) La demostración de la baja contaminación del aislante debido a la formulación de la tinta, el depósito a partir de la tecnología de inyección de tinta y los procesos de recocido a baja temperatura para la fabricación de los dispositivos MIM.
(4) La evidencia, usando medidas dependientes de capacitancia y voltaje, de que los MIMs funcionan adecuadamente dentro de los requisitos de hoja de ruta del ITRS 2016.
Los resultados anteriormente mencionados se explican en términos de las propiedades dieléctricas de HfO_2: por un lado, la elevada energía de banda prohibida (5.8 eV) del óxido impreso, que asegura la alta barrera para los electrones; por otro lado, su permitividad relativa y tangente de pérdida dieléctrica, que garantizan bloquear la conducción a través de impurezas. En general, el documento apunta a la correlación entre la impresión por inyección de tinta de un óxido de capa fina y las propiedades eléctricas de los dispositivos basados en óxido de hafnio de alta costante dieléctrica (HfO_2).

Paper V:*Memristor Au / HfO_2 / Ag Basado en HfO_2 Impreso a partir de Inyección de Tinta*

En el ***Paper V*** se trataron los siguientes temas en detalle:
(1) La fabricación, por primera vez, de un componente memristor con estructura MIM simple, Au / HfO_2 / Ag, basado en óxido de hafnio (de alta constante dieléctrica) como aislante flexible, mediante la tecnología de impresión por inyección de tinta.
(2) La observación de un fenómeno de conmutación resistiva bipolar, donde los sucesivos cambios controlados entre dos estados conductores, LRS y HRS, se obtienen aplicando tensiones positivas SET (proceso de formación del filamento conductivo) y tensiones negativas RESET (proceso de ruptura del filamento).
(3) La demostración del alto rendimiento del sistema, con una relación I_{ON} / I_{OFF} de tres órdenes de magnitud y bajos voltajes de operación de conmutación (alrededor de 0.2 V), permitiendo así una

reducción del consumo. Estos parámetros son comparables a los obtenidos por las tecnologías CMOS convencionales.

(4) La evidencia, a través de medidas cíclicas de corriente y voltaje, de que los dispositivos ReRAM basados en HfO_2 funcionan correctamente, alcanzando más de 128 ciclos de conmutación resistiva.

Los resultados anteriormente mencionados se explican en términos del proceso de formación de un filamento conductor conmutable en la capa dieléctrica de capa fina impresa por inyección de tinta. En primer lugar, el proceso SET se caracteriza por una corriente de túnel muy baja (1 pA a 1 V). Posteriormente, los valores de corriente elevados, medidos después de SET, sugieren que la conducción durante LRS es controlada por un filamento conductor creado dentro de la capa impresa de HfO_2. Por consiguiente, las corrientes medidas después de RESET indican que el filamento conductor no está completamente cerrado, lo que implica que la conducción durante HRS es, posiblemente, también controlada por el mismo filamento conductor, más débil porque está parcialmente cerrado. El documento tiene como objetivo la demostración de la tecnología de impresión por inyección de tinta como método alternativo para el depósito de capas finas de HfO_2 basadas en nanopartículas para la fabricación de dispositivos ReRAMs.

Paper VI: *Memristor Pt / HfO_2 / Ag basado en HfO_2 Impreso mediante Inyección de Tinta*

En el ***Paper VI*** se trataron los siguientes temas en detalle:

(1) Se investiga la fabricación de un componente memristor con estructura MIM simple, Pt/HfO_2/Ag sobre sustratos Si/SiO_2 y se compara con las estructuras Au/HfO_2/Ag para estudiar la interacción del electrodo inferior con la capa dieléctrica HfO_2 y los efectos resultantes sobre los fenómenos de conmutación resistiva.

(2) La observación de un fenómeno de conmutación resistiva bipolar obtenido aplicando tensiones positivas SET (proceso de formación) y RESET negativo. Las medidas de corriente mostraron que el electrodo inferior de Pt mejora la ventana de memoria y aumenta la resistencia de las operaciones SET y RESET, ~ 10^3 ciclos de escritur y lectura. Además, los dispositivos mostraron bajos voltajes SET y RESET y una corriente de conmutación relativamente baja (~ 1 μA), que son comparables a las características de las memorias CMOS comerciales actuales.

(3) La demostración de características de alto rendimiento como la relación I_{ON} / I_{OFF} de más de seis órdenes de magnitud y bajos voltajes de operación de conmutación alrededor de 0.2V, permitiendo así una reducción de consumo.

Los resultados anteriormente mencionados se explican en términos del proceso de formación en la capa dieléctrica de capa fina impresa por inyección de tinta, que crea un filamento conductor

conmutable. Los análisis de las imágenes transversales mostraron acumulación asimétrica de oxígeno en la capa de óxido bajo polarización eléctrica. Las inspecciones de EELS demostraron en ambas estructuras la ausencia de un posible efecto de electromigración de plata, justificando así que el mecanismo de conmutación resistivo se debe a la formación de un filamento conductor de vacantes de oxígeno en la capa de HfO_2.

Impresiòn de estrucutras basadas en materiales 2D: h-BN– grafeno

- El tercer bloque muestra la formulación, para la producción a gran escala, de una tinta biocompatible (*eco-friendly*) y aislante basada en láminas (*flakes-nanosheets*) de h-BN. Se demuestran componentes flexibles capacitivos, con estructura MIM y totalmente impresos mediante la técnica de inyección de tinta. A partir de la caracterización eléctrica se confirma el valor elevado de constante dieléctrica *k* esperado para la tinta h-BN formulada. Por consiguiente, se demuestra que la capa dieléctrica de h-BN es un material adecuado para actuar como óxido de puerta para heterostructuras de *grafeno* / h-BN flexibles y totalmente impresas por inyección de tinta para dispositivos transistores. Asimismo, se han determinado propiedades eléctricas exclusivas de los dispositivos impresos, tanto en condiciones mecánicas normales (configuración plana) o bajo estrés mecánico (flexión).

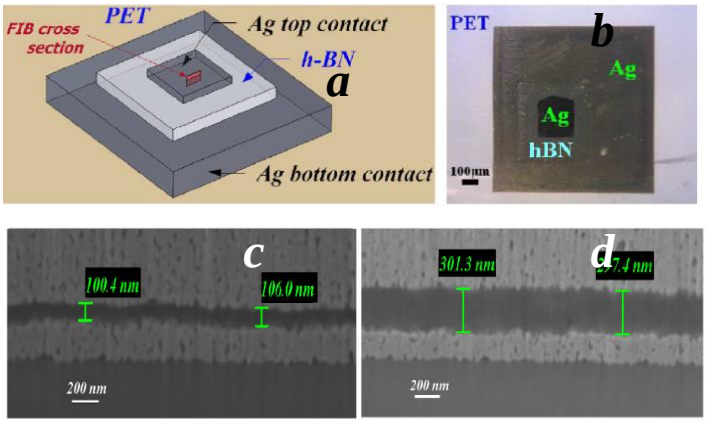

Fig. 7 (a) *Esquema de un condensador Ag / h-BN /Ag sobre sustrato PET.* ***(b)*** *Imagen mediante microscopio óptico de un condensador totalmente impreso por inyección de tinta.* ***(c), (d)*** *Imágenes de la sección transversal de dos dispostivos con distinto espesor de la capa dieléctrica de h-BN, 100 nm* ***(c)*** *y 300 nm* ***(d)****. [Paper VII]*

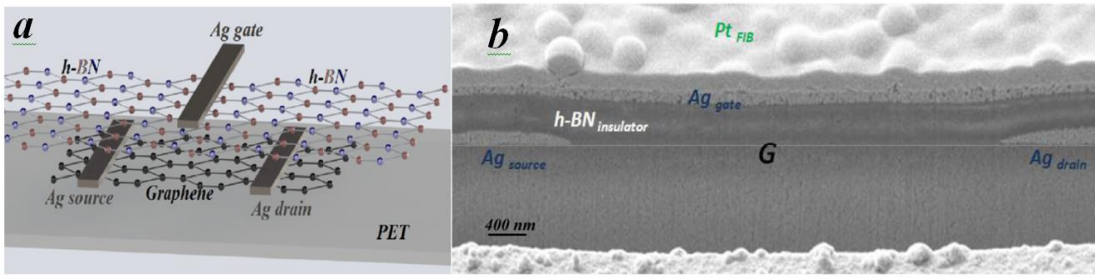

Fig. 8 (a) *Esquema 3D de los dispositivos TFT basados en h-BN/grafeno.* ***(b)****, imagen en sección transversal de TFT impreso mediante inyección de tinta. [Paper VII]*

Paper VII*: Transistores de Capa Delgada (TFT) Flexibles Basados en Gr / h-BN Totalmente Impresos mediante Inyección de Tinta*

En el ***Paper VII*** se estudiaron y discutieron en detalle los siguientes aspectos:

(1) El diseño de una tinta h-BN con base de agua (solución de agua / CMC) con alta concentración de láminas de h-BN (BNNSs) exfoliados obtenidos utilizando un procesador microfluídico para realizar el proceso LPE. Las tintas desarrolladas mostraron buena estabilidad y la caracterización microscópica de las láminas de h-BN confirmó el espesor nanométrico y el tamaño lateral de los BNNSs.

(2) La impresión por inyección de tinta de h-BN con el fin de obtener capas finas dieléctricas de espesor controlado como dieléctrico en dispositivos con estructura MIM sobre sustrato flexible PET. Además, el dieléctrico h-BN validado ha mostrado una alta costante dieléctrica, $\varepsilon \sim 6{,}92$.

(3) La fabricación de dispositivos flexibles de *grafeno* / h-BN para TFTs completamente flexibles, que dan como resultado una movilidad de huecos del canal de *grafeno* de hasta 110 $cm^2V^{-1}s^{-1}$, ya sea en condiciones mecánicas normales o bajo estrés mecánico de flexión.

En este trabajo se seleccionó la técnica de microfluidización a alta presión como un método eficiente, rentable y de producción en masa para la exfoliación de h-BN. Se seleccionó un derivado de celulosa, carboxymethy celulosa (CMC) para estabilizar las láminas de h-BN en solución. Se demostró que el método da lugar a dispersiones de BNNSs altamente concentradas que son adecuadas para la tecnología de impresión por inyección de tinta. Para determinar las propiedades aislantes de la capa de h-BN, se estudiaron tanto la estructura como la morfología de las capas finas impresas por inyección de tinta. Mediante depósito selectivo de capas finas de BNNSs, se

fabricaron dispositivos MIM y, en consecuencia, se erigieron heteroestructuras de multicapa en las que los BNNSs y las láminas de *grafeno* exfoliados se apilan alternativamente para formar un transistor TFT, donde el *grafeno* constituye el canal, totalmente impreso sobre sustrato flexible PET, a temperatura y presión ambiente.

Entonces, se imprimieron por inyección de tinta capas finas uniformes de h-BN (~50 nm por capa), y se demostró que los condensadores Ag / h-BN / Ag totalmente impresos presentan un valor de constante dieléctrica del h-BN de $\varepsilon_r = 6{,}92$, logrando una capacidad por unidad de área de 1 nF mm^{-2}. Finalmente, se caracterizaron los TFTs basados en materiales 2D e impresos por inyección de tinta utilizando h-BN y tinta de *grafeno* como capas dieléctricas y de canal, respectivamente. La reproducibilidad de los TFTs se confirmó mediante una estadística de más de 20 dispositivos, reportando una movilidad de huecos récord, para dispositivos totalmente impresos sobre substratos flexibles PET, de hasta 110 $cm^2 V^{-1} s^{-1}$,.

En general, este trabajo ha demostrado por primera vez que el h-BN exfoliado constituye un material dieléctrico de elevada constante dieléctrica, de este modo siendo adecuado para actuar como óxido de puerta y así ser complementario con el *grafeno* en estructuras flexibles y procesadas a baja temperatura (~100 °C, adecuada para el sustrato PET seleccionado).

B.5 Conclusiones

Creando una sinergia entre diferentes universidades europeas, este trabajo se ha llevado a cabo en las instalaciones de la Universitat de Barcelona (UB), la Universitat Autònoma de Barcelona (UAB) y el Cambridge Graphene Center (CGC) de la Universidad de Cambridge. En consecuencia, esta Tesis se ha desarrollado basándose en un conocimiento establecido y consolidado sobre la tecnología de impresión por inyección de tinta, la caracterización de dispositivos de memoria y la formulación de tinta de materiales 2D basados en el *grafeno*, respectivamente.

En esta Tesis, se ha demostrado que la tecnología de impresión por inyección de tinta es un método versátil para la fabricación de diferentes aplicaciones robustas (sensores flexibles y circuitos híbridos), y especialmente como complemento y alternativa a la fabricación estándar de tecnología de silicio para el desarrollo de componentes flexibles de alta calidad totalmente impresos mediante inyección de tinta, donde los materiales utilizados han sido, por primera vez en la literatura, el óxido metálico HfO_2 basado en nanoparticulas 3D y el h-BN basado en láminas 2D. Ambos materials han presentado elevadas constantes dieléctricas.

El objetivo principal de esta Tesis fue demostrar la tecnología de impresión por inyección de tinta como una herramienta poderosa para el futuro desarrollo de la electrónica impresa flexible.

Básicamente, se ha abordado la investigación de nuevas áreas de aplicación prometedoras en las que la tecnología de impresión por inyección de tinta podría contribuir a resolver problemas tradicionales y mejorar los procesos de fabricación.

En primer lugar, hemos demostrado la viabilidad de la impresión por inyección de tinta como una técnica prometedora en comparación con otros métodos de impresión actuales para la fabricación de plataformas robustas de circuitos de sensores de gas, y como método alternativo a la tecnología de montaje en superficie (SMT) para soldadura de SMDs en circuitos impresos previamente por inyección de tinta para aplicaciones electrónicas flexibles. Una vez que se ha aseverado la adecuación de la impresión por inyección de tinta para una producción robusta, de bajo coste y a gran escala, el segundo tema principal de este trabajo fue la implementación de nuevas soluciones para perseguir y seguir las pautas de las hojas de ruta del ITRS para la próxima generación de aplicaciones electrónicas flexibles, mediante la formulación de nuevas tintas dieléctricas que permiten la fabricación de dispositivos de alta calidad totalmente impresos por inyección de tinta.

Principalmente, el estudio se centró en la tinta dieléctrica de HfO_2, de elevada constante dieléctrica, y se investigaron las propiedades físicas y químicas de dicho aislante impreso por inyección de tinta. Posteriorment, se demostró, por primera vez en la literatura, que el HfO_2 es un material de alta costante dieléctrica adecuado para obtener dispositivos electrónicos flexibles totalmente impresos por inyección de tinta, tales como condensadores MIM y dispositivos ReRAM.

Finalmente, a pesar de las excelentes propiedades probadas de la tinta a base de nanopartículas de HfO_2, y debido a la incompatibilidad con la tinta de *grafeno* disponible (formulada por el grupo CGC de la Universidad de Cambridge), los objetivos de investigación se trasladaron a la formulación de una tinta de h-BN con base de agua, especialmente diseñada para ser impresa como material dieléctrico. La tinta h-BN dieléctrica confirmó el elevado valor de constante dieléctrica esperado (k ~ 6.9) mediante una caracterización en profundidad de componentes MIM flexibles completamente impresos por inyección de tinta. Entonces, el h-BN impreso por inyección de tinta se empleó exitosamente como óxido de puerta adecuado para heteroestructuras de *grafeno* / h-BN flexibles completamente impresas por inyección de tinta para dispositivos TFT. Se obtuvieron, por primera vez en la literatura, propiedades eléctricas distintivas para dichas estructuras que logran una movilidad de huecos del canal de *grafeno* de hasta 110 $cm^2V^{-1}s^{-1}$ en condiciones mecánicas normales, con una reducción de solamente el 20% cuando están sometidas a estrés mecánico de flexión.

En resumen, de los resultados obtenidos durante el presente Proyecto de Tesis Doctoral, se concluye que la técnica de inyección de tinta es un método altamente válido para proveer una alternativa real a los procesos industriales existentes para la fabricación de plataformas de circuitería flexible.

Además, los experimentos se han realizado sobre estructuras muy presentes en la electrónica convencional (condensadores, transistores, memorias) y a partir de materiales de alto interés en la actualidad debido a sus propiedades eléctricas particulares (HfO_2, h-BN, *grafeno*). Debido a ello, la presente Tesis se erige en un trabajo sistemático y riguroso, a la vez que imaginativo y creativo, dentro de un campo novedoso y en auge, el de la circuitería electrónica flexible de bajo coste, con elevadas expectativas de cara al sector industrial del presente y del futuro.

B.6 Lista de publicaciones

Solamente las publicaciones incluidas en esta lista serán consideradas para la evaluación de esta Tesis doctoral, de los cuales los ***Papers I, II, III, IV y V*** cumplen con las condiciones estipuladas para la presentación de una Tesis en formato de publicaciones. Se puede encontrar una reproducción de cada publicación en las páginas indicadas a continuación. Una lista completa de las publicaciones del autor, actualizada en abril de 2017, se incluye en el *curriculum vitae* científico (Apéndice E).

Paper I. Beatriz Medina-Rodriguez, Francisco Ramos, Giovanni Vescio, Xavier Arrese, Aïda Varea, and Albert Cirera, "Fabrication, Performances and Aging of Flexible Gas Sensor Platforms," *J. Mater. Sci. Eng. B*, vol. **5**, no. 4, pp. 170–176, Apr. 2015.

** Contribución del autor: planificación y realización de partes de los experimentos y escritura de partes del manuscrito.*

Paper II. M. Gardon, O. Monereo, S. Dosta, G. Vescio, A. Cirera, and J. M. Guilemany, "New procedures for building-up the active layer of gas sensors on flexible polymers," *Surf. Coatings Technol.*, vol. **235**, pp. 848–852, Nov. 2013.

** Contribución del autor: planificación y realización de partes de los experimentos y escritura de partes del manuscrito.*

Paper III. J. Arrese, G. Vescio, E. Xuriguera, B. Medina-Rodriguez, A. Cornet, and A. Cirera, "Flexible hybrid circuit fully inkjet-printed: Surface mount devices assembled by silver nanoparticles-based inkjet ink," *J. Appl. Phys.*, vol. **121**, no. 10, p. 104904, Mar. 2017.

** Contribución del autor: planificación y realización de partes de los experimentos y escritura de partes del manuscrito.*

Paper IV. G. Vescio, J. López-Vidrier, R. Leghrib, A. Cornet, and A. Cirera, "Flexible inkjet printed high-k HfO 2 -based MIM capacitors," *J. Mater. Chem. C*, vol. **4**, no. 9, pp. 1804–1812, 2016.

** Contribución del autor: planificación y realización de los experimentos, evaluación de los resultados y redacción de las partes principales del manuscrito.*

Paper V. G. Vescio, A. Crespo-Yepes, D. Alonso, S. Claramunt, M. Porti, R. Rodriguez, A. Cornet, A. Cirera, M. Nafria, and X. Aymerich, "Inkjet Printed HfO 2 -Based ReRAMs: First Demonstration and Performance Characterization," *IEEE Electron Device Lett.*, vol. **38**, no. 4, pp. 457–460, Apr. 2017.

** Contribución del autor: planificación y realización de los experimentos, evaluación de los resultados y redacción de las partes principales del manuscrito.*

Paper VI. The article has been SUBMITTED to Advanced Materials; G. Vescio*, G. Martín, A. Crespo-Yepes, S. Claramunt, D. Alonso, J. López-Vidrier, S. Estradé, M. Porti, R. Rodriguez, F. Peiró A. Cornet, A. Cirera, M. Nafría. — Low-Power High-Performance Low-Cost Non-Volatile Inkjet Printed HfO2-based ReRAM: from nanoscale to device characterization.

** Contribución del autor: planificación y realización de los experimentos, evaluación de los resultados y redacción de las partes principales del manuscrito.*

Paper VII. The article has been SUBMITTED to the Journal NATURE COMMUNICATIONS; Vescio G., Lombardi L., López-Vidrier J., Martín G., López-Conesa L., Estradé S., Karagiannidis P., Hodge S., Peiró F., Cornet A., Ferrari A. C., Cirera A., Torrisi F. — Flexible fully inkjet-printed Gr/h-BN thin film transistor ; with permission from NATURE COMMUNICATIONS

** Contribución del autor: planificación y realización de los experimentos, evaluación de los resultados y redacción de las partes principales del manuscrito.*

Appendix C. Scientific curriculum vitae

EUROPEAN CURRICULUM VITAE FORMAT

PERSONAL INFORMATION

Name	***Vescio Giovanni***
Address	***Carrer Gayarre 19, E- 08014 (Barcelona) SPAIN***
Telephone	***Work: +34 93 40 39176 , Mobile: +34 693 744 911***
E-mail	***gvescio@el.ub.edu***
Nationality	***Italian***
Date of birth	***25-08-1986 Chişinau (Rep. Moldova)***
Gender	***Male***

EDUCATION AND TRAINING

• Dates (from – to)	*09/2014 - 04/2015* *Academic Visitor at the Cambridge Graphene Centre, Engineering Department, University of Cambridge. Stay in the Nanomaterials and Spectroscopy Group in the Electrical Engineering Division.*
• Dates (from – to)	*02/2012 - present* *Ph.D. student in Engineering and Advanced Technologies line of research in Micro-Nanotechnology for Electronics Devices and Photonic Nanoscopy at Department of Electronics at the Universitat de Barcelona (UB). Project title: "Flexible Transistor Based on Graphene by inkjet Process". National Spanish fellowship holder.*
• Dates (from – to)	*09/2010 – 04/2011* *Erasmus Placement for master thesis at Universitat Politècnica of Catalunya in Barcelona. Title of master thesis: " Muscle fatigue monitoring using a multifrequency bioimpedance technique".*
• Dates (from – to)	*11/2008 – 09/2010*
• Name and type of organisation providing education and training	*University of Calabria (UNICAL), Faculty of Engineering, Degree Course in Electronics Engineering, Microelectronics specialty.*
• Principal subjects/occupational skills covered	✓ *Semiconductor Physics – Integrated Robotics* ✓ *Integrated Circuits and Methods for Implementing* ✓ *Mobile Radio Networks - Circuits and RF devices* ✓ *Microtechnology – Characterization- Optoelectronics – Photonics* ✓ *VLSI - Innovative Architecture - Measuring Instruments* ✓ *Power Electronics - Microcontrollers*
• Title of qualification awarded	*Master's degree with a final mark: 110/110 cum laude on 05/05/2011*

• Dates (from – to)	*09/2005 - 09/2008*
• Name and type of organisation providing education and training	*University of Calabria (UNICAL), Faculty of Engineering,Bachelor degree in Electronic Engineering.*
• Principal subjects/occupational skills covered	✓ *Analog and digital electronics* ✓ *High and low level programming (C + +, Java, VHDL, Assembly)* ✓ *Electronic computers - Electrical engineering – Electrical system* ✓ *Electronic Measurements* ✓ *Electromagnetic Fields - Electromagnetic Compatibility* ✓ *Transmission and Propagation* *Internship and thesis, for 4 months, at UNICAL. Thesis title: " Test for spectral analysis of high resolution DACs using oversampling and ADC low-resolution."*
• Title of qualification awarded	*Bachelor's Degree with a final mark: 105/110 (on 24-09-2008)*
• Dates (from – to) *• Name and type of organisation* • Title of qualification awarded	*09/2000 – 07/2009* *State High School Institute "F. Fiorentino" in Lamezia Terme* Diploma of Education Classical address P.N.I. with a final vote:100/100

PERSONAL SKILLS AND COMPETENCES

Acquired in the course of life and career but not necessarily covered by formal certificates and diplomas.

MOTHER TONGUE **[ITALIAN]**

OTHER LANGUAGES

	[English]	**[Spanish]**	**[Catalan]**	**[French]**
• Reading skills	[Good]	[Excellent]	[Excellent]	[Elementary]
• Writing skills	[Good]	[Excellent]	[Elementary]	[Elementary]
• Verbal skills	[Good]	[Excellent]	[Good]	[Elementary]

•

TECHNICAL SKILLS AND COMPETENCES
With computers, specific kinds of equipment, machinery, etc.

Good PC knowledge in terms of hardware and software.

- ✓ *InkJet printing technology (Dimatix Fujifilm and Xennia Xenjet)*
- ✓ *User of AFM and C-AFM, Raman and FE-SEM (EDX and FIB)*
- ✓ *Probe station microscope Cascade and custom station*
- ✓ *Keithley 4200-scs, Agilent B1500A and Agilent LCR 4294*
- ✓ *Software related course of study: Orcad (excellent), Labview (excellent)*
- ✓ *Programming: Java (basic), C + + (basic), Matlab (excellent), VHDL (excellent), AVR(good)*
- ✓ *Operating Systems: Windows (excellent), Linux (basic)*
- ✓ *Office Package (excellent)*

OTHER SKILLS AND COMPETENCES
Competences not mentioned above.

Ability to organize and manage the work. Preparedness initiative and leaderschip.

- ✓ Winner FPU Spanish National Fellowship (2013-2017)
- ✓ Winner Erasmus Placement 2010-2011 at UPC Barcelona (Spain) for the period 09/2010 – through 04/2011
- ✓ Winner Erasmus scholarship - LLP 2009/2010 at UAB Barcelona (Spain) for the period 09/2009 - through 09/2010.

Published Articles

G. Vescio, L. Lombardi, J. López-Vidrier, P. Karagiannidis, S. Hodge, G. Martín, L. Conesa-Lopez, S. Estradé, F. Peiró, A. Cornet, A. C. Ferrari, A. Cirera, and F. Torrisi, "Fully inkjet-printed hBN – Graphene 2d transistors on flexible substrate", 2017. ***SUBMITTED***

G. Vescio, G. Martín, A. Crepo-Yepes, D. Alonso, S. Claramunt, J. López-Vidrier, S. Estradé, M. Porti, R. Rodriguez, A. Cornet Calveras, F. Peiró, A. Cirera Hernandez, M. Nafria, and X. Aymerich, "Low-Power High-Performance Low-Cost Non-Volatile Inkjet Printed HfO2-based ReRAM: from nanoscale to device characterization", 2017. ***SUBMITTED***

G. Vescio, A. Crepo-Yepes, D. Alonso, S. Claramunt, M. Porti, R. Rodriguez, A. Cornet Calveras, A. Cirera Hernandez, M. Nafria, and X. Aymerich, "Inkjet Printed HfO2-based ReRAMs: first demonstration and performance characterization," *IEEE Electron Device Lett.*, vol. **38**, no. 4, pp. 457–460, 2017.

J. Arrese, G. Vescio, E. Xuriguera, B. Medina-Rodriguez, A. Cornet, and A. Cirera, "Flexible hybrid circuit fully inkjet-printed: Surface mount devices assembled by silver nanoparticles-based inkjet ink," *J. Appl. Phys.*, vol. **121**, no. 10, p. 104904, Mar. 2017.

G. Vescio, J. López-Vidrier, R. Leghrib, A. Cornet, and A. Cirera, "Flexible inkjet printed high-k HfO 2 -based MIM capacitors," *J. Mater. Chem. C*, vol. **4**, no. 9, pp. 1804–1812, 2016.

M. Gardon, O. Monereo, S. Dosta, G. Vescio, A. Cirera, and J. M. Guilemany, "New procedures for building-up the active layer of gas sensors on flexible polymers," *Surf. Coatings Technol.*, vol. **235**, pp. 848–852, Nov. 2013.

B. Medina-Rodriguez, F. Ramos, G. Vescio, X. Arrese, A. Varea, and A. Cirera, "Fabrication, Performances and Aging of Flexible Gas Sensor Platforms," *J. Mater. Sci. Eng. B*, vol. **5**, no. 4, pp. 170–176, Apr. 2015.

Proceedings

O. Monereo, S. Claramunt, G. Vescio, H. Lahlou, R. Leghrib, J. D. Prades, A. Cornet, and A. Cirera, "Carbon nanofiber flexible gas sensor modulated by UV light," in *2013 Transducers & Eurosensors XXVII: The 17th International Conference on Solid-State Sensors, Actuators and Microsystems (TRANSDUCERS & EUROSENSORS XXVII)*, 2013, pp. 1154–1157.

G. Vescio, J. Rosell, L. Nescolarde, and G. Giovinazzo, "Muscle Fatigue Monitoring Using a Multifrequency Bioimpedance Technique," in IFMBE Proceedings, vol. **37**, 2011, pp. 1257–1260.

Participations in congress

- BioEl2016 International Winterschool on Bioelectronics, Kirchberg in Tirol, Austria. March 19 2016, Poster G. Vescio et al.; A

- MRS 2015 Fall MEETING Boston, Congress Center, Boston, Estados Unidos , November 2015, Poster, G. Vescio et al.;

- SURFOCAP'15 Agadir, Agadir, 27-28 of May 2015, Oral Presentation, G. Vescio et al.;

- ICREA Workshop on Graphene Nanobiosensors, Barcelona 27-27 of May 2015, Oral Presentation, O. Olmedo, G. Vescio et al.;

- E-MRS Spring Meeting Lille 26-30 of May 2014, Oral Presentation symposium S, G.Vescio et al.;

- E-MRS Spring Meeting Lille 26-30 of May 2014, Oral Presentation symposium I, G.Vescio et al.;

- E-MRS Spring Meeting Lille 26-30 of May 2014, Oral Presentation symposium B, B.Mediana et al.;

- E-MRS Spring Meeting Lille 26-30 of May 2014, dos Poster symposium B, O.Monereo et al.;

- E-MRS Fall Meeting Warsaw 15-19 of September 2013, Oral Presentation symposium Paper Electronics